THE ACQUISITION AND ANALYSIS OF CRANIOFACIAL DATA IN THREE DIMENSIONS

Amanda Helen Abbott, B.D.S., B.Sc.Dent. (Hons).

A thesis submitted for the degree of Doctor of Philosophy

Volume 2 Figures

Department of Dentistry,
The University of Adelaide
December 1988

TABLE OF CONTENTS

VOLUME 2 FIGURES

PREFACE

A stereo-viewer is provided in the pocket on the inside of the back cover of this volume to facilitate fusing of the three dimensional CT reconstructions and the stereo wire frame models.

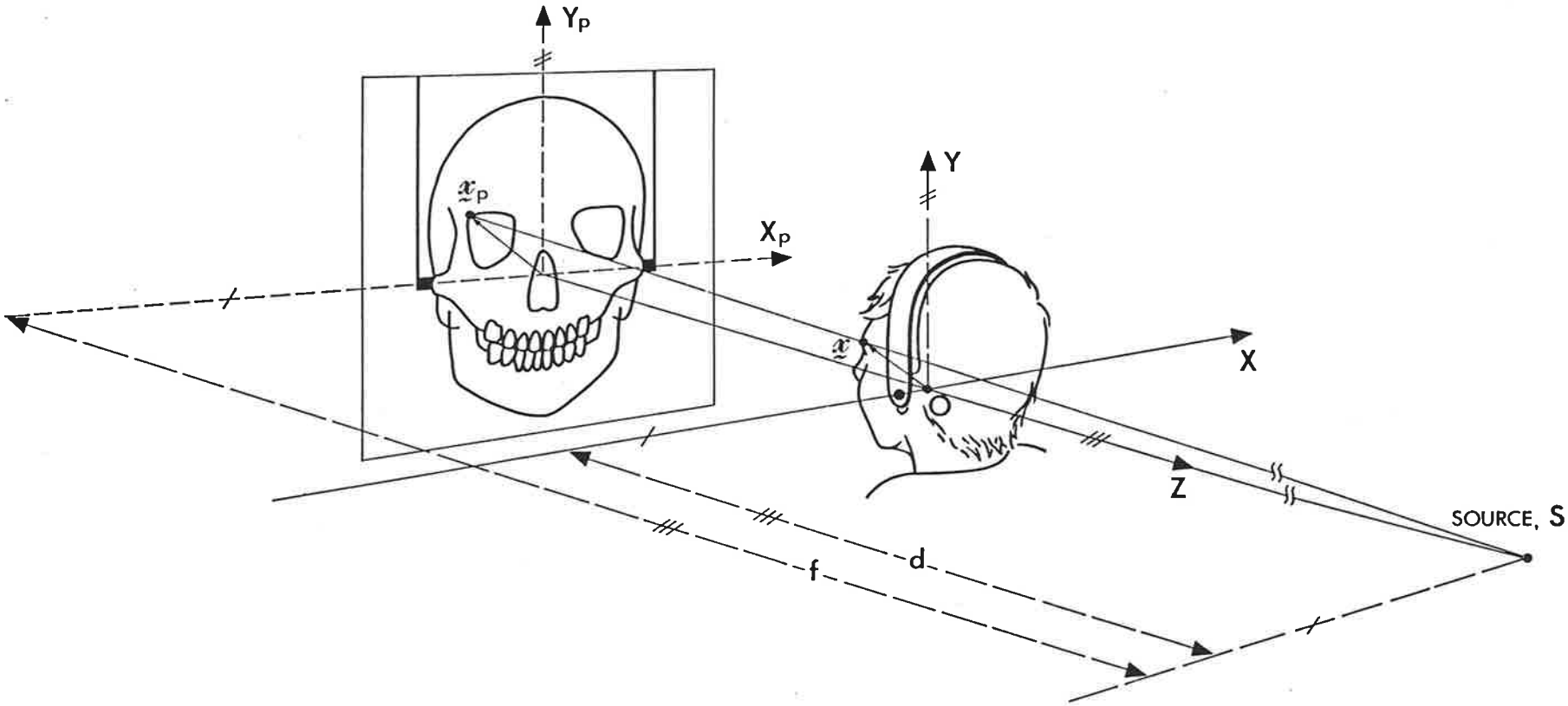

Figure 2.1 The geometry of a typical radiographic configuration.

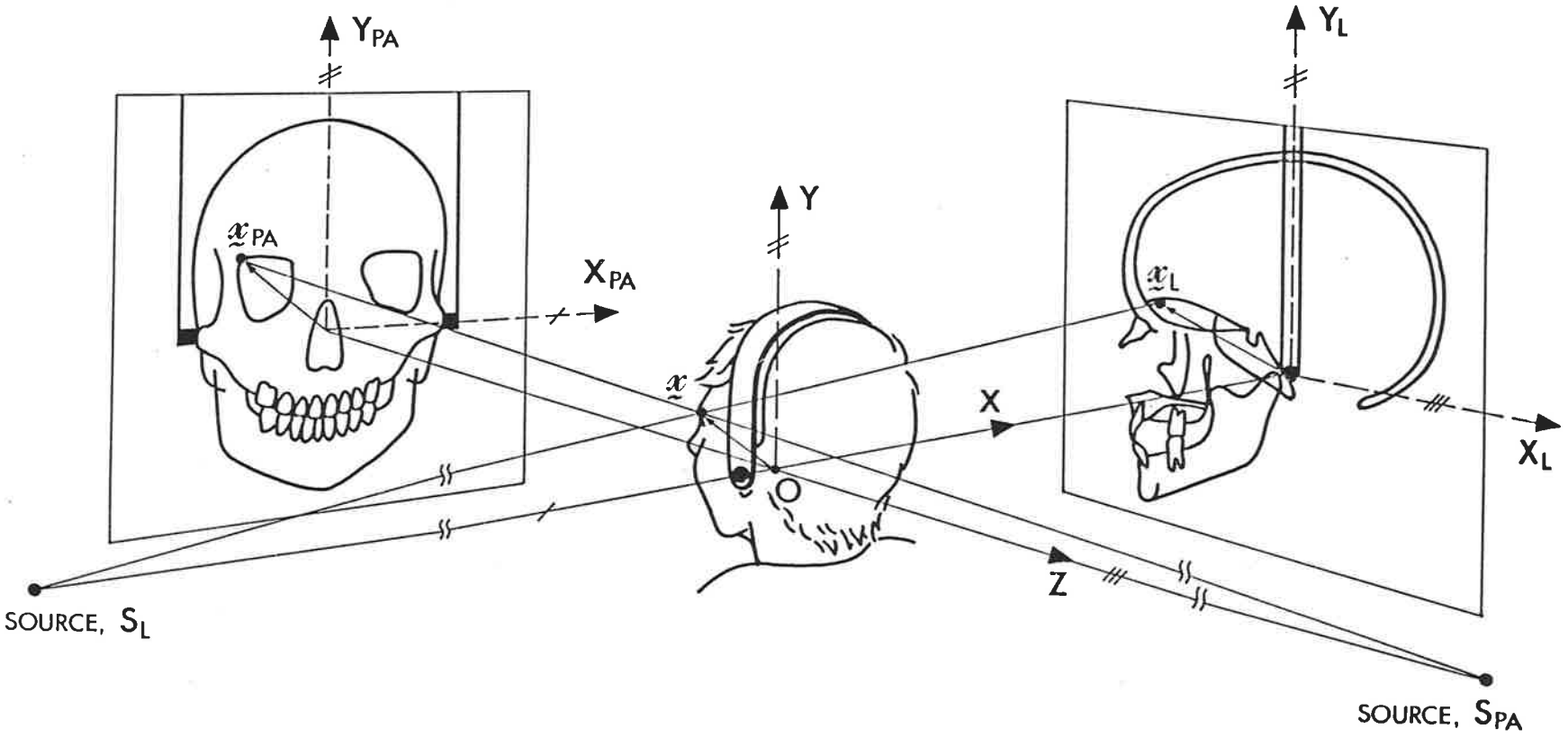

Figure 2.2 (a) The geometry for the Adelaide Dental Hospital biplanar configuration. The two exposures are achieved by rotating the patient rather than through the use of a second radiographic unit.

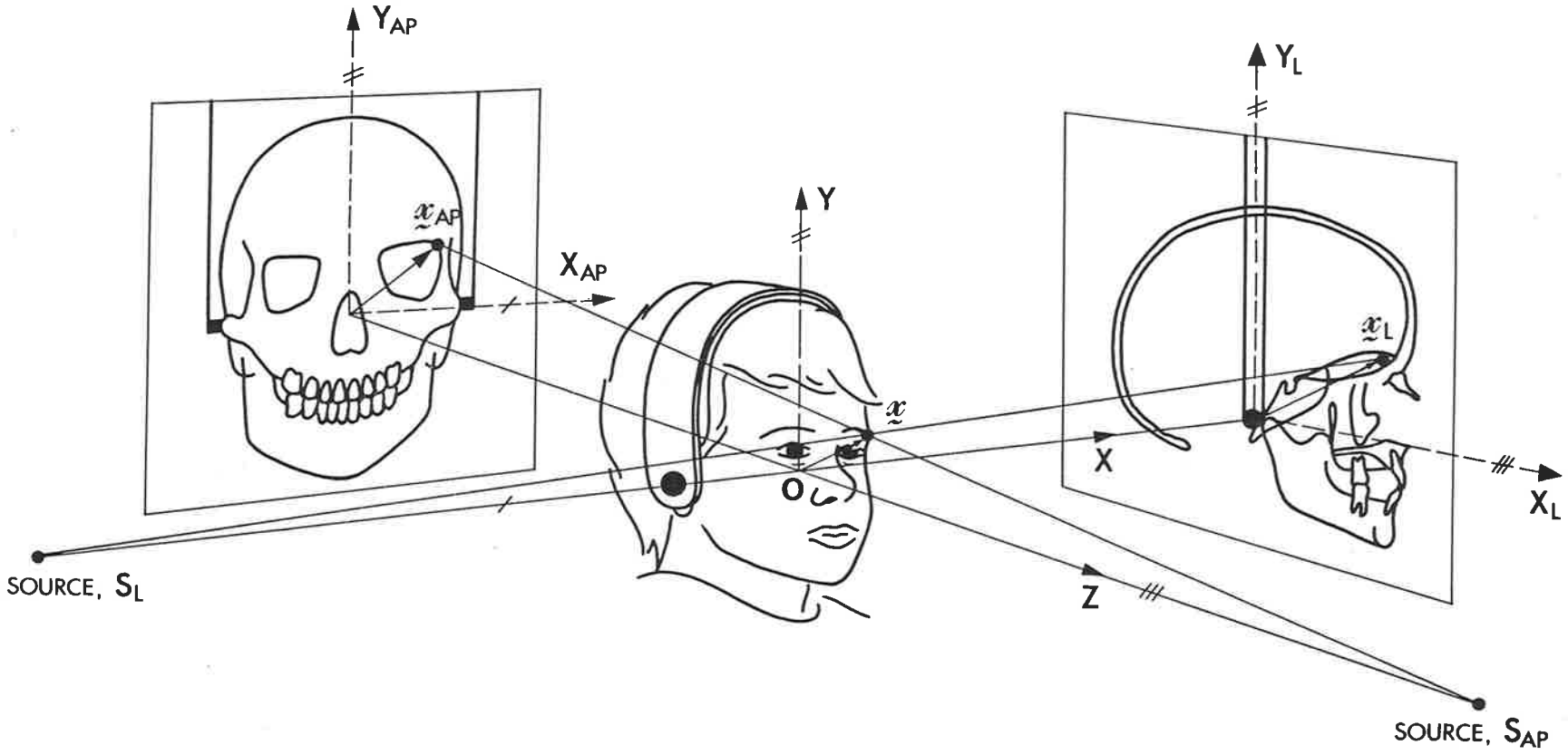

Figure 2.2 (b) The geometry for the Adelaide Children's Hospital simultaneous biplanar configuration.

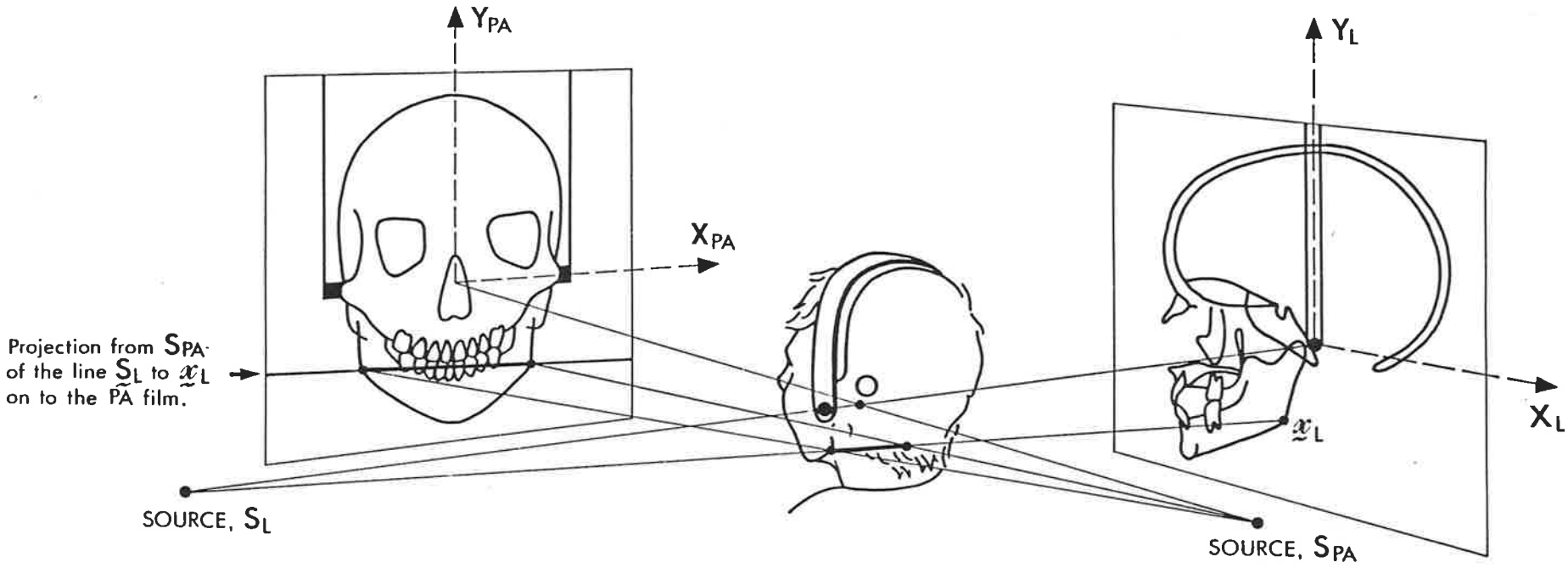

Figure 2.3 The projection on to the postero-anterior (PA) film of the line defined by a landmark located on the lateral film and the source, S_L.

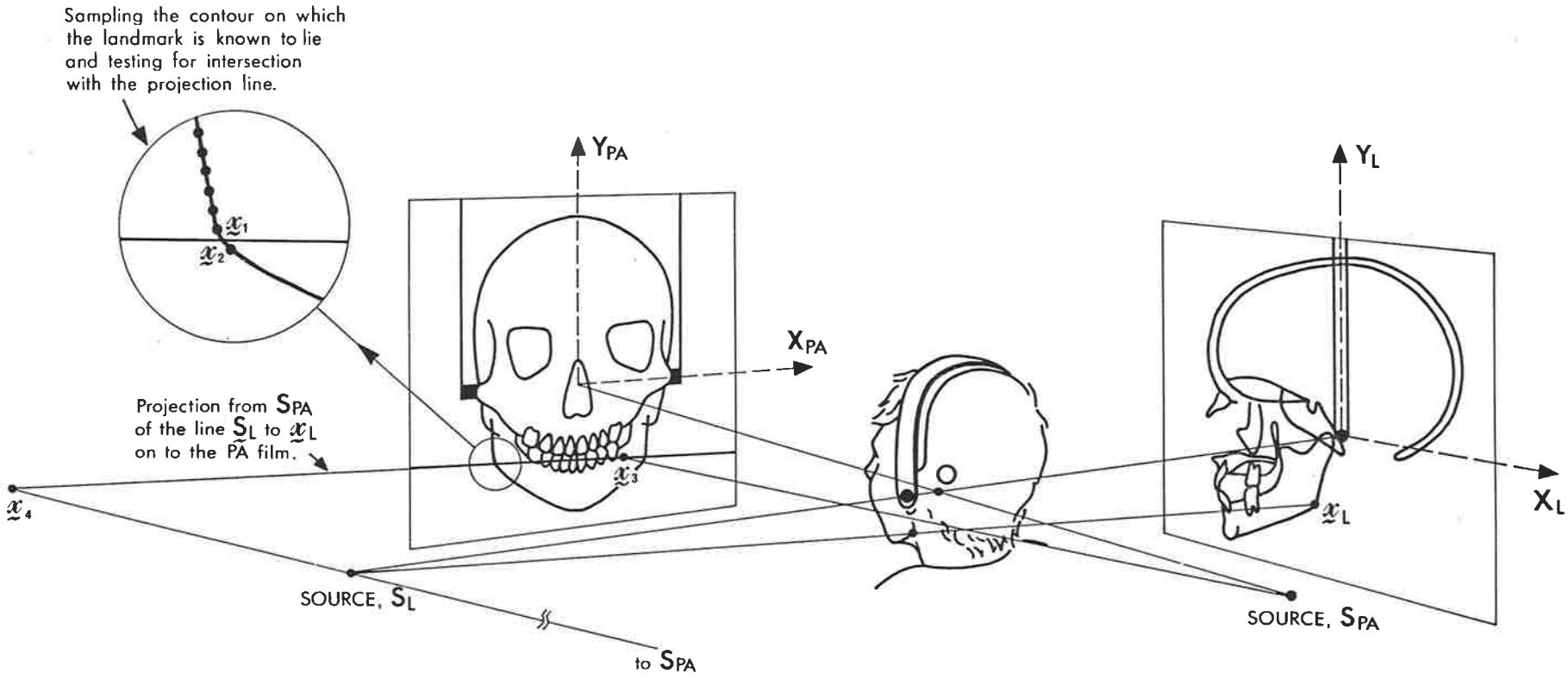

Figure 2.4 Intersection of a projection line with a contour to determine the three dimensional location of a difficult to locate landmark.

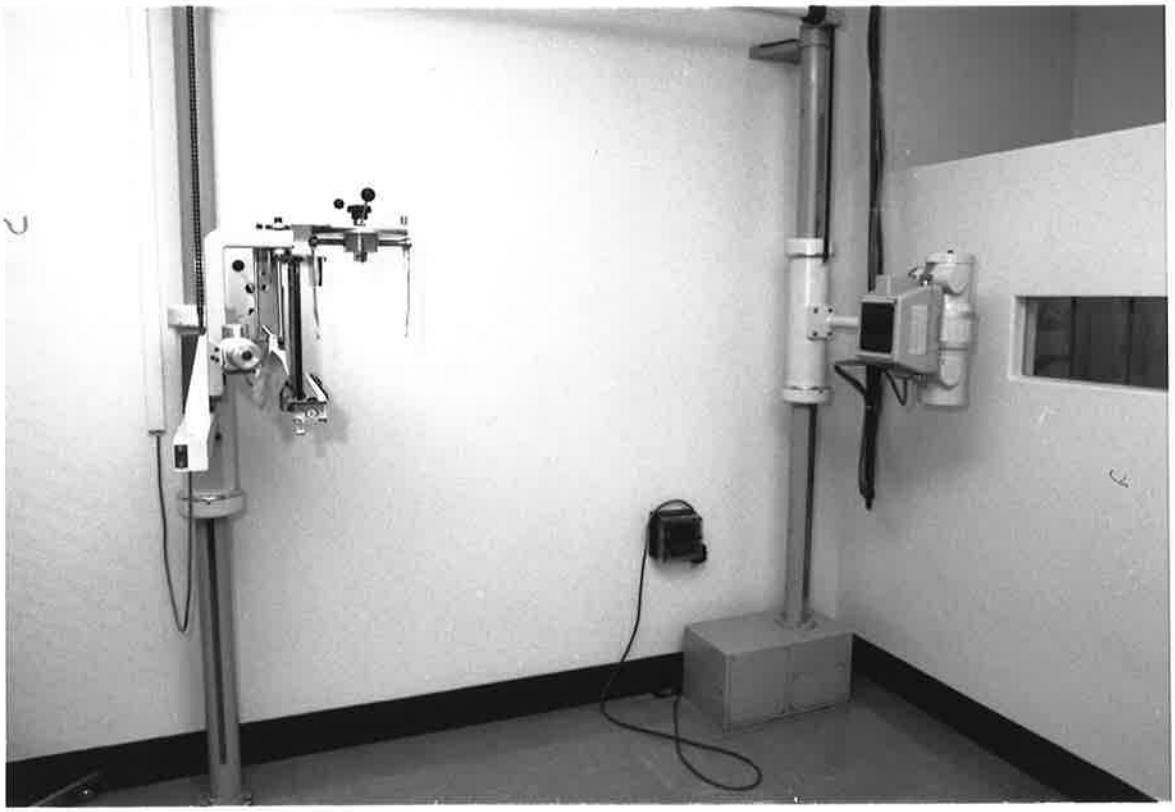

Figure 2.5 (a) General view of the radiographic unit used at the Adelaide Dental Hospital.

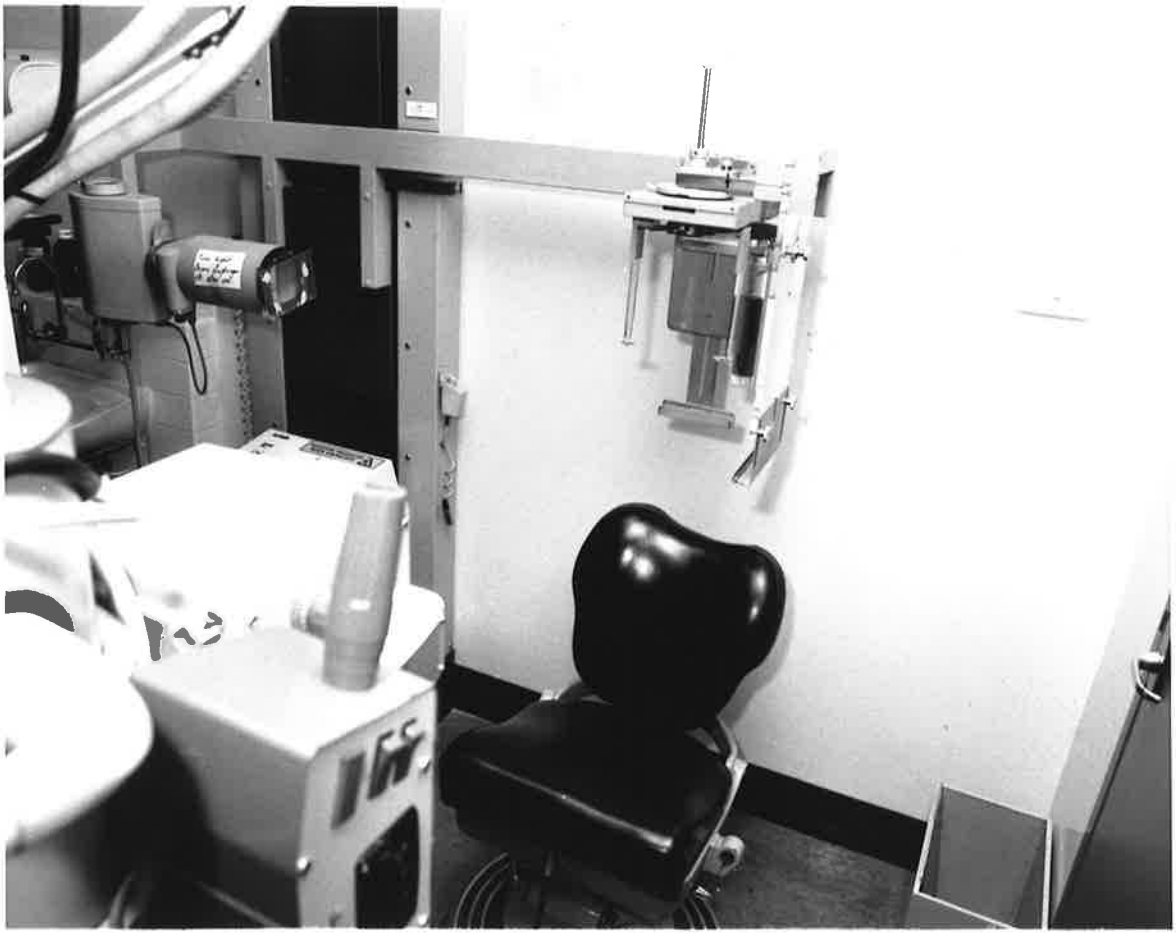

Figure 2.5 (b) General view of the biplanar radiographic unit used at the Adelaide Children's Hospital.

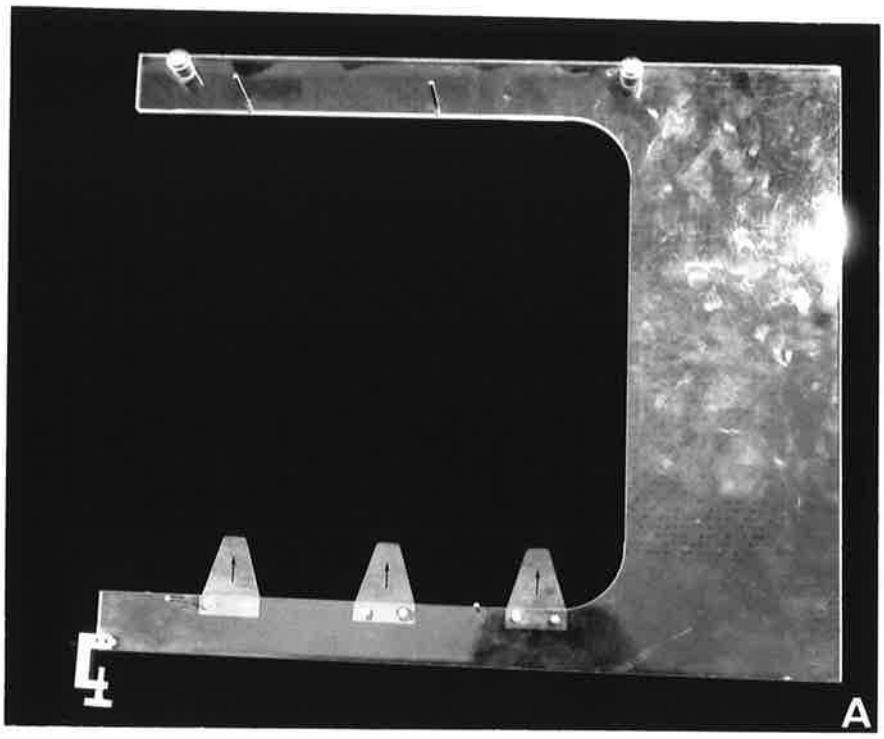

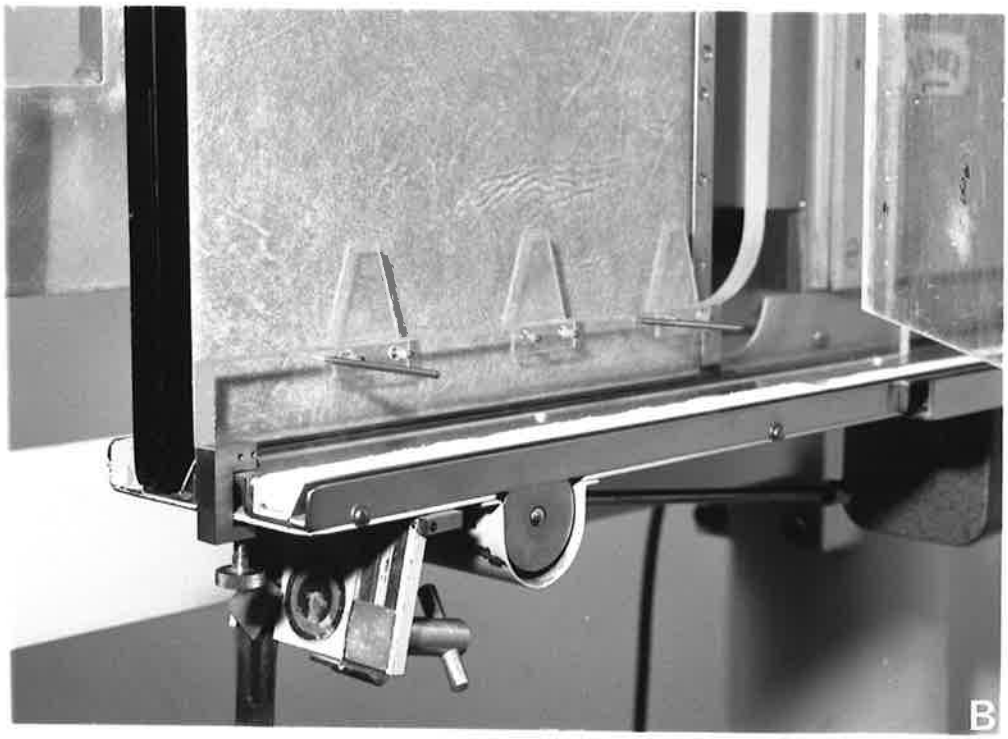

Figure 2.6 (a) Acrylic alignment sheet, with metal fiducial markers indicated by arrows.

(b) Acrylic alignment sheet rigidly mounted immediately in front of the film cassette.

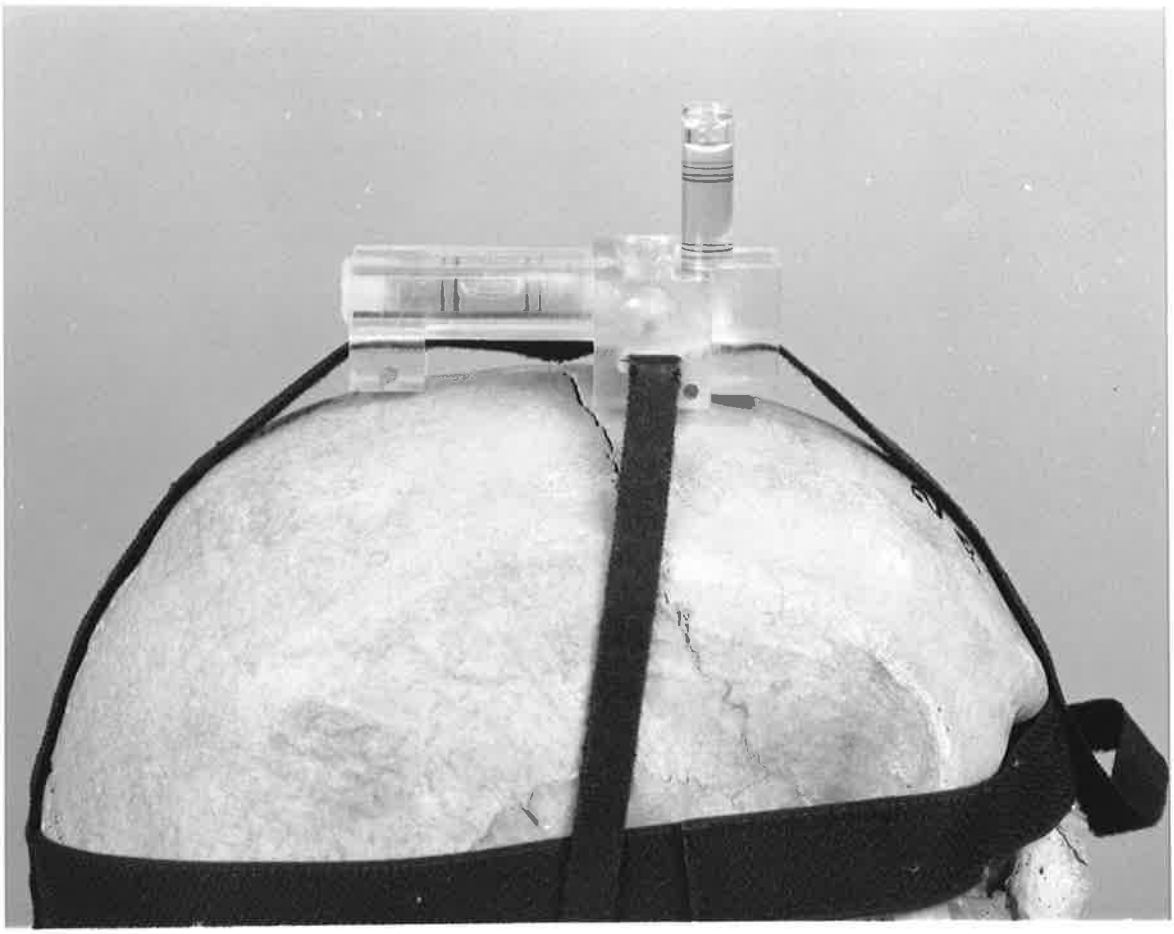

Figure 2.7 Levelling device used at the Adelaide Dental Hospital to ensure that the head remains level between lateral and postero-anterior (PA) exposures.

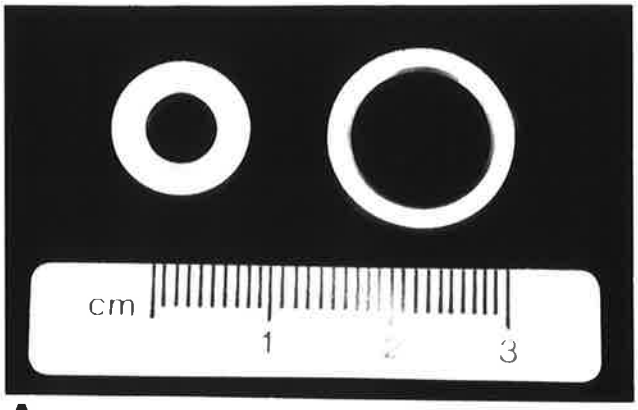

A

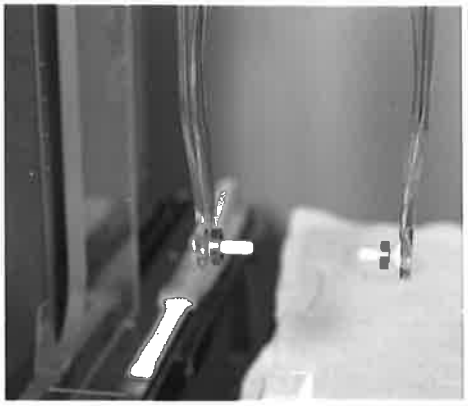

B

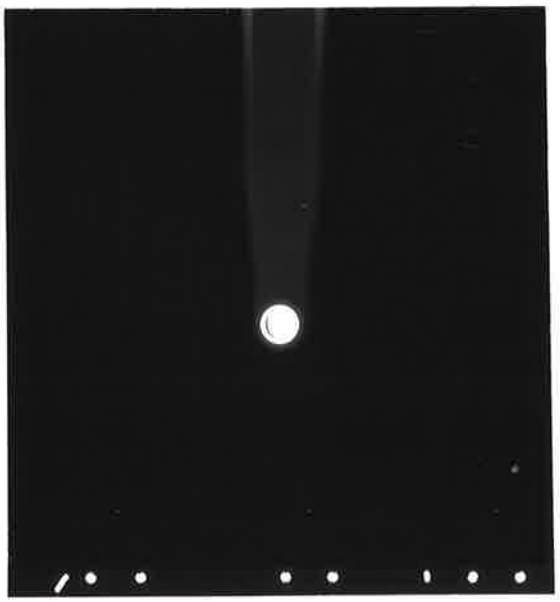

C

Figure 2.8 (a) **The two rings placed on the ear rods for alignment of the radiographic unit.**

(b) Alignment rings in place on ear rods.

(c) Alignment of the anode with the centre of the ear rods is achieved when the projected images of the two brass rings are concentric.

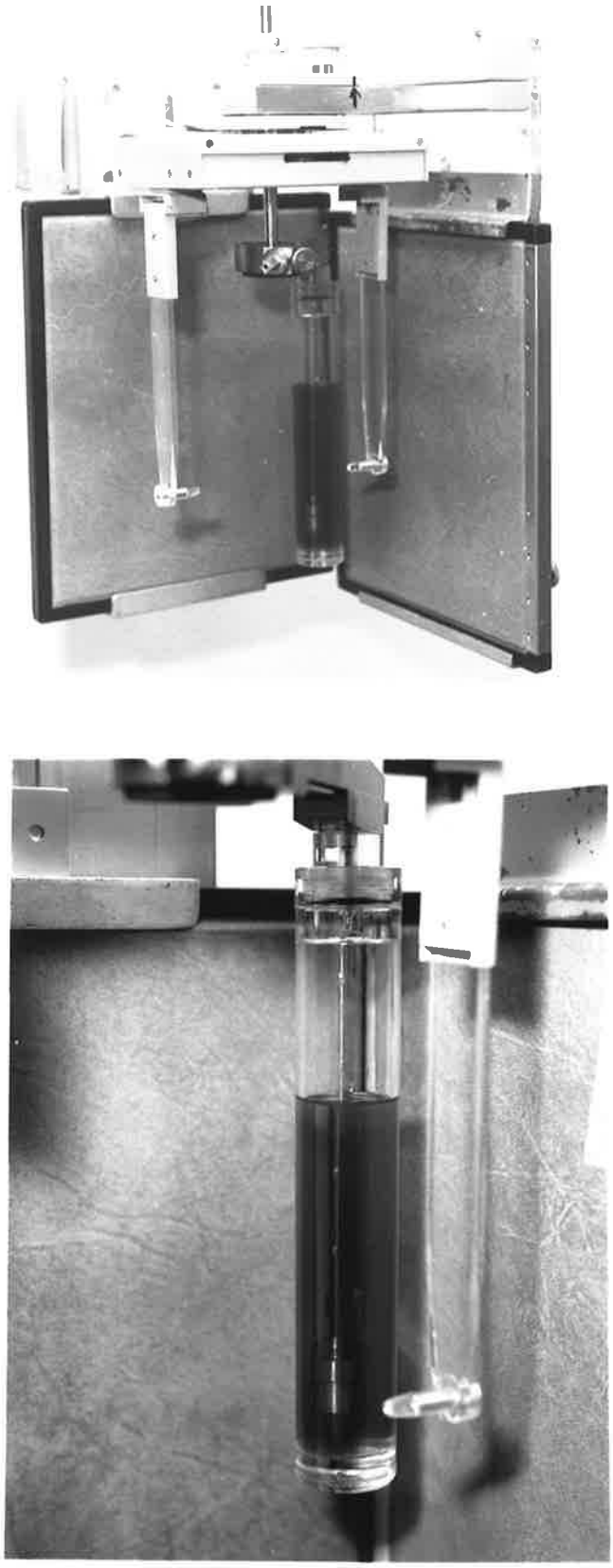

Figure 2.9 Oil damped plumb line positioned such that it is projected on to both the antero-posterior (AP) and lateral films for alignment purposes.

Figure 2.10 Brass rod with fixing screw to ensure the two independent anodes of the biplanar radiographic equipment are maintained at the same height.

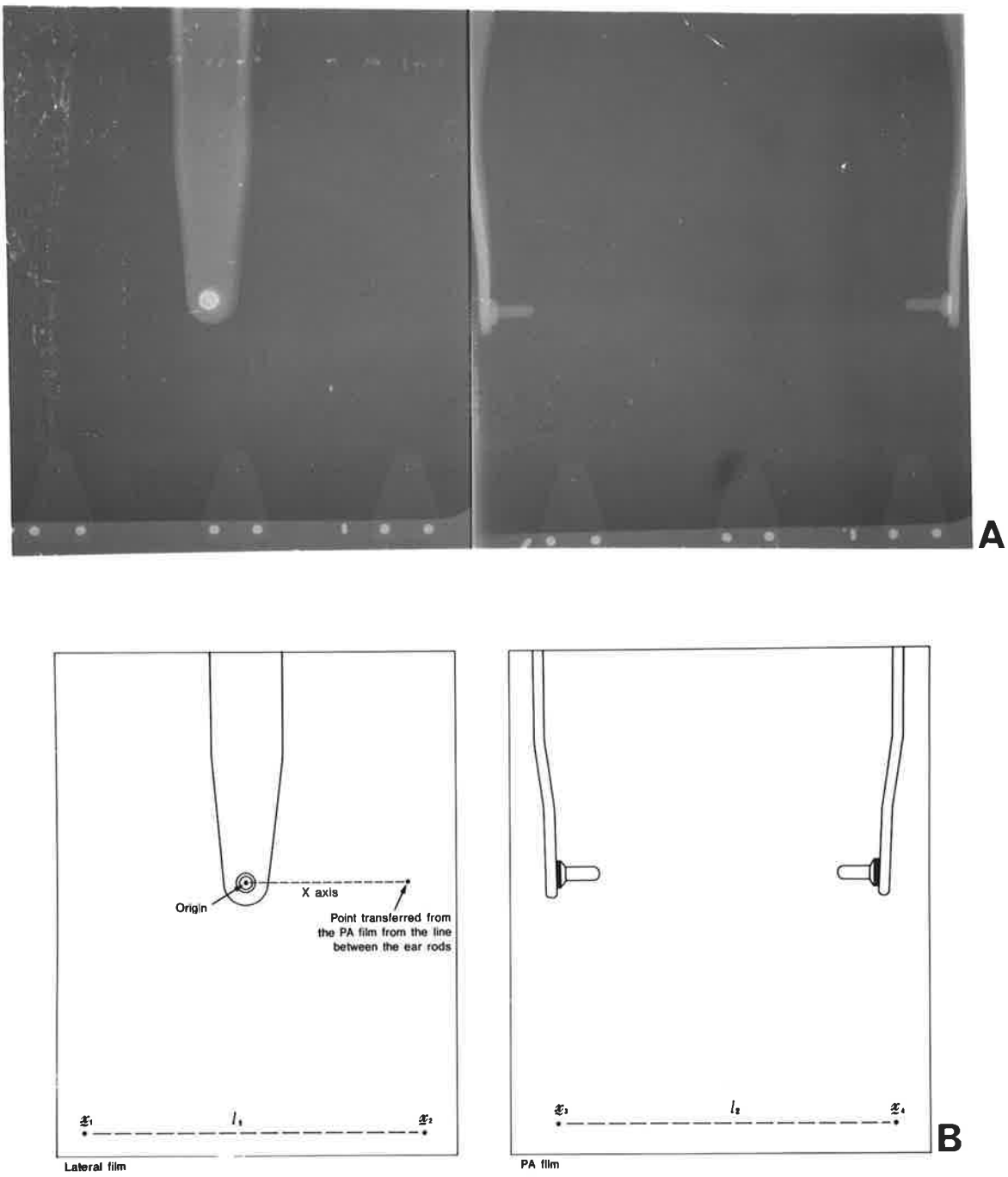

Figure 2.11 (a) Lateral and postero-anterior (PA) radiographs showing the acrylic alignment sheet used at the Adelaide Dental Hospital, with the head holder positioned appropriately for these radiographs.

(b) Definition of points and lines used for alignment of the lateral and postero-anterior (PA) radiographs using the fiducial markers.

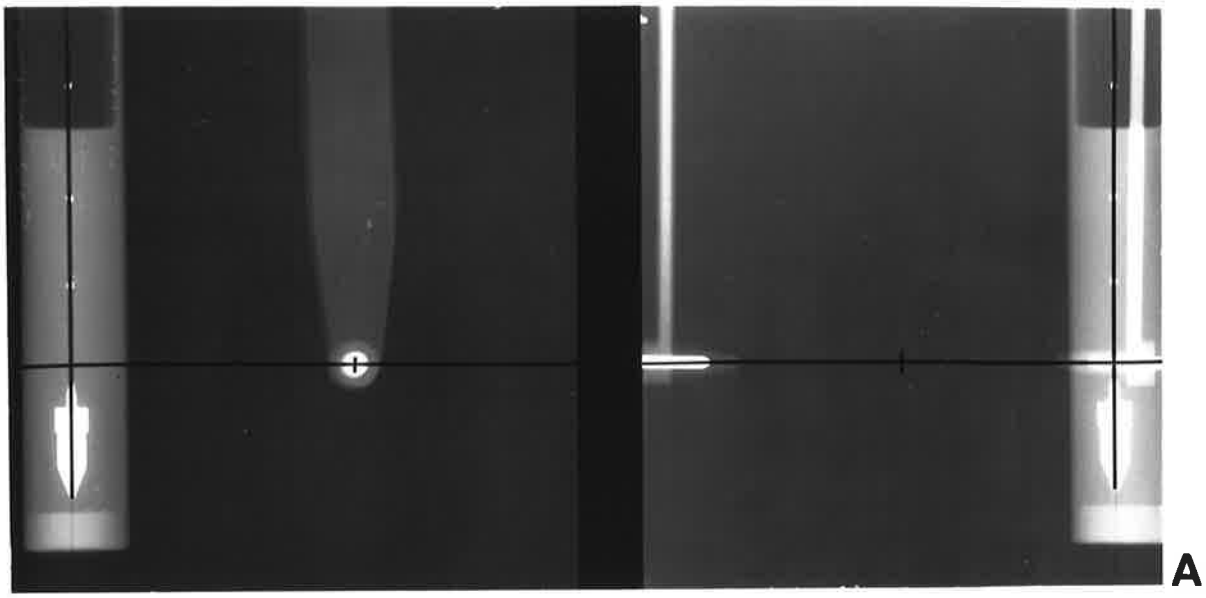

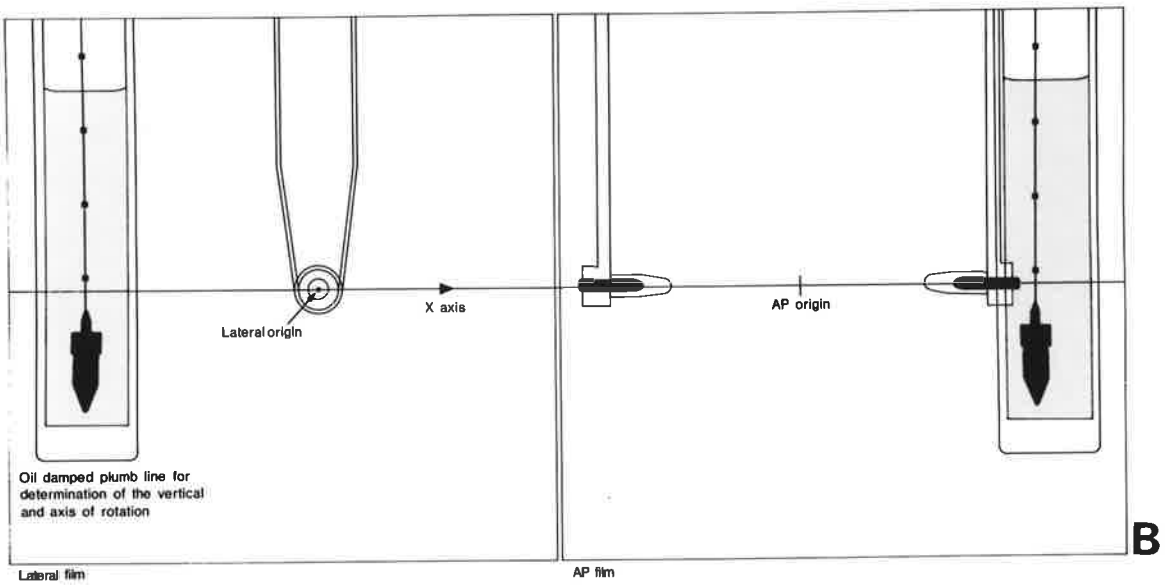

Figure 2.12 (a) Lateral and antero-posterior (AP) radiographs showing the plumb line used for alignment of the simultaneous biplanar radiographs at the Adelaide Children's Hospital, and

(b) diagrammatic representation.

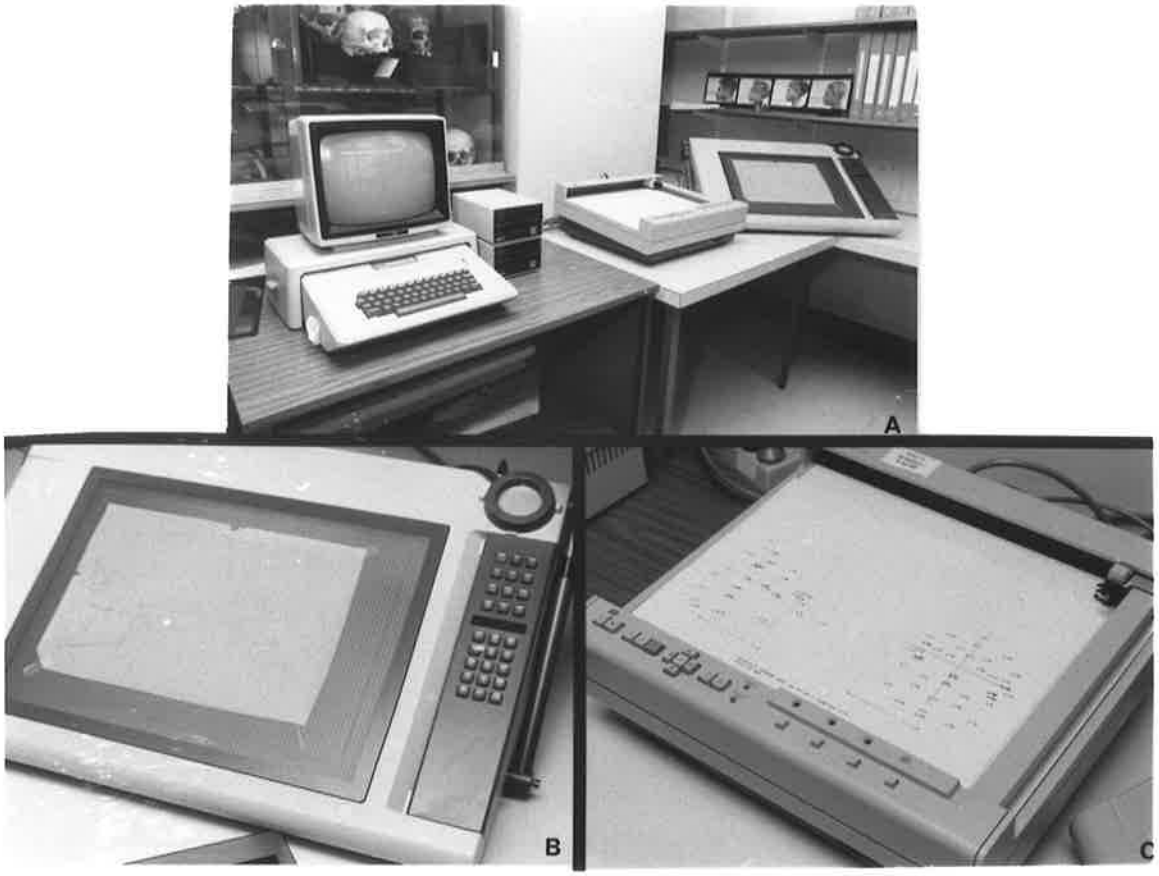

Figure 2.13 The facilities used for data collection of coordinates from tracings of radiographs (and CT images) -

(a) general view of Apple plus, plotter and digitizer,

(b) digitizer, and

(c) plotter.

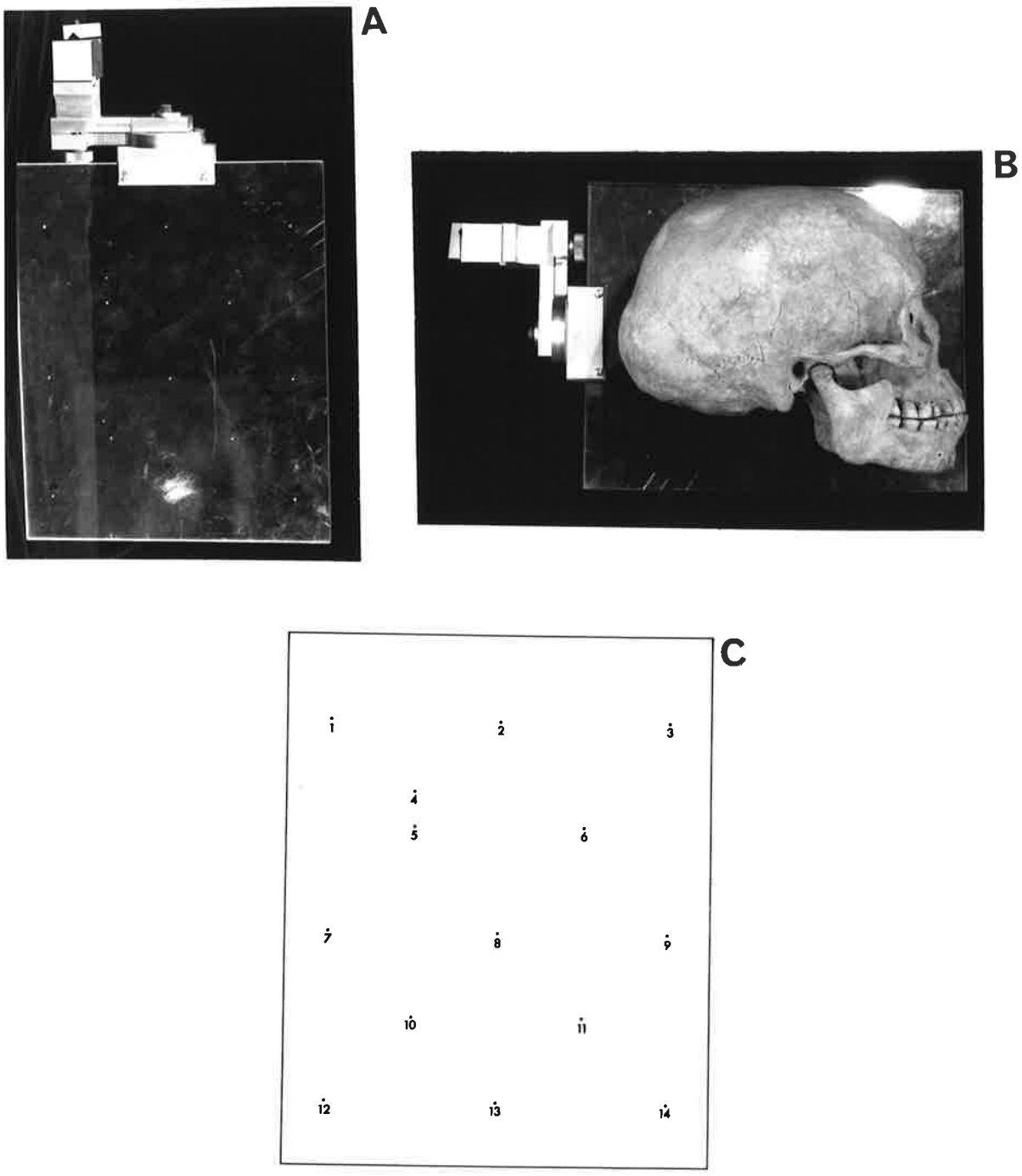

Figure 2.14 (a) Acrylic test object.

(b) Comparison of the relative size of the acrylic test object with a skull.

(c) Illustration of the position of the metal markers within the acrylic test object.

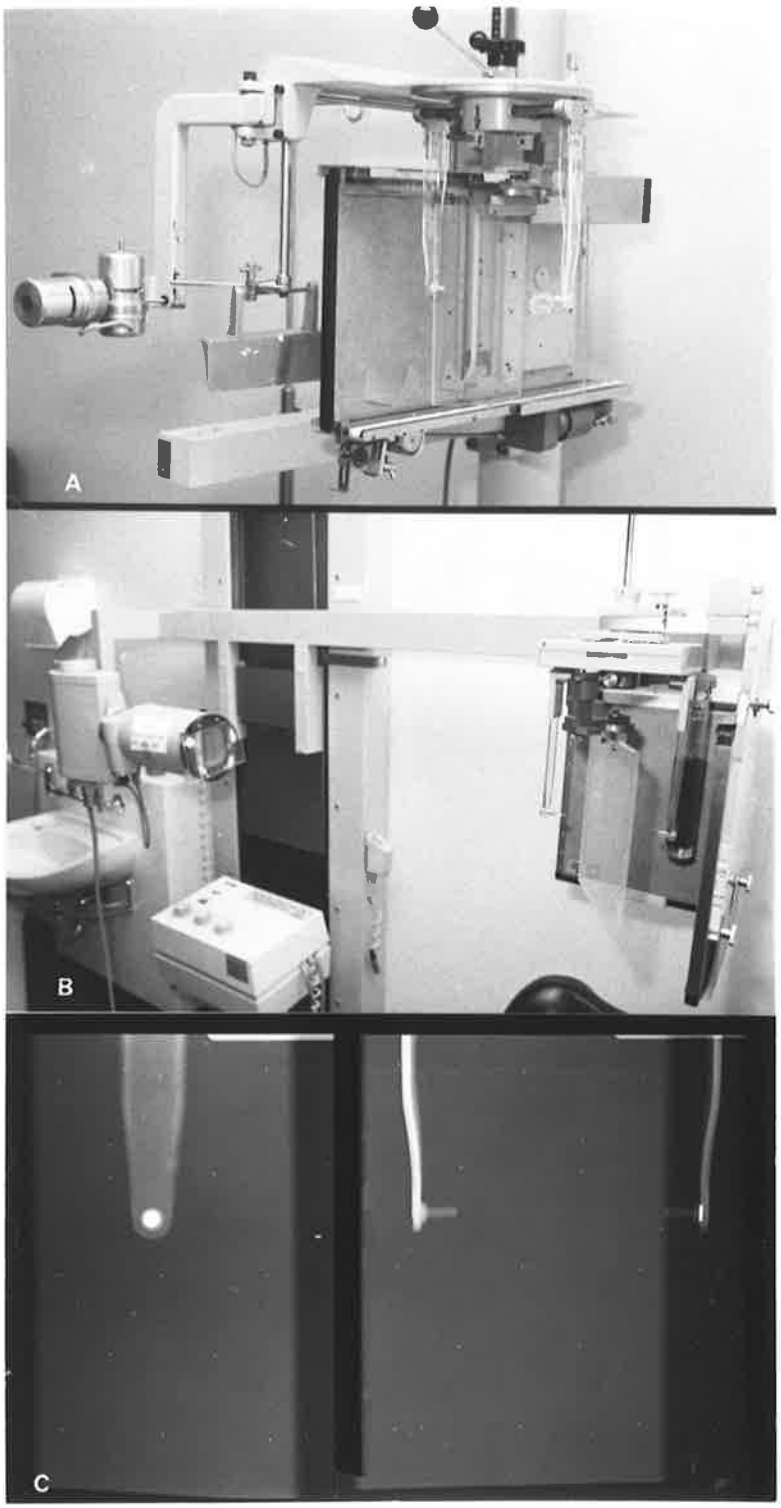

Figure 2.15 Acrylic test object mounted for biplanar radiography at the

(a) Adelaide Dental Hospital (subject rotated through 90° between exposures), and

(b) Adelaide Children's Hospital (simultaneous exposures).

(c) An example biplanar radiograph of the acrylic test object.

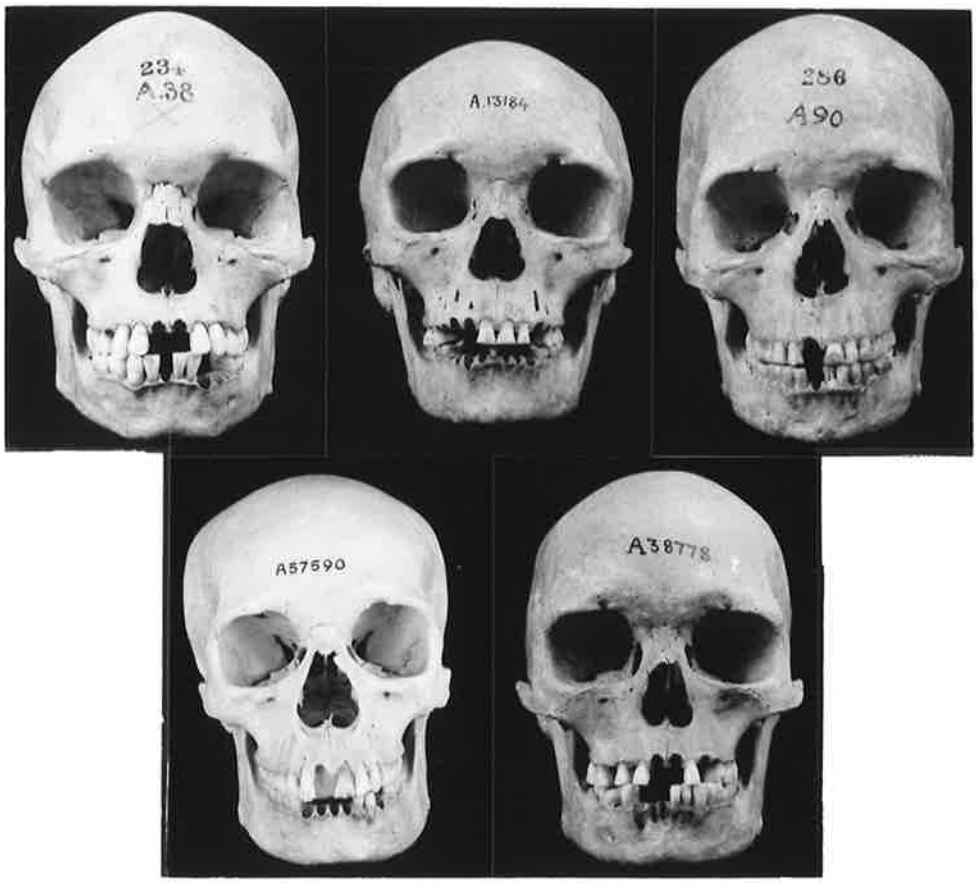

Figure 2.16 The five Australian Aboriginal skulls from the South Australian Museum's skeletal collection studied in this thesis.

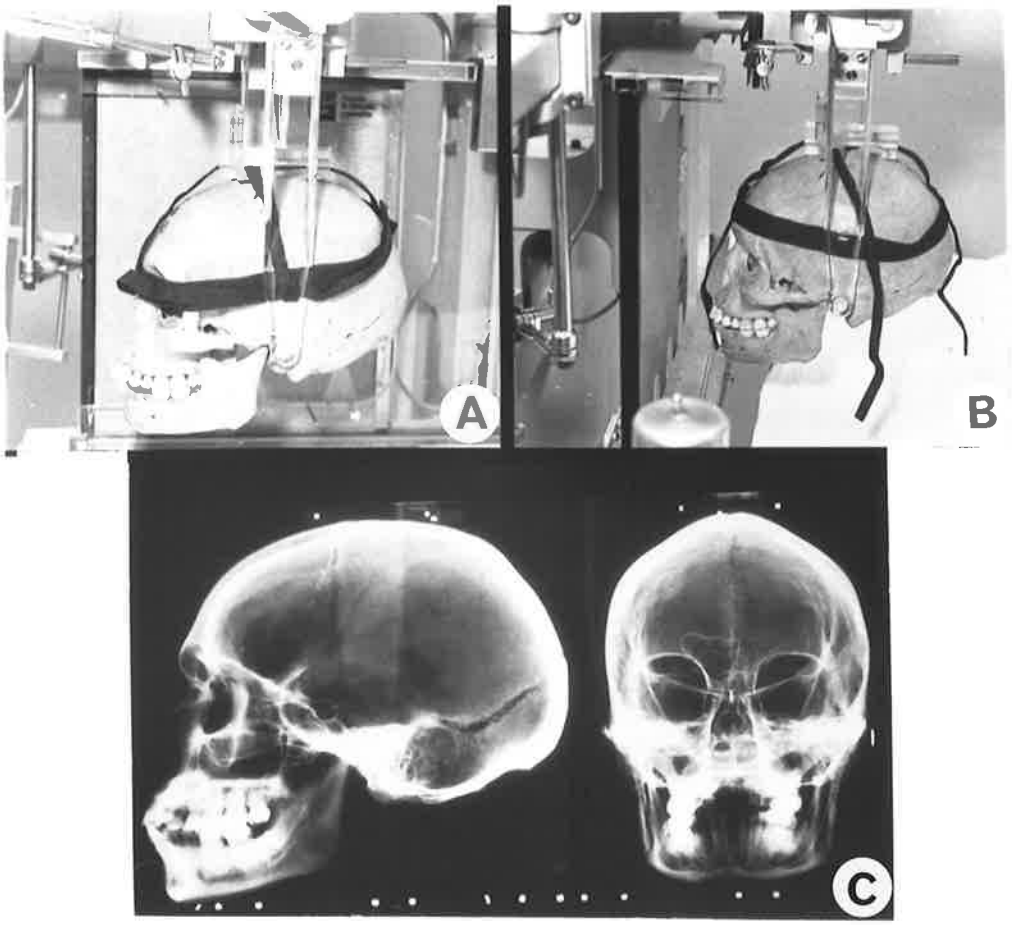

Figure 2.17 (a) Skull positioned along the Frankfort horizontal for a lateral radiograph at the Adelaide Dental Hospital.

(b) Skull positioned along the Frankfort horizontal for a postero-anterior (PA) radiograph at the Adelaide Dental Hospital.

(c) Corresponding radiographs.

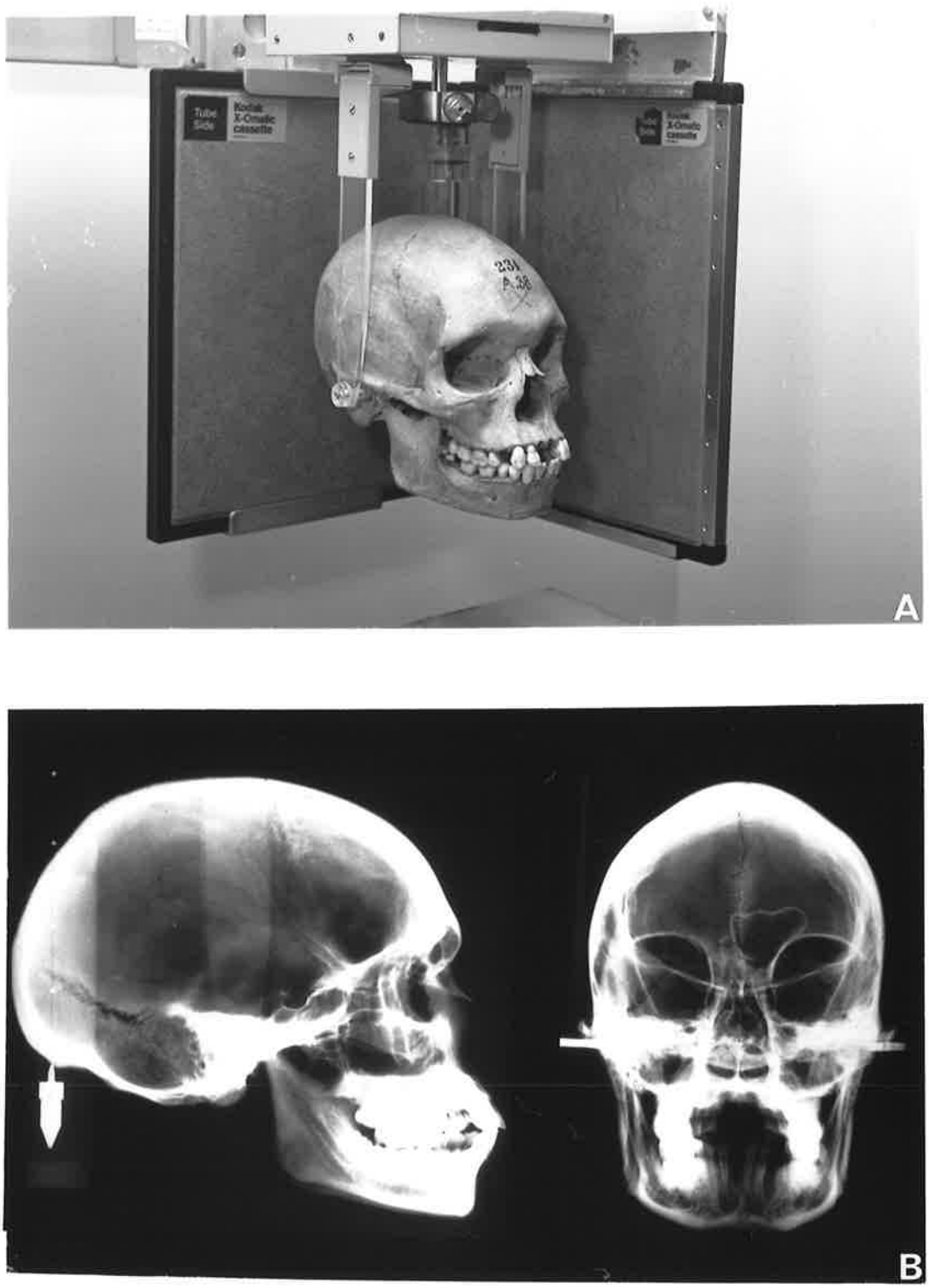

Figure 2.18 (a) Skull positioned along the Frankfort horizontal for simultaneous biplanar radiographs at the Adelaide Children's Hospital.

(b) Corresponding radiographs.

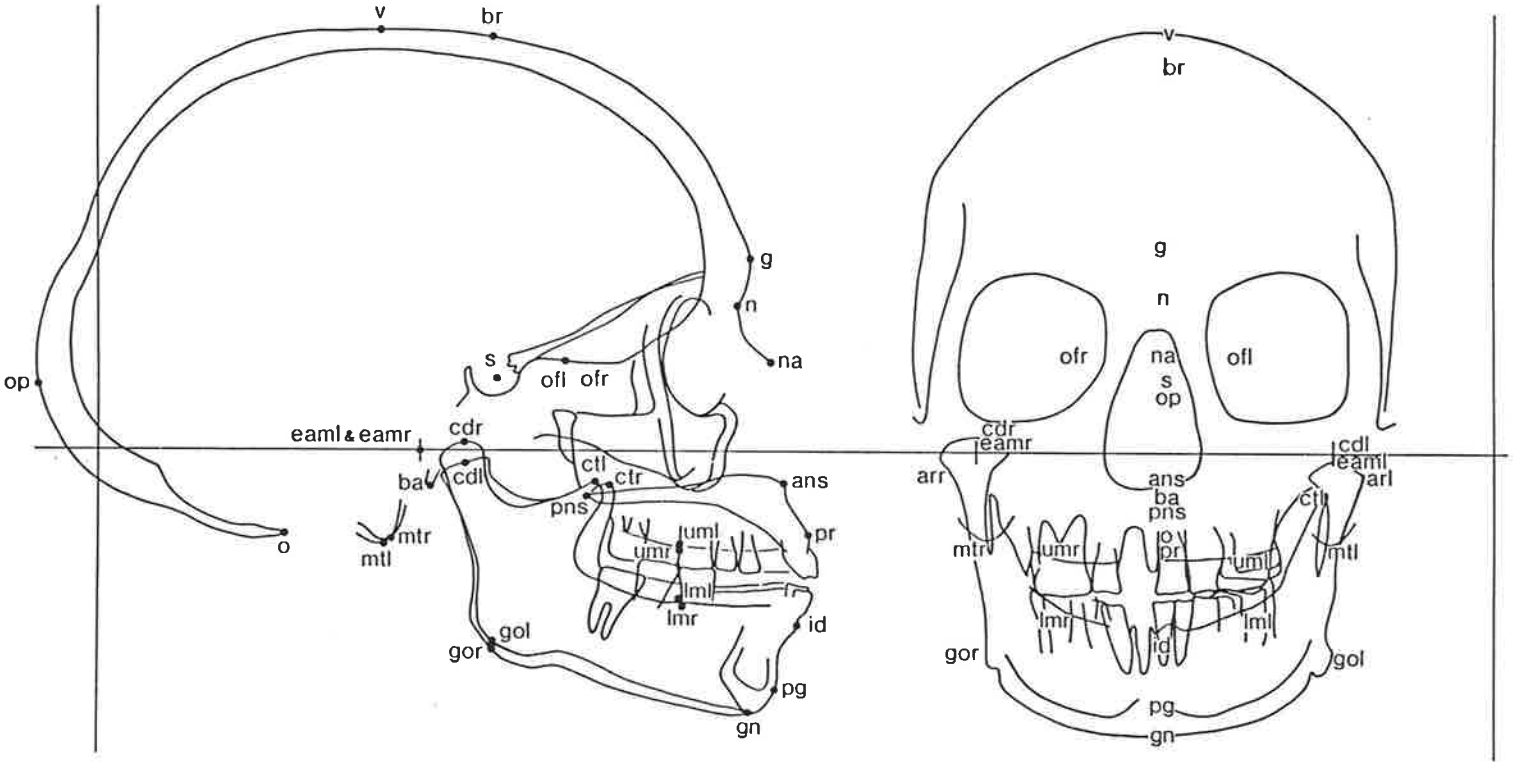

Figure 2.19 Position of the biplanar osseous landmarks used in this study. It should be noted that landmarks are identified on the lateral projection by name and dot, and contours, on which they lie, are identified on the coronal projection by name near contour but without dot.

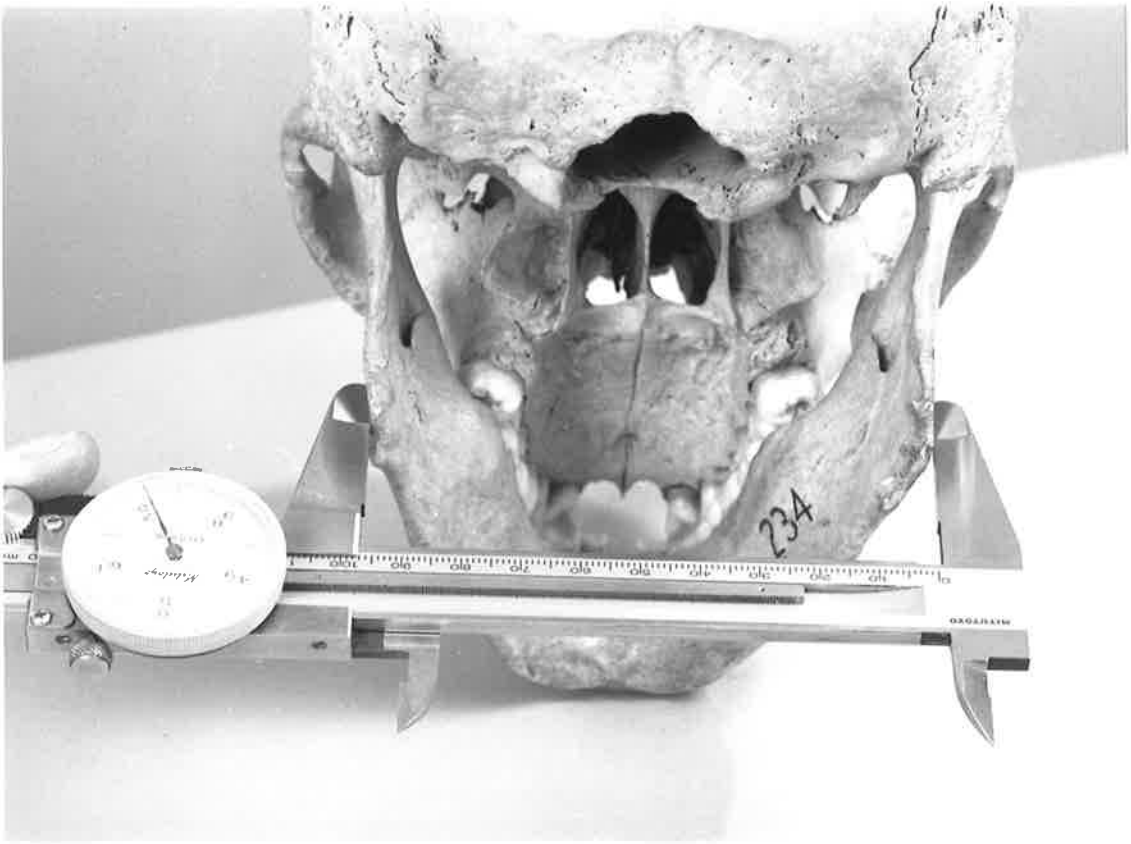

Figure 2.20 An example of the use of calipers for craniometric measurement.

Figure 2.21 (a) Pre-operative and

(b) post-operative photographs of the Treacher Collins Syndrome patient.

Figure 2.22 Patient position in cephalostat for simultaneous biplanar radiographs (that is, lateral and antero-posterior (AP) projections).

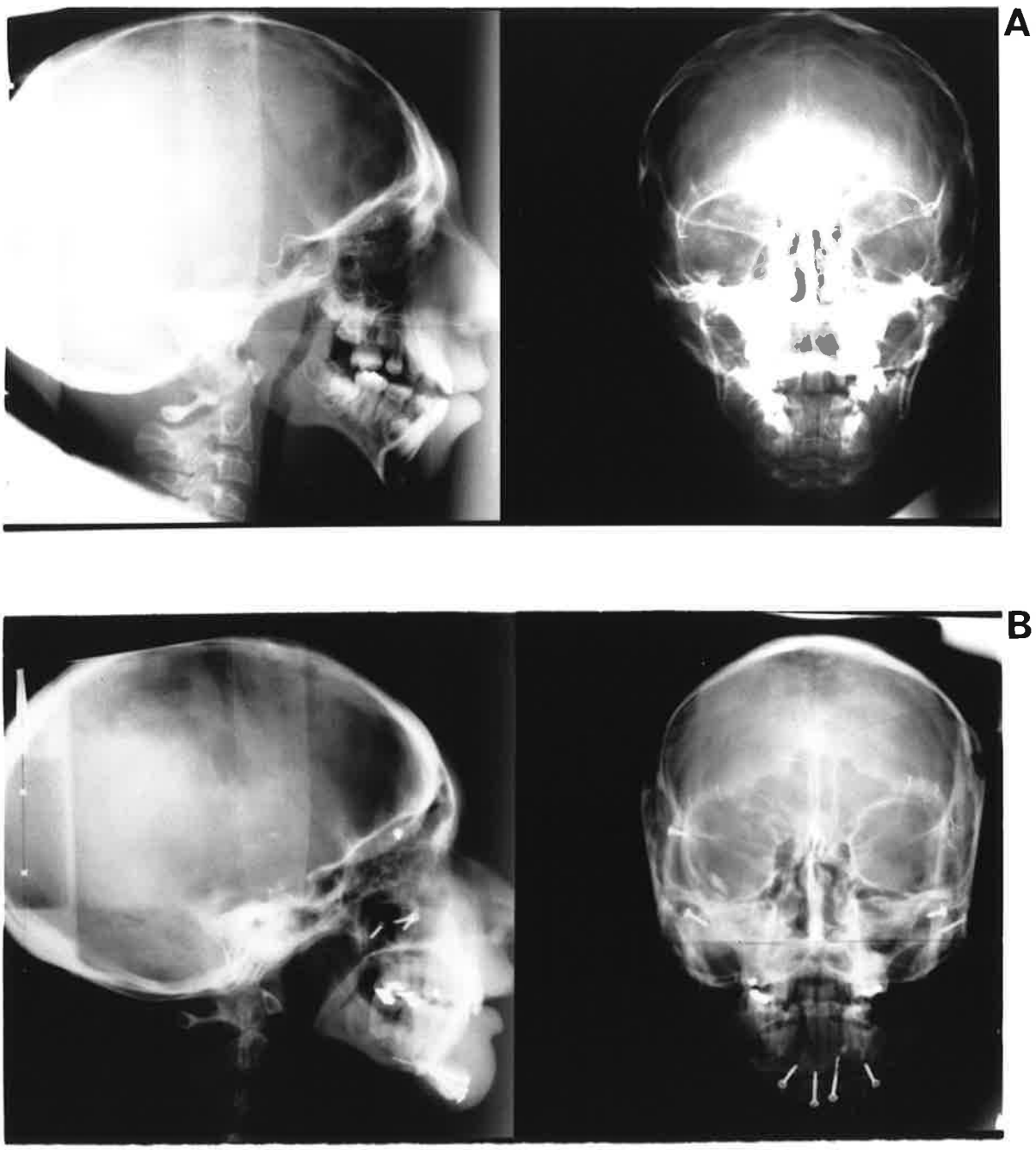

Figure 2.23 (a) Pre-operative and
(b) post-operative radiographs of the Treacher Collins Syndrome patient.

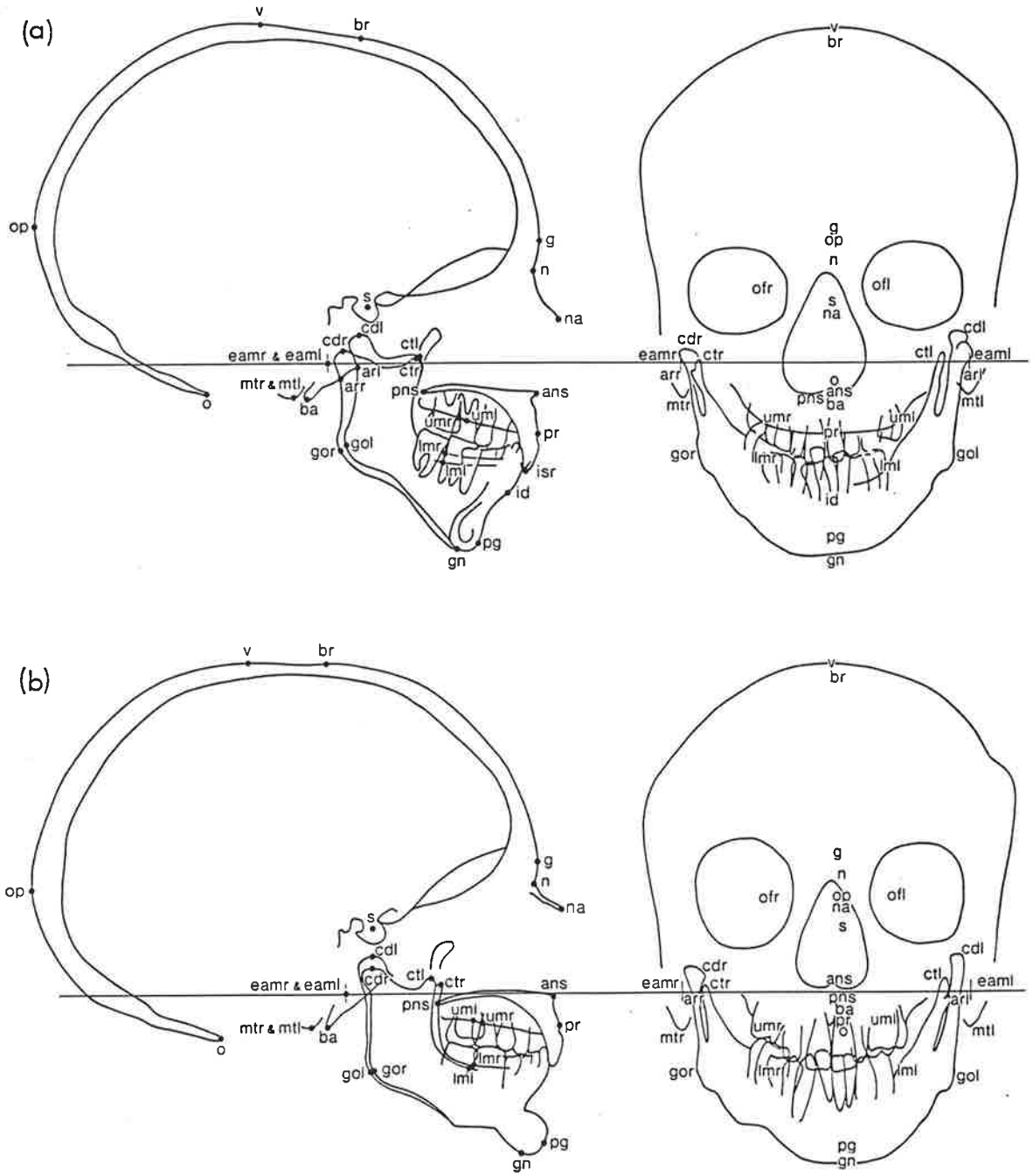

Figure 2.24 Tracings of the

(a) pre-operative, and

(b) post-operative radiographs of Figure 2.22.

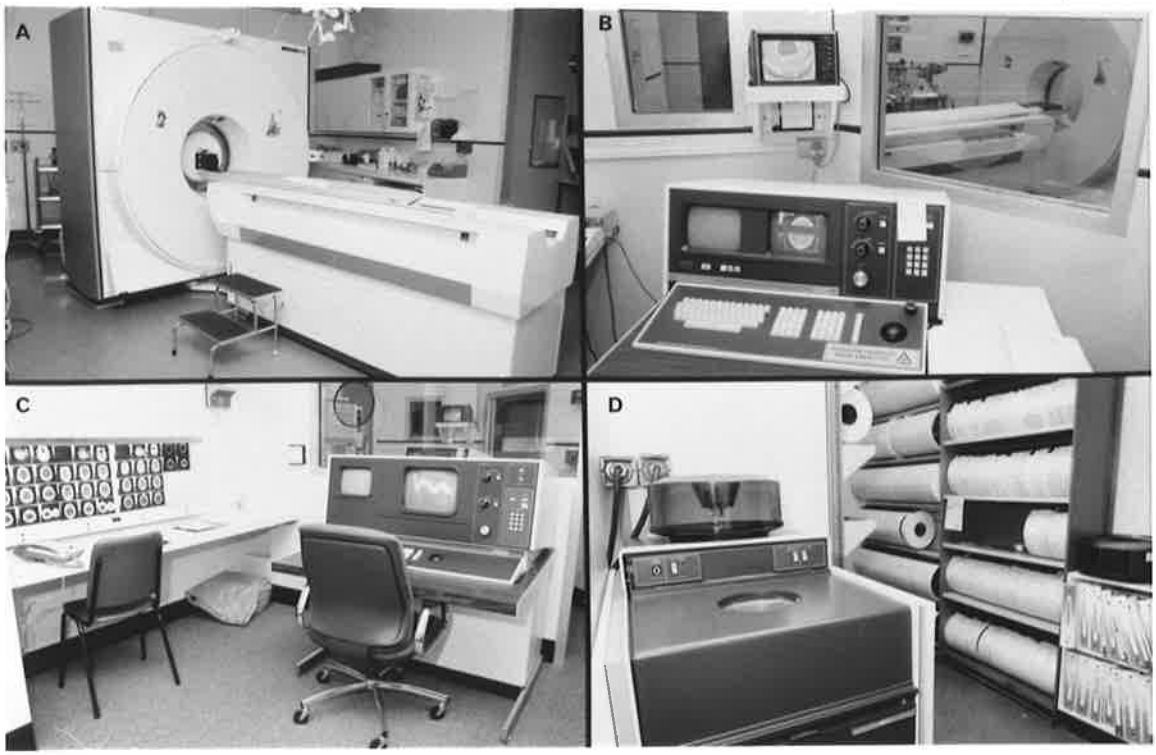

(a) CT scanner.

(b) Operator's console.

(c) Independent physician's console.

(d) Disc drive and tape storage area.

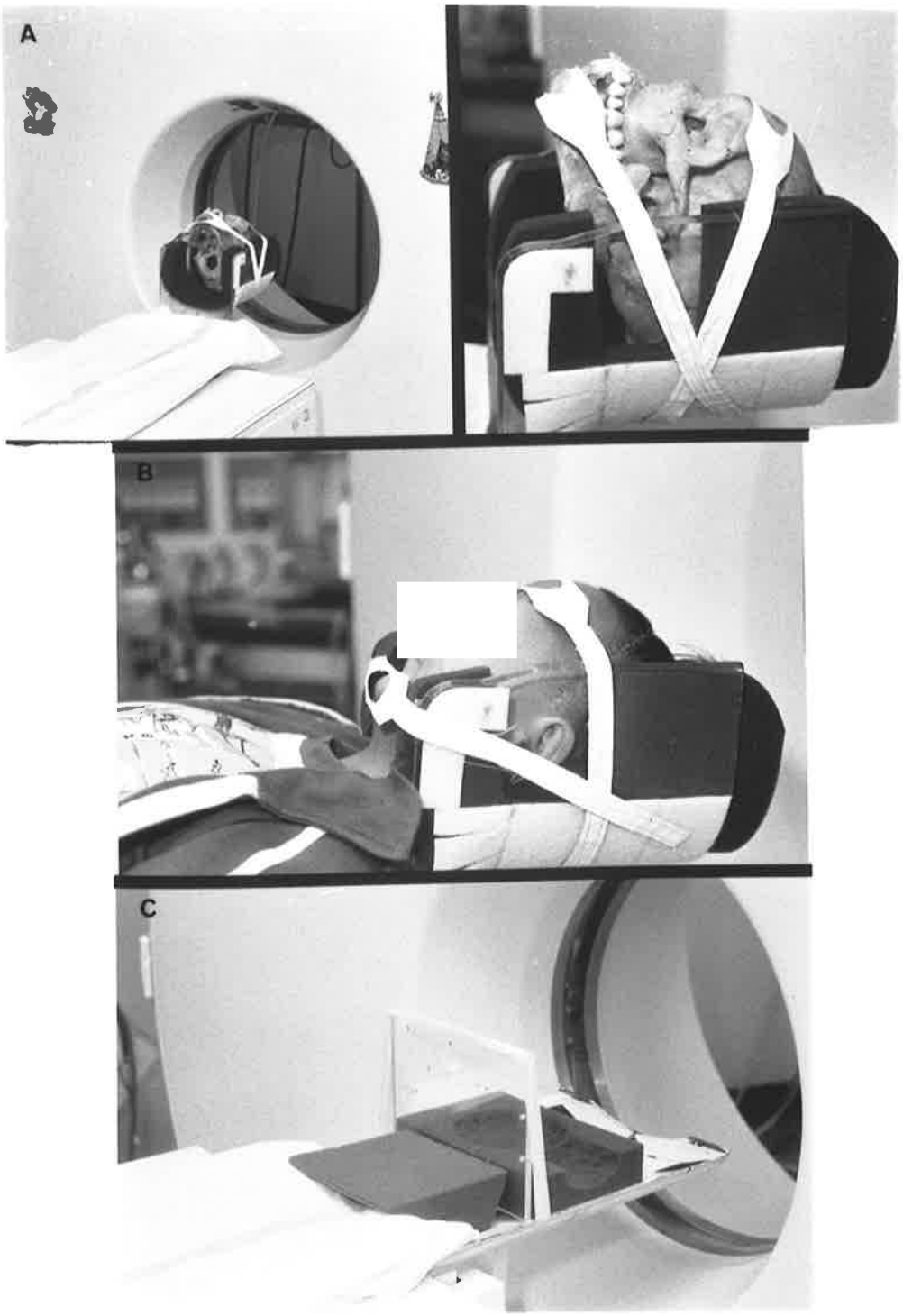

Figure 3.2 (a) Photographs showing how the skull was positioned and secured within the acrylic head holder.

(b) Immobilisation of the patient's head through the use of head holder and straps.

(c) The acrylic test object fastened to the scanning table.

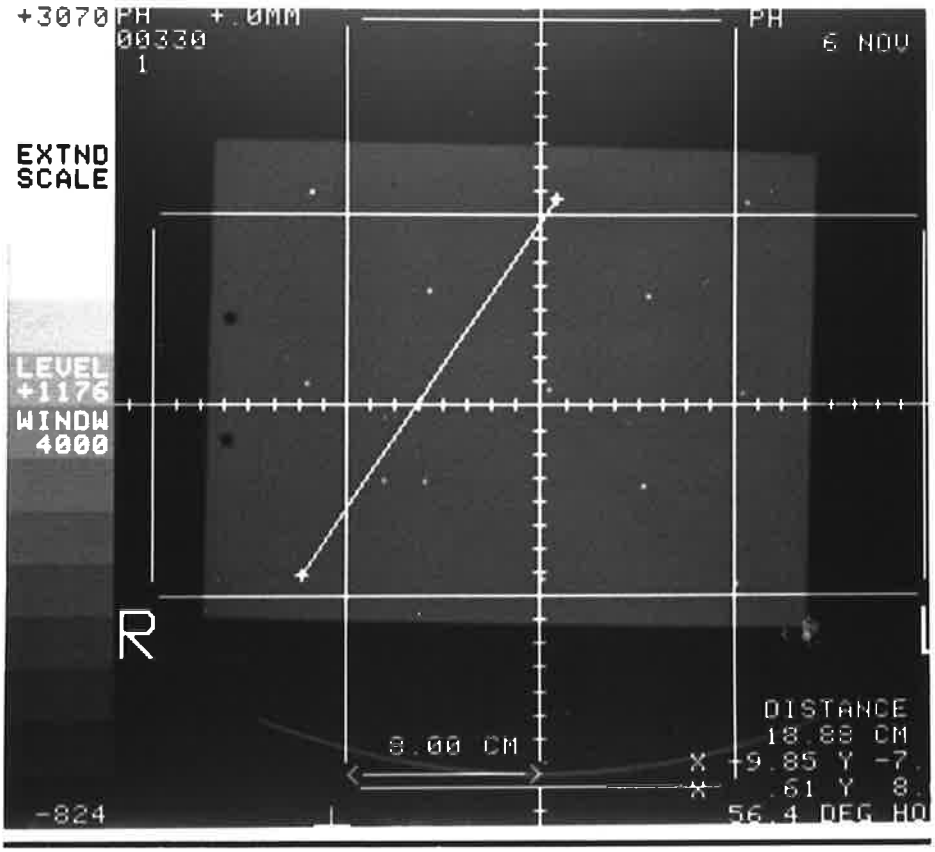

Figure 3.3 The determination of the coordinates of the metal markers in the acrylic test object using the independent physician's display console.

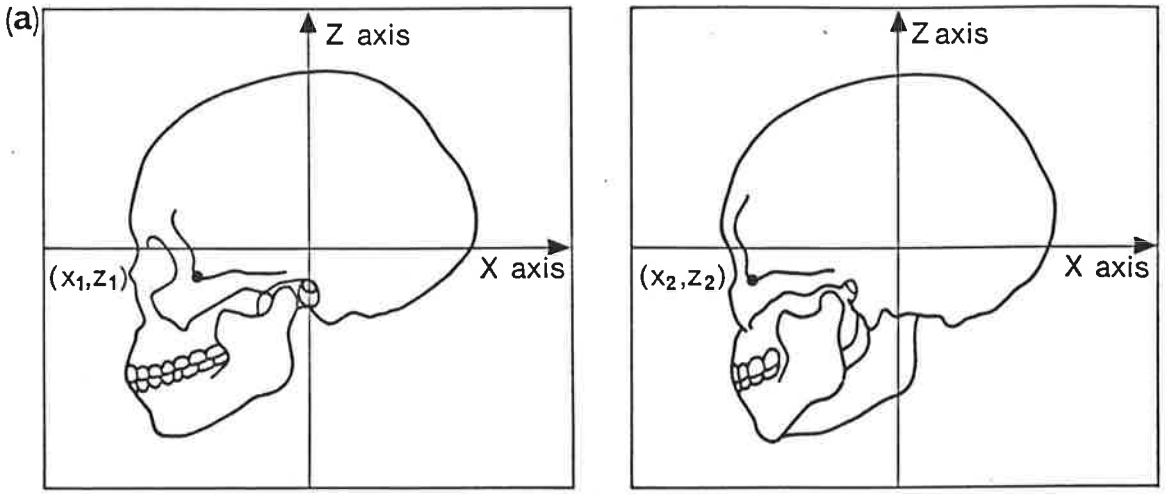

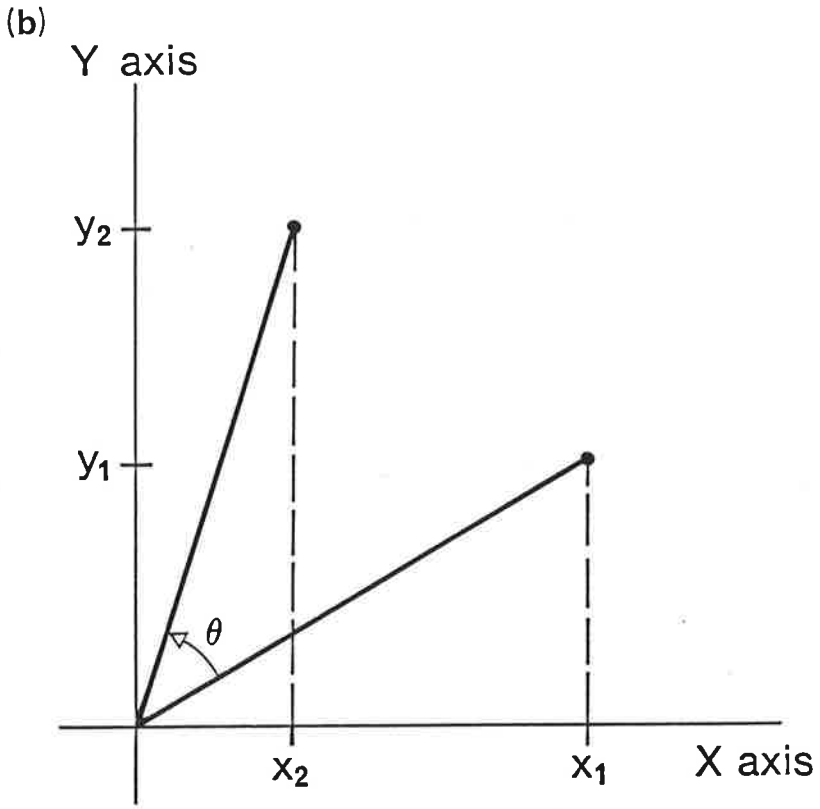

Figure 3.4 (a) Tracings of three dimensional CT reconstructions separated by an angle θ about the Z-axis, with the projection down the Y-axis. The point (x, y, z) projected at (x_1, z_1) in the left image is rotated to (x_2, y_2, z_2) and projected in the right image to (x_2, z_2).

(b) Rotation of the point (x_1, y_1, z_1) to (x_2, y_2, z_2), viewed down the rotation axis to illustrate Equations 3.1 and 3.2.

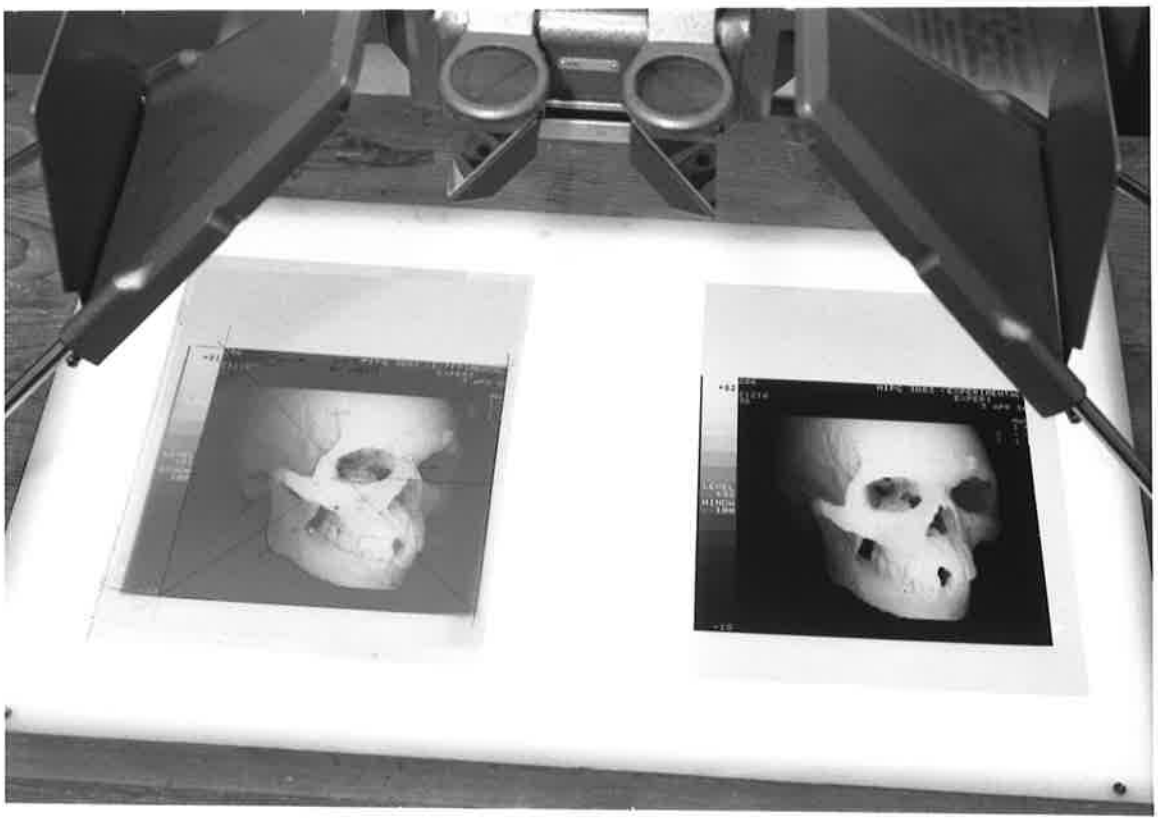

Figure 3.5 Stereo images facilitated tracing of anatomical features and osseous landmark location.

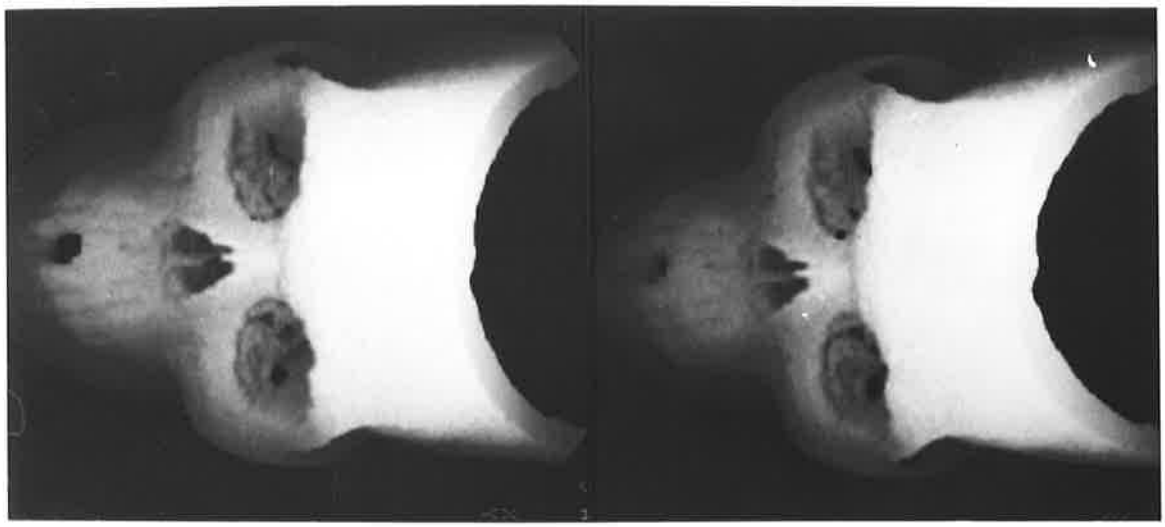

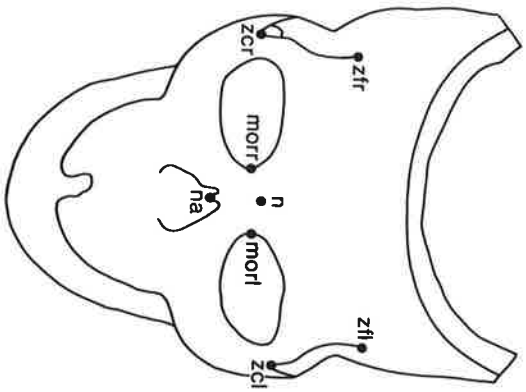

Figure 3.6 (a) Stereo pair and tracing of the left CT image for skull A90 for rotations about the X-axis of 27° and 36°. Anatomical abreviations and definitions are given in Table 3.3.

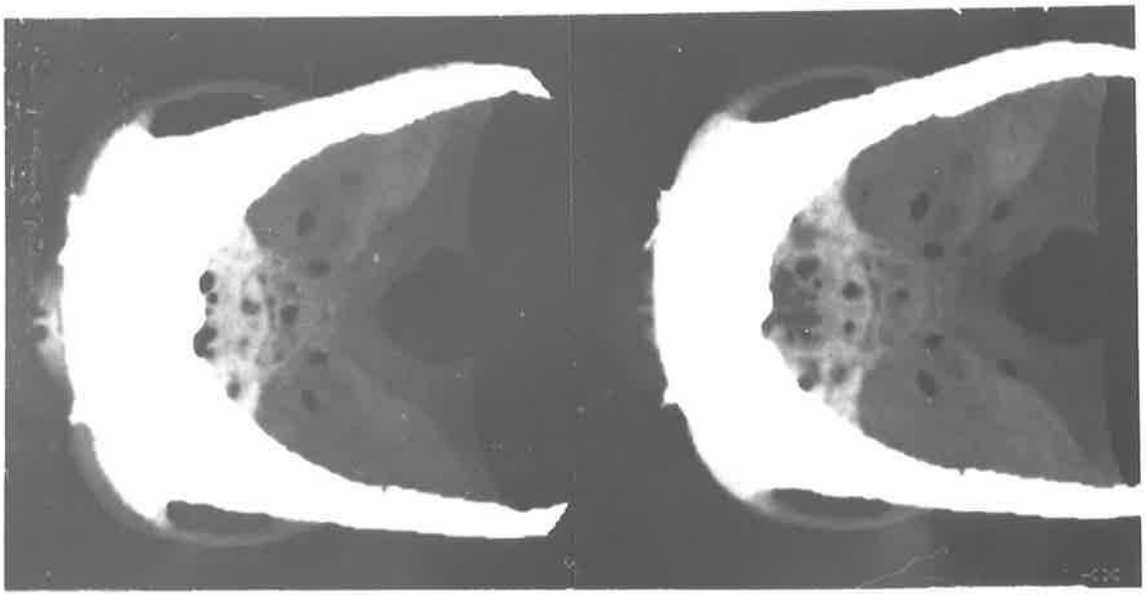

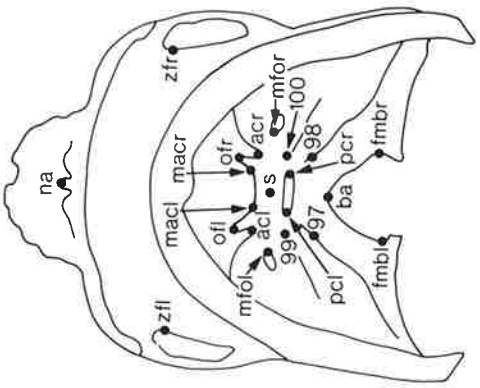

Figure 3.6 (b) Stereo pair and tracing of the left CT image for skull A90 for rotations about the X-axis of 72° and 81°. Anatomical abreviations and definitions are given in Table 3.3.

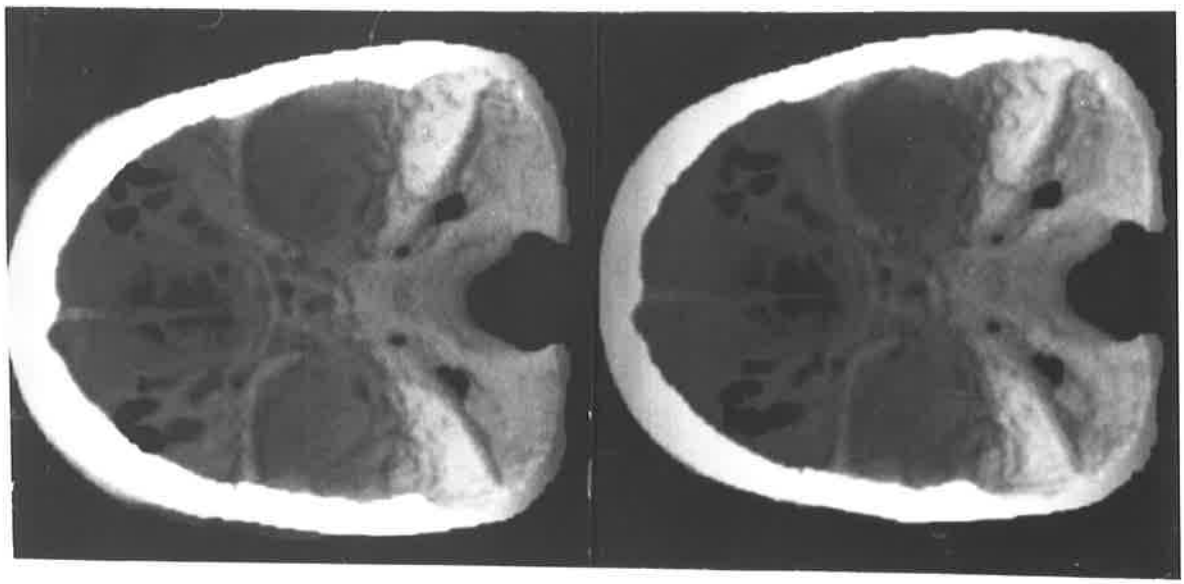

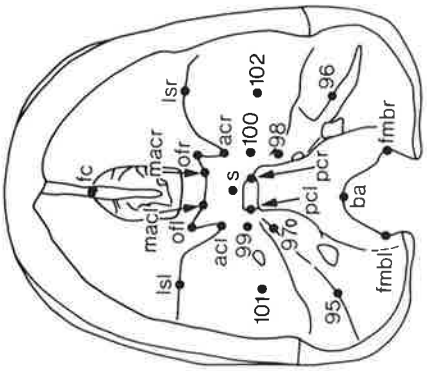

Figure 3.6 (c) Stereo pair and tracing ot the left CT image for skull A90 for rotations about the X-axis of 117° and 126°. Anatomical abreviations and definitions are given in Table 3.3.

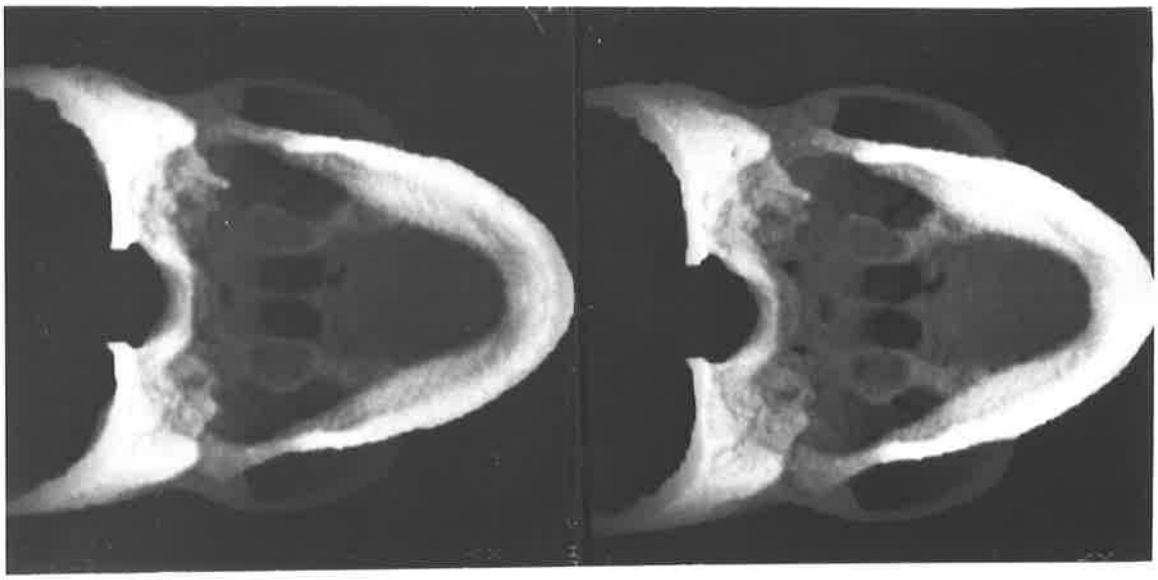

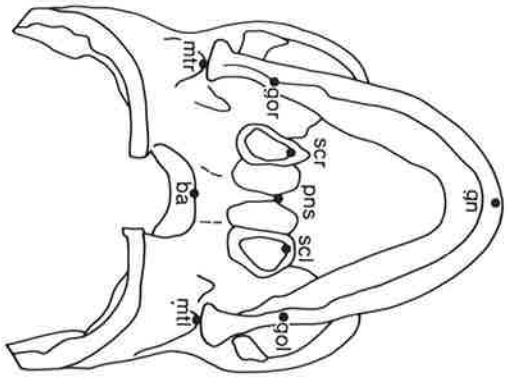

Figure 3.6 (d) Stereo pair and tracing of the left CT image for skull A90 for rotations about the X-axis of 225° and 234°. Anatomical abreviations and definitions are given in Table 3.3.

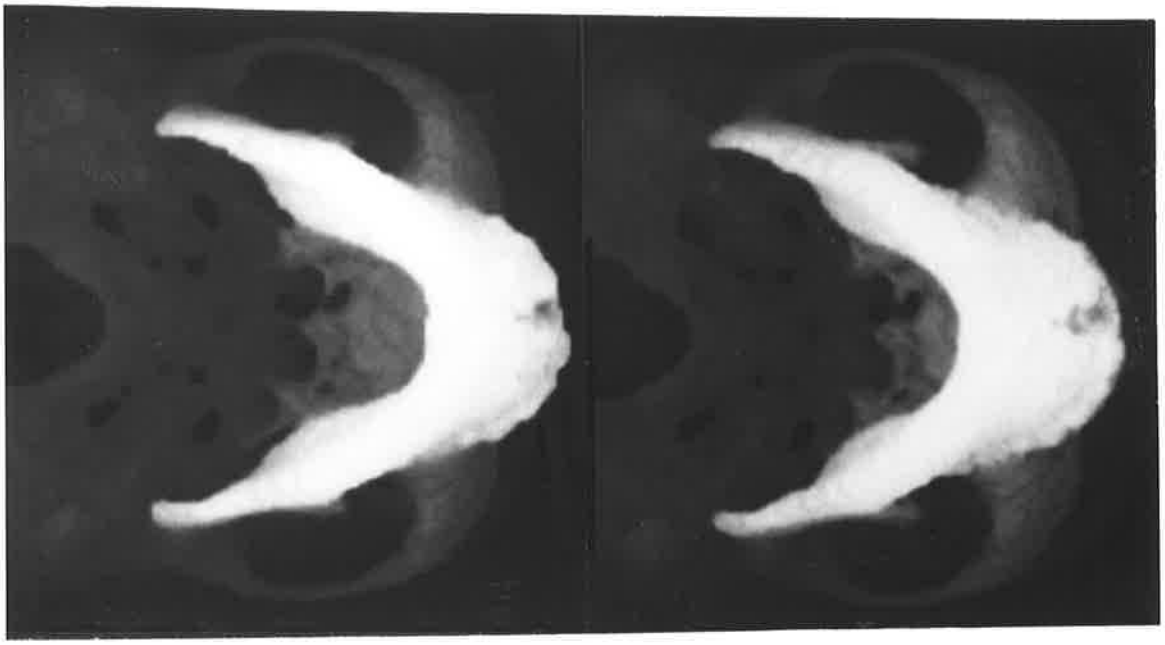

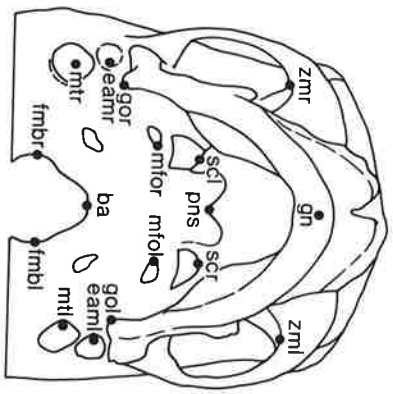

Figure 3.6 (e) Stereo pair and tracing of the left CT image for skull A90 for rotations about the X-axis of 270° and 279°. Anatomical abreviations and definitions are given in Table 3.3.

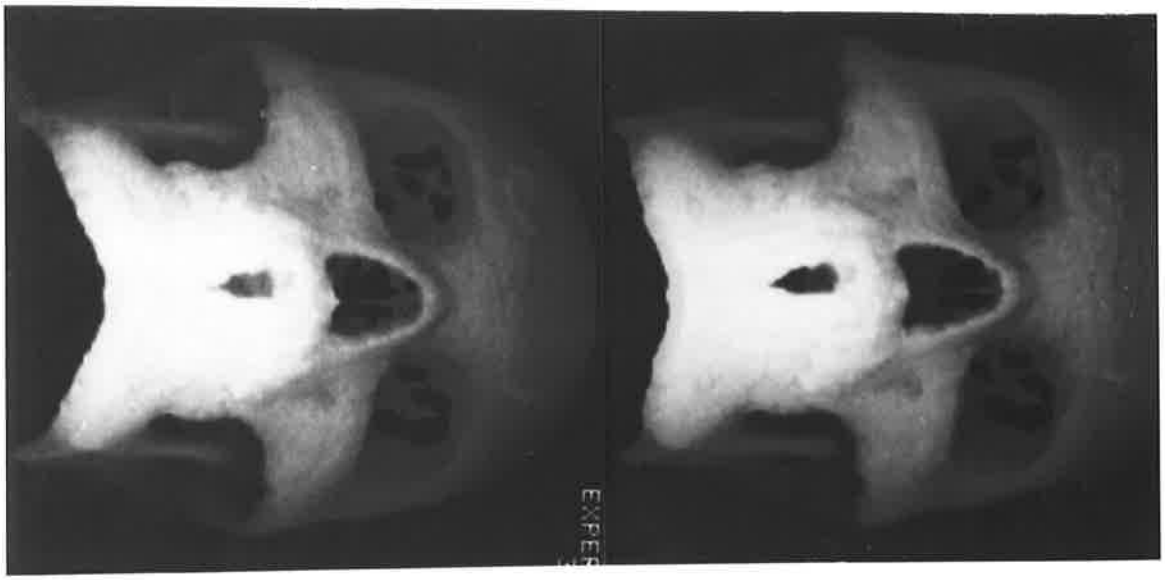

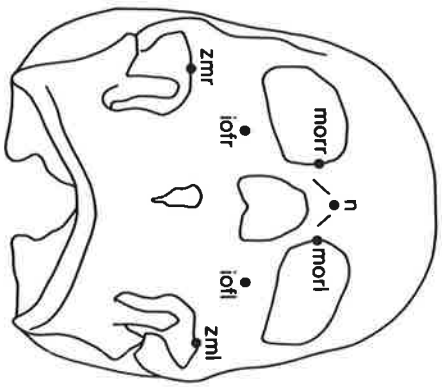

Figure 3.6 (f) Stereo pair and tracing of the left CT image for skull A90 for rotations about the X-axis of 315° and 324°. Anatomical abreviations and definitions are given in Table 3.3.

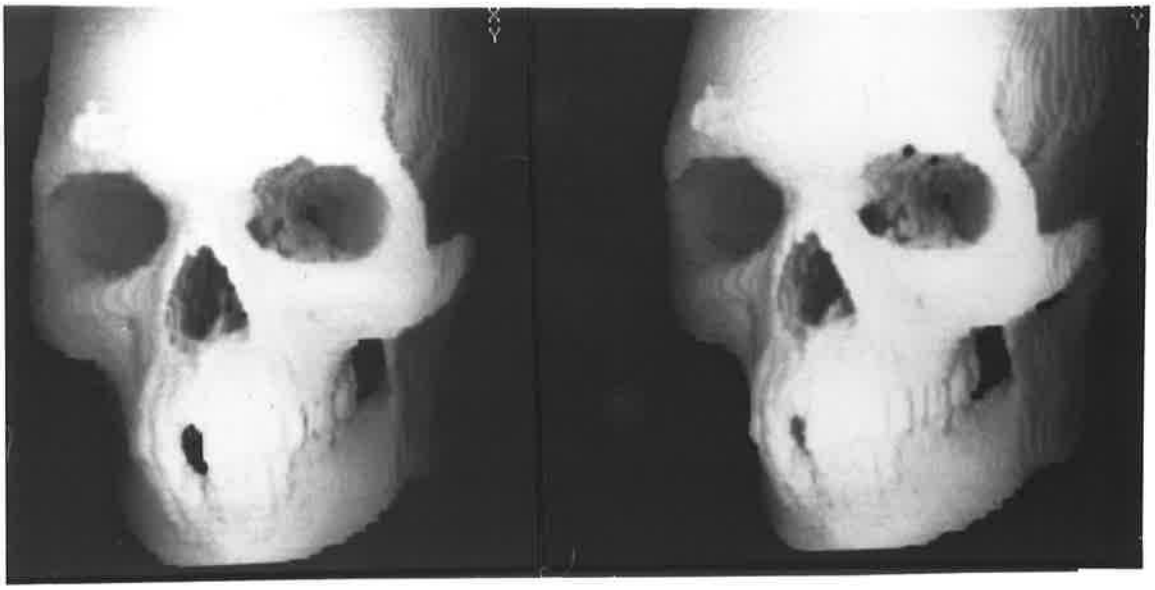

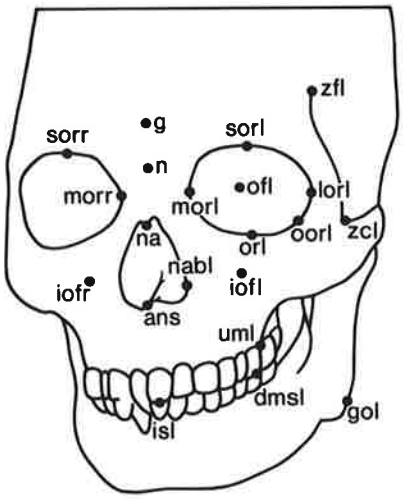

Figure 3.7 (a) Stereo pair and tracing of the left CT image for skull A90 for rotations about the Z-axis of 18° and 27°. Anatomical abreviations and definitions are given in Table 3.3.

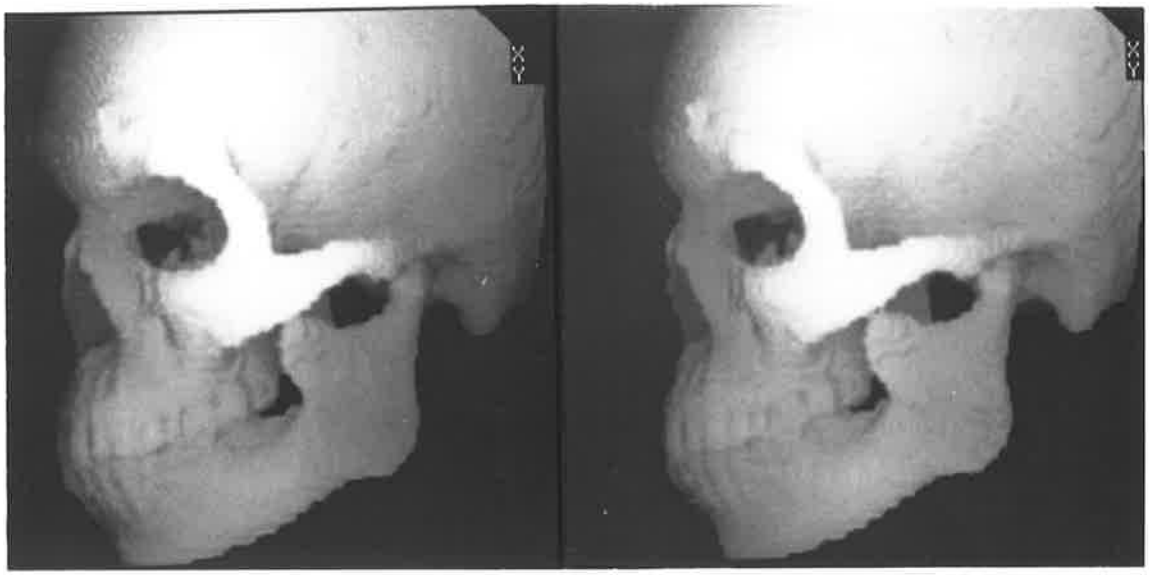

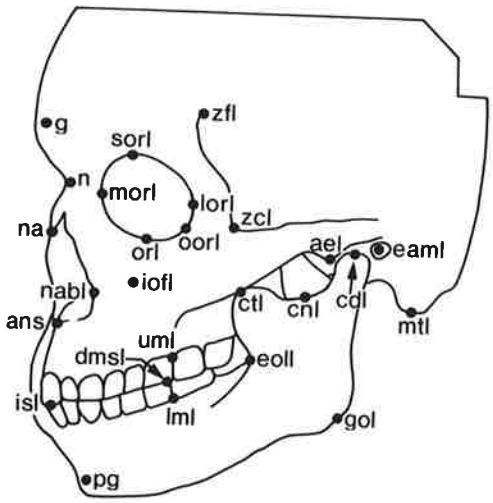

Figure 3.7 (b) Stereo pair and tracing of the left CT image for skull A90 for rotations about the Z-axis of 63° and 72°. Anatomical abreviations and definitions are given in Table 3.3.

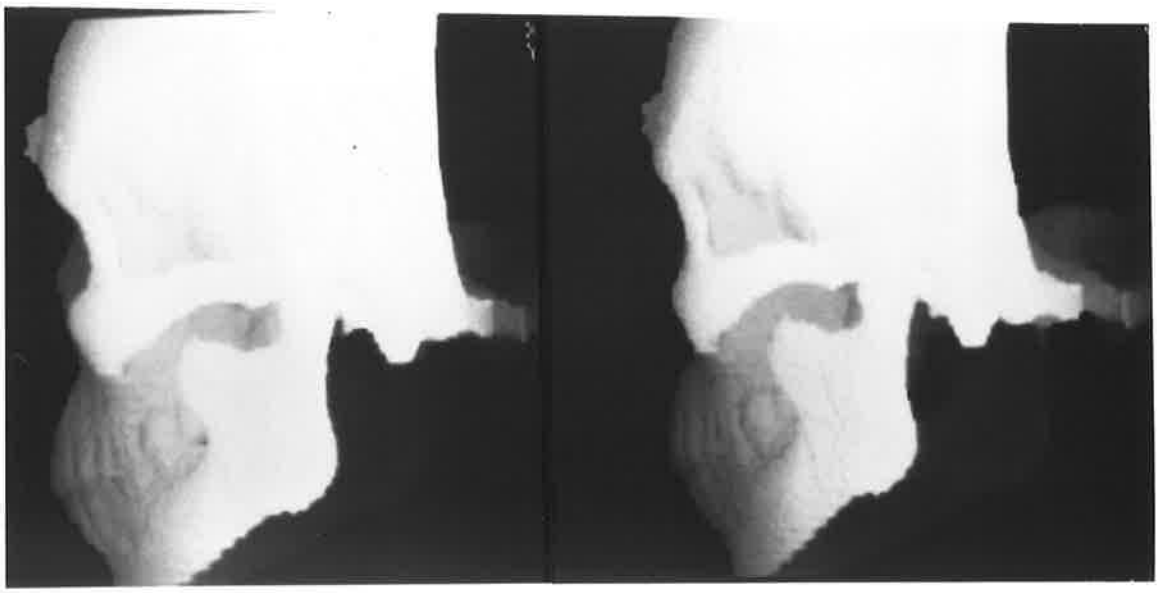

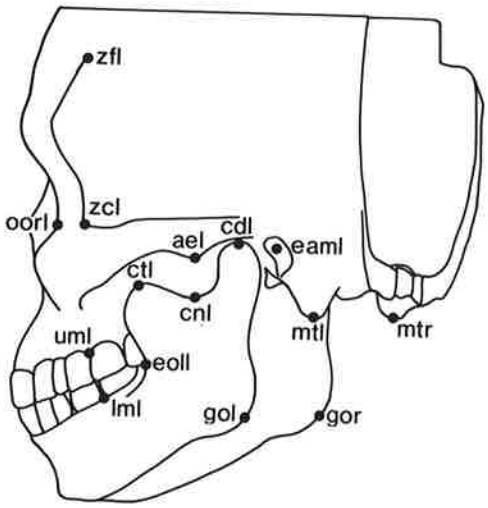

Figure 3.7 (c) Stereo pair and tracing of the left CT image for skull A90 for rotations about the Z-axis of 108° and 117°. Anatomical abreviations and definitions are given in Table 3.3.

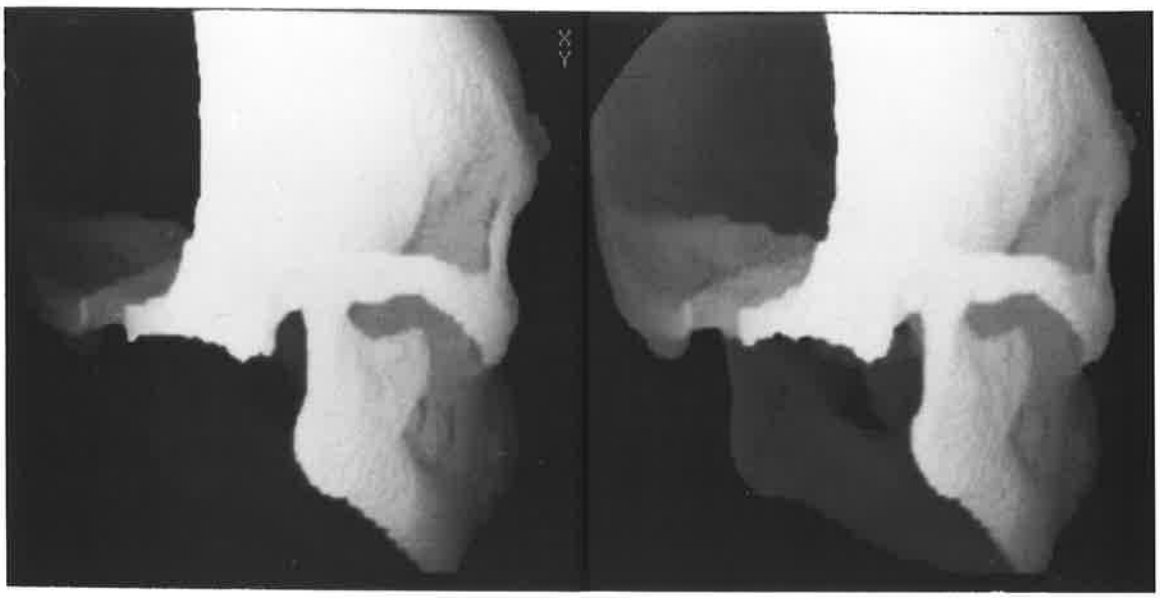

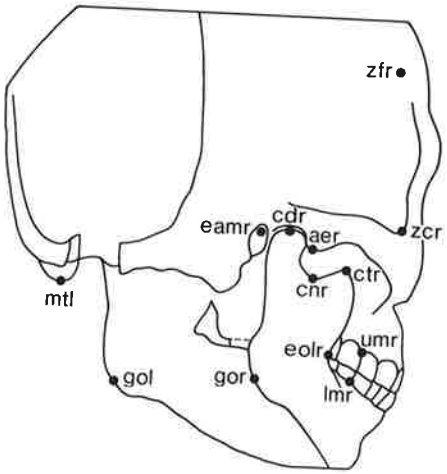

Figure 3.7 (d) Stereo pair and tracing of the left CT image for skull A90 for rotations about the Z-axis of 234° and 243°. Anatomical abreviations and definitions are given in Table 3.3.

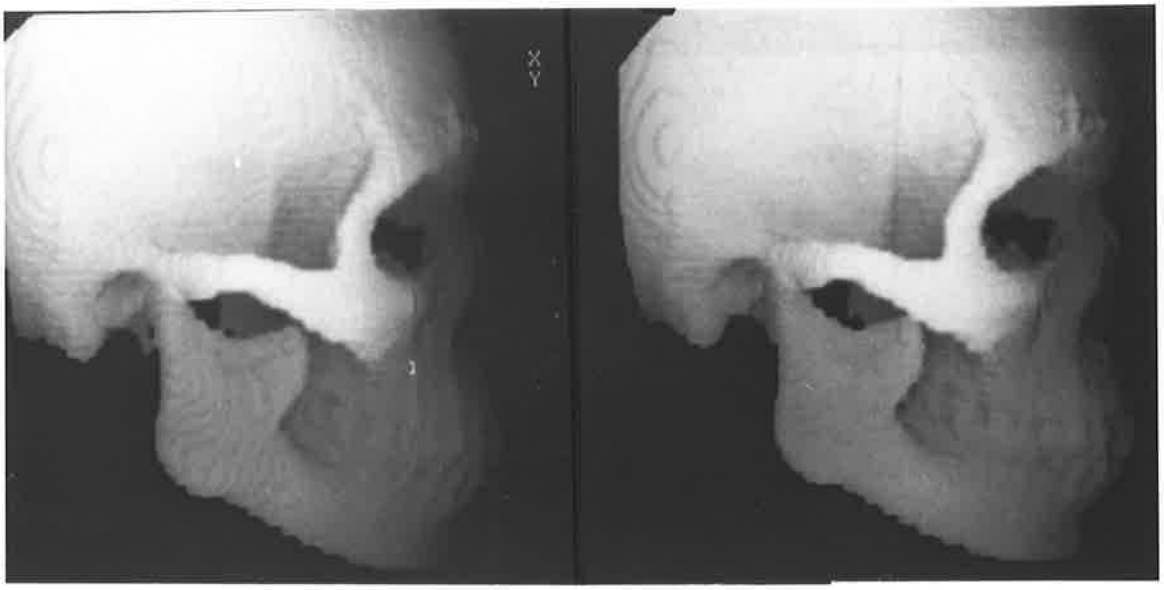

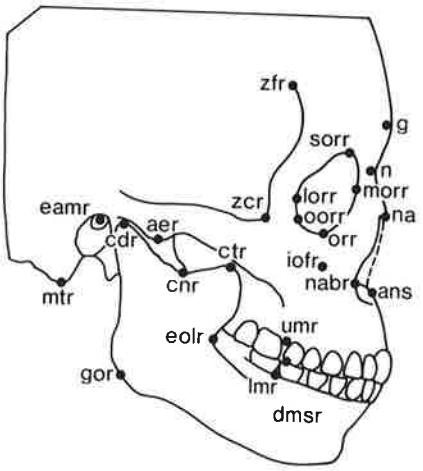

Figure 3.7 (e) Stereo pair and tracing of the left CT image for skull A90 for rotations about the Z-axis of 279° and 288°. Anatomical abreviations and definitions are given in Table 3.3.

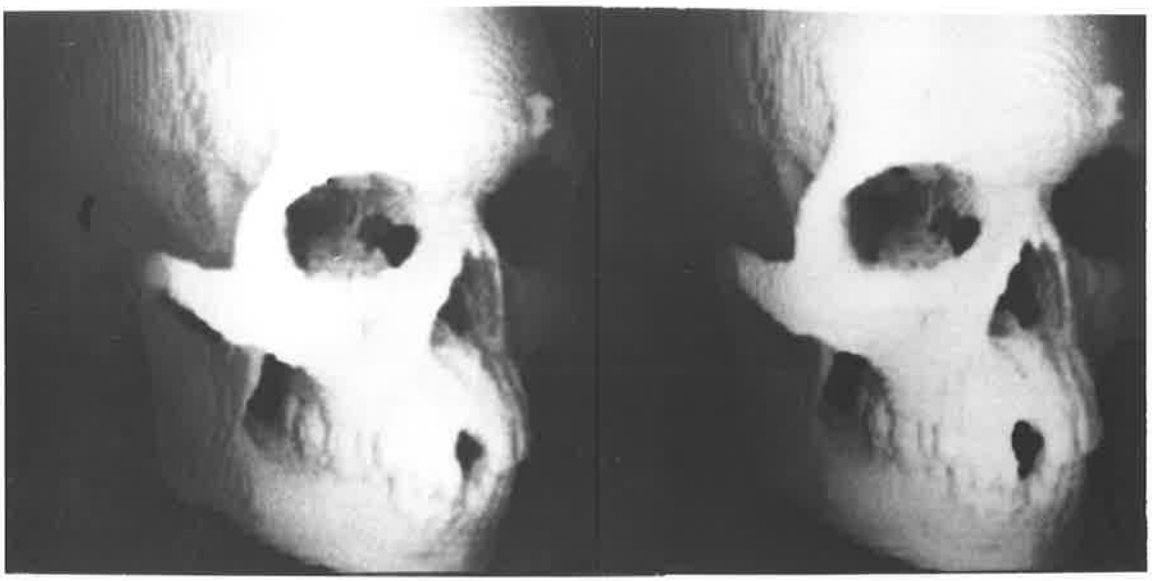

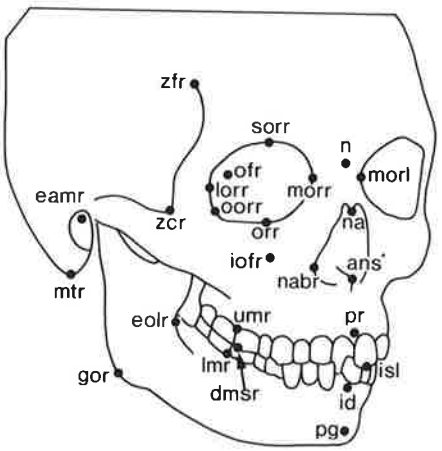

Figure 3.7 (f) Stereo pair and tracing of the left CT image for skull A90 for rotations about the Z-axis of 324° and 333°. Anatomical abreviations and definitions are given in Table 3.3.

Figure 3.8 (a) Stereo CT images of skull A38 used for determination of osseous landmarks for rotations about the X-axis of (a) 27° and 36°, (b) 72° and 81°, (c) 117° and 126°, (d) 225° and 234°, and (e) 270° and 279°, and (f) 315° and 324°.

F
E
D
A
B
C

Figure 3.8 (b) Stereo CT images of skull A38 used for determination of osseous landmarks for rotations about the Z-axis of (a) 18° and 27°, (b) 63° and 72°, (c) 108° and 117°, (d) 234° and 243°, and (e) 279° and 288°, and (f) 324° and 333°.

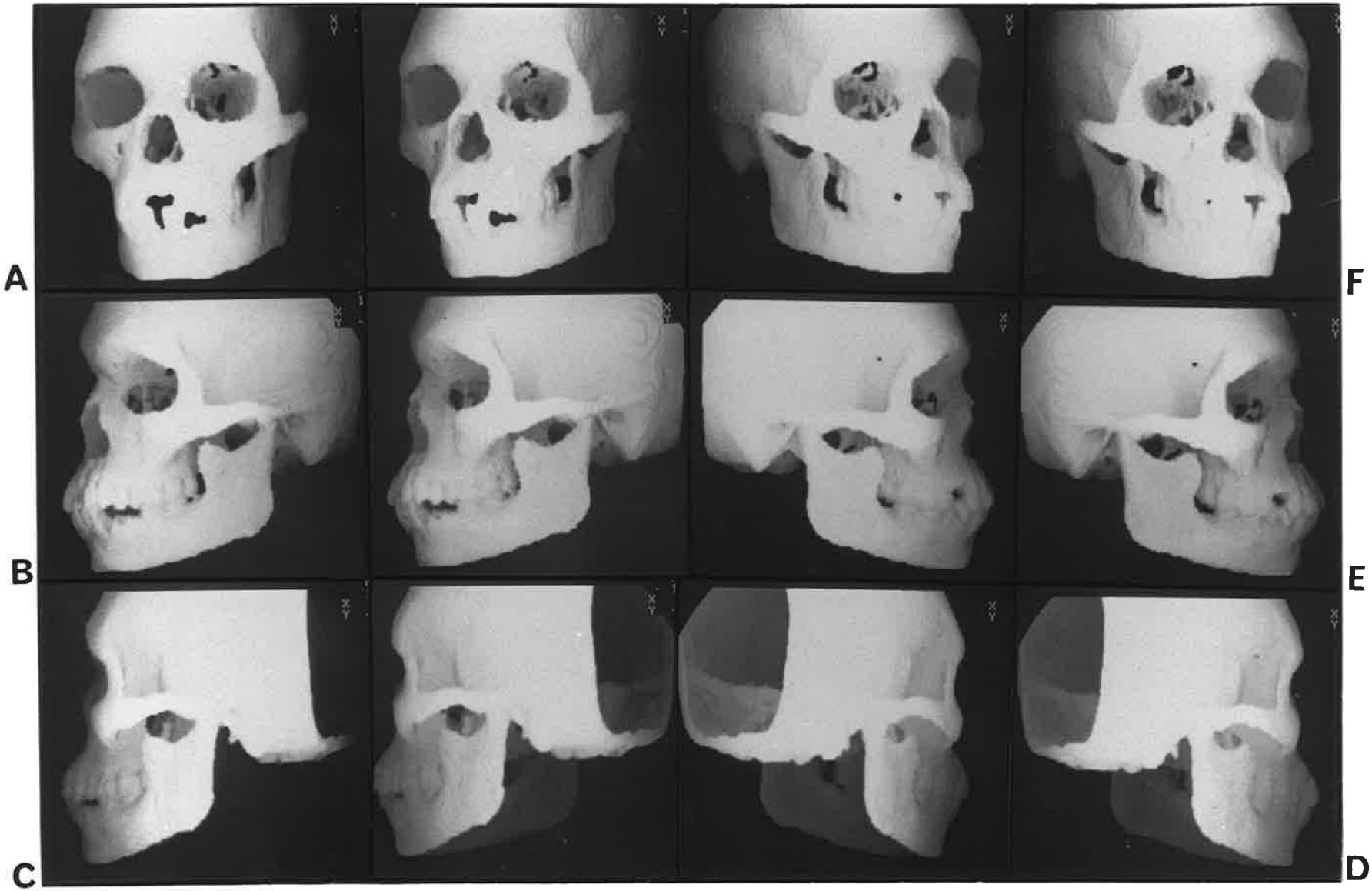
A
B
C
F
E
D

Figure 3.9 (a) Stereo CT images of skull A90 used for determination of osseous landmarks for rotations about the X-axis of (a) 27° and 36°, (b) 72° and 81°, (c) 117° and 126°, (d) 225° and 234°, and (e) 270° and 279°, and (f) 315° and 324°.

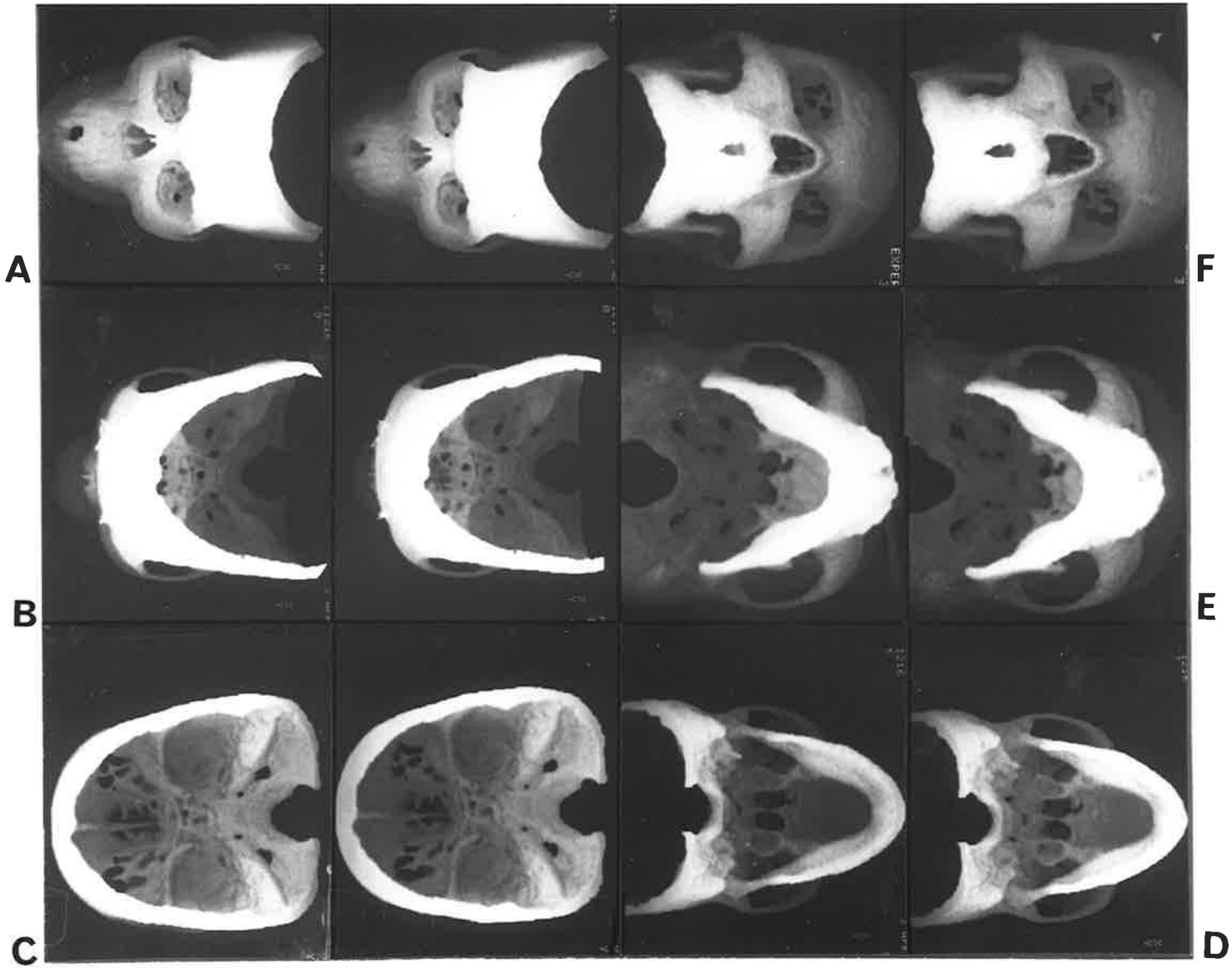
A
F
B
E
C
D

Figure 3.9 (b) Stereo CT images of skull A90 used for determination of osseous landmarks for rotations about the Z-axis of (a) 18° and 27°, (b) 63° and 72°, (c) 108° and 117°, (d) 234° and 243°, and (e) 279° and 288°, and (f) 324° and 333°.

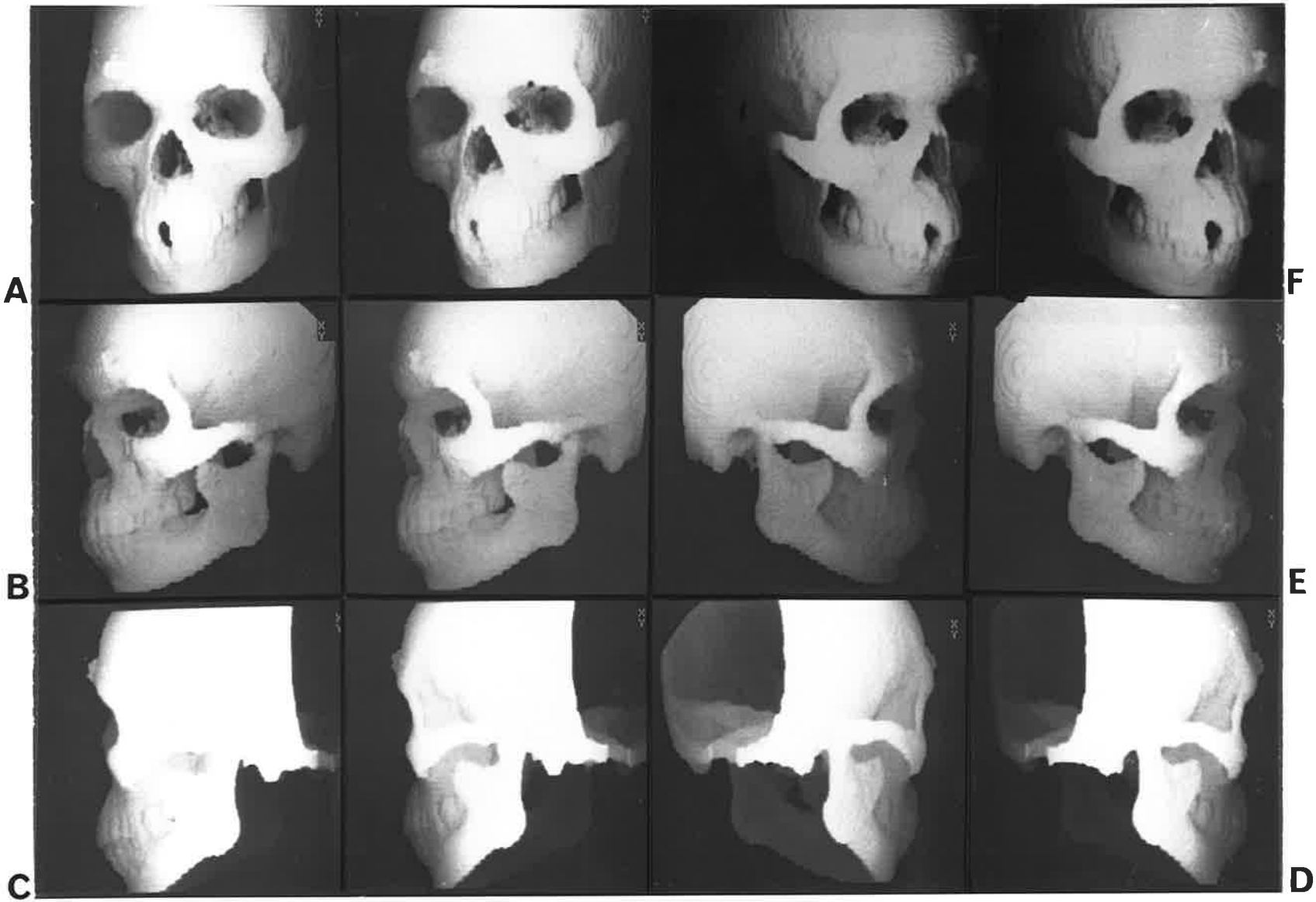
A
F
B
E
C
D

Figure 3.10 (a) Stereo CT images of skull A13184 used for determination of osseous landmarks for rotations about the X-axis of (a) 27° and 36°, (b) 72° and 81°, (c) 117° and 126°, (d) 225° and 234°, and (e) 270° and 279°, and (f) 315° and 324°.

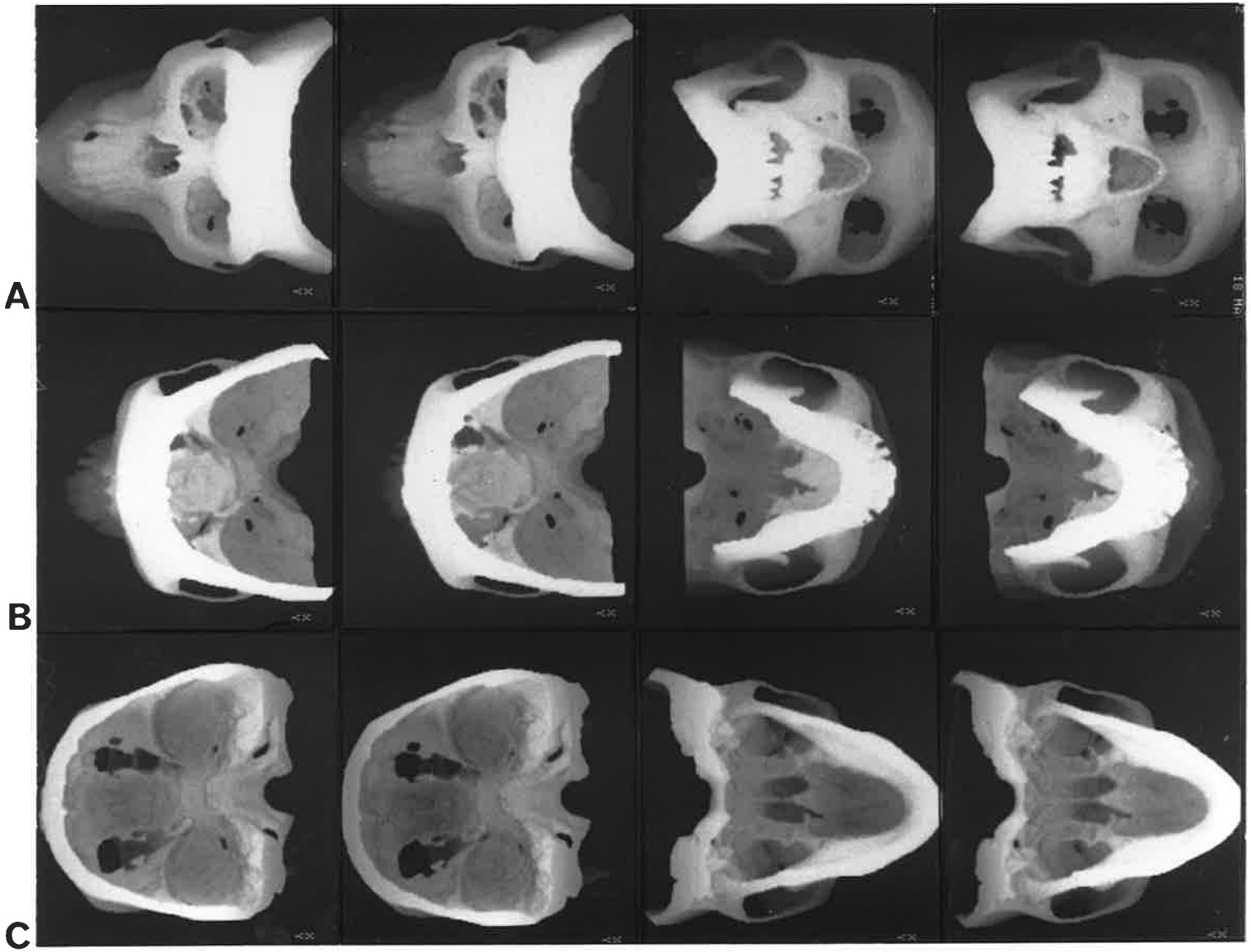
A
F
B
E
C
D

Figure 3.10 (b) Stereo CT images of skull A13184 used for determination of osseous landmarks for rotations about the Z-axis of (a) 18° and 27°, (b) 63° and 72°, (c) 108° and 117°, (d) 234° and 243°, and (e) 279° and 288°, and (f) 324° and 333°.


A
B
C
D
E
F

Figure 3.11 (a) Stereo CT images of skull A38778 used for determination of osseous landmarks for rotations about the X-axis of (a) 27° and 36°, (b) 72° and 81°, (c) 117° and 126°, (d) 225° and 234°, and (e) 270° and 279°, and (f) 315° and 324°.

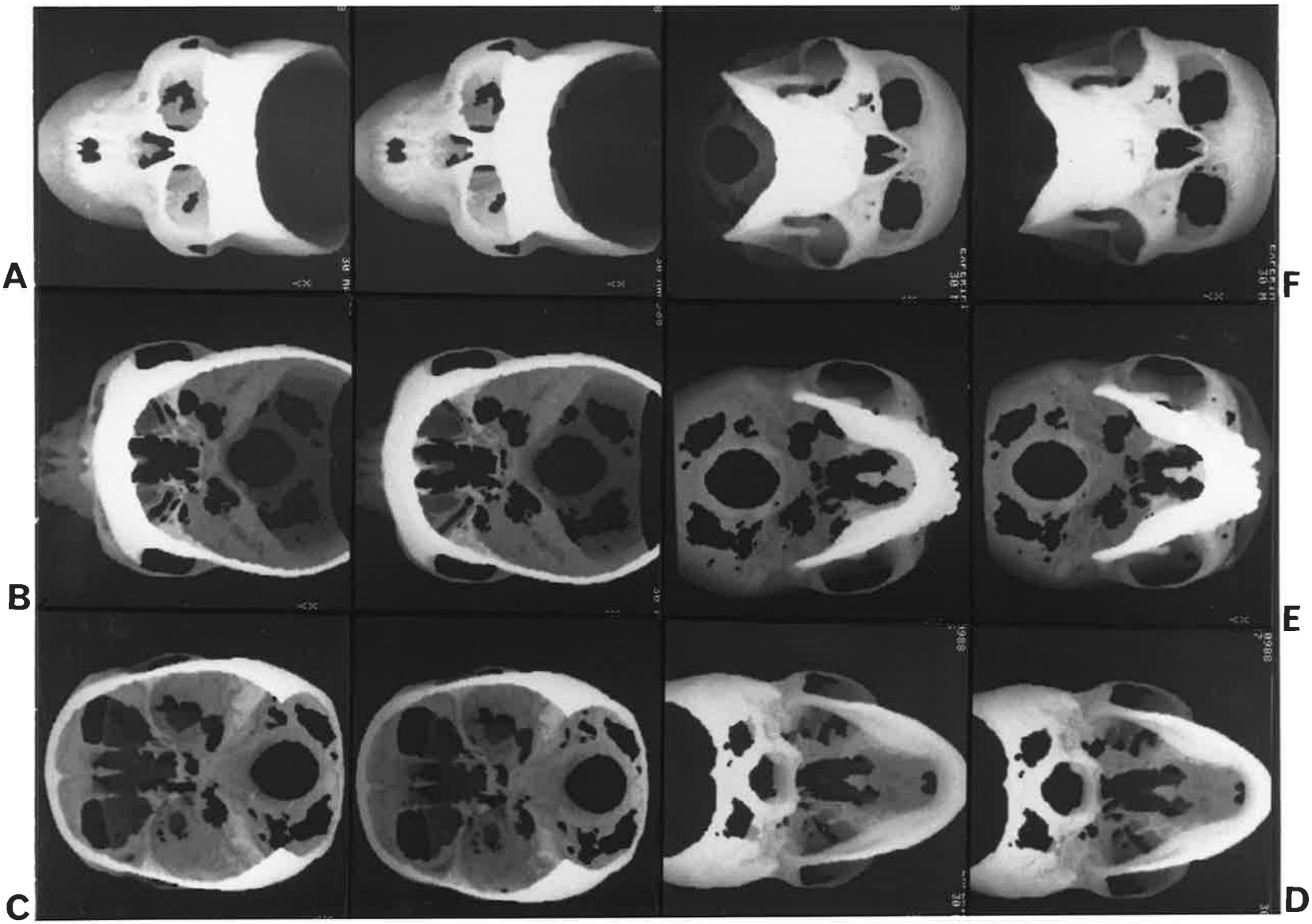
A
B
C
D
E
F

Figure 3.11 (b) Stereo CT images of skull A38778 used for determination of osseous landmarks for rotations about the Z-axis of (a) 18° and 27°, (b) 63° and 72°, (c) 108° and 117°, (d) 234° and 243°, and (e) 279° and 288°, and (f) 324° and 333°.

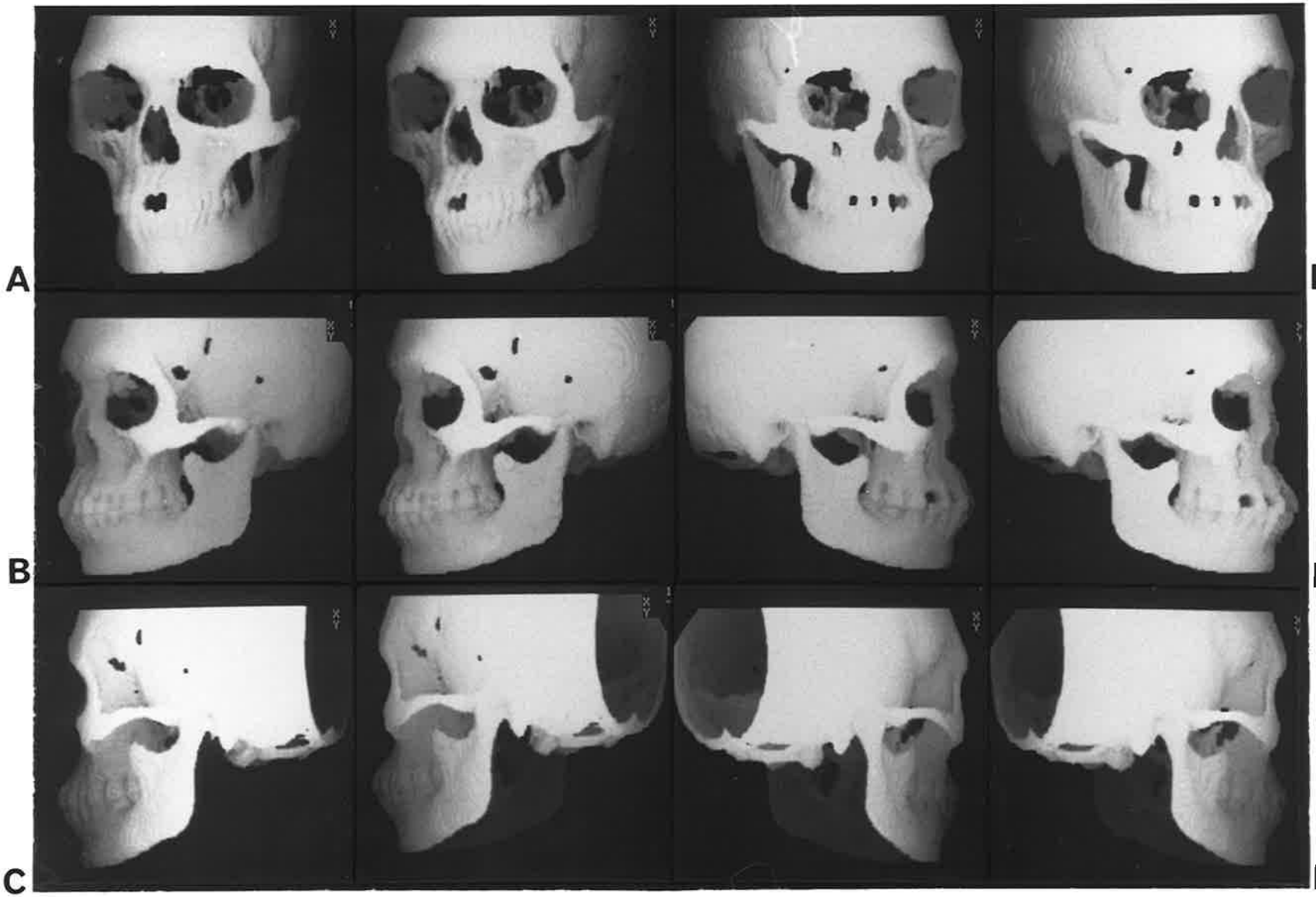
A
B
C
D
E
F

Figure 3.12 (a) Stereo CT images of skull A57590 used for determination of osseous landmarks for rotations about the X-axis of (a) 27° and 36°, (b) 72° and 81°, (c) 117° and 126°, (d) 225° and 234°, and (e) 270° and 279°, and (f) 315° and 324°.

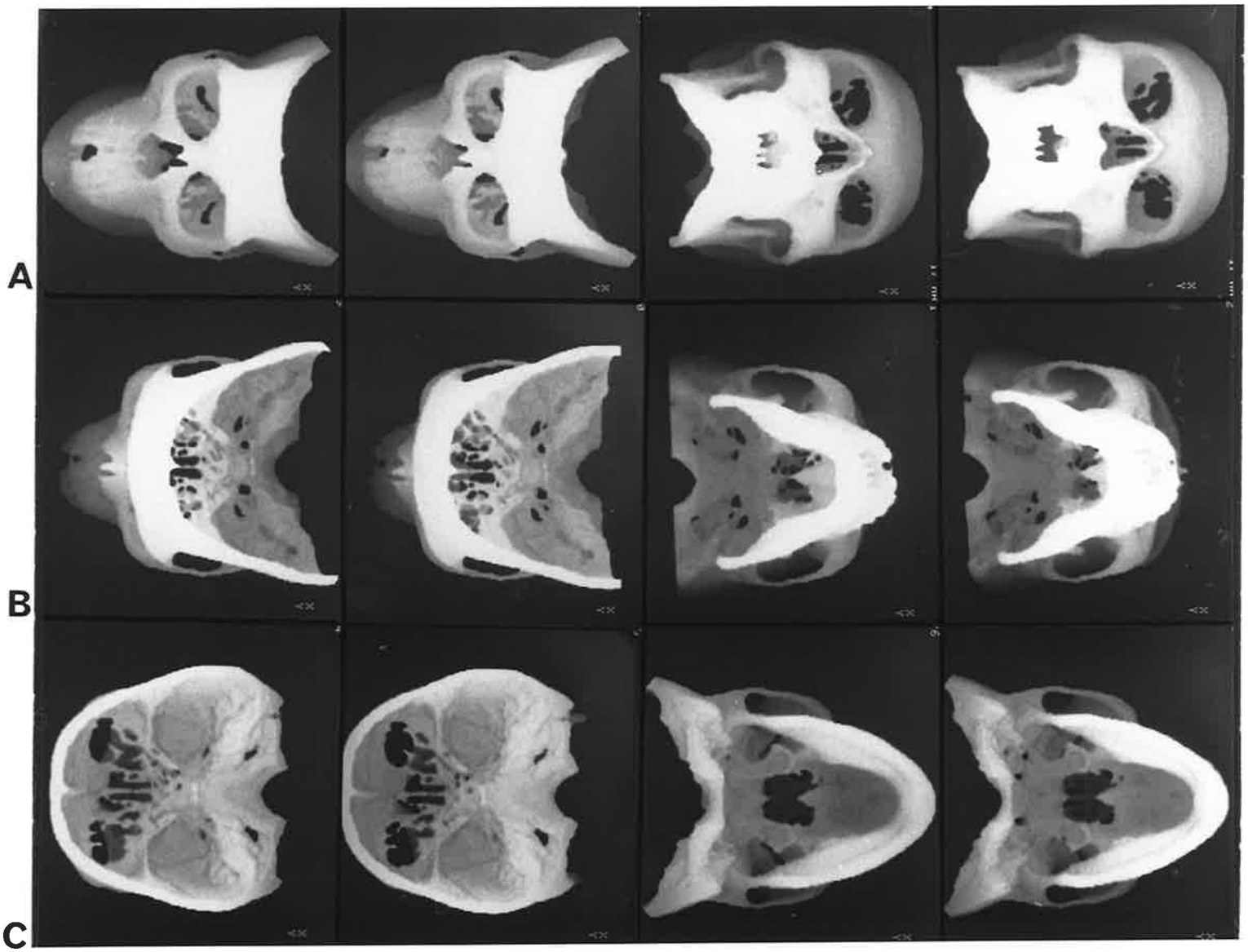
A
B
C
D
E
F

Figure 3.12 (b) Stereo CT images of skull A57590 used for determination of osseous landmarks for rotations about the Z-axis of (a) 18° and 27°, (b) 63° and 72°, (c) 108° and 117°, (d) 234° and 243°, and (e) 279° and 288°, and (f) 324° and 333°.


A
B
C
D
E
F

Figure 3.13 The three patients selected for assessment of osseous landmark identification

(a) Adult untreated Treacher Collins Syndrome (864405)

(b) An eleven year old, at mixed phase of treatment Treacher Collins Syndrome (796025)

(c) An twelve month old child untreated Apert's Syndrome (866790)

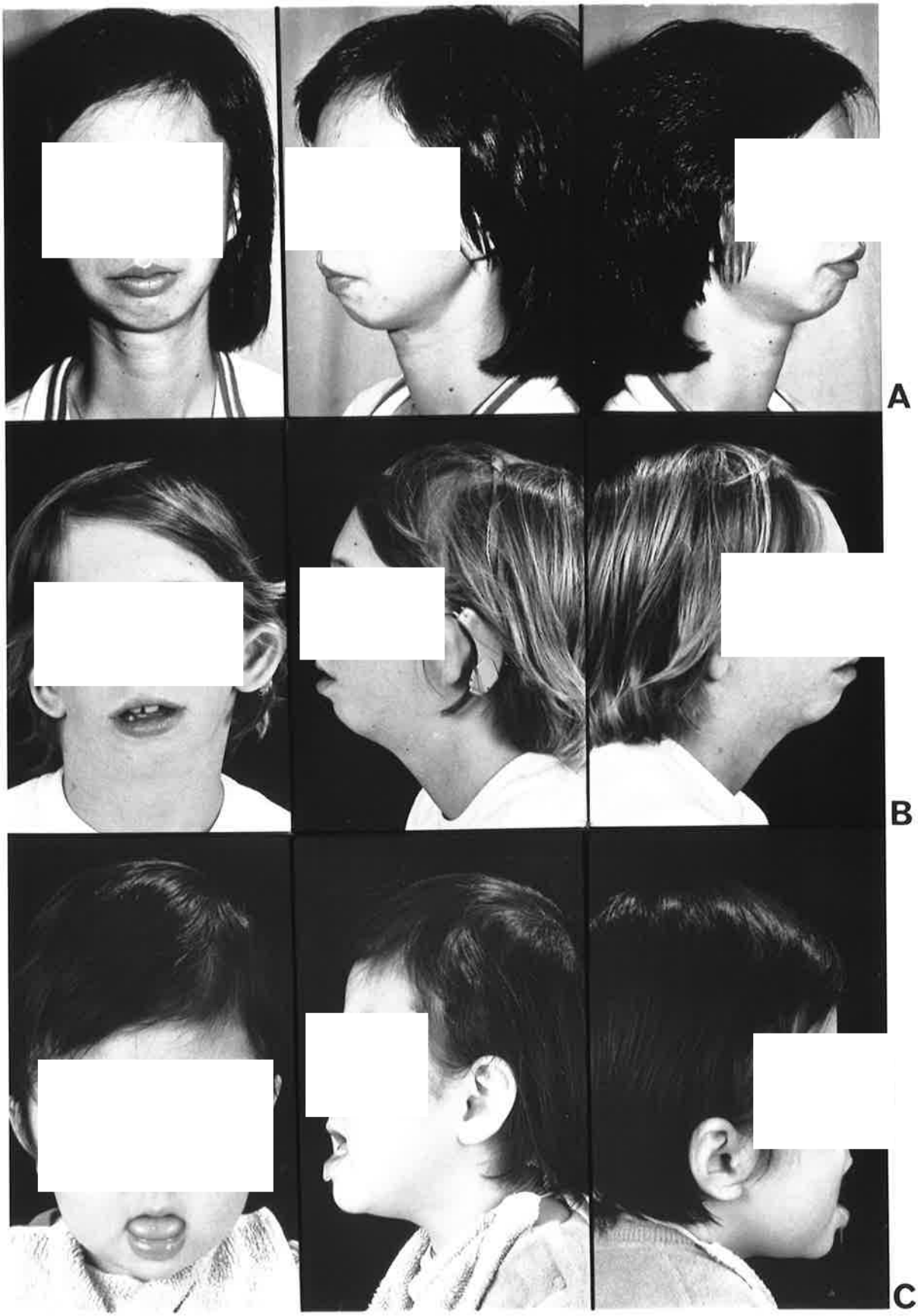
A
B
C

Figure 3.14 (a) Stereo CT images of patient 864405 used for determination of osseous landmarks for rotations about the X-axis of (a) 27° and 36°, (b) 72° and 81°, (c) 117° and 126°, (d) 225° and 234°, and (e) 270° and 279°, and (f) 315° and 324°.

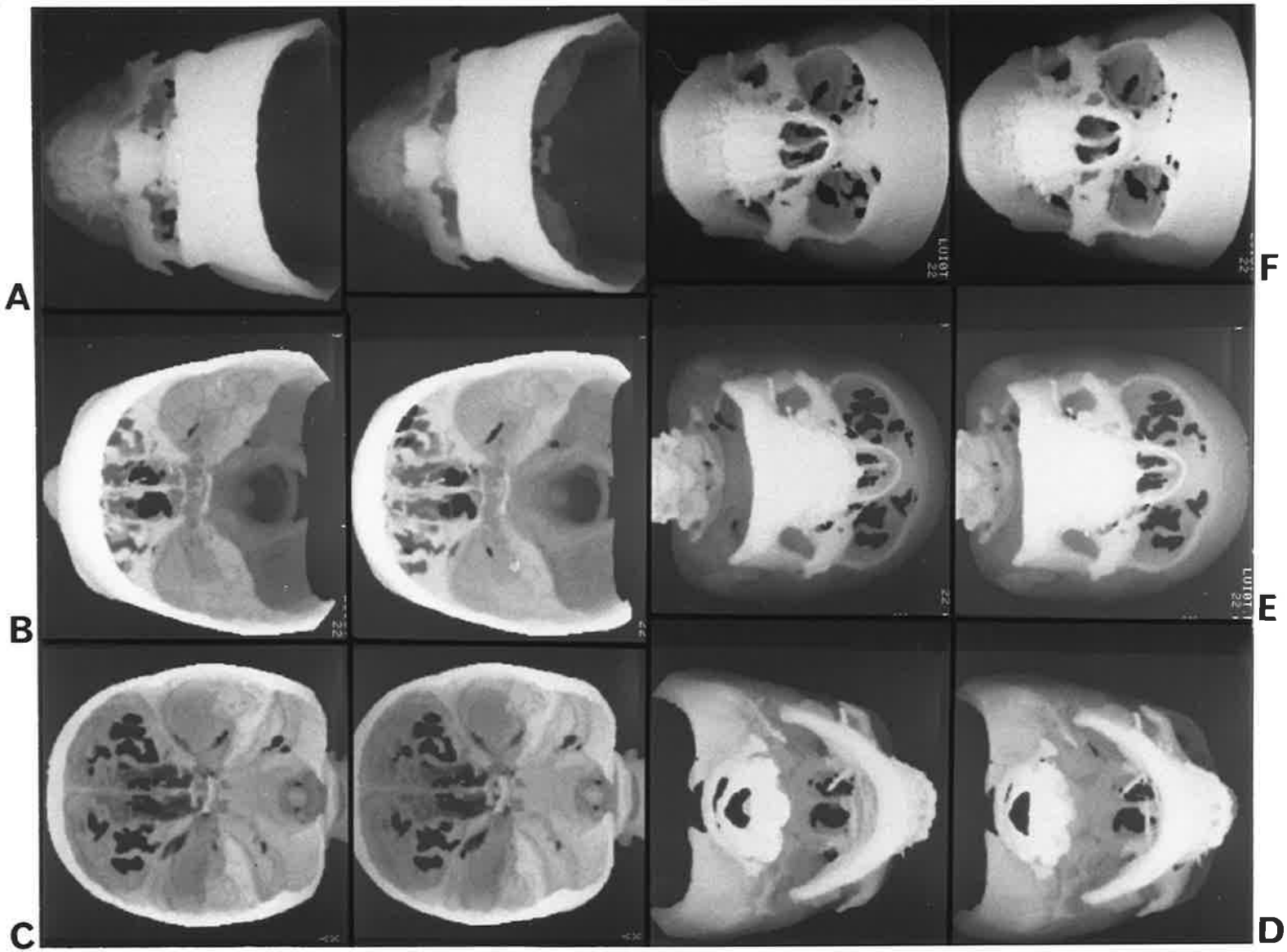
A
B
C
D
E
F

Figure 3.14 (b) Stereo CT images of patient 864405 used for determination of osseous landmarks for rotations about the Z-axis of (a) 18° and 27°, (b) 63° and 72°, (c) 108° and 117°, (d) 234° and 243°, and (e) 279° and 288°, and (f) 324° and 333°.

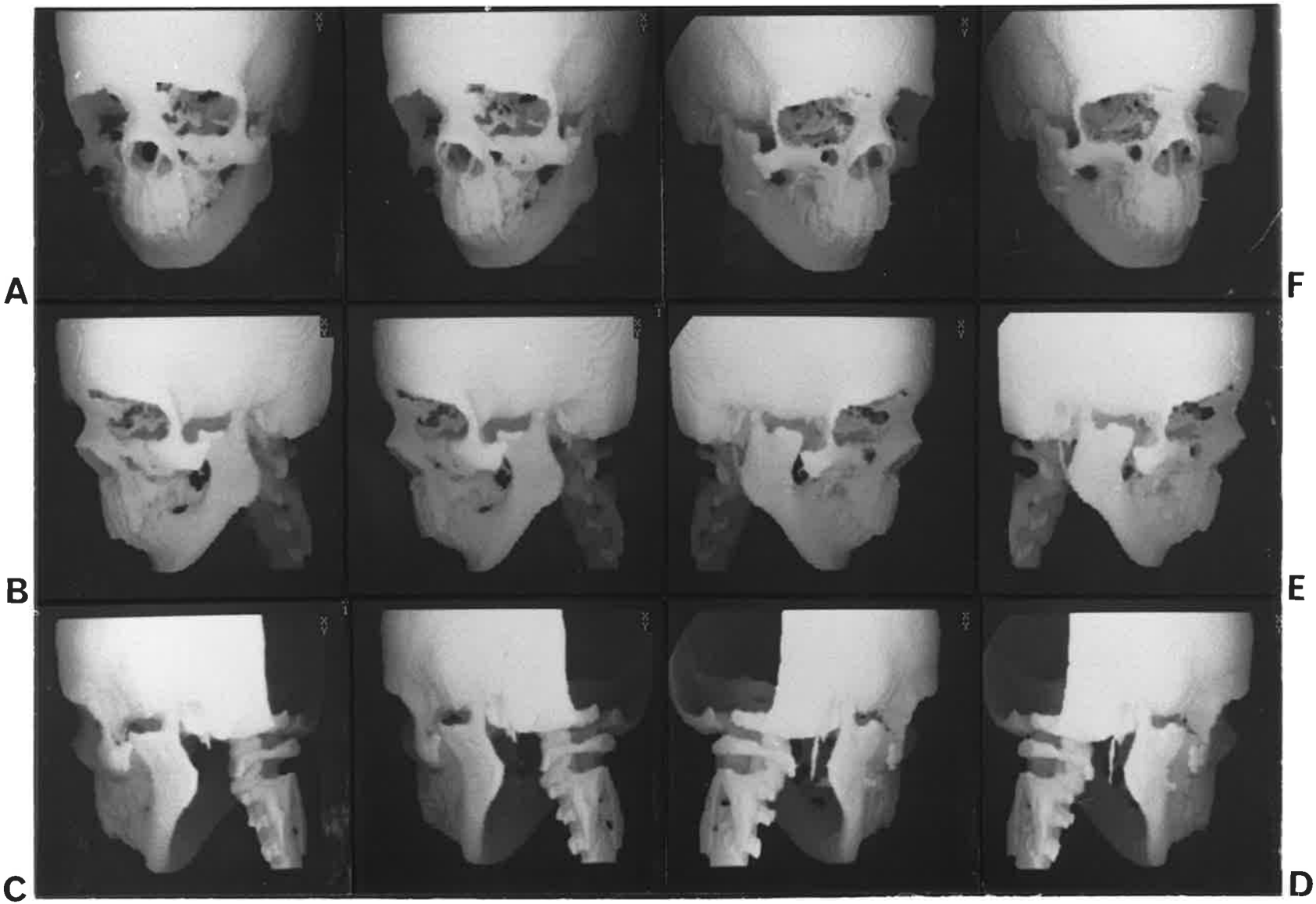
A
B
C
D
E
F

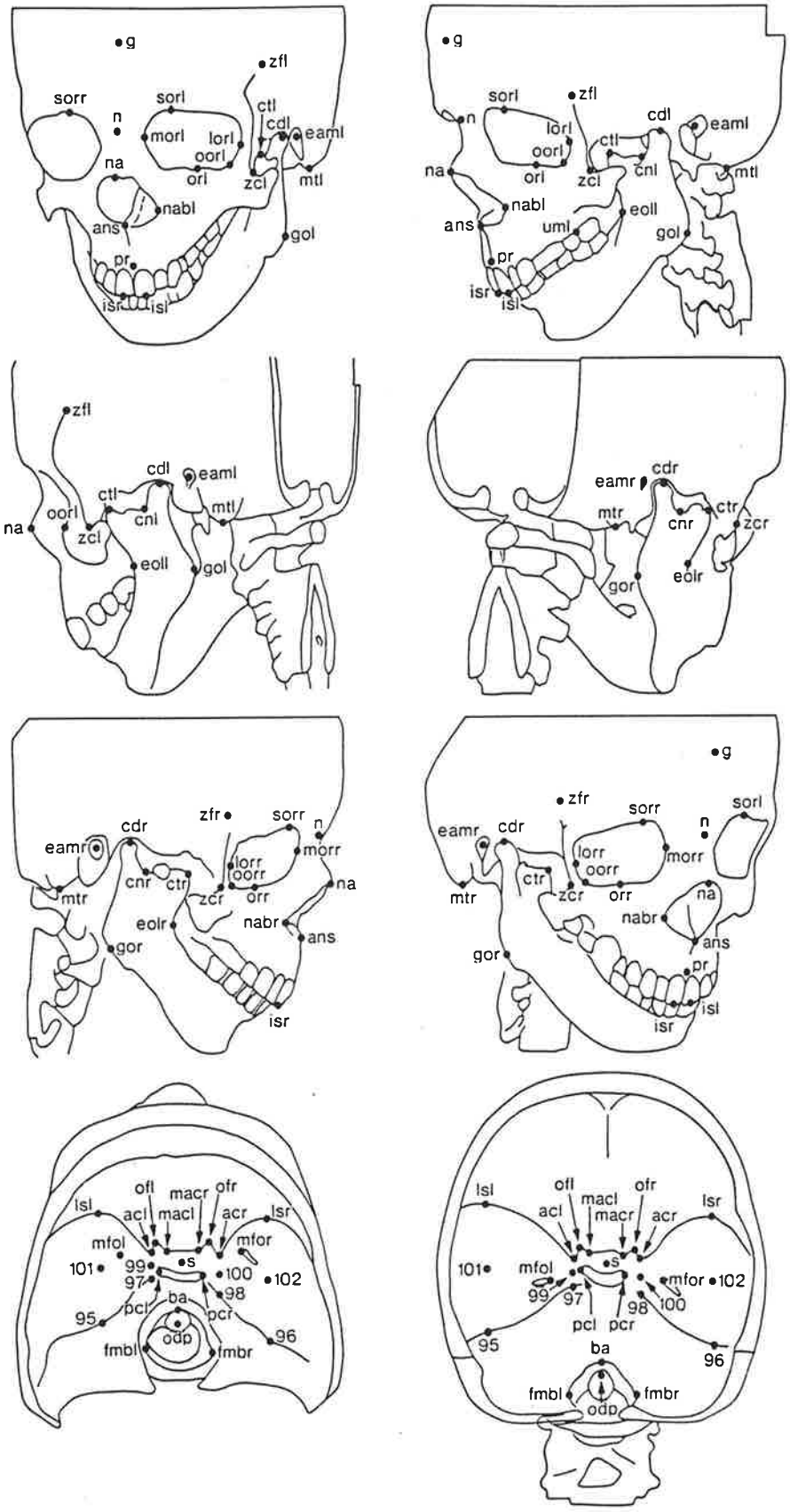

Figure 3.14 (c) Tracings utilized for landmark determination from CT reconstructions of patient 864405.

Figure 3.15 (a) Stereo CT images of patient 796025 used for determination of osseous landmarks for rotations about the X-axis of (a) 27° and 36°, (b) 72° and 81°, (c) 117° and 126°, (d) 225° and 234°, and (e) 270° and 279°, and (f) 315° and 324°.

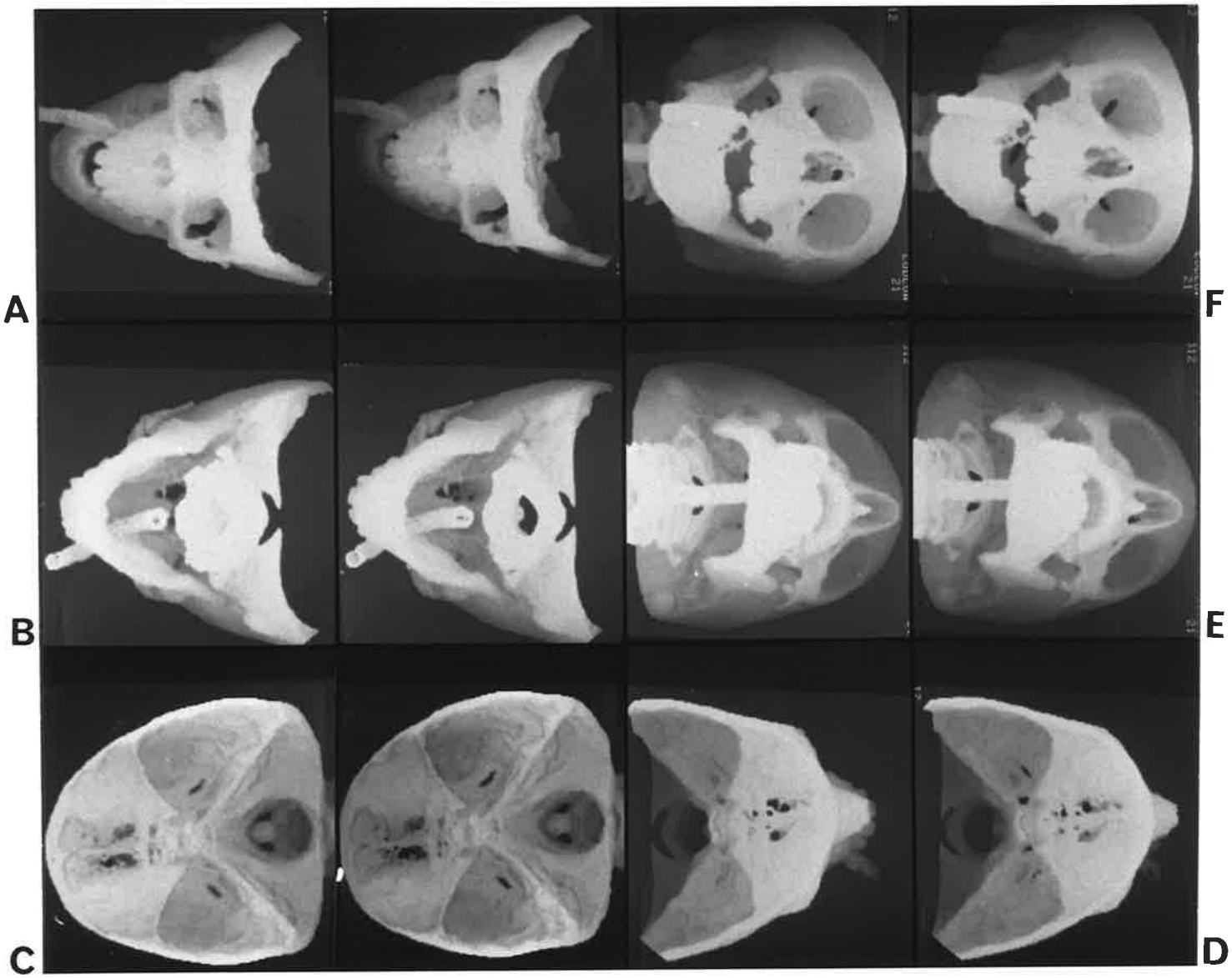
A
F
B
E
C
D

Figure 3.15 (b) Stereo CT images of patient 796025 used for determination of osseous landmarks for rotations about the Z-axis of (a) 18° and 27°, (b) 63° and 72°, (c) 108° and 117°, (d) 234° and 243°, and (e) 279° and 288°, and (f) 324° and 333°.

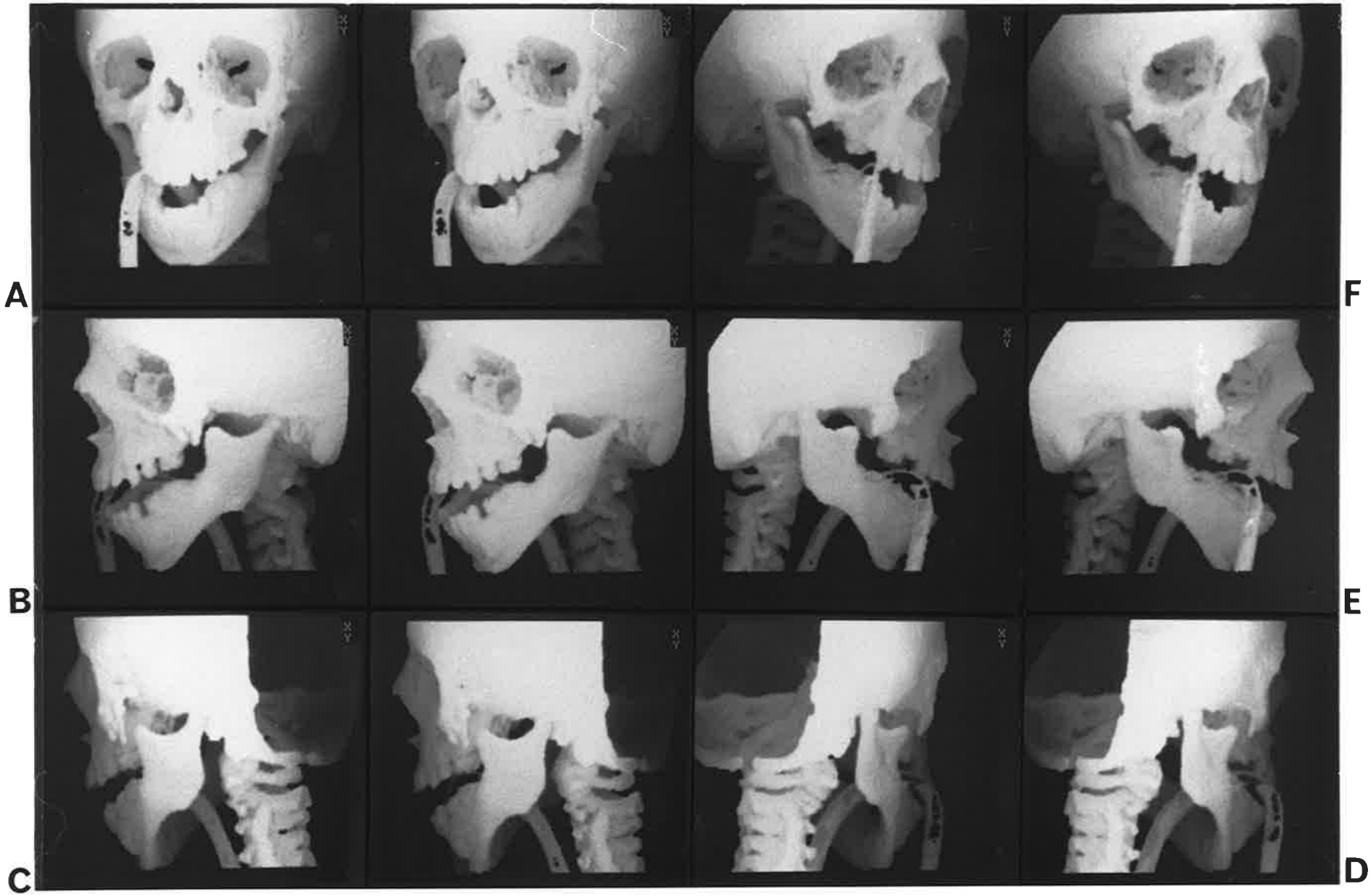
A
B
C
D
E
F

Figure 3.16 (a) Stereo CT images of patient 866790 used for determination of osseous landmarks for rotations about the X-axis of (a) 27° and 36°, (b) 72° and 81°, (c) 117° and 126°, (d) 225° and 234°, and (e) 270° and 279°, and (f) 315° and 324°.

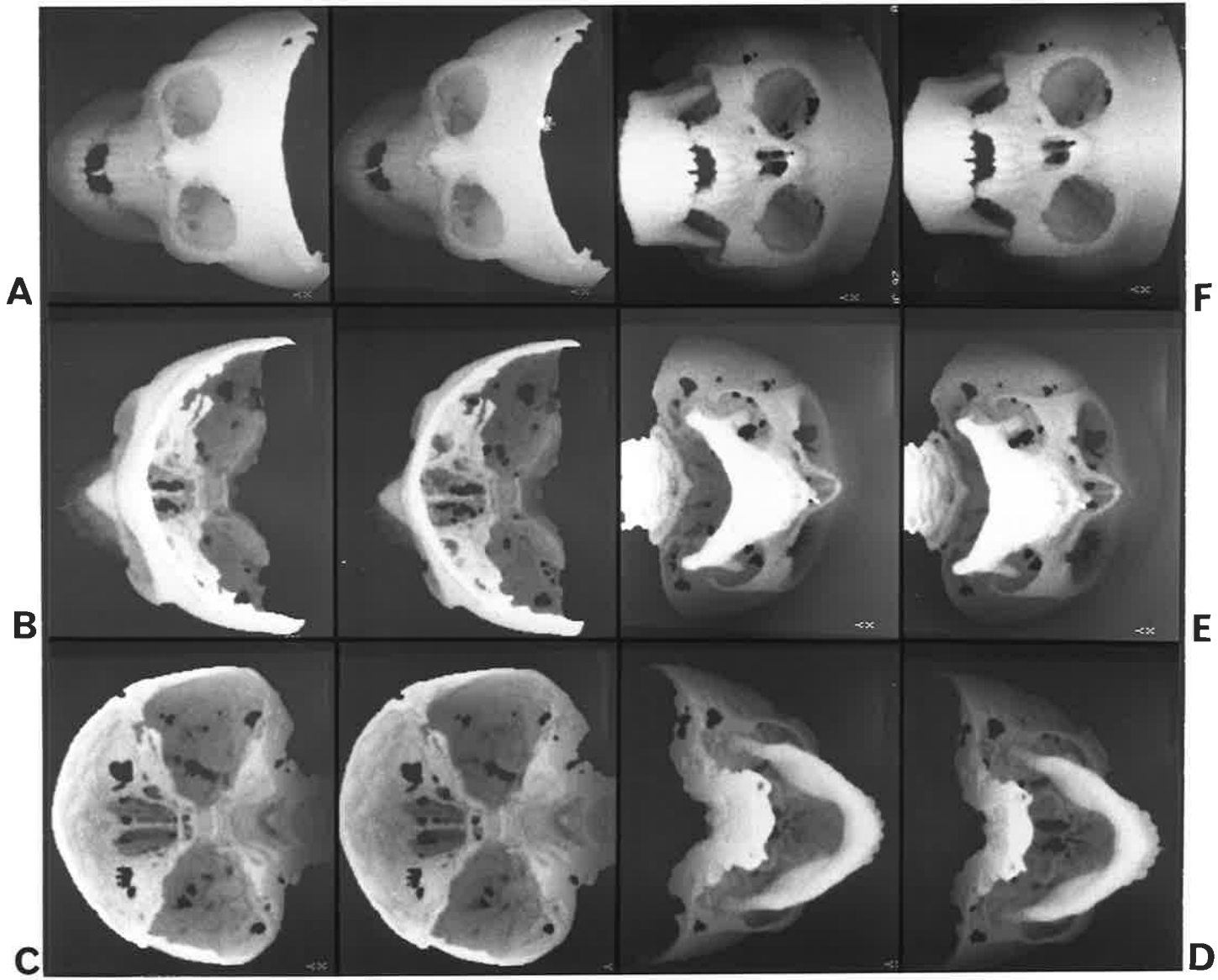
A
F
B
E
C
D

Figure 3.16 (b) Stereo CT images of patient 866790 used for determination of osseous landmarks for rotations about the Z-axis of (a) 18° and 27°, (b) 63° and 72°, (c) 108° and 117°, (d) 234° and 243°, and (e) 279° and 288°, and (f) 324° and 333°.

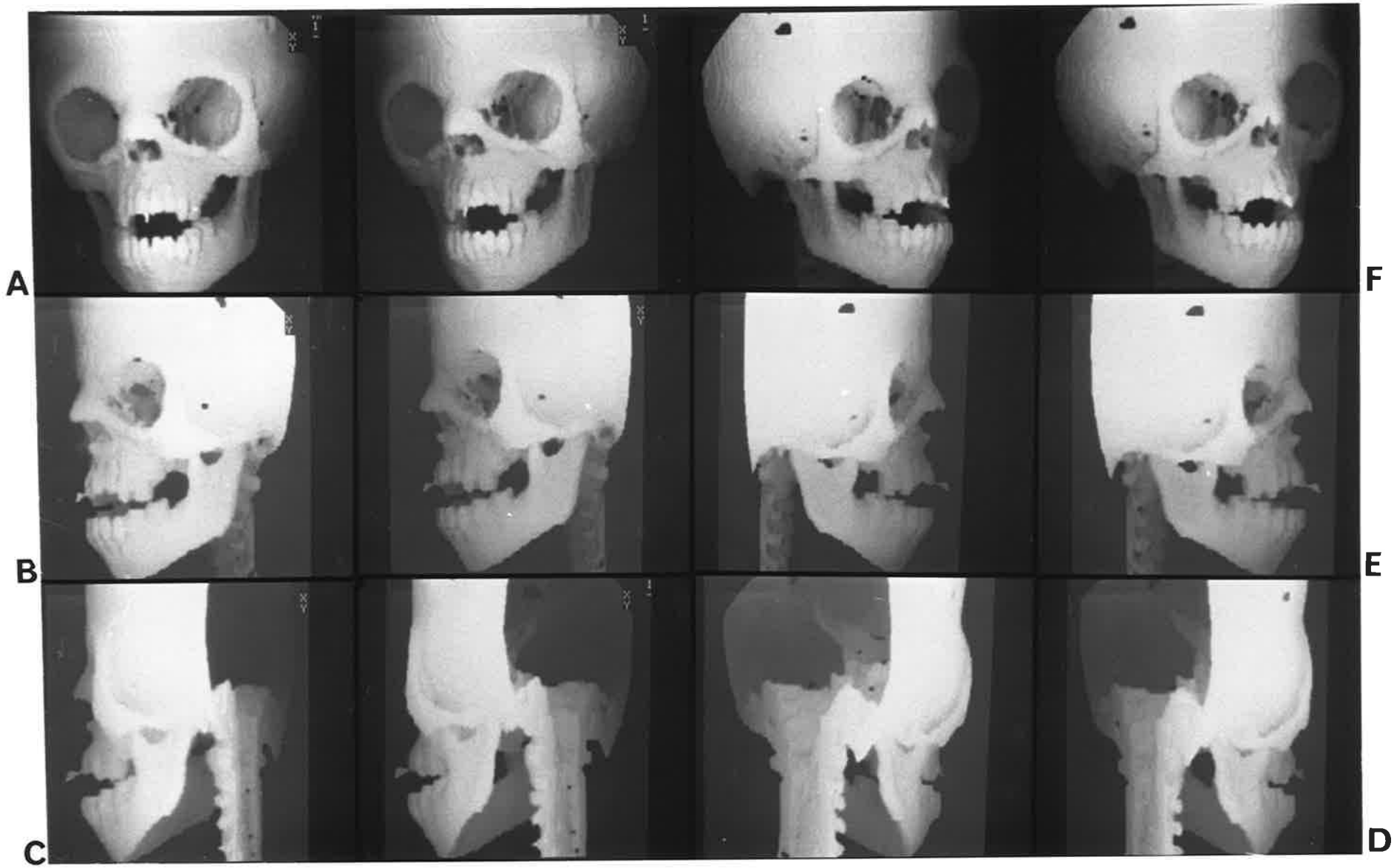
A
F
B
E
C
D

Figure 4.1 Stereo pairs of three dimensional wire frame models of the five test skulls and the adult patient with Treacher Collins Syndrome - (a) A38, (b) A90, (c) A13184, (d) A38778, (e) A57590, (f) 864405.

Landmarks have been colour coded by regions:

- mandible - red,
- maxilla and nasal bones - green,
- orbit - purple,
- zygoma and zygomatic process of the temporal bone - orange,
- cranium - blue,
- cranial base - brown.

Some landmarks were not determined and therefore lines defining bone edges involving these landmarks could not be drawn.

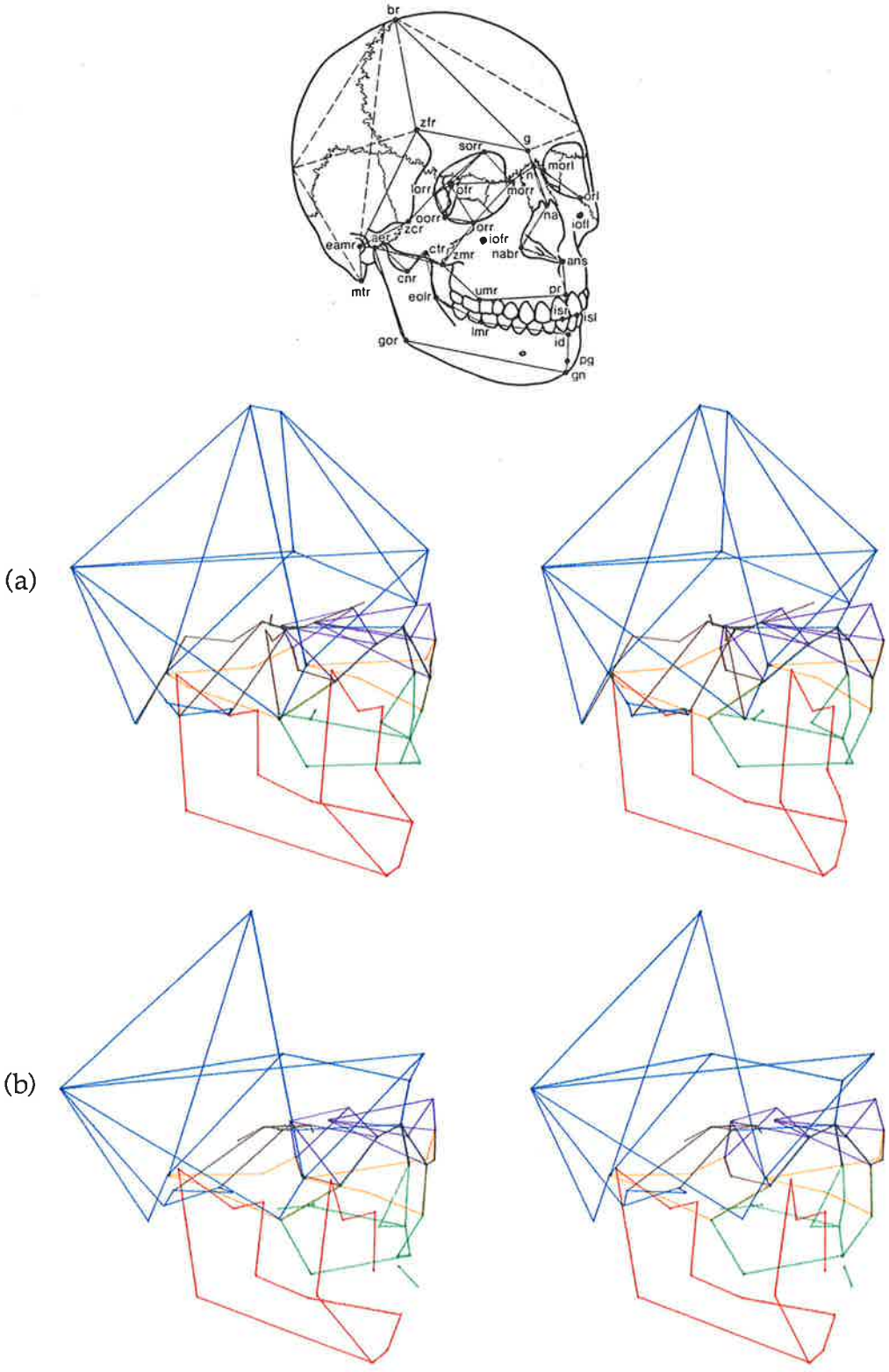

Figure 4.1 (a) Stereo pair of a wire frame model of skull A38.

(b) Stereo pair of a wire frame model of skull A90.

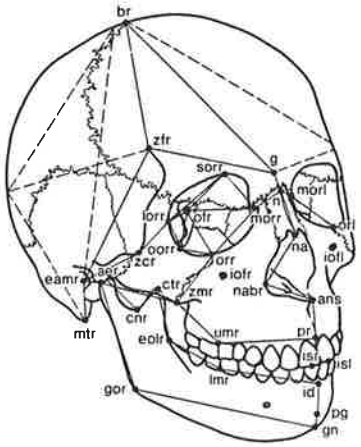

(c)

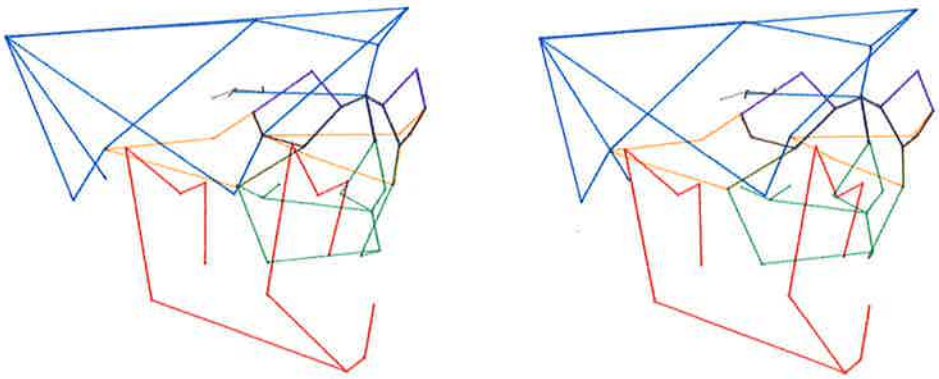

(d)

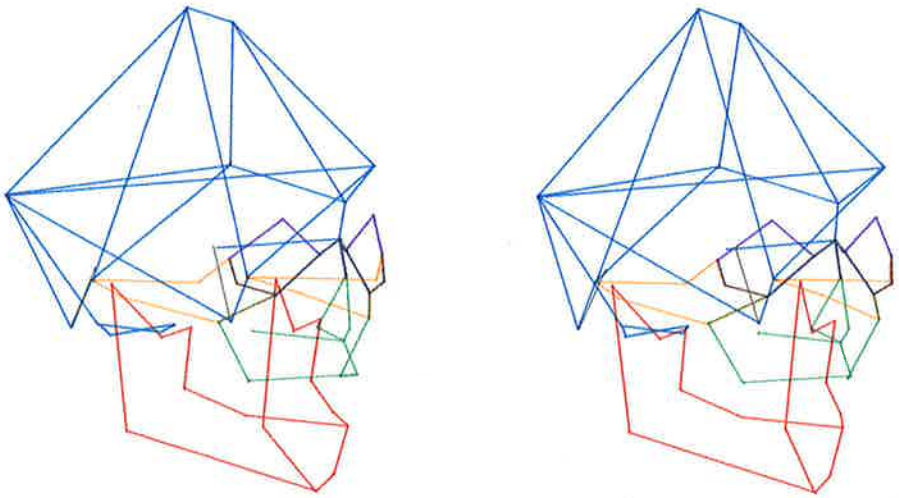

Figure 4.1 (c) Stereo pair of a wire frame model of skull A13184.

(d) Stereo pair of a wire frame model of skull A38778.

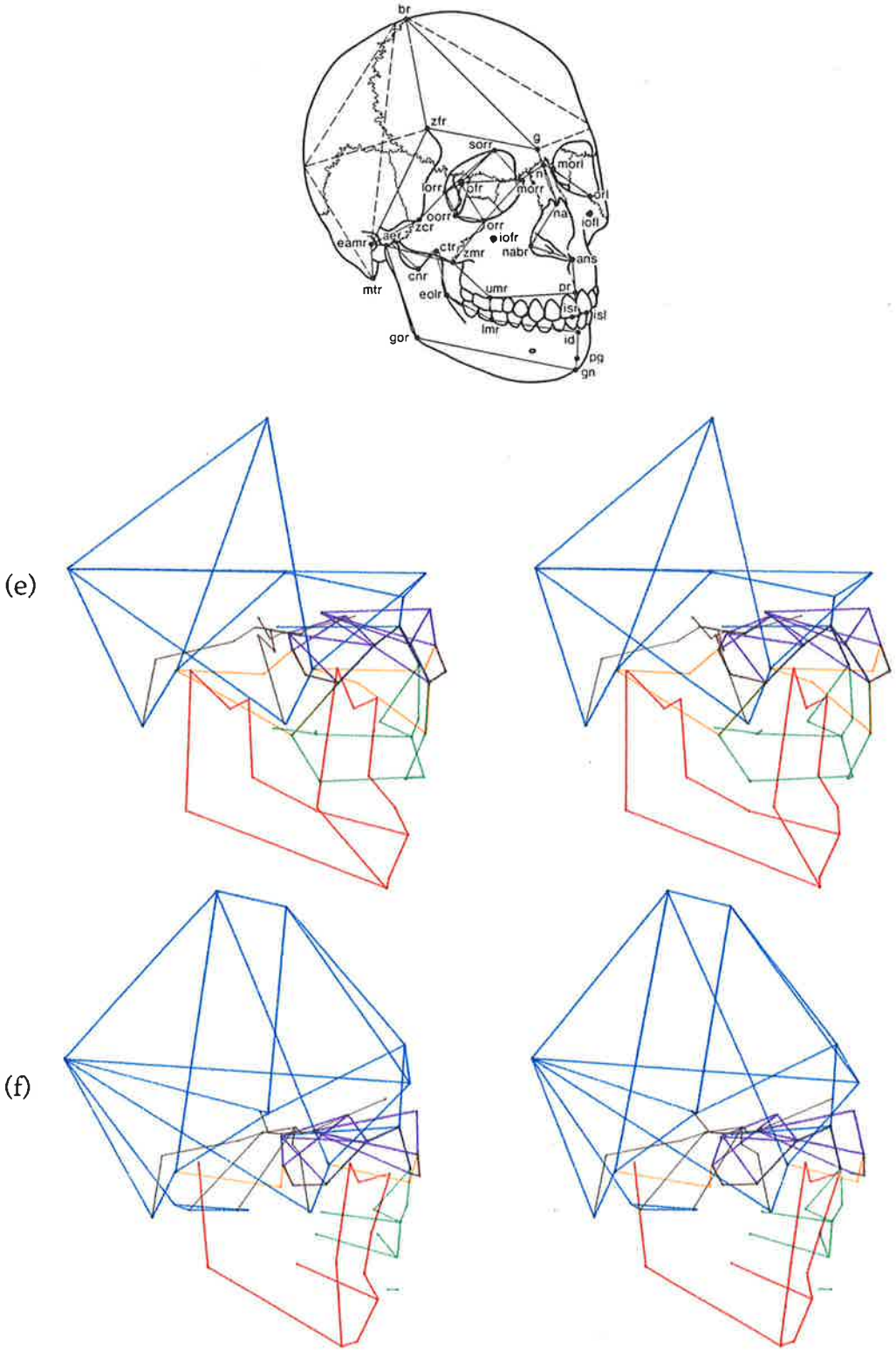

Figure 4.1 (e) Stereo pair of a wire frame model of skull A57590.

(f) Stereo pair of a wire frame model of the adult patient with Treacher Collins Syndrome 864405.

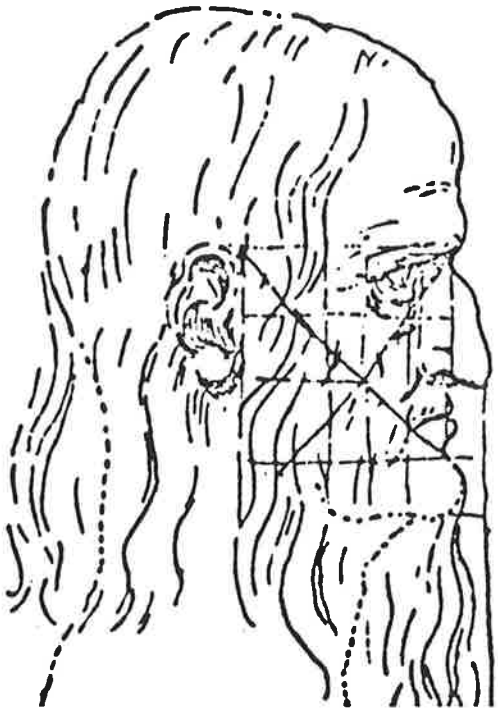

Figure 5.1 Drawing by Leonardo da Vinci demonstrating facial proportion through the use of a grid (Keele and Roberts, 1977).

Figure 5.2 Dürer's demonstration of the principles of perspective using a glass screen and a vertical rod to keep the eye at a constant height (Ernst, 1976).

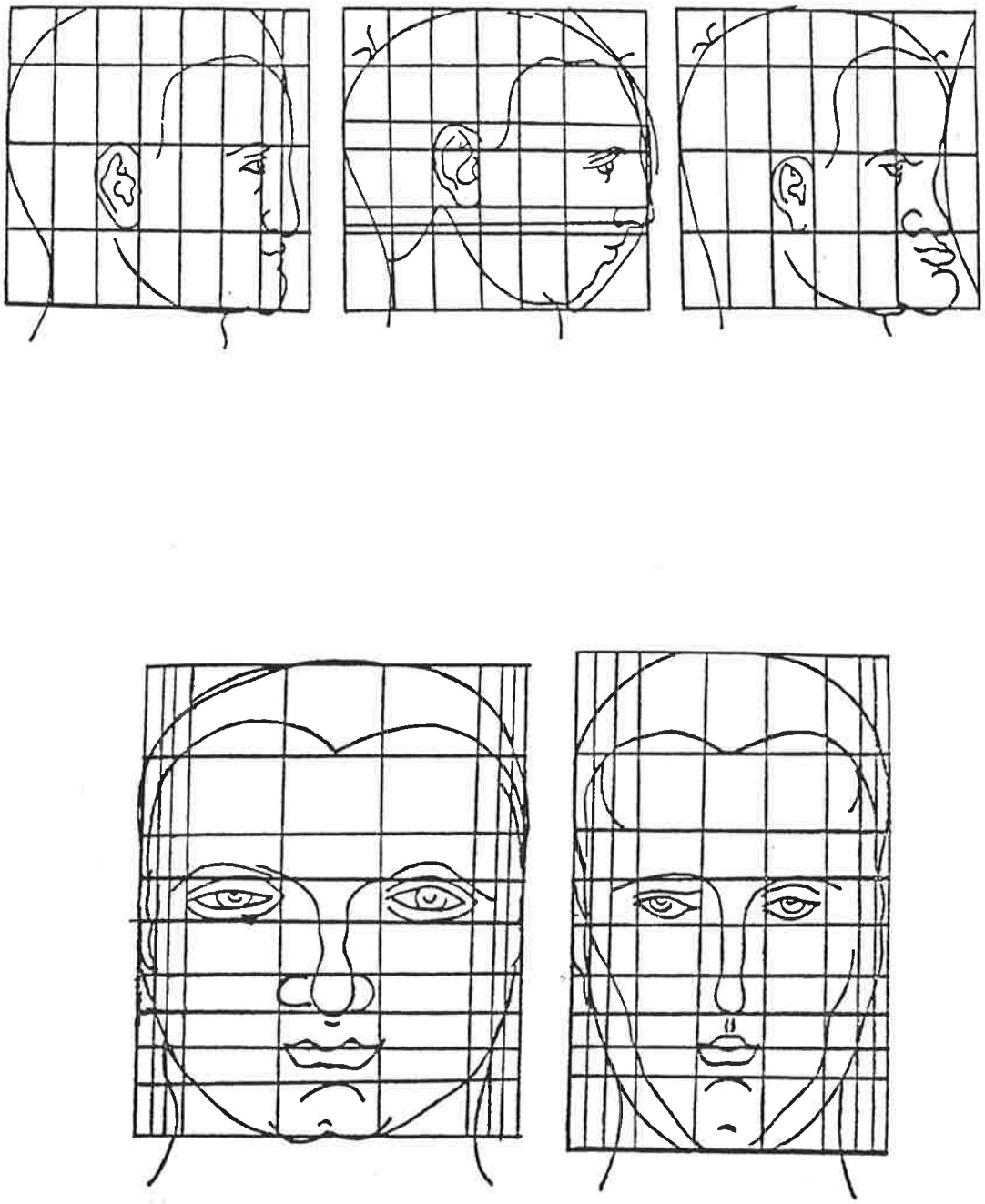

Figure 5.3 Facial type variation as described by Dürer's mesh grid system (De Coster, 1939).

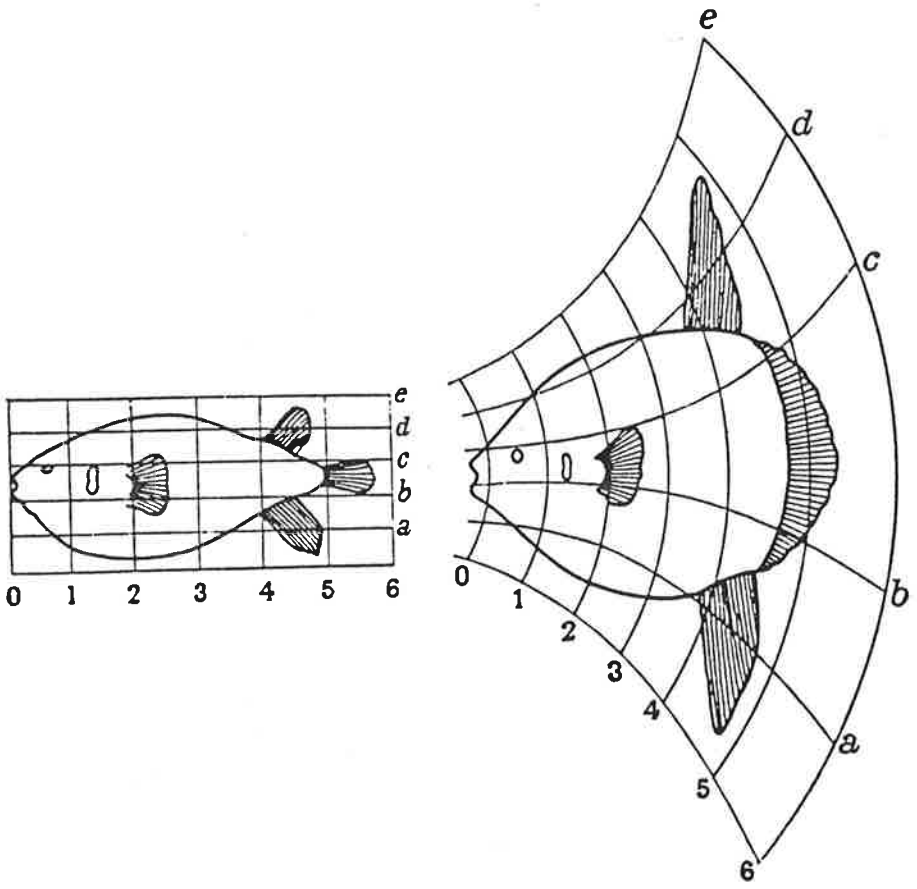

Figure 5.4 Thompson's use of coordinate transformation to describe the relationship between a Diodon (small fish) and Orthagoriscus (large fish) (Thompson, 1917).

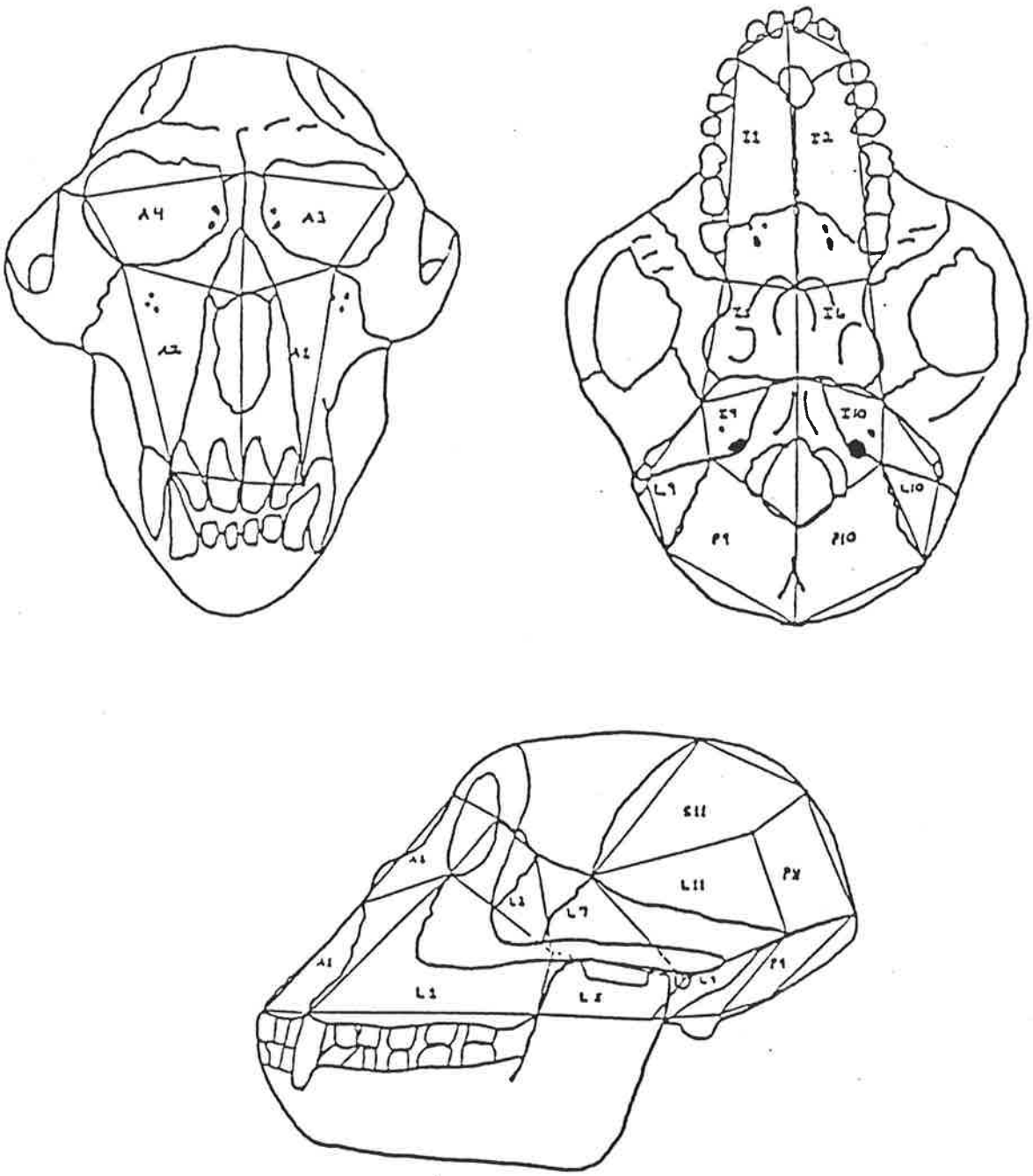

Figure 5.5 Cheverud et al., (1983) divided the rhesus marque cranium into 12, eight noded hexahedra in order to describe shape differences between fifty male rhesus marque crania and an average cranium using finite element analysis.

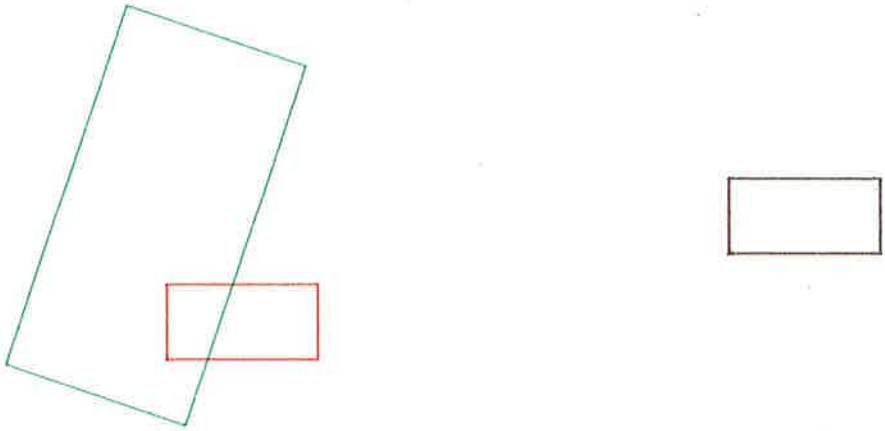

(a) (b)

Figure 5.6 Two identically shaped, but rotated, scaled and translated rectangles (a) before and (b) after least squares alignment. The green rectangle is aligned with the red rectangle.

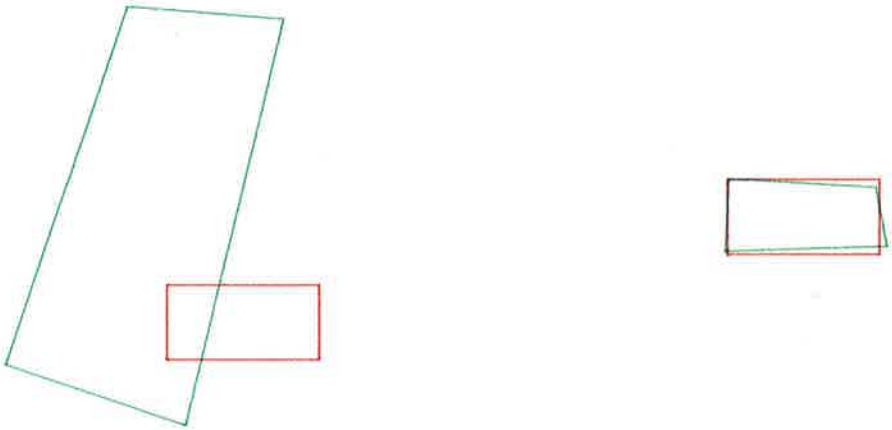

(a) (b)

Figure 5.7 Alignment of a rotated, translated and scaled rectangle that has been deformed at one vertex (green) with the original (red), using the least squares method (a) before and (b) after alignment.

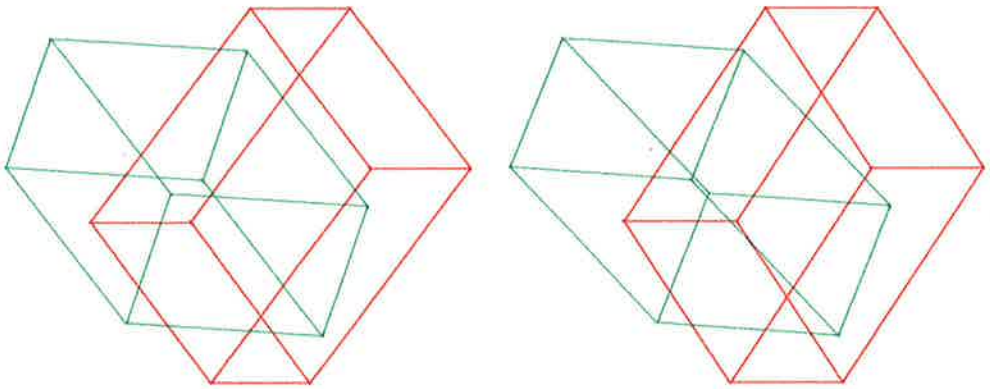

(a)

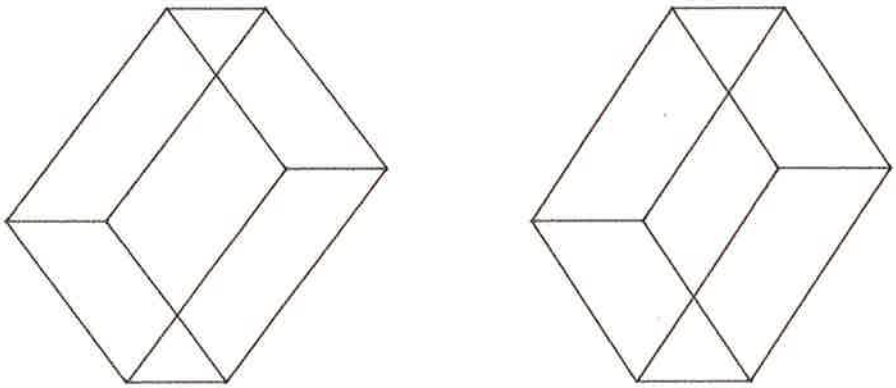

(b)

Figure 5.8 Stereo pairs showing identically shaped, but rotated, scaled and translated orthorhombic figures (a) before and (b) after least squares alignment. The green figure is aligned with the red figure.

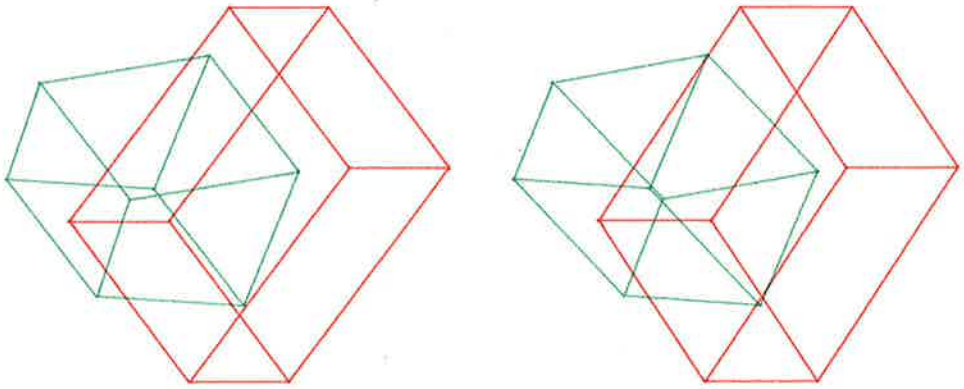

(a)

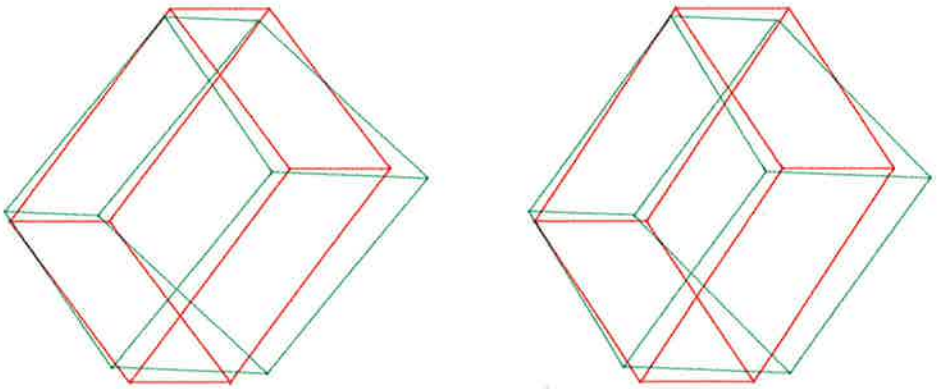

(b)

Figure 5.9 Stereo pairs showing alignment of a rotated, translated and scaled orthorhombic figure that has been deformed at two vertices (green) with the original (red) using the least squares method (a) before and (b) after alignment.

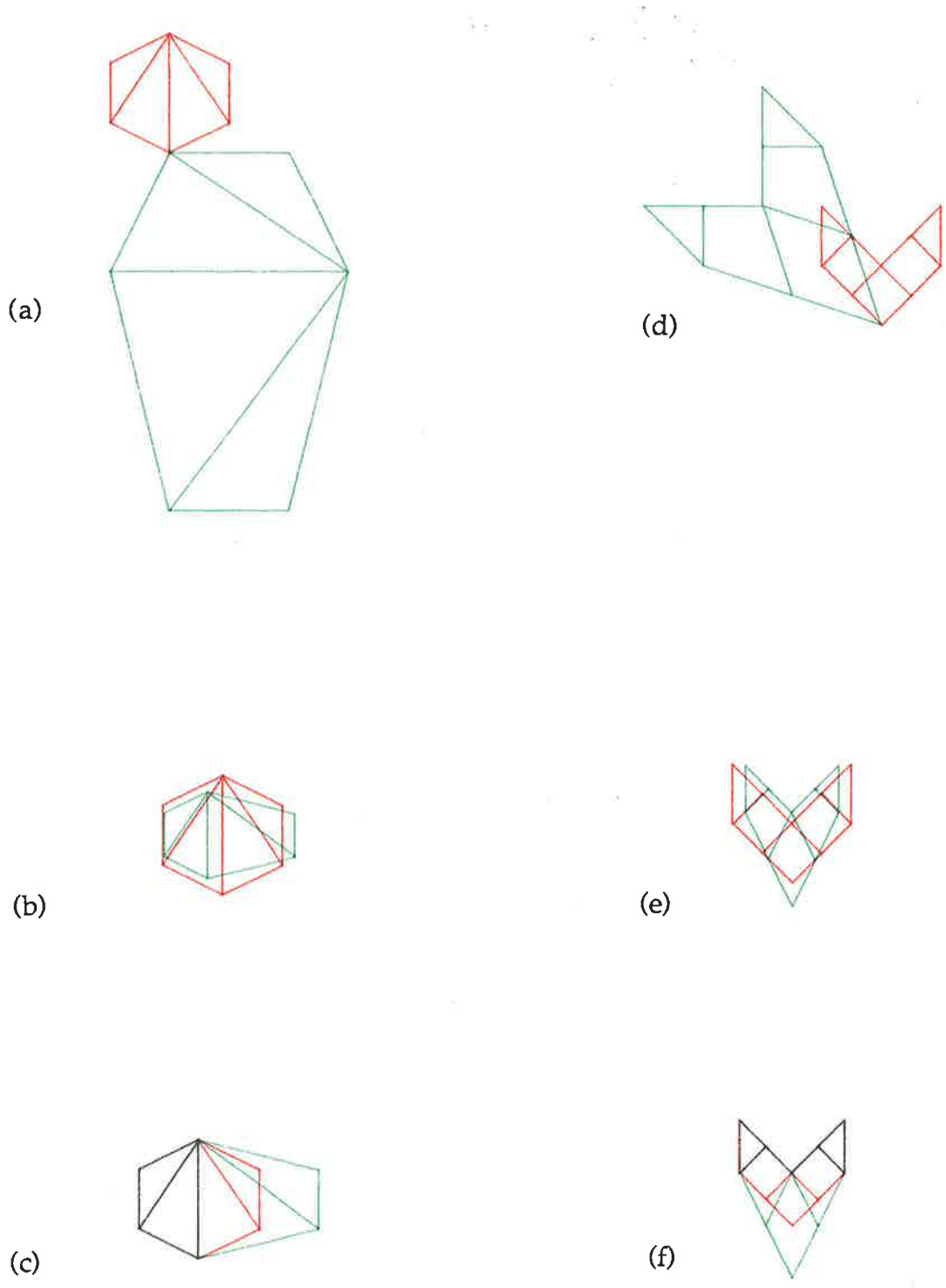

Figure 5.10 Geometric two dimensional shapes similar to those used by Siegel and Benson (1982) to illustrate the differences between least squares and repeated median alignment - (a) and (d) original figures, (b) and (e) after least squares alignment, and (c) and (f) after repeated median alignment.

(a)

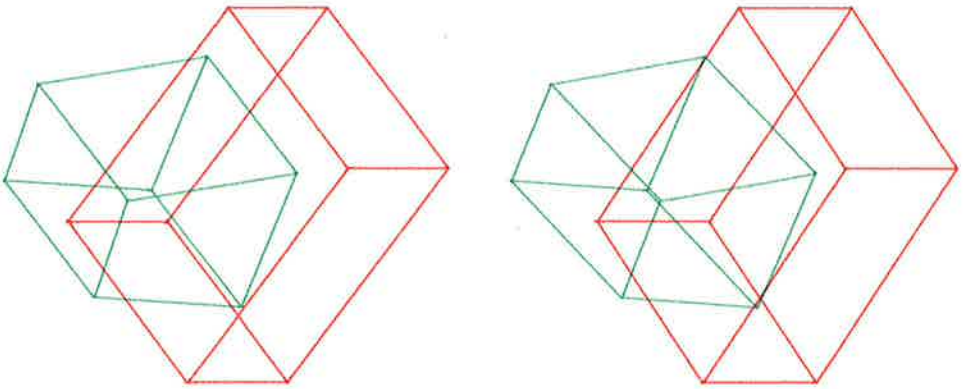

(b)

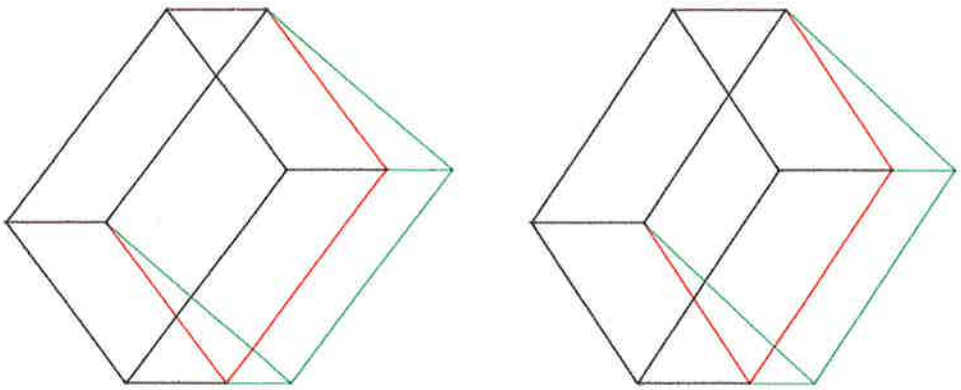

Figure 5.11 Stereo pairs showing alignment of a rotated, translated and scaled orthorhombic figure that has been deformed at two vertices (green) with the original figure (red) using the repeated median method, (a) before and (b) after alignment.

(a)

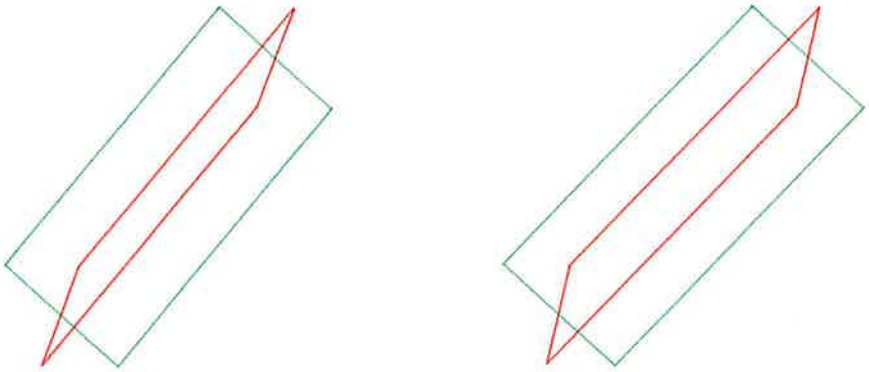

(b)

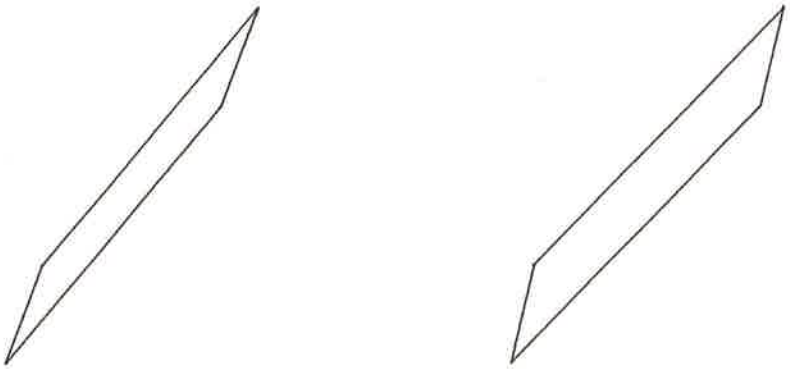

Figure 5.12 Stereo pairs of

(a) identical rectangles in three dimensional space with one rectangle rotated relative to the other about the rectangle's longitudinal axis, and

(b) the superimposition of the rectangles after repeated median alignment.

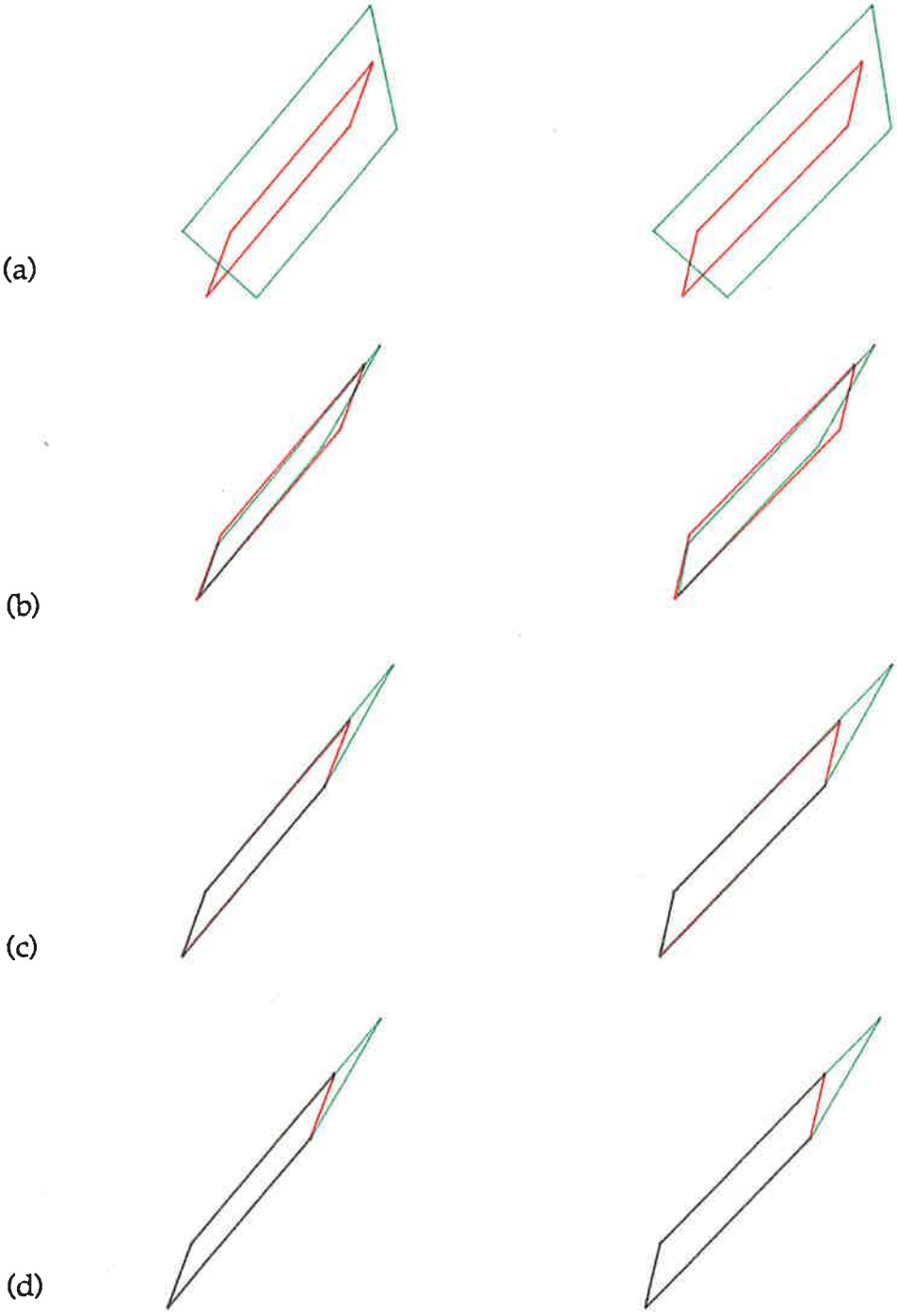

Figure 5.13 Stereo pairs of

(a) the original rectangle (red) and the same rectangle rotated, scaled and deformed at one vertex (green),

(b) the two objects after least squares alignment,

(c) the two objects after repeated median alignment, and

(d) the two objects after least squares alignment followed by repeated median alignment.

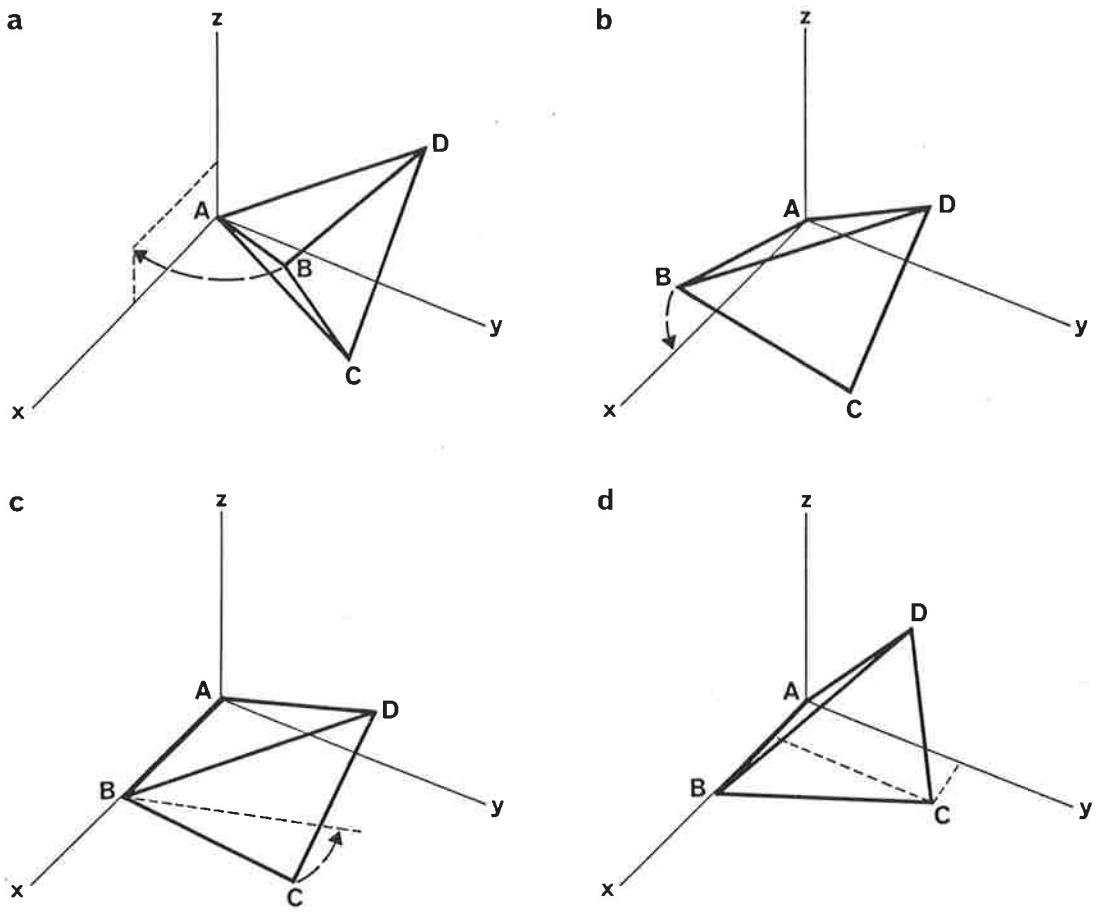

Figure 5.14 Each tetrahedral element is re-oriented as follows:

(a) translation of vertex A to the origin,

(b) rotation about the Z-axis, so that the line segment $\overline{AB}$ is in the X-Z plane,

(c) rotation about the Y-axis, so that the line segment $\overline{AB}$ is coincident with the X- axis, and

(d) rotation about the X-axis to bring vertex C, and thus the base of the tetrahedral element into the X-Y plane.

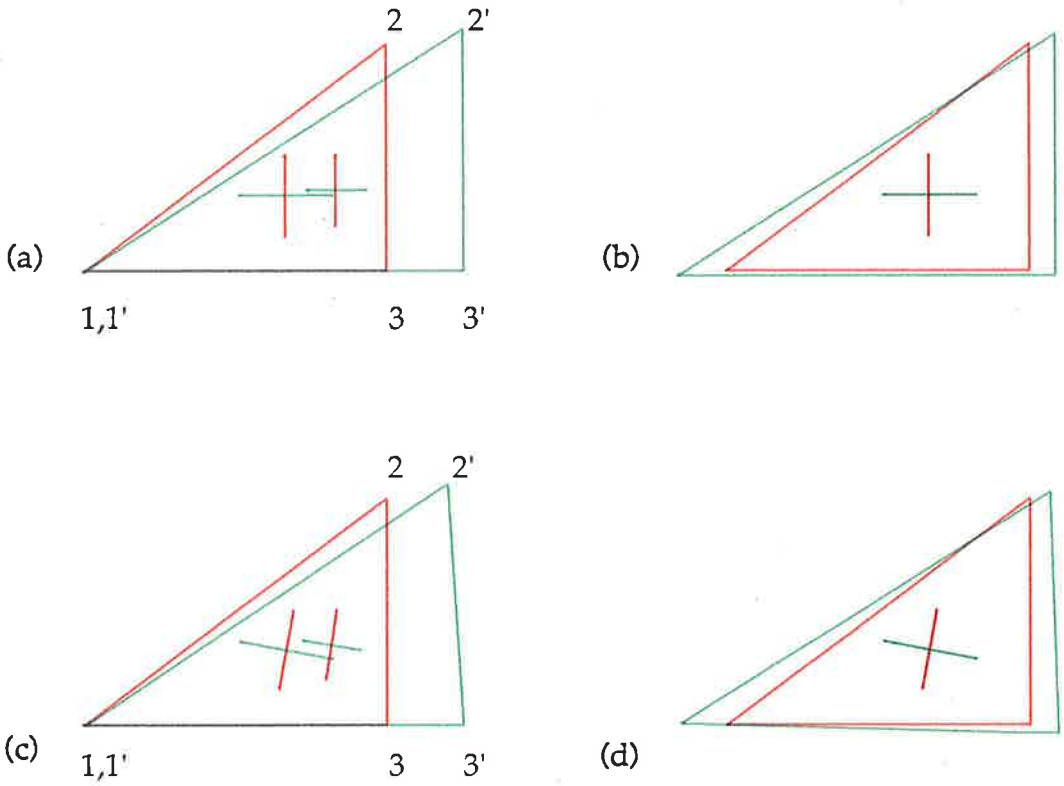

Figure 5.15 Shape comparison of two triangles using strain analysis. In (a) the green triangle was generated by extension of the red triangle in the X and Y directions and in (c) by a further displacement of vertex 2' along the negative X direction. The principal strain directions are plotted at the centroids of the triangles and indicate the direction in which contraction or dilation would change the shape of one triangle to match the shape of the other triangle, but not necessarily match its orientation. The major and minor principal strain directions are shown in green and red respectively, for the initial (red) triangle and vice versa for the deformed triangle (green).

In (a) and (c) the triangles are oriented with vertices 1 and 1' coincident and the line segments $\overline{13}$ and $\overline{13}'$ coincident in direction to illustrate the generation of the green triangle from the red triangle.

In (b) and (d) alignment is on the centroids of the triangles and on the principal strain directions.

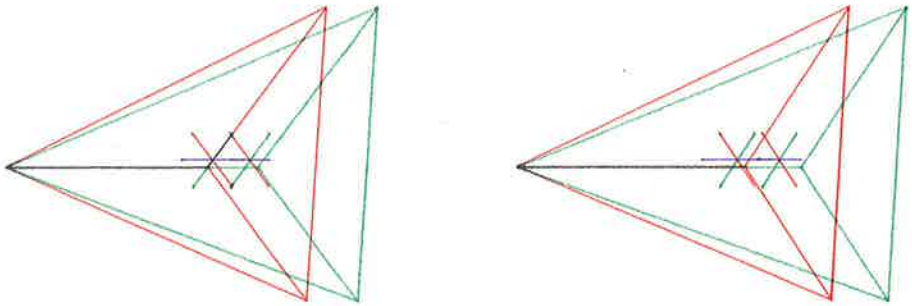

Figure 5.16 Stereo pair of two tetrahedra illustrating shape comparison using strain analysis. The green tetrahedron was generated by extension of the red tetrahedron in the X direction. The principal strain directions are plotted at the centroids of the tetrahedra. There are three principal strain directions: the minor, semi-major and major, colour coded in red, green and purple respectively when describing the transformation from the red to the green tetrahedron. The major principal strain direction is naturally along the X direction. The minor and semi-major are along the Y and Z directions, but having equal magnitude their directions are not independent and could have been oriented at any direction in the Y-Z plane (remaining orthogonal to each other).

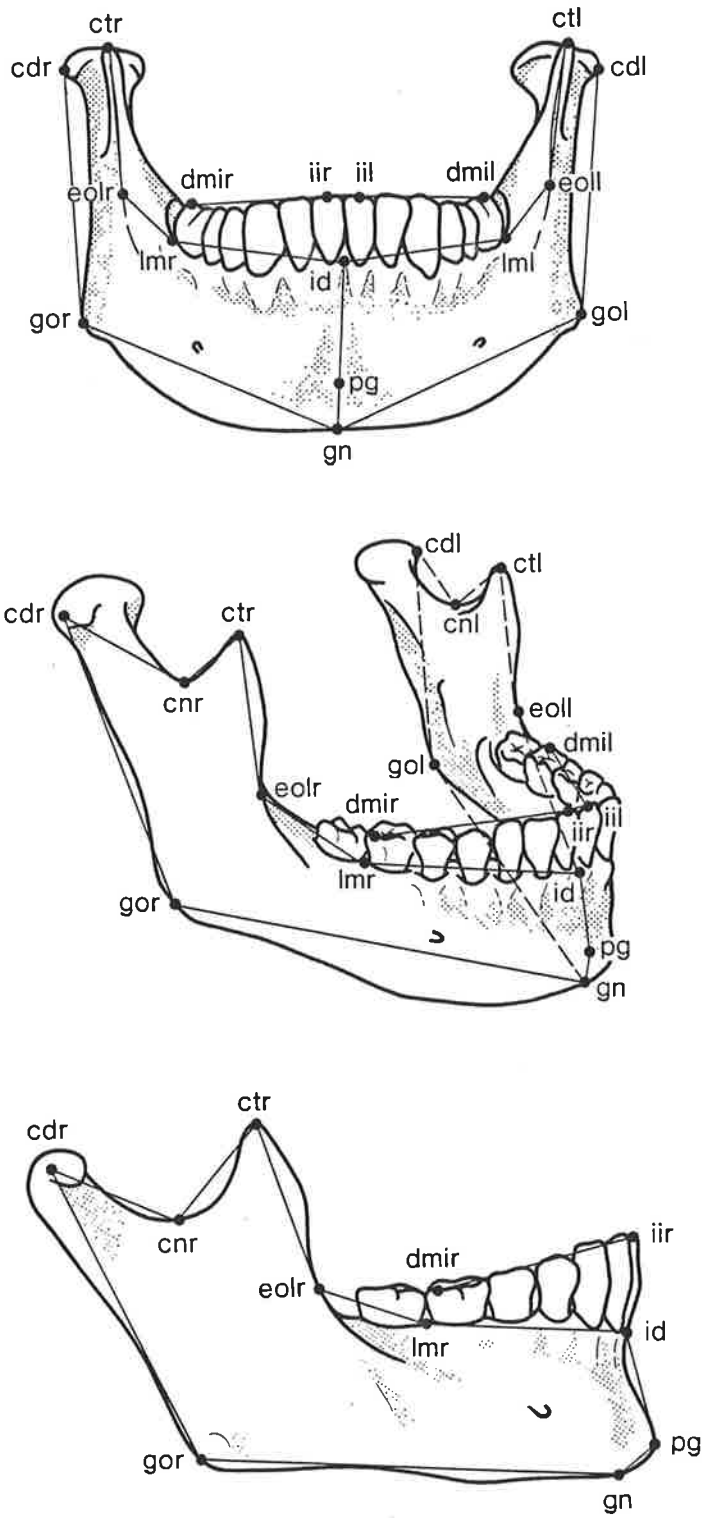

Figure 6.1 (a) Illustration of the wire frame model used to represent the mandible.

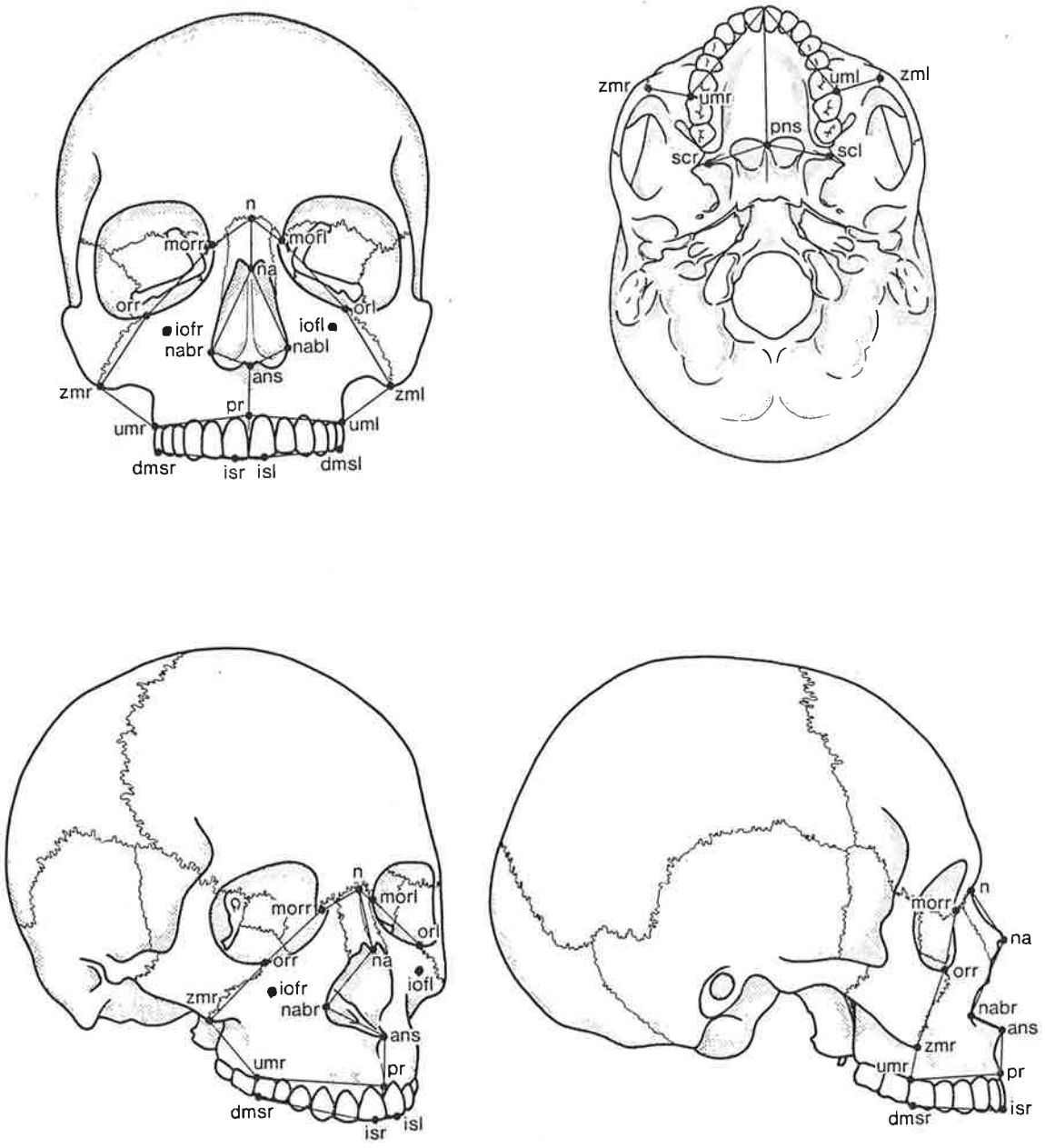

Figure 6.1 (b) Illustration of the wire frame model used to represent the region of the maxilla.

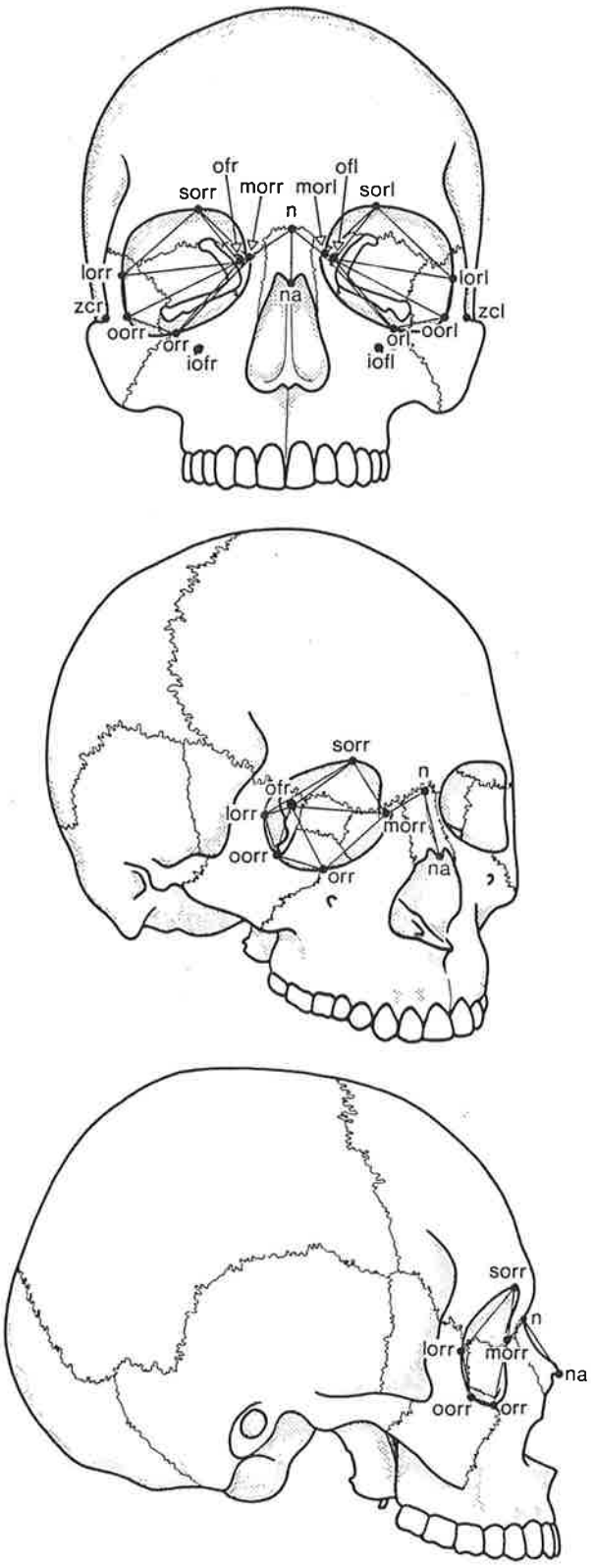

Figure 6.1 (c) Illustration of the wire frame model used to represent the region of the orbits.

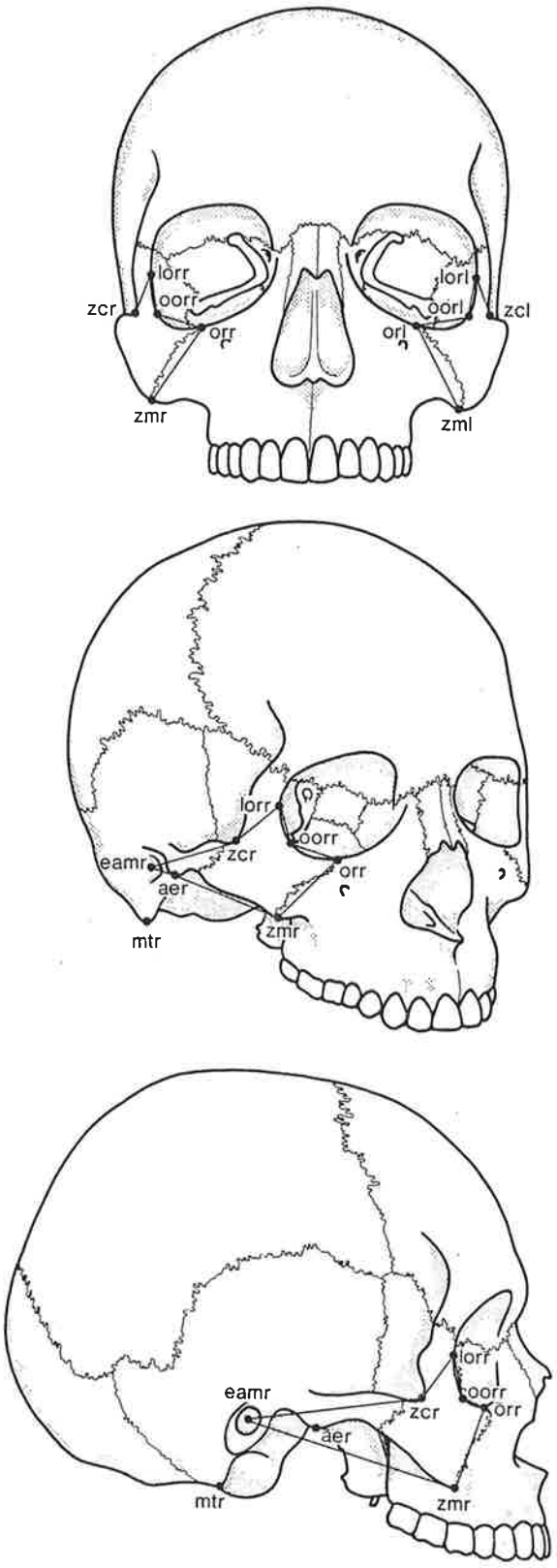

Figure 6.1 (d) Illustration of the wire frame model used to represent the region of the zygoma.

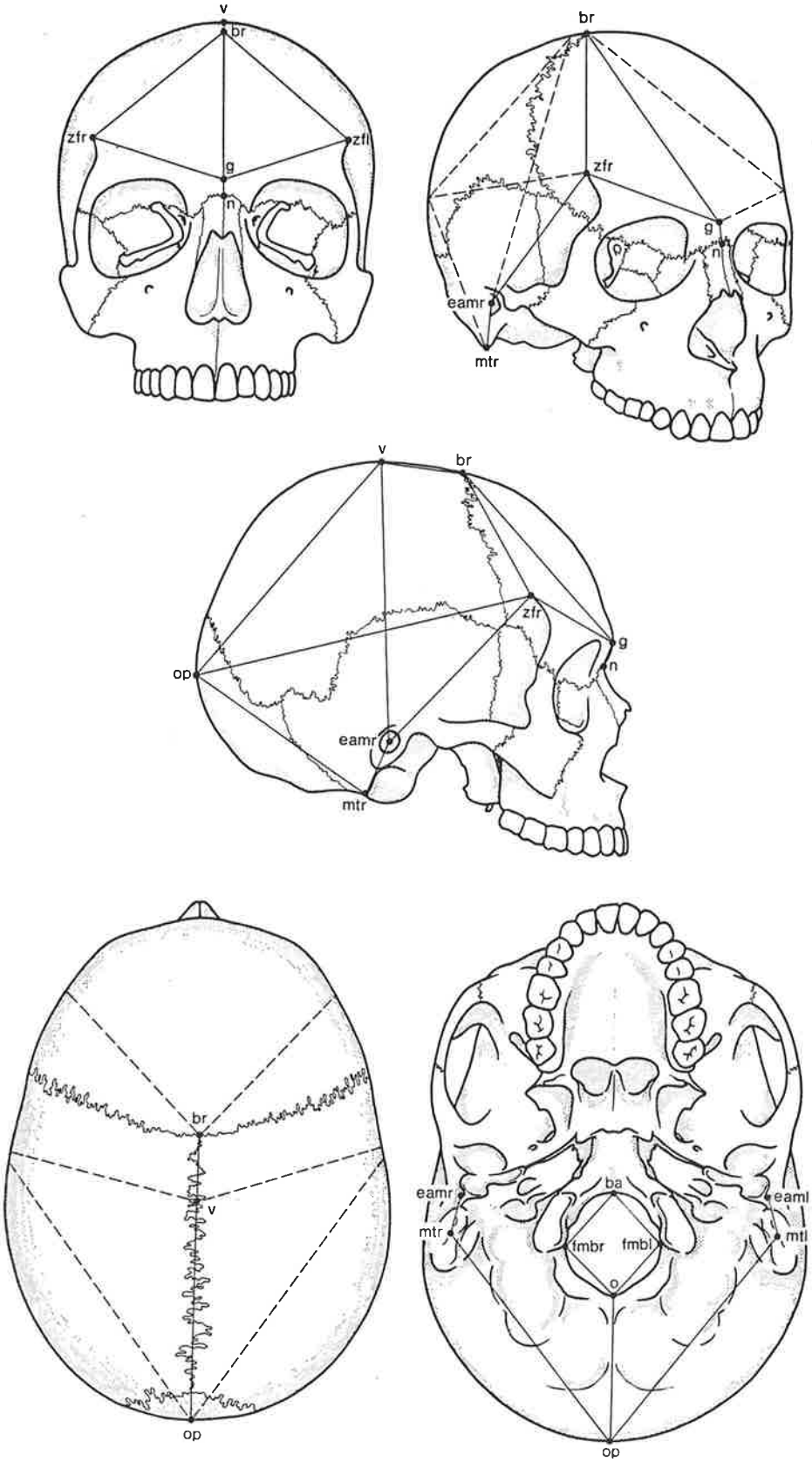

Figure 6.1 (e) Illustration of the wire frame model used to represent the region of the cranium.

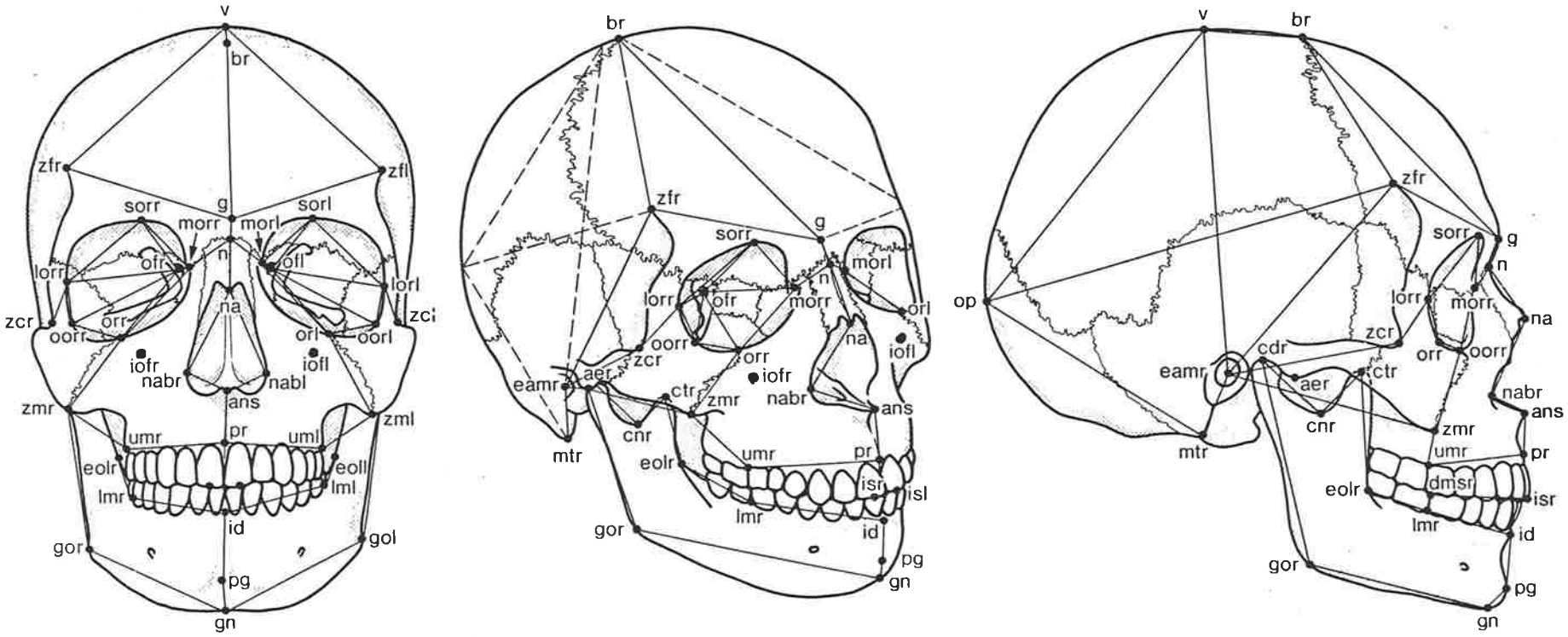

Figure 6.1 (f) Illustration of the wire frame model used to represent the skull.

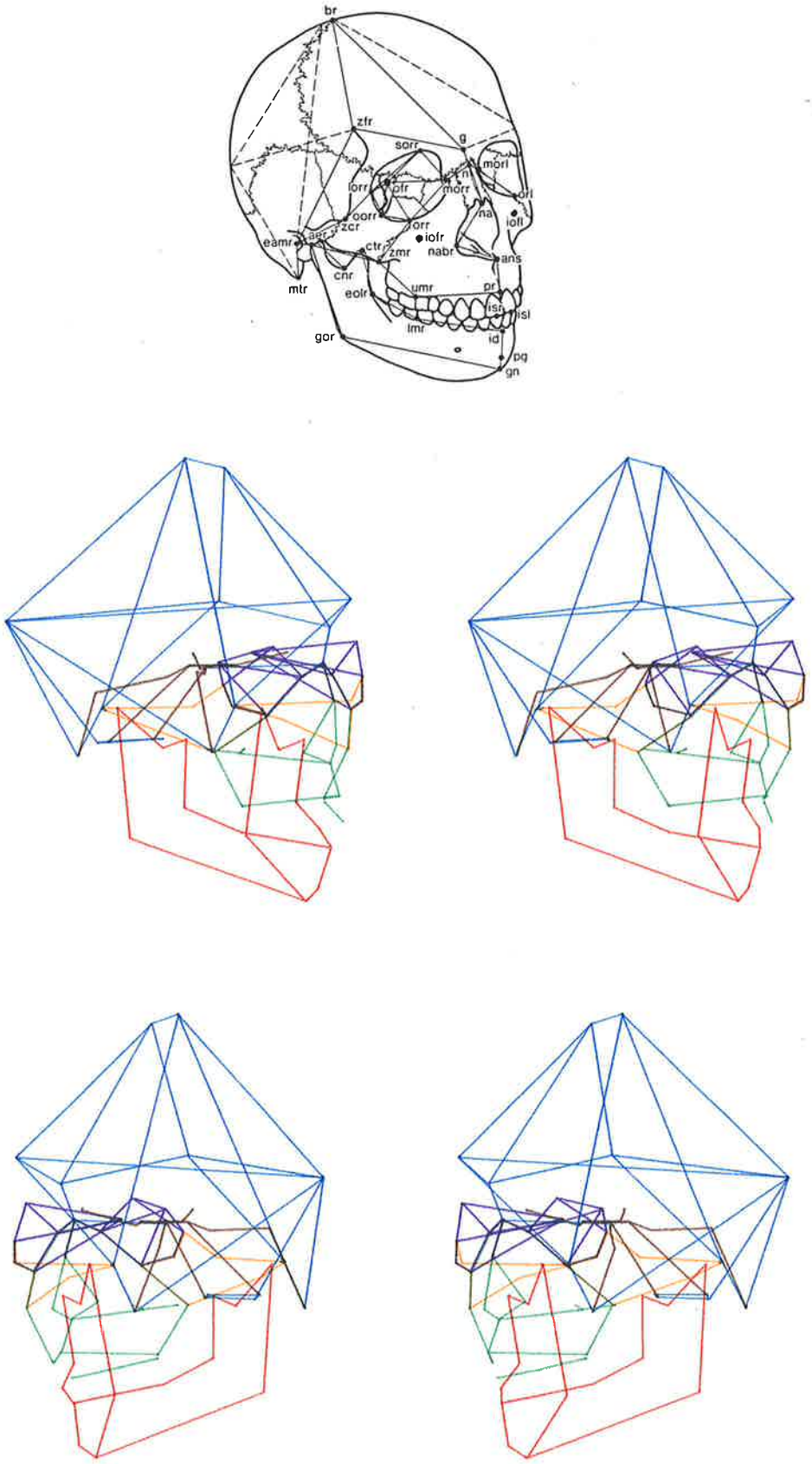

Figure 6.2 Stereo pair showing the wire frame model of the least squares skull standard.

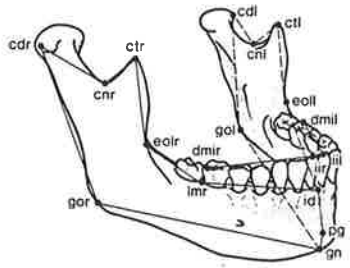

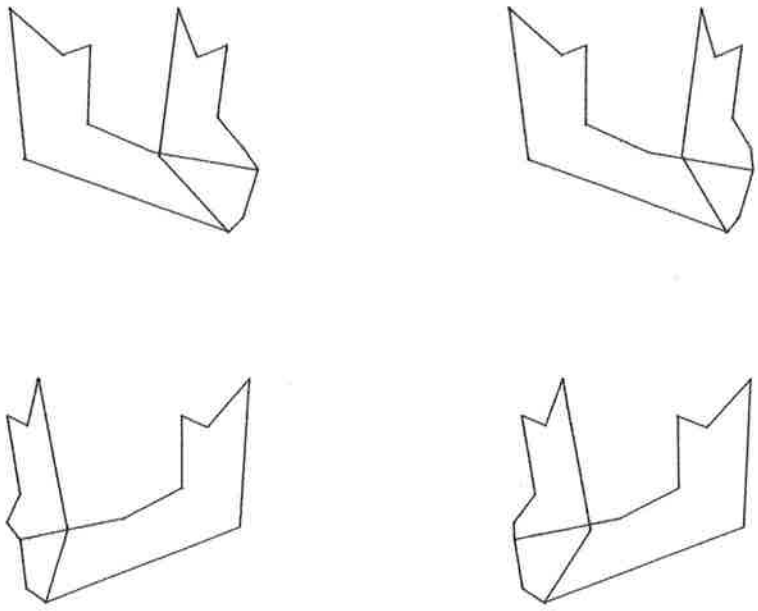

Figure 6.3 (a) Non-scaled least squares comparison of the least squares mandible standard with the least squares skull standard.

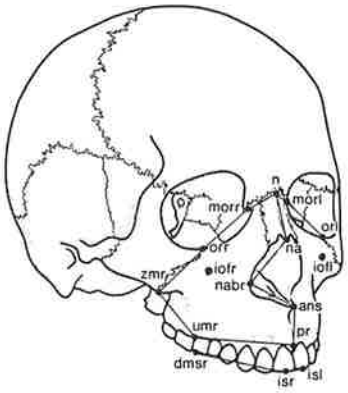

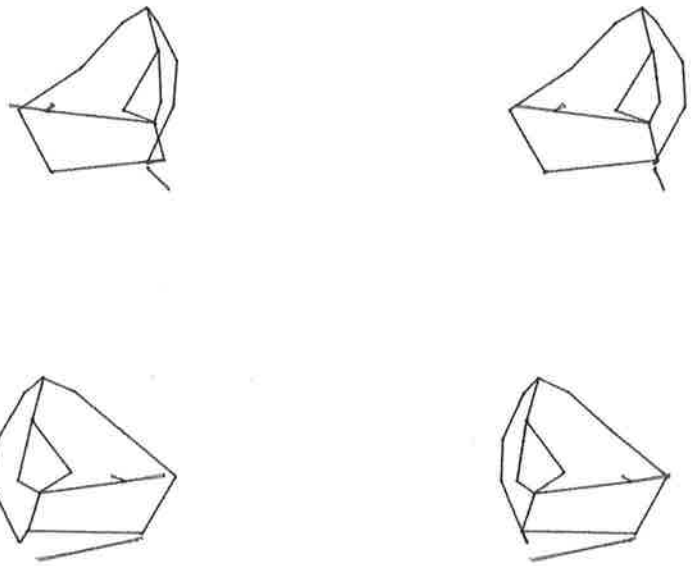

Figure 6.3 (b) Non-scaled least squares comparison of the least squares maxilla standard with the least squares skull standard.

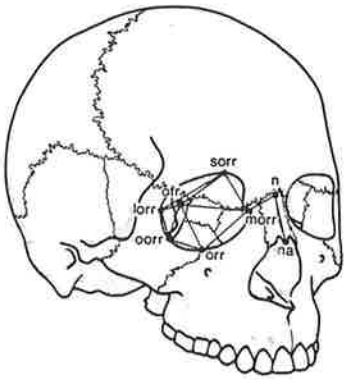

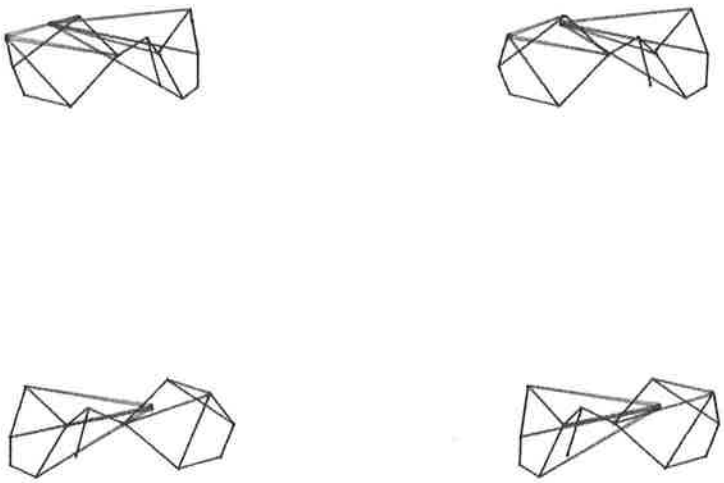

Figure 6.3 (c) Non-scaled least squares comparison of the least squares orbit standard with the least squares skull standard.

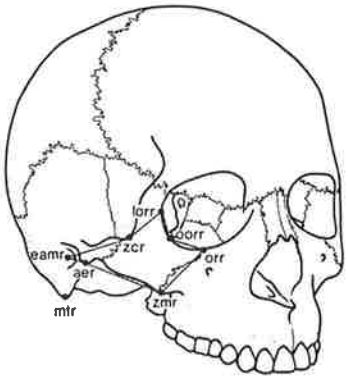

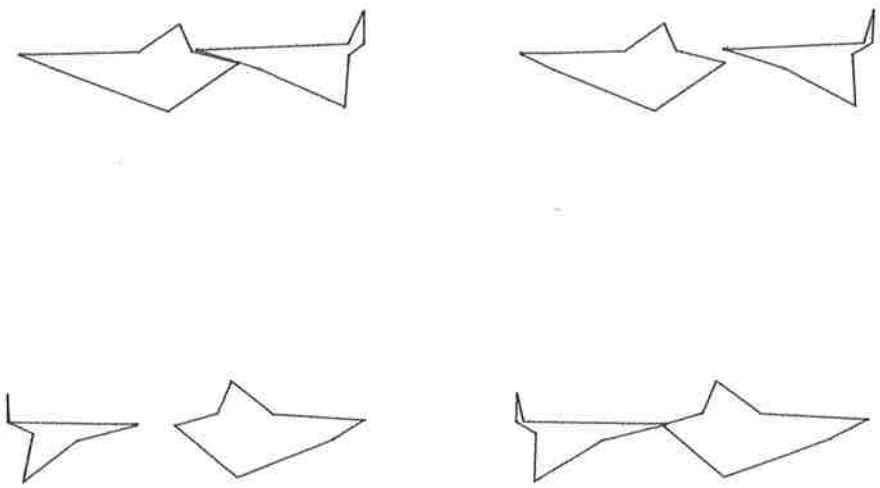

Figure 6.3 (d) Non-scaled least squares comparison of the least squares zygoma standard with the least squares skull standard.

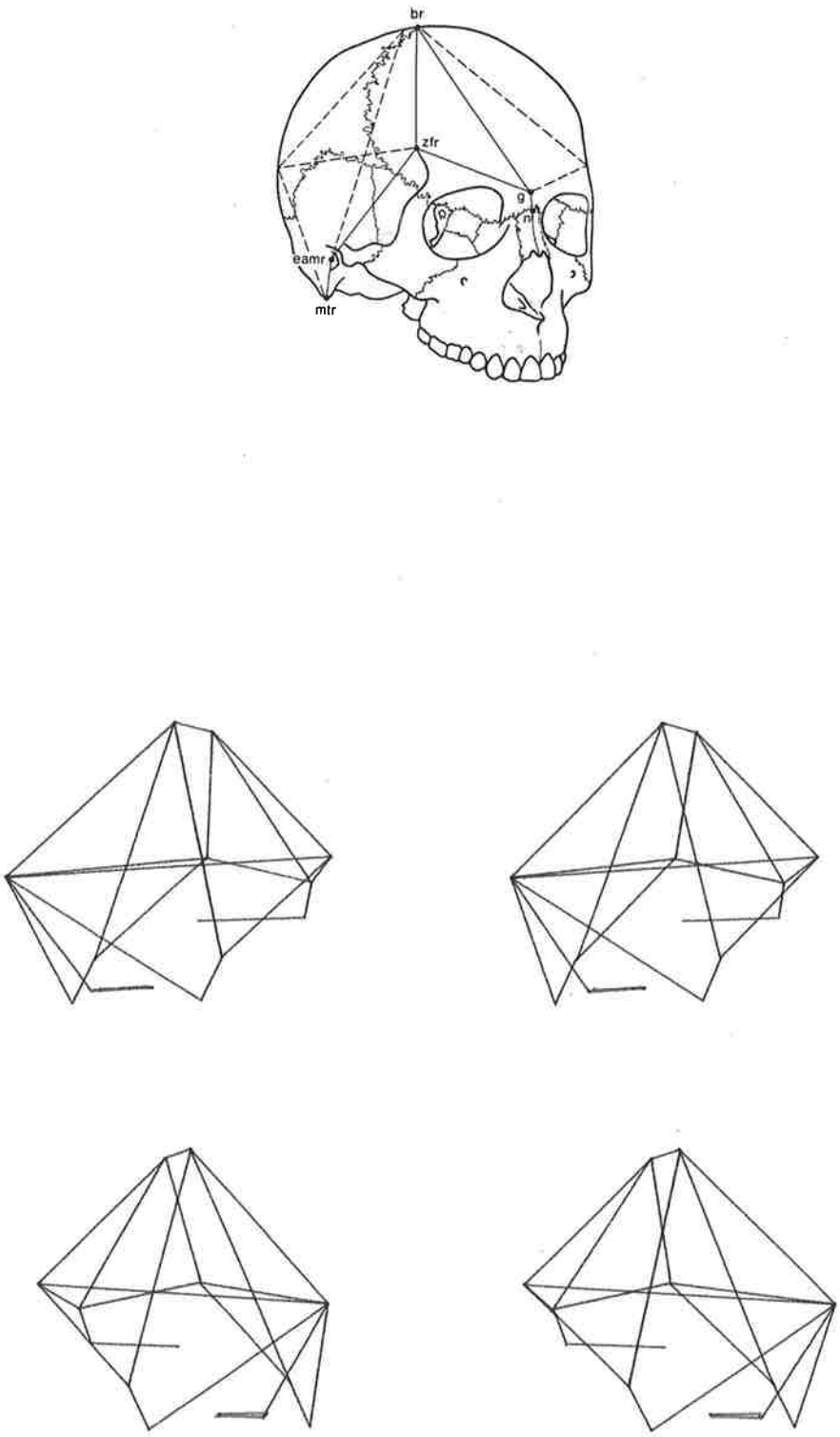

Figure 6.3 (e) Non-scaled least squares comparison of the least squares cranium standard with the least squares skull standard.

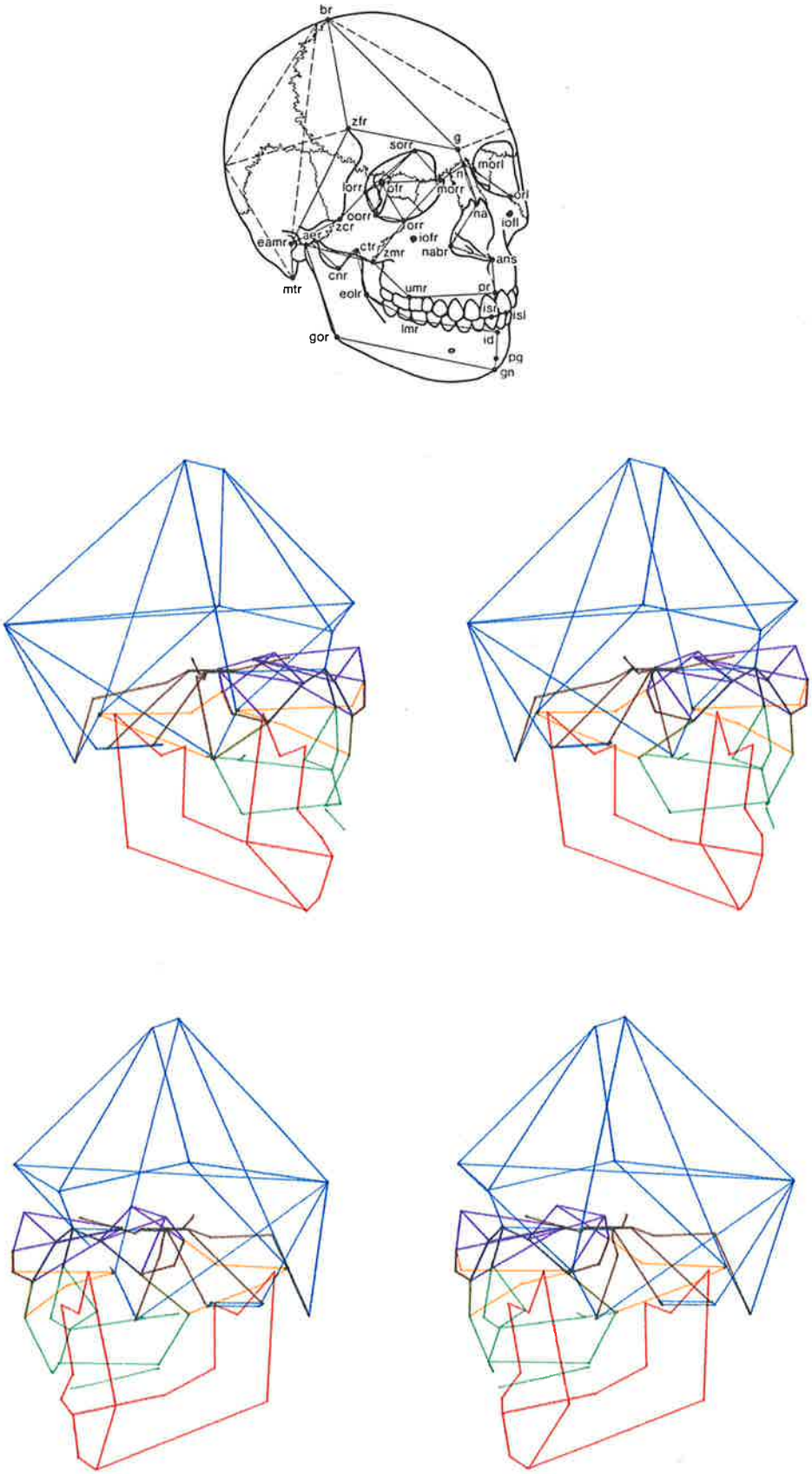

Figure 6.4 Stereo pair showing the wire frame model of the repeated median skull standard.

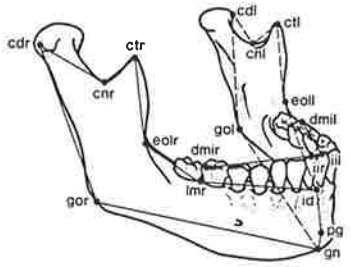

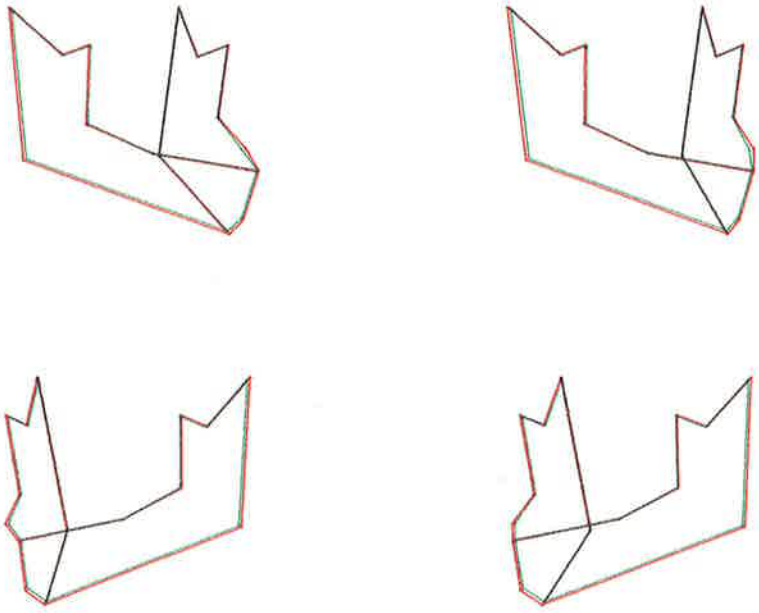

Figure 6.5 (a) Non-scaled repeated median comparison of the repeated median mandible standard with the repeated median skull standard.

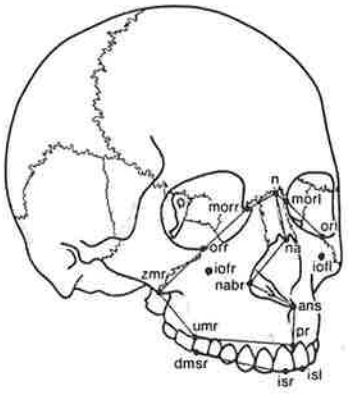

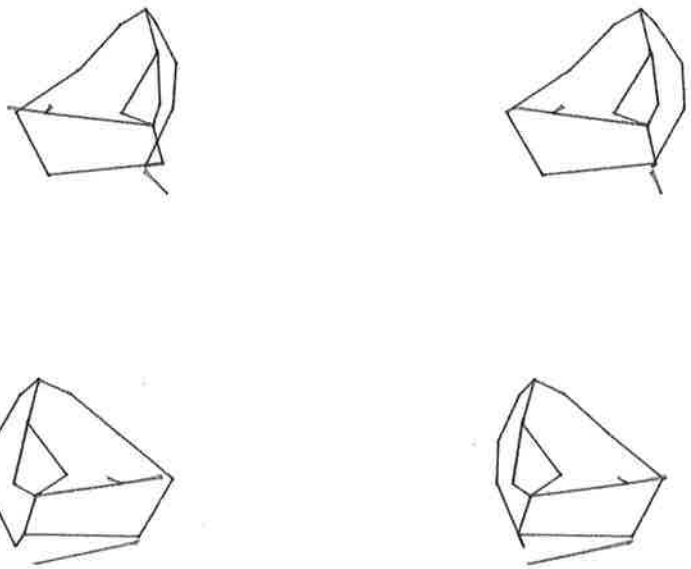

Figure 6.5 (b) Non-scaled repeated median comparison of the repeated median maxilla standard with the repeated median skull standard.

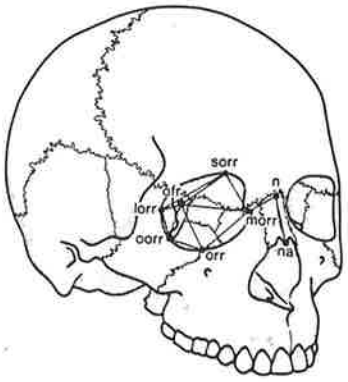

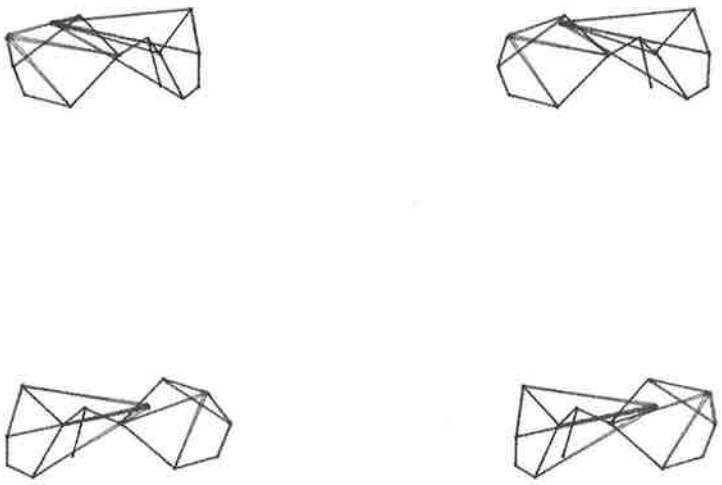

Figure 6.5 (c) Non-scaled repeated median comparison of the repeated median orbit standard with the repeated median skull standard.

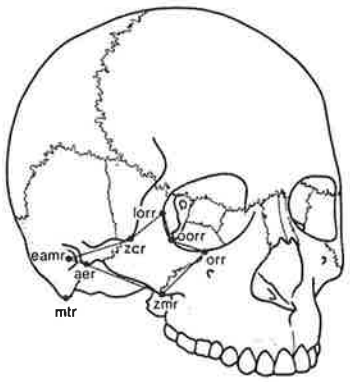

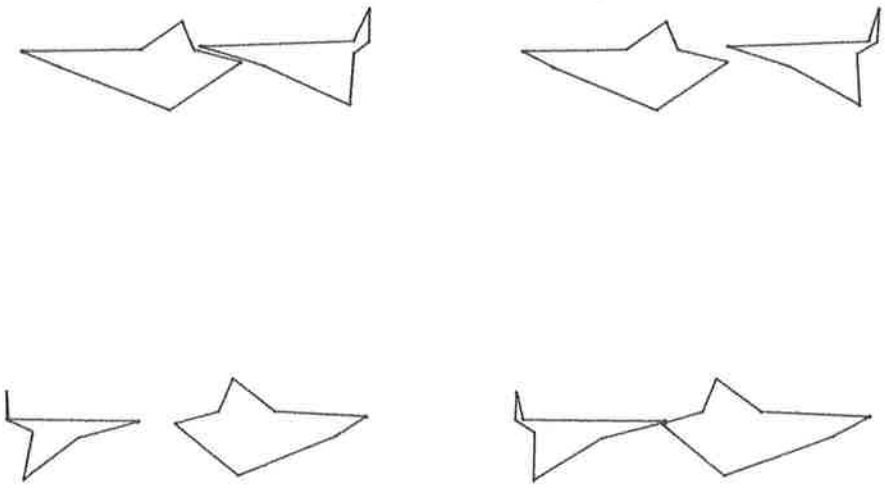

Figure 6.5 (d) Non-scaled repeated median comparison of the repeated median zygoma standard with the repeated median skull standard.

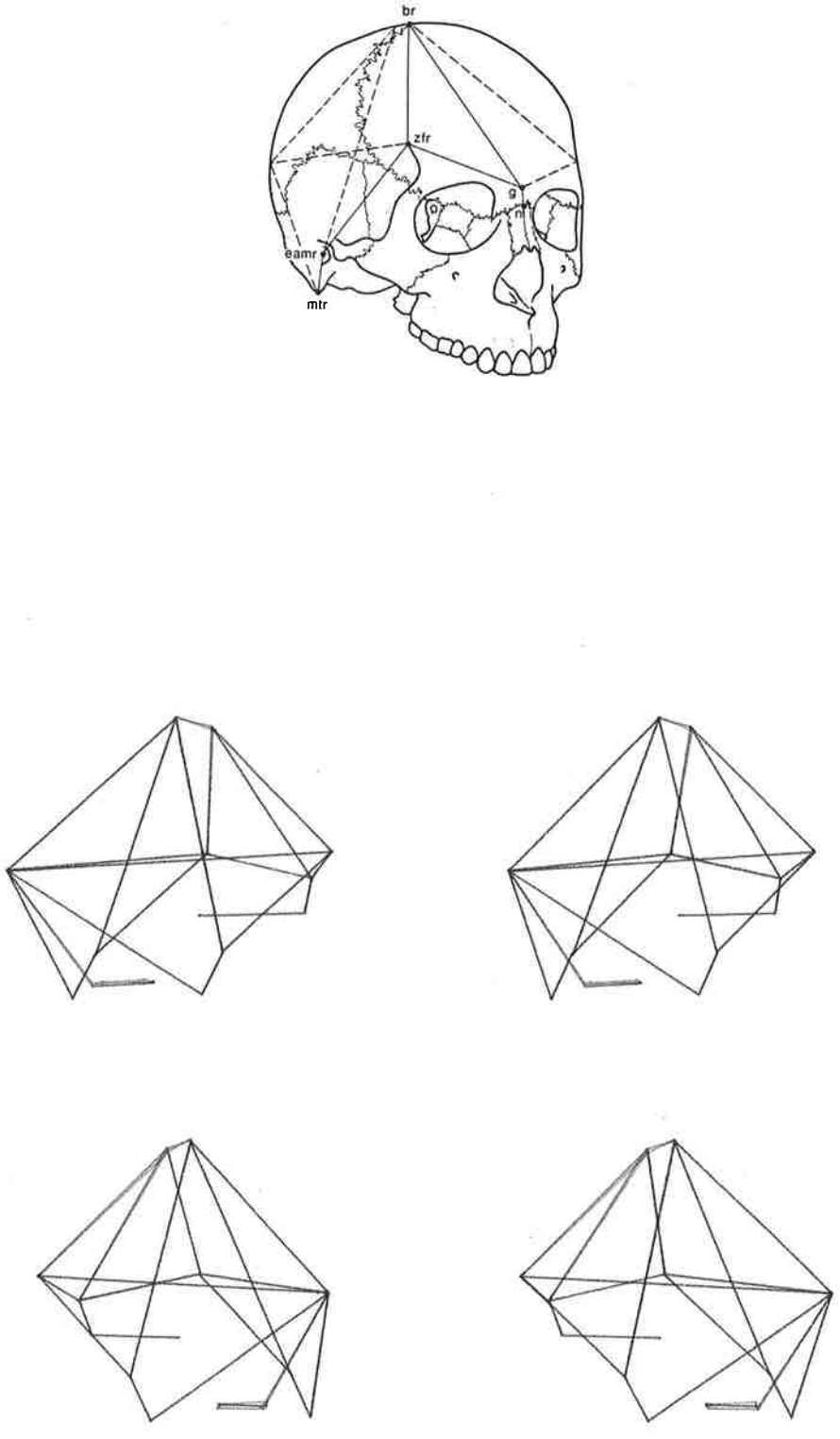

Figure 6.5 (e) Non-scaled repeated median comparison of the repeated median cranium standard with the repeated median skull standard.

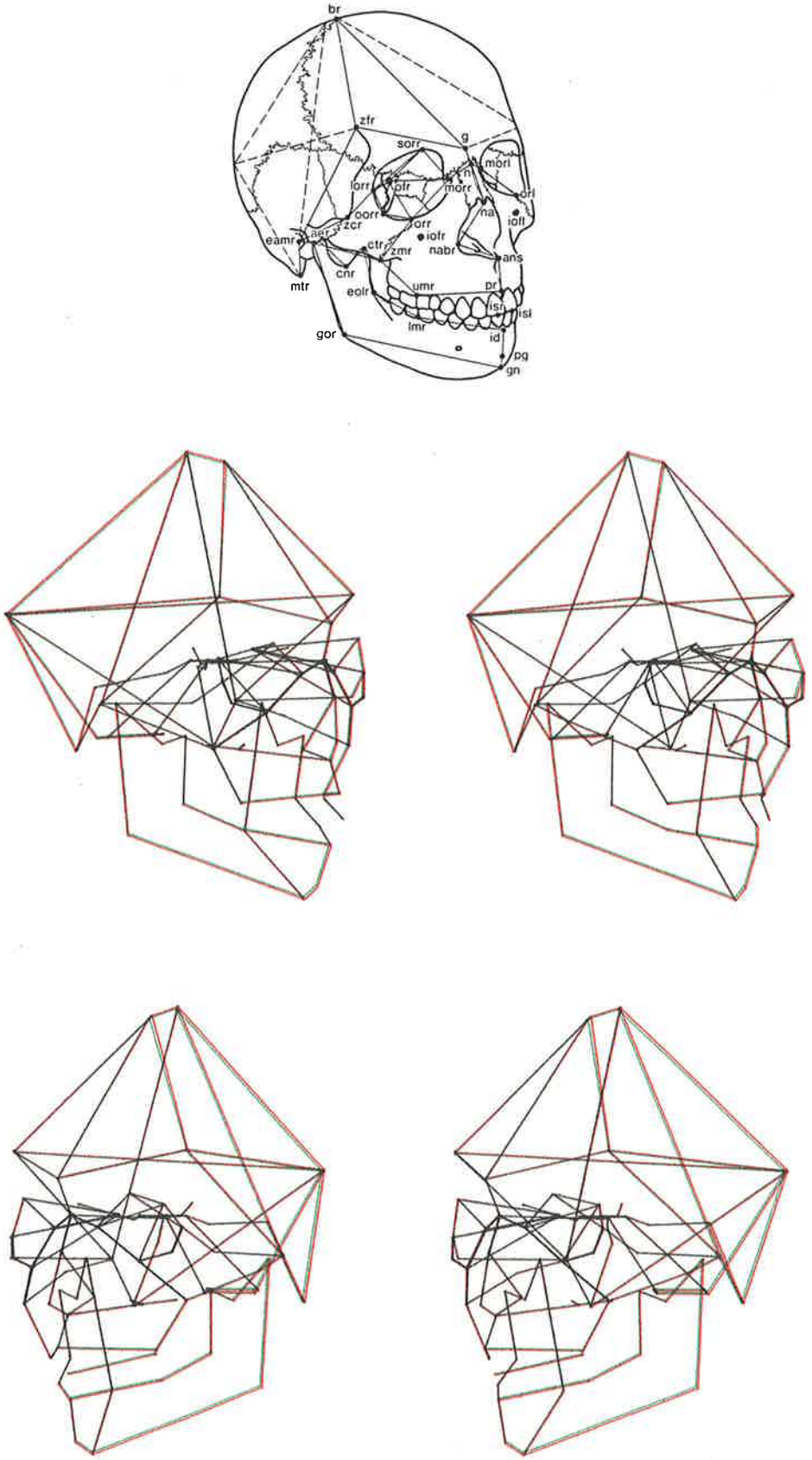

Figure 6.6 (a) Comparison of the least squares and repeated median skull standards using repeated median alignment without scaling.

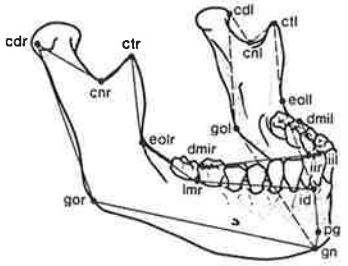

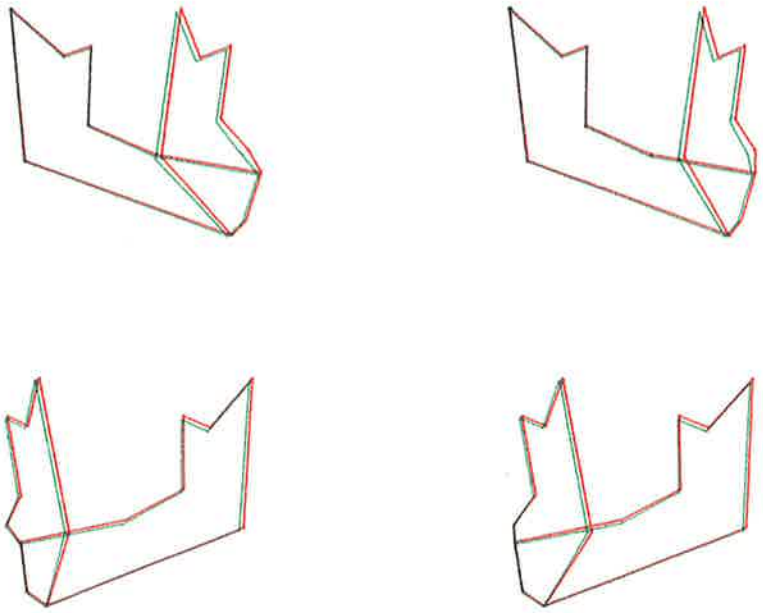

Figure 6.6 (b) Comparison of the least squares and repeated median mandible standards using repeated median alignment without scaling.

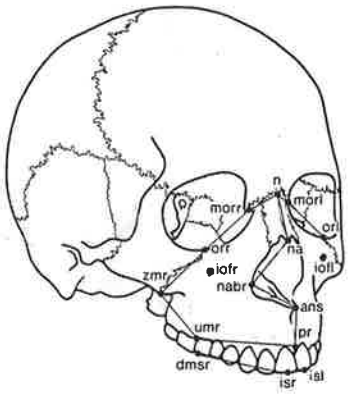

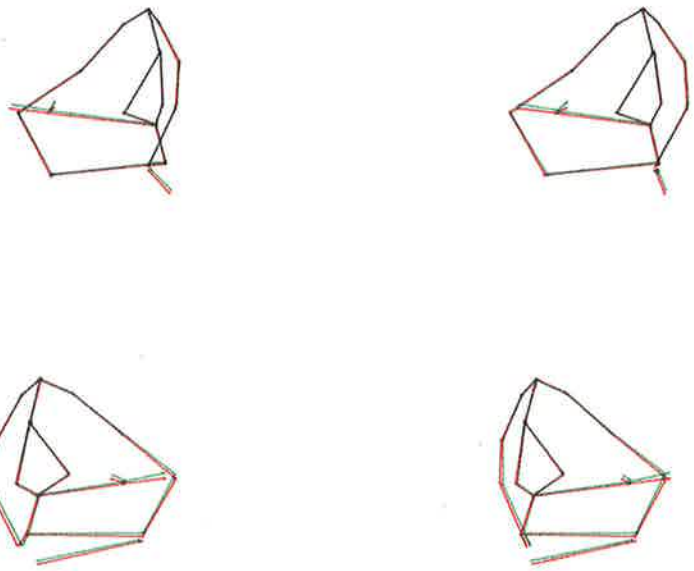

Figure 6.6 (c) Comparison of the least squares and repeated median maxilla standards using repeated median alignment without scaling.

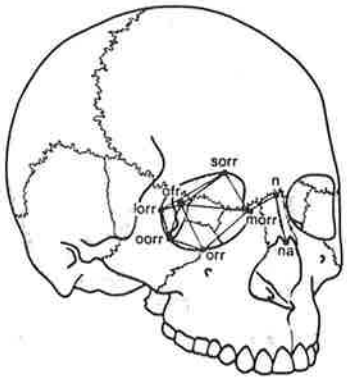

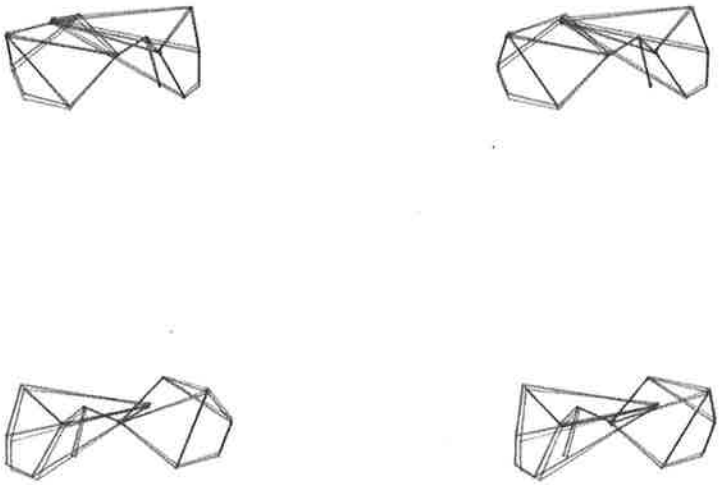

Figure 6.6 (d) Comparison of the least squares and repeated median orbit standards using repeated median alignment without scaling.

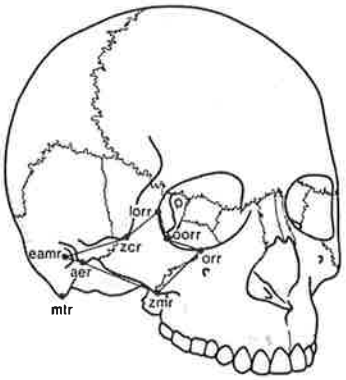

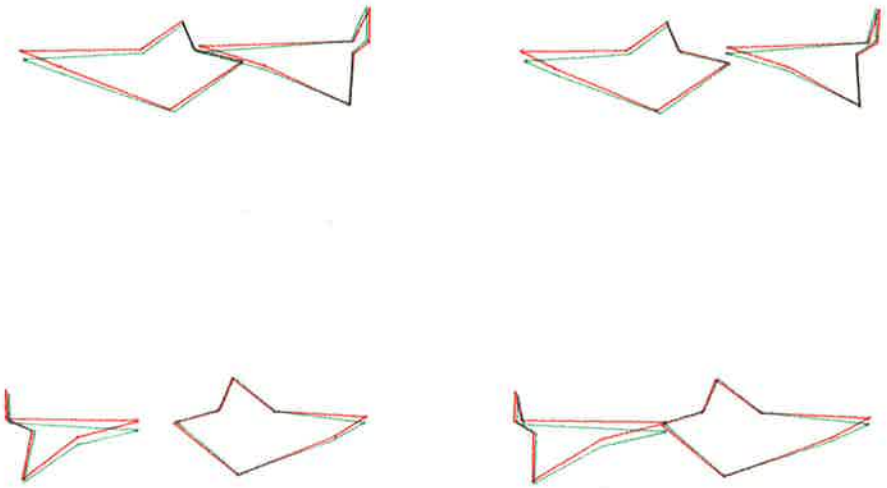

Figure 6.6 (e) Comparison of the least squares and repeated median zygoma standards using repeated median alignment without scaling.

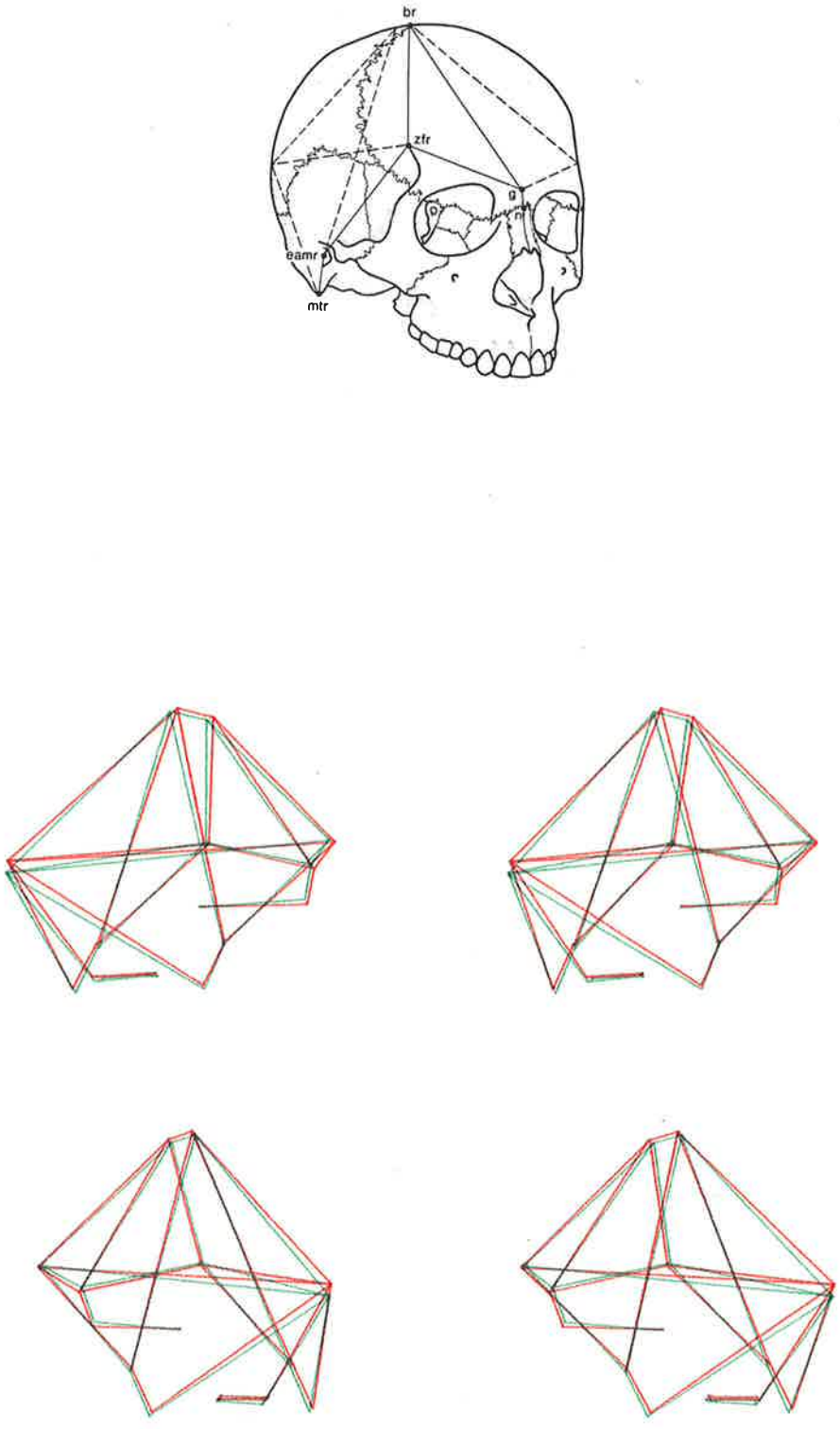

Figure 6.6 (f) Comparison of the least squares and repeated median cranium standards using repeated median alignment without scaling.

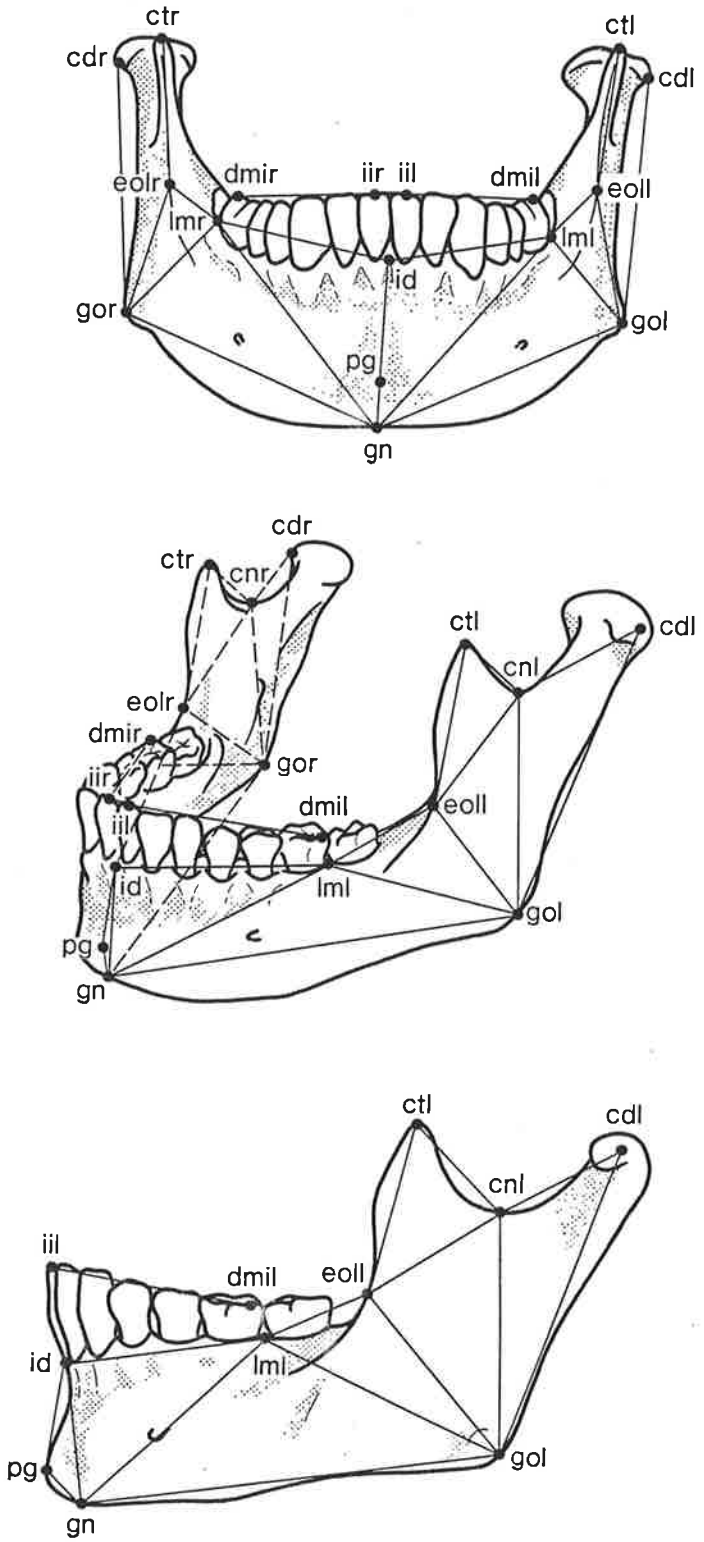

Figure 6.7 (a) The division of the surface of the mandible into thirteen finite triangular elements for strain analysis.

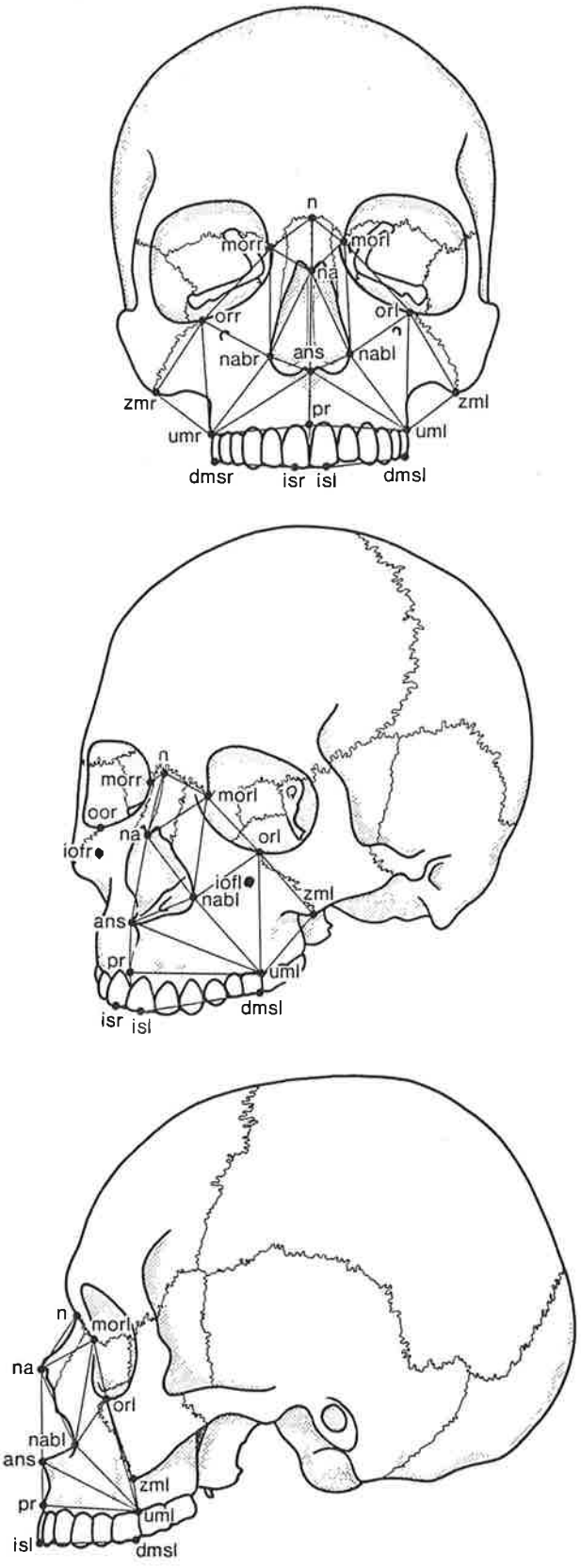

Figure 6.7 (b) The division of the surface of the maxilla into twenty-four finite triangular elements for strain analysis.

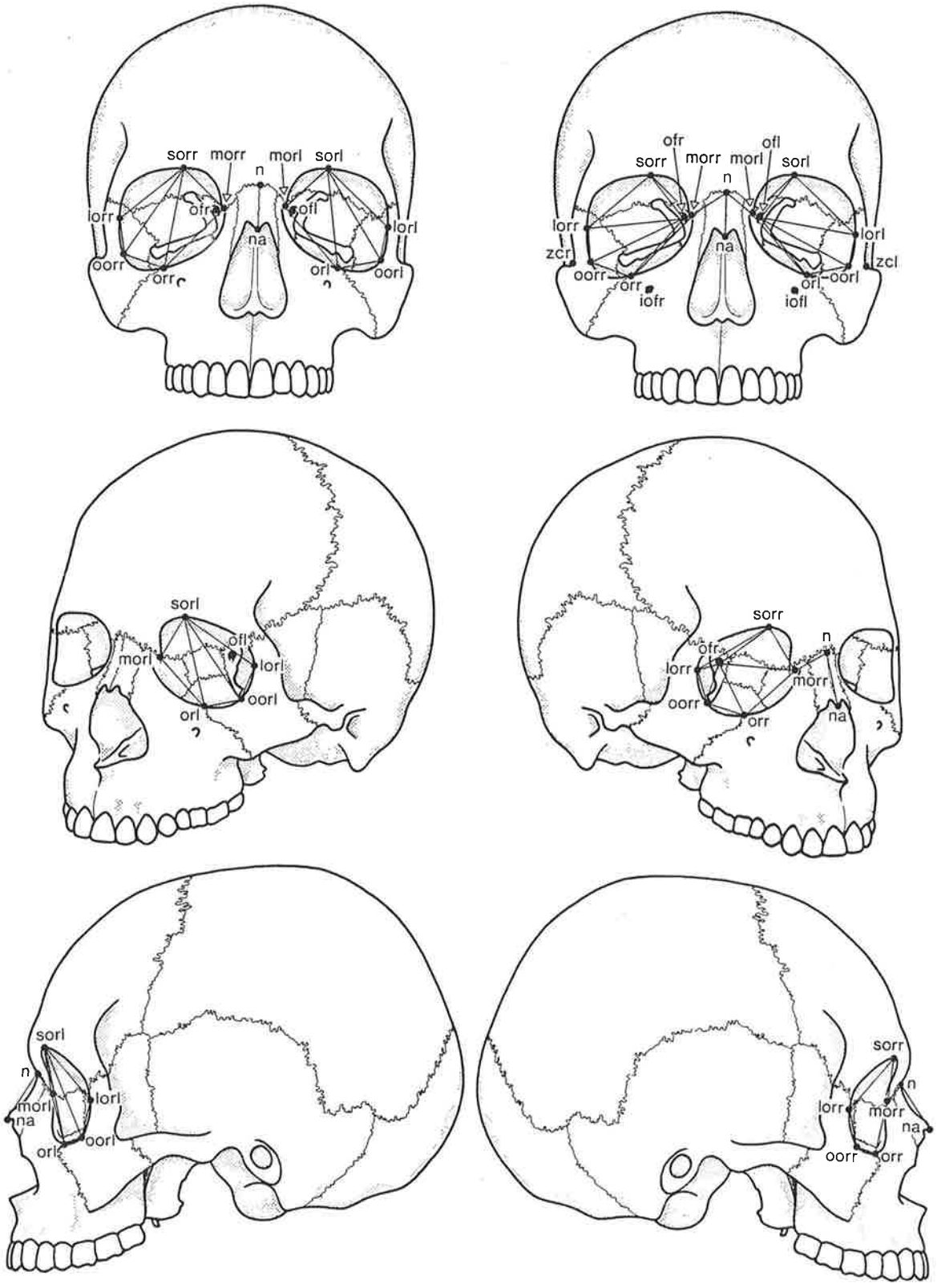

Figure 6.7 (c) The division of the surface of the orbit into sixteen finite triangular elements for strain analysis.

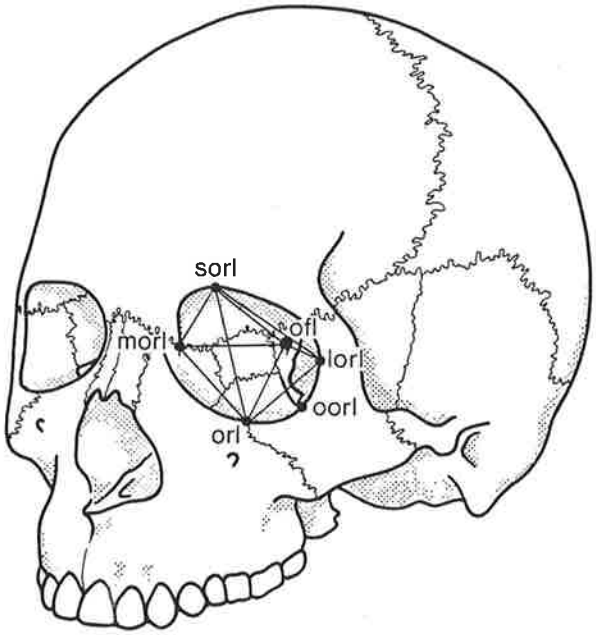

Figure 6.7 (d) The division of the volume of each orbit into two finite tetrahedral elements for strain analysis.

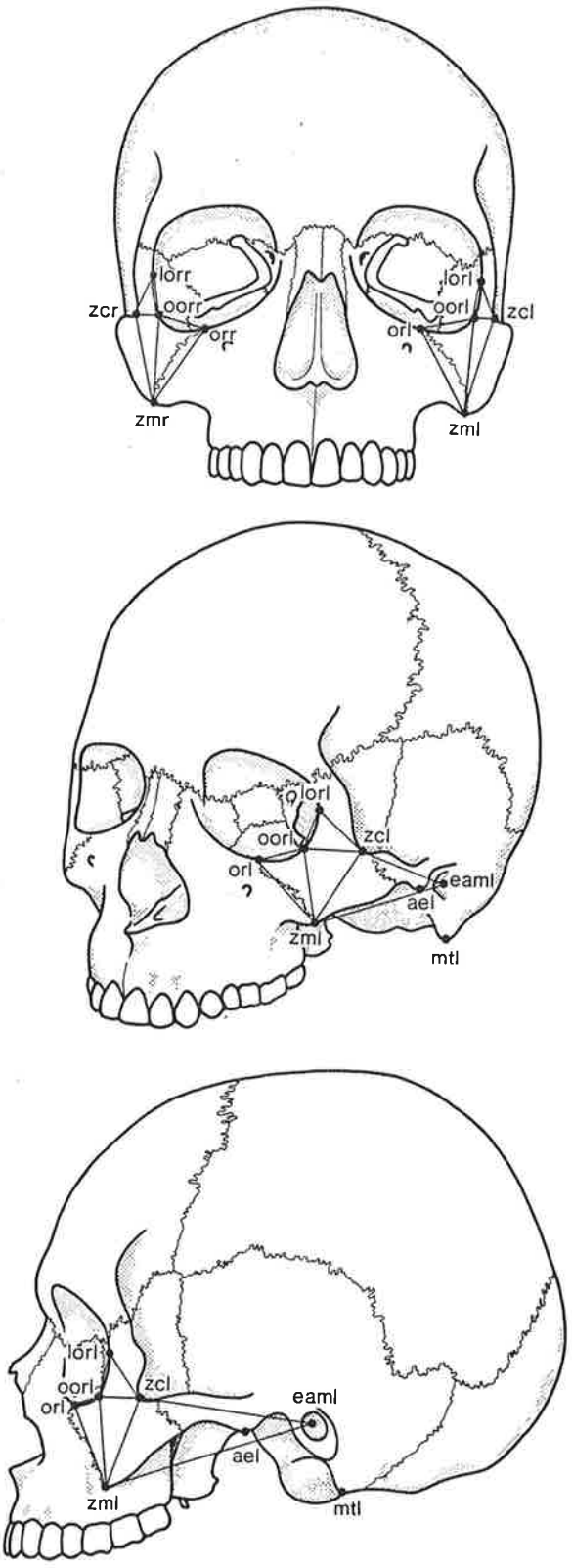

Figure 6.7 (e) The division of the surface of the zygoma into eight finite triangular elements for strain analysis.

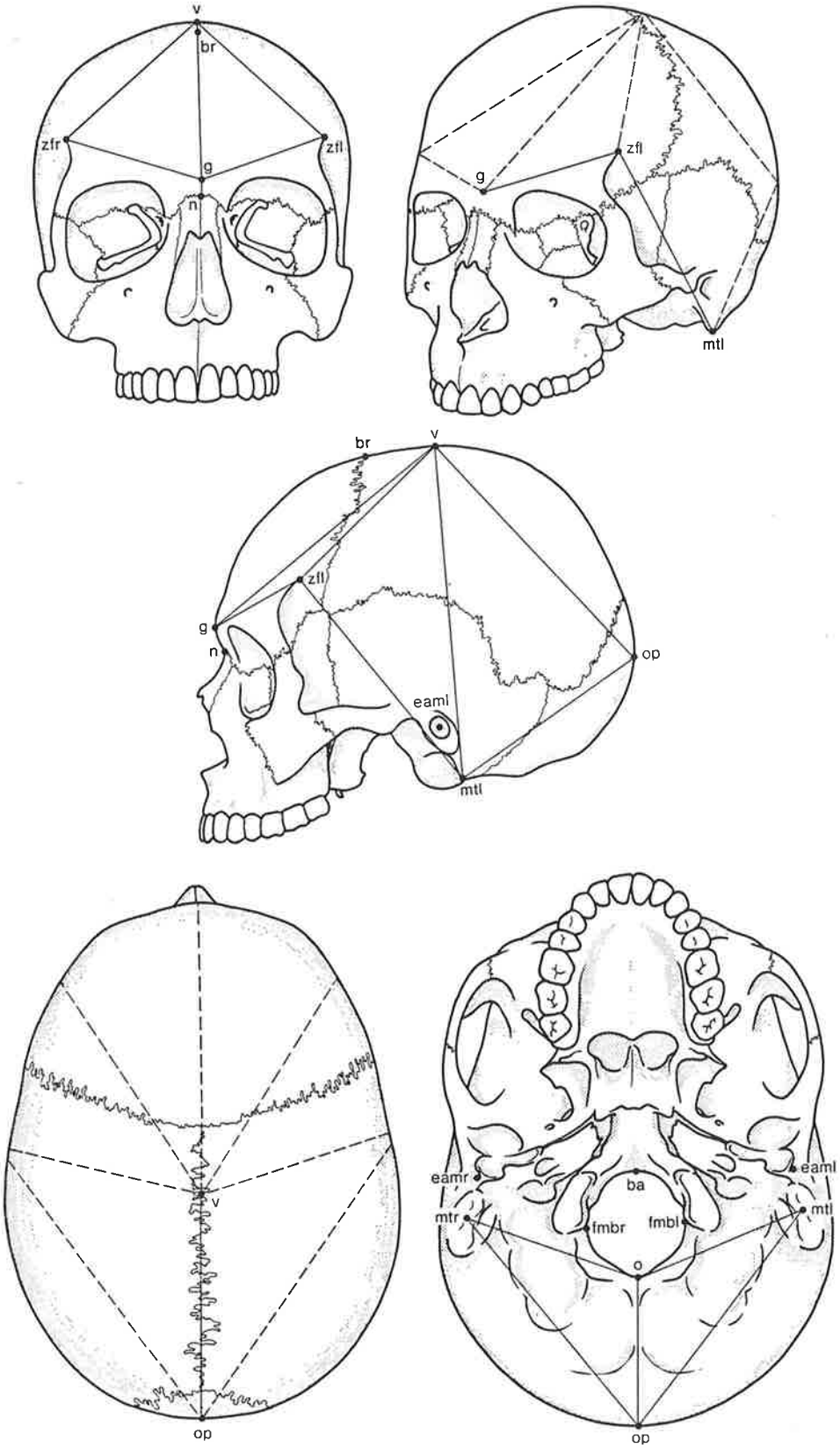

Figure 6.7 (f) The division of the surface of the cranium into nine finite triangular elements for strain analysis.

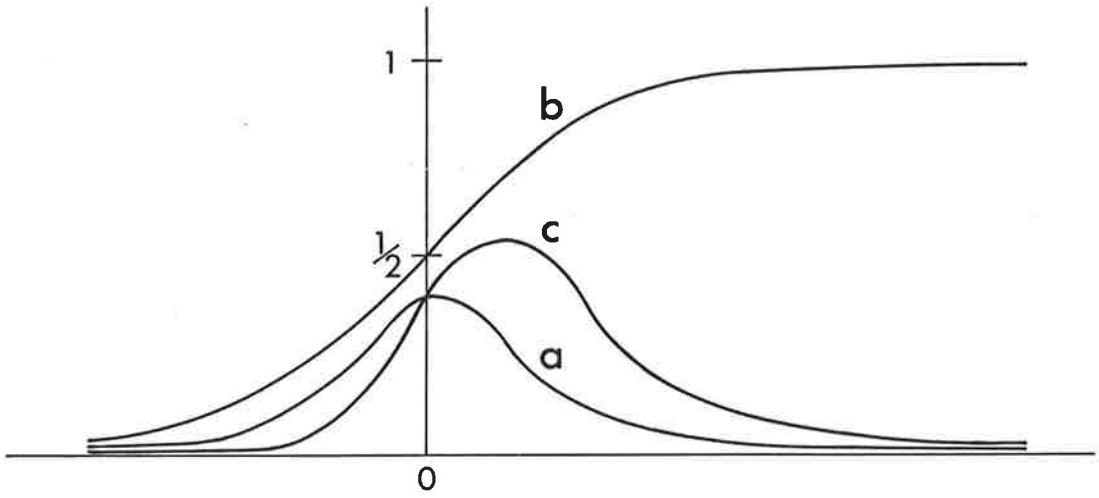

Figure 6.8 (a) The Gaussian probability density function,

(b) The Gaussian distribution function, and

(c) The probability density function for the major principal strain. The probability density function for the minor principal strain is the mirror image of (c).

For all subsequent least squares and repeated median comparisons the figures plotted in red are the experimental reference standards while those in green, either the male skull for Chapter 6 illustrations, or the adult female patient with Treacher Collins Syndrome for Chapter 7 illustrations. Both right and left 45° views are plotted.

Some landmarks/lines are behind the skull surface and therefore not visible in the reference line diagram at the top of each figure. Figures 6.1 (a) to (f) and 6.7 (a) to (f) provide illustrations showing all the landmarks plotted.

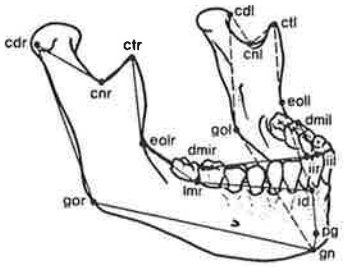

(a)

(b)

Figure 6.9 (a) Scaled least squares comparison of the male skull with the least squares mandible standard.

(b) Scaled repeated median comparison of the male skull with the repeated median mandible standard.

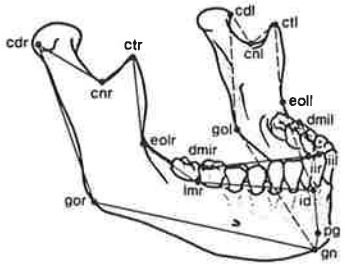

(c)

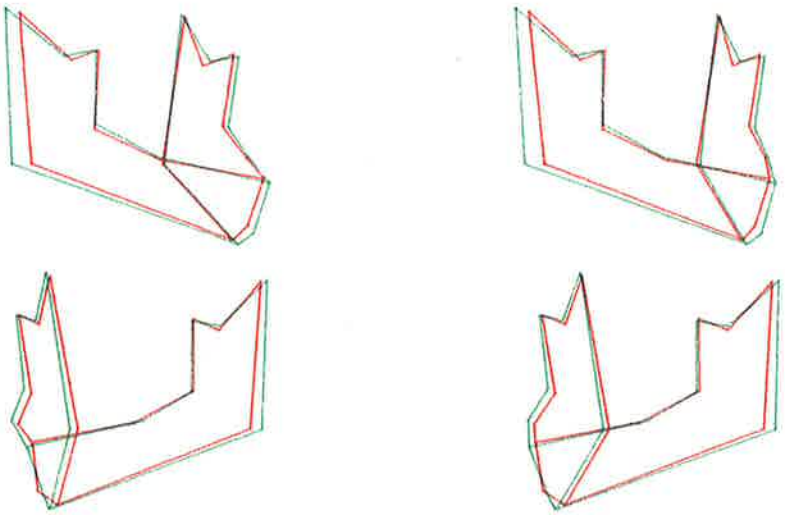

(d)

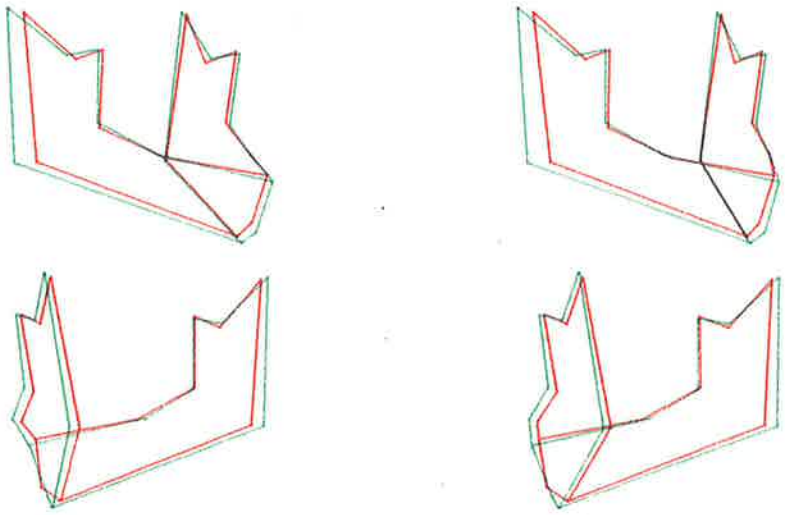

Figure 6.9 (c) Non-scaled least squares comparison of the male skull with the least squares mandible standard.

(d) Non-scaled repeated median comparison of the male skull with the repeated median mandible standard.

Figure 6.10 (a) Left 45° and (b) right 45° views showing shape comparison between the male's mandible and the experimental reference mandible standard using strain analysis. The upper stereo pairs show the principal strains and directions (red - minor, green - major) required to deform the mandible standard to produce the shape of the male's mandible. The lower stereo pairs show the principal strains and directions (green - minor, red - major) required to deform the male's mandible to produce the shape of the mandible standard.

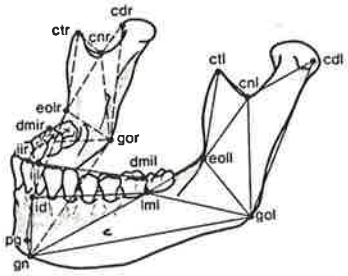
cdr
ctr
cnr
ctl
cnl
cdl
eolr
dmir
gor
ilr
dmil
eoll
id
lmi
gol
pg
gn

(a)

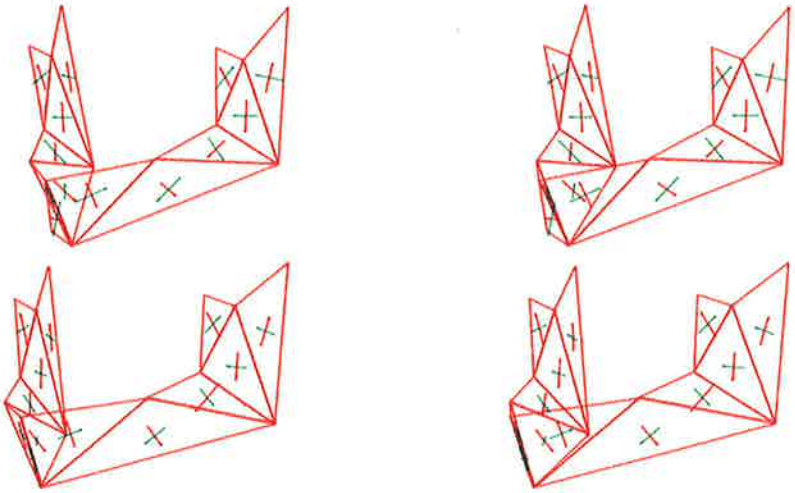

(b)

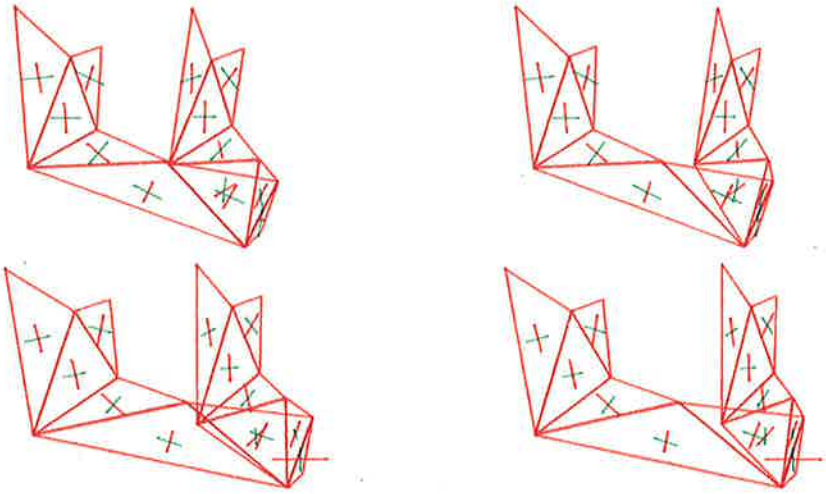

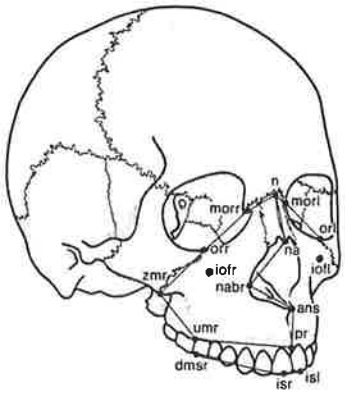

(a)

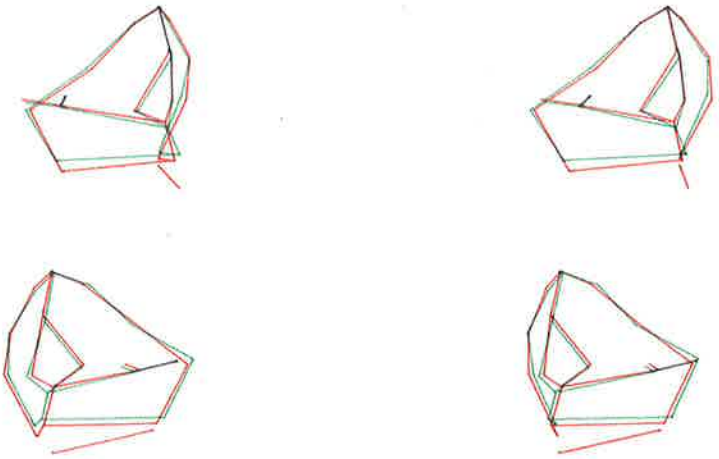

(b)

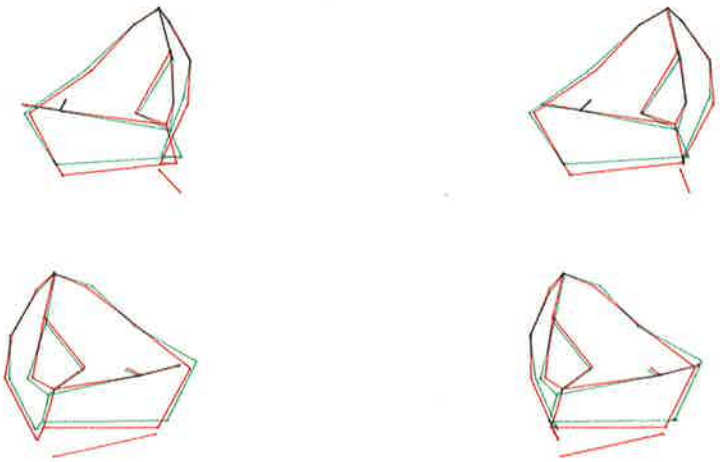

Figure 6.11 (a) Scaled least squares comparison of the male skull with the least squares maxilla standard.

(b) Scaled repeated median comparison of the male skull with the repeated median maxilla standard.

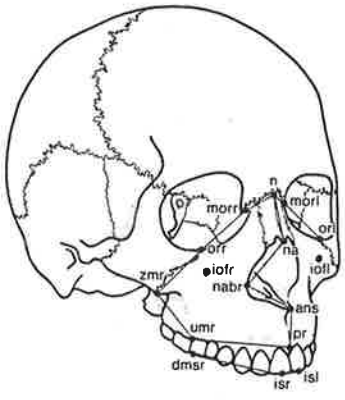

(c)

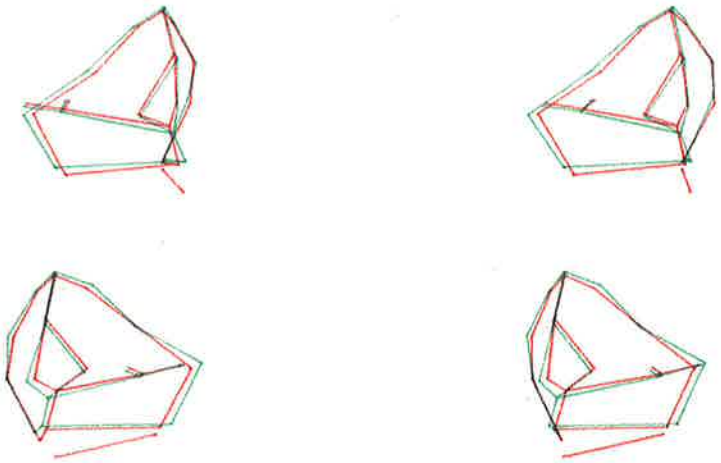

(d)

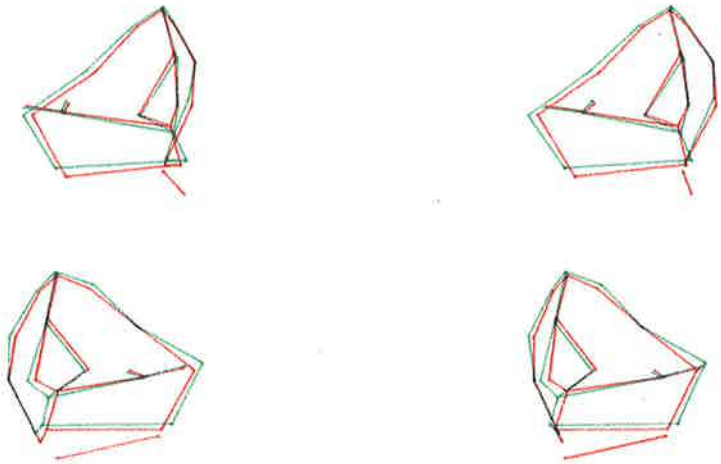

Figure 6.11 (c) Non-scaled least squares comparison of the male skull with the least squares maxilla standard.

(d) Non-scaled repeated median comparison of the male skull with repeated median maxilla standard.

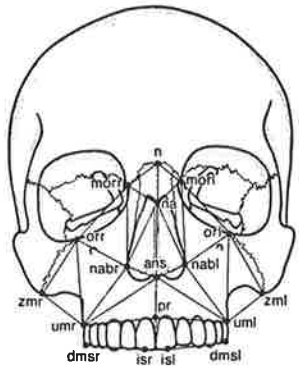

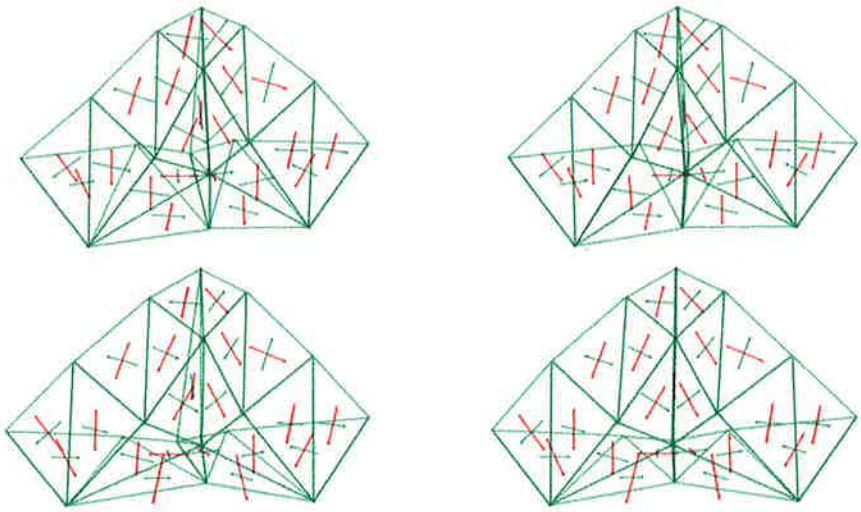

Figure 6.12 Shape comparison between the male's maxilla and the experimental reference maxilla standard using strain analysis. The upper stereo pair shows the principal strains and directions (red - minor, green - major) required to deform the maxilla standard to produce the shape of the male's maxilla. The lower stereo pairs shows the principal strains and directions (green - minor, red - major) required to deform the male's maxilla to produce the shape of the maxilla standard.

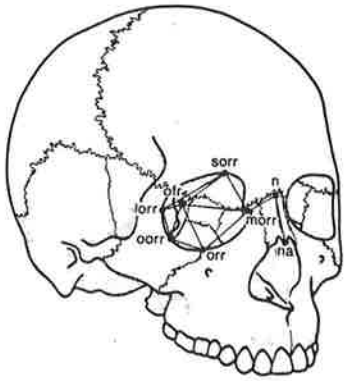

(a)

(b)

Figure 6.13 (a) Scaled least squares comparison of the male skull with the least squares orbit standard.

(b) Scaled repeated median comparison of the male skull with the repeated median orbit standard.

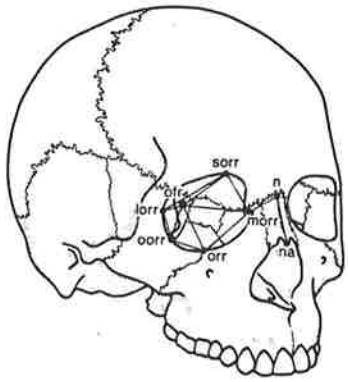

(c)

(d)

Figure 6.13 (c) Non-scaled least squares comparison of the male skull with the least squares orbit standard.

(d) Non-scaled repeated median comparison of the male skull with the repeated median orbit standard.

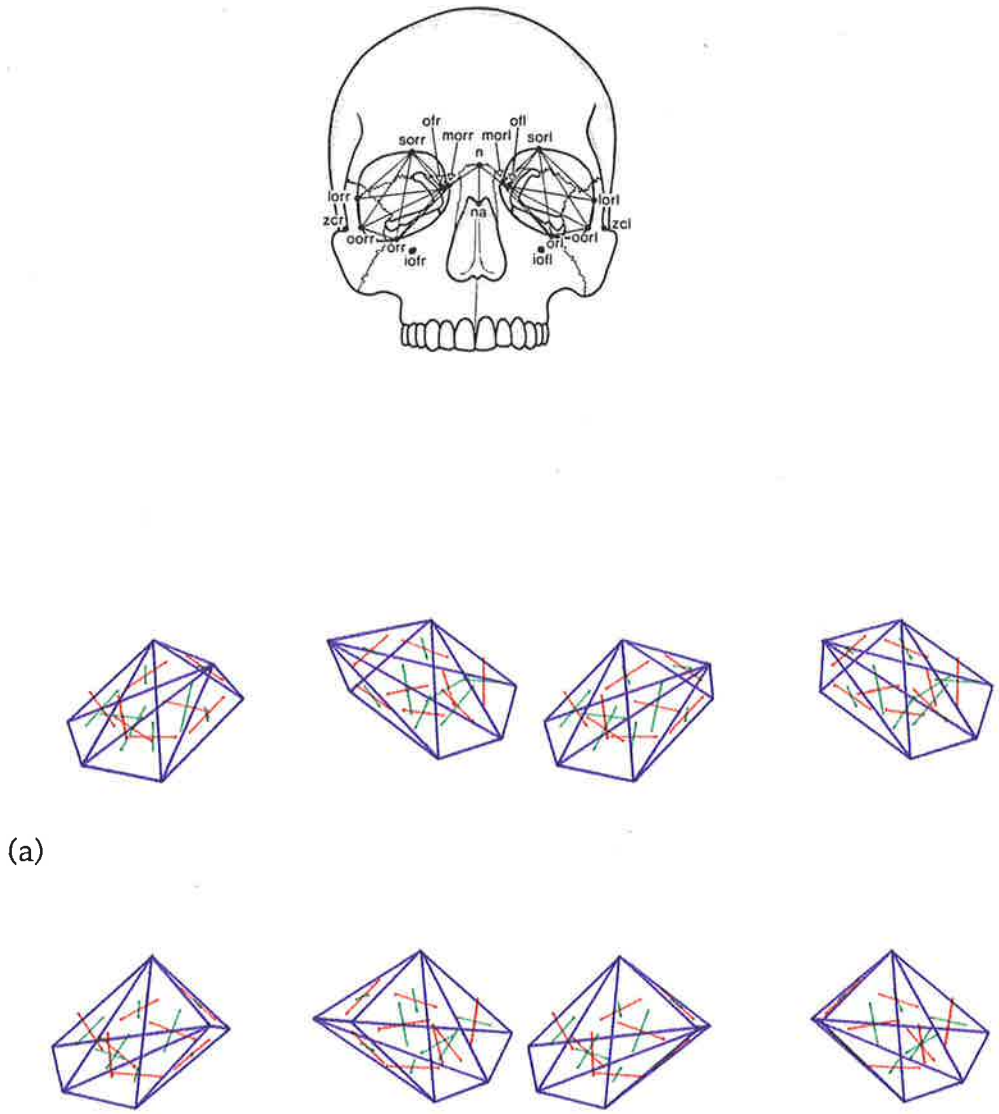

(a)

Figure 6.14 (a) Shape comparison between the male's orbit and the experimental reference orbit standard using strain analysis of both the anterior border of the orbit and the surface of the orbital cone. The upper stereo pairs show the principal strains and directions (red - minor, green - major) required to deform the orbit standard to produce the shape of the male's orbit. The lower stereo pairs show the principal strains and directions (green - minor, red - major) required to deform the male's orbit to produce the shape of the orbit standard.

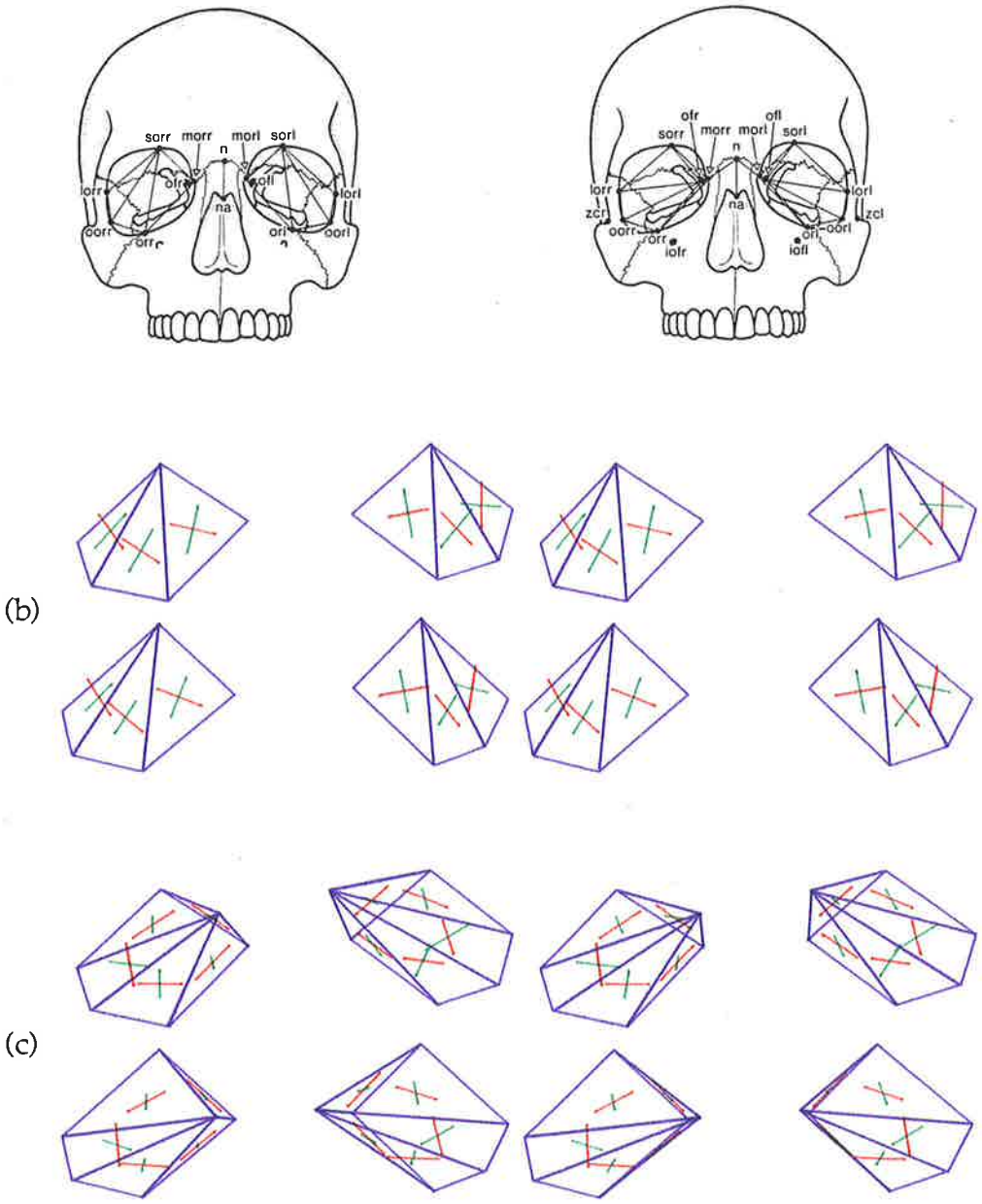

Figure 6.14 Shape comparison between the male's orbit and the experimental reference orbit standard using strain analysis of (b) the anterior border of the orbit and (c) the surface of the orbital cone. The upper stereo pairs show the principal strains and directions (red - minor, green - major) required to deform the orbit standard to produce the shape of the male's orbit. The lower stereo pairs show the principal strains and directions (green - minor, red - major) required to deform the male's orbit to produce the shape of the orbit standard.

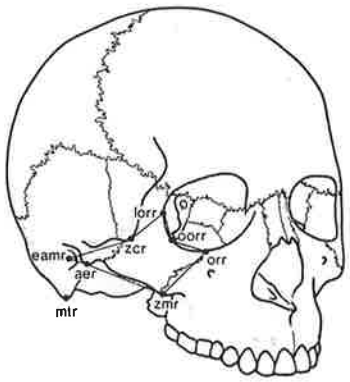

(a)

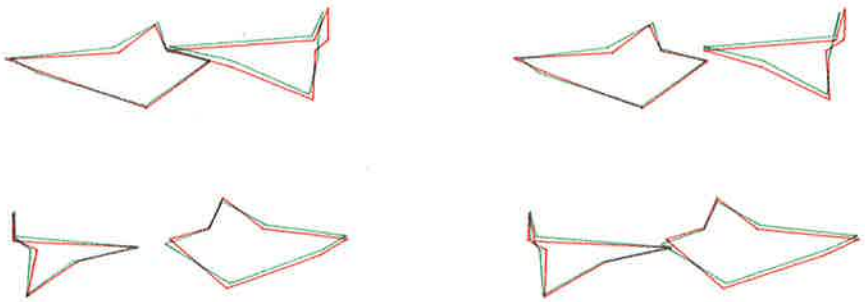

(b)

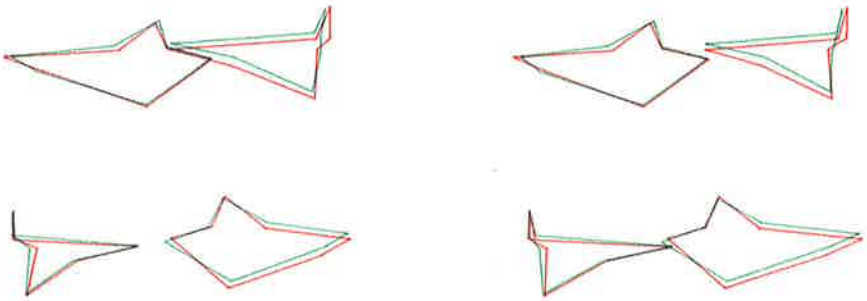

Figure 6.15 (a) Scaled least squares comparison of the male skull with the least squares zygoma standard.

(b) Scaled repeated median comparison of the male skull with the repeated median zygoma standard.

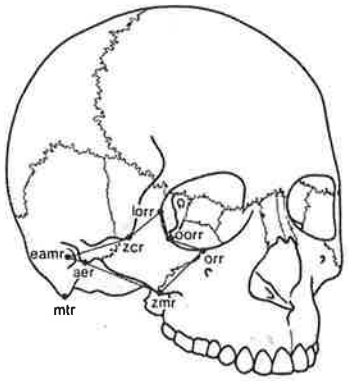

(c)

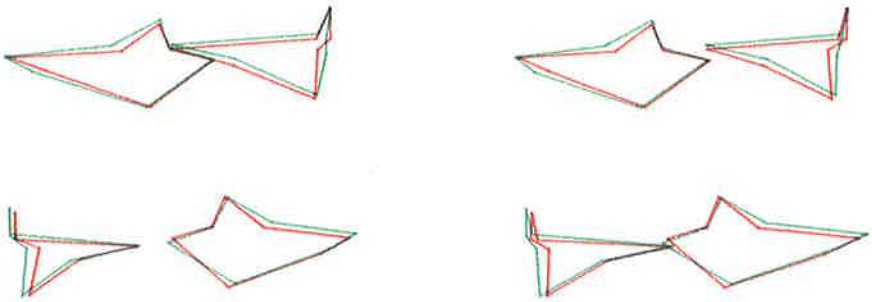

(d)

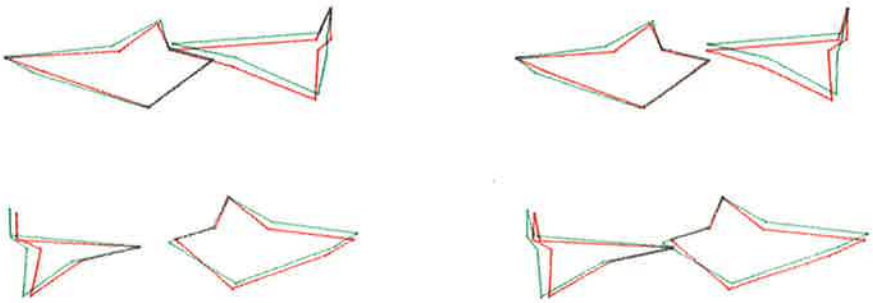

Figure 6.15 (c) Non-scaled least squares comparison of the male skull with the least squares zygoma standard.

(d) Non-scaled repeated median comparison of the male skull with the repeated median zygoma standard.

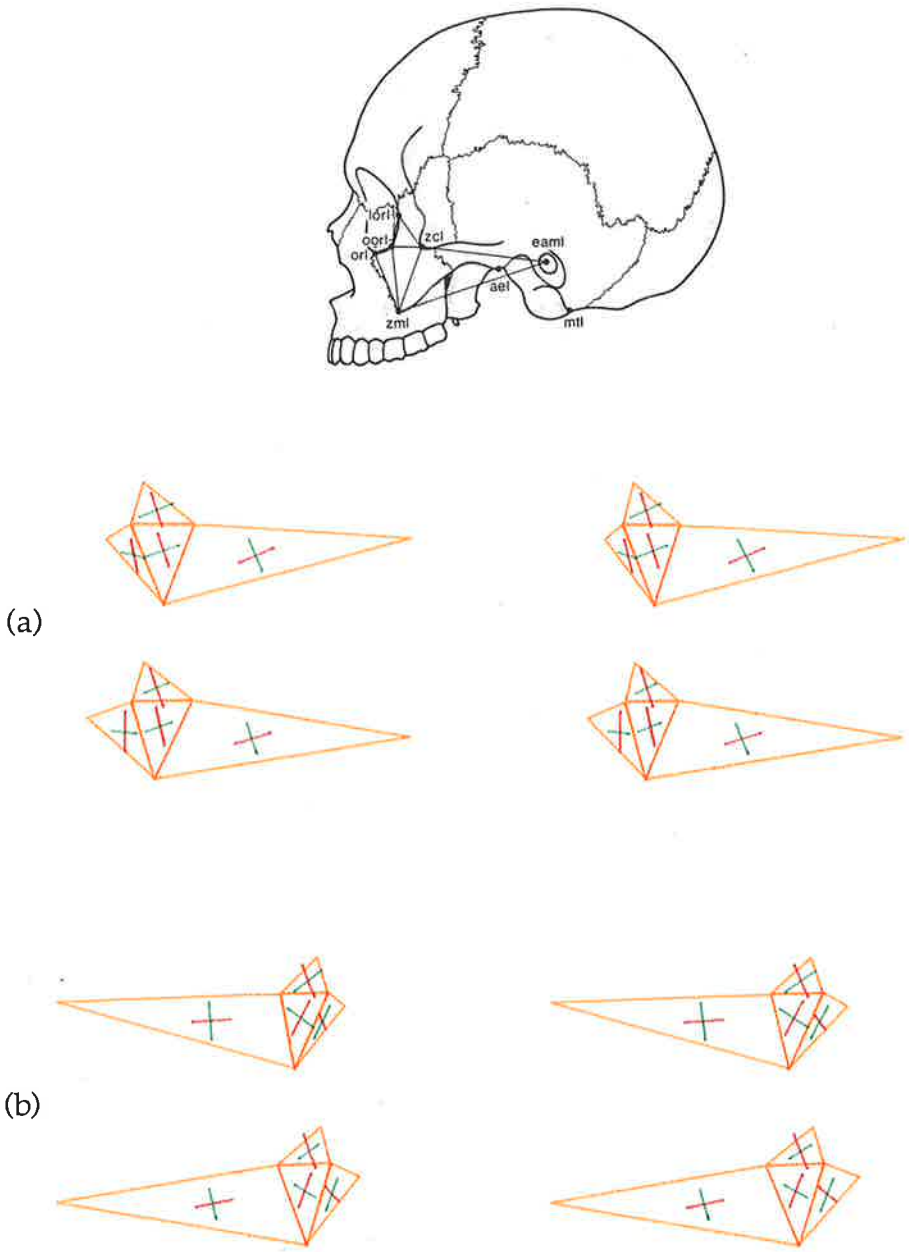

Figure 6.16 Shape comparison between (a) the left and (b) the right zygomas of the male and the experimental reference zygoma standard using strain analysis. The upper stereo pairs show the principal strains and directions (red - minor, green - major) required to deform the zygoma standard to produce the shape of the male's zygoma. The lower stereo pairs show the principal strains and directions (green - minor, red - major) required to deform the male's zygoma to produce the shape of the zygoma standard.

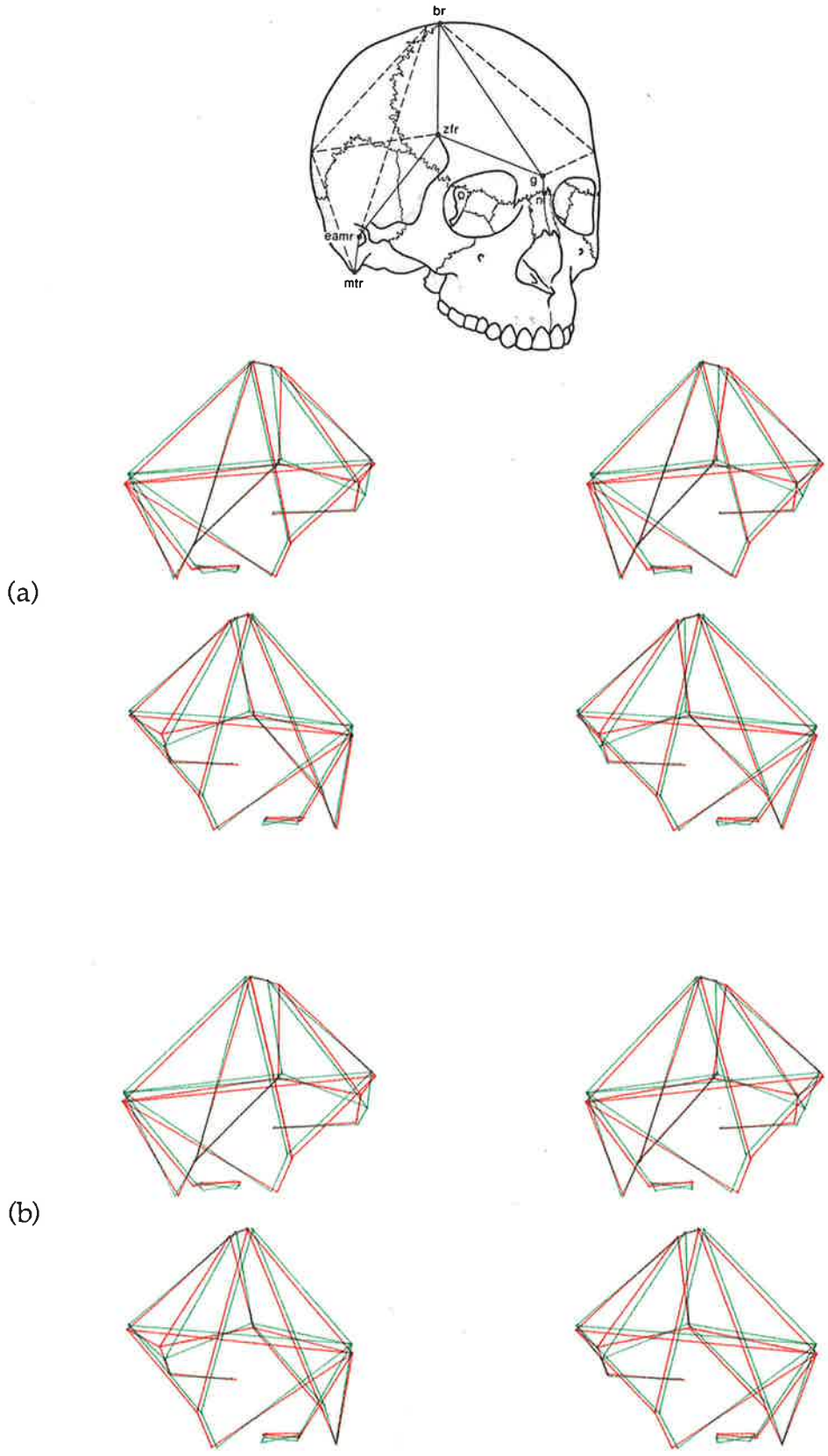

Figure 6.17 (a) Scaled least squares comparison of the male skull with the least squares cranium standard.

(b) Scaled repeated median comparison of the male skull with the repeated median cranium standard.

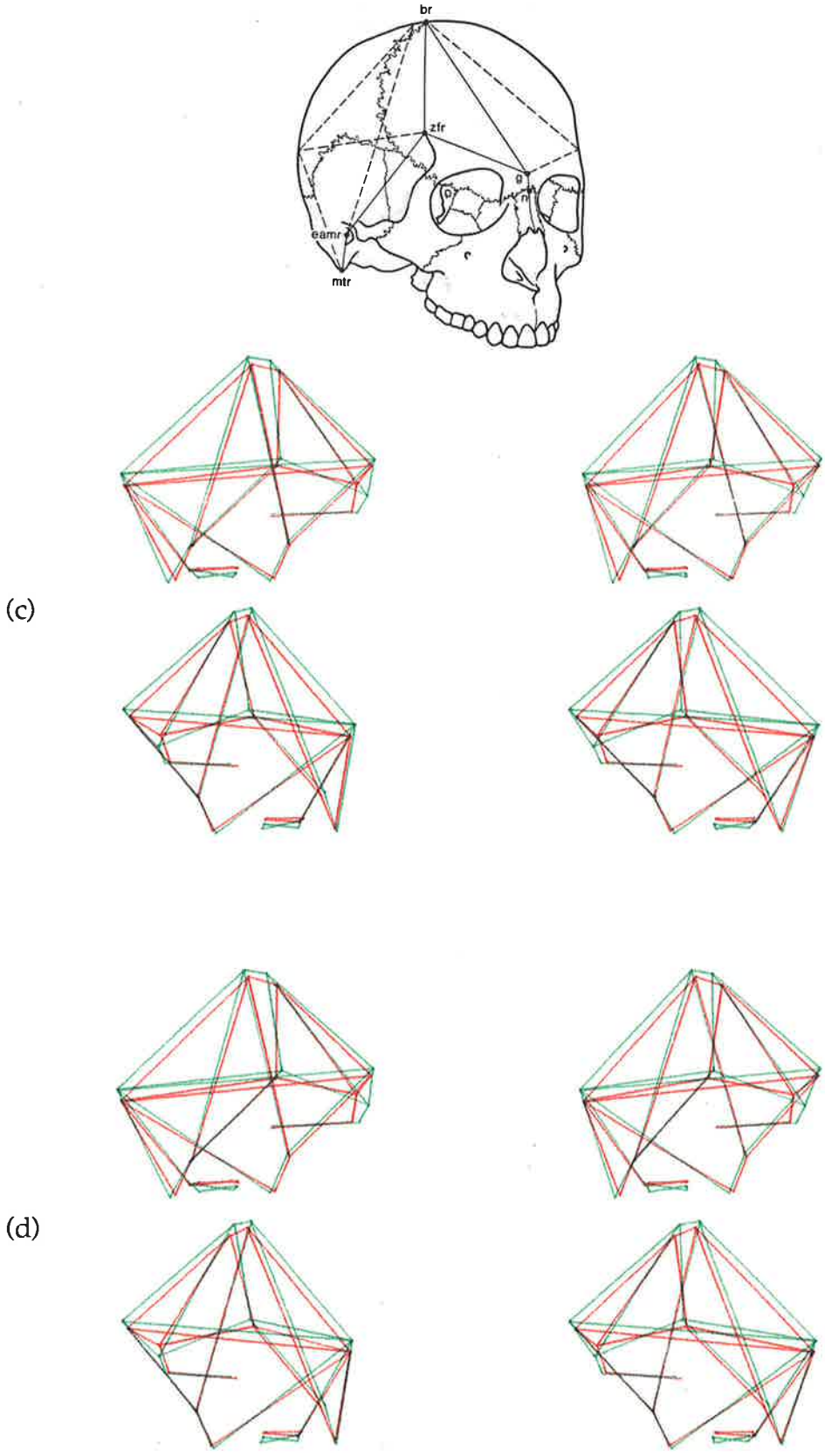

Figure 6.17 (c) Non-scaled least squares comparison of the male skull with the least squares cranium standard.

(d) Non-scaled repeated median comparison of the male skull with the repeated median cranium standard.

Figure 6.18 (a) Left 90° and (b) right 90° views showing shape comparison between the male's cranium and the experimental reference cranium standard using strain analysis. The upper stereo pairs show the principal strains and directions (red - minor, green - major) required to deform the cranium standard to produce the shape of the male's cranium. The lower stereo pairs show the principal strains and directions (green - minor, red - major) required to deform the male's cranium to produce the shape of the cranium standard.

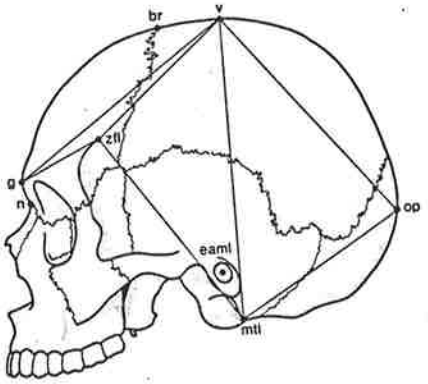

(a)

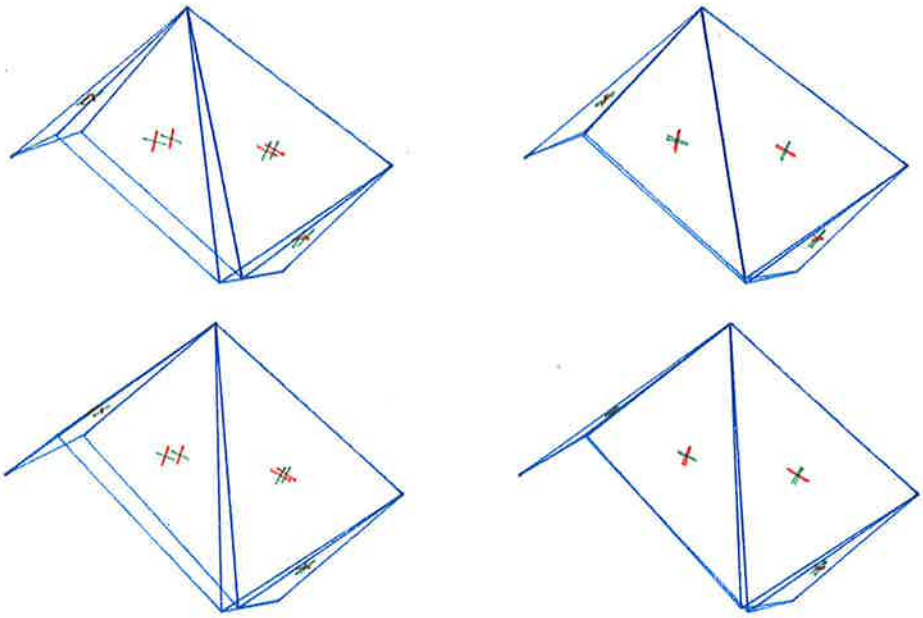

(b)

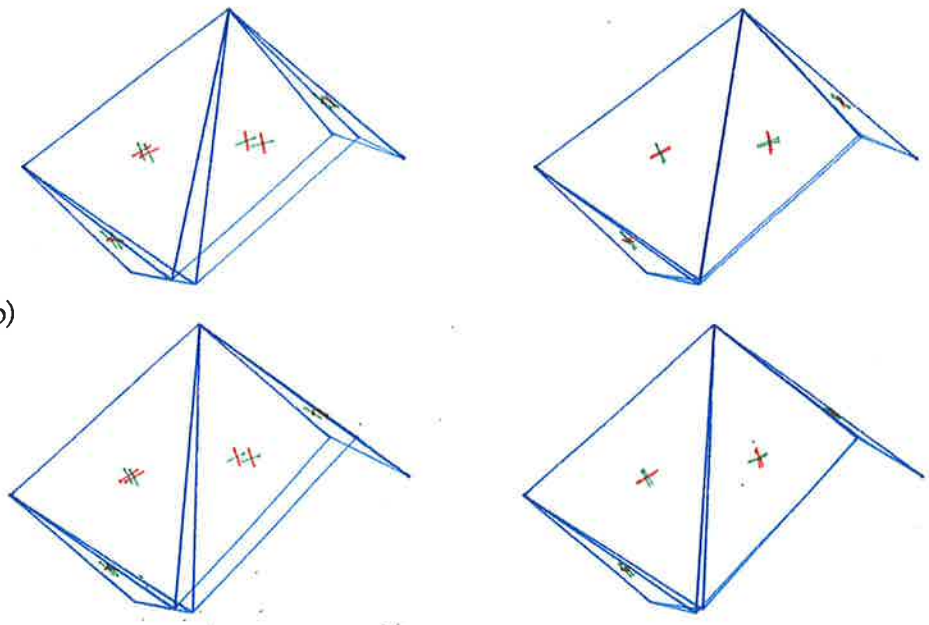

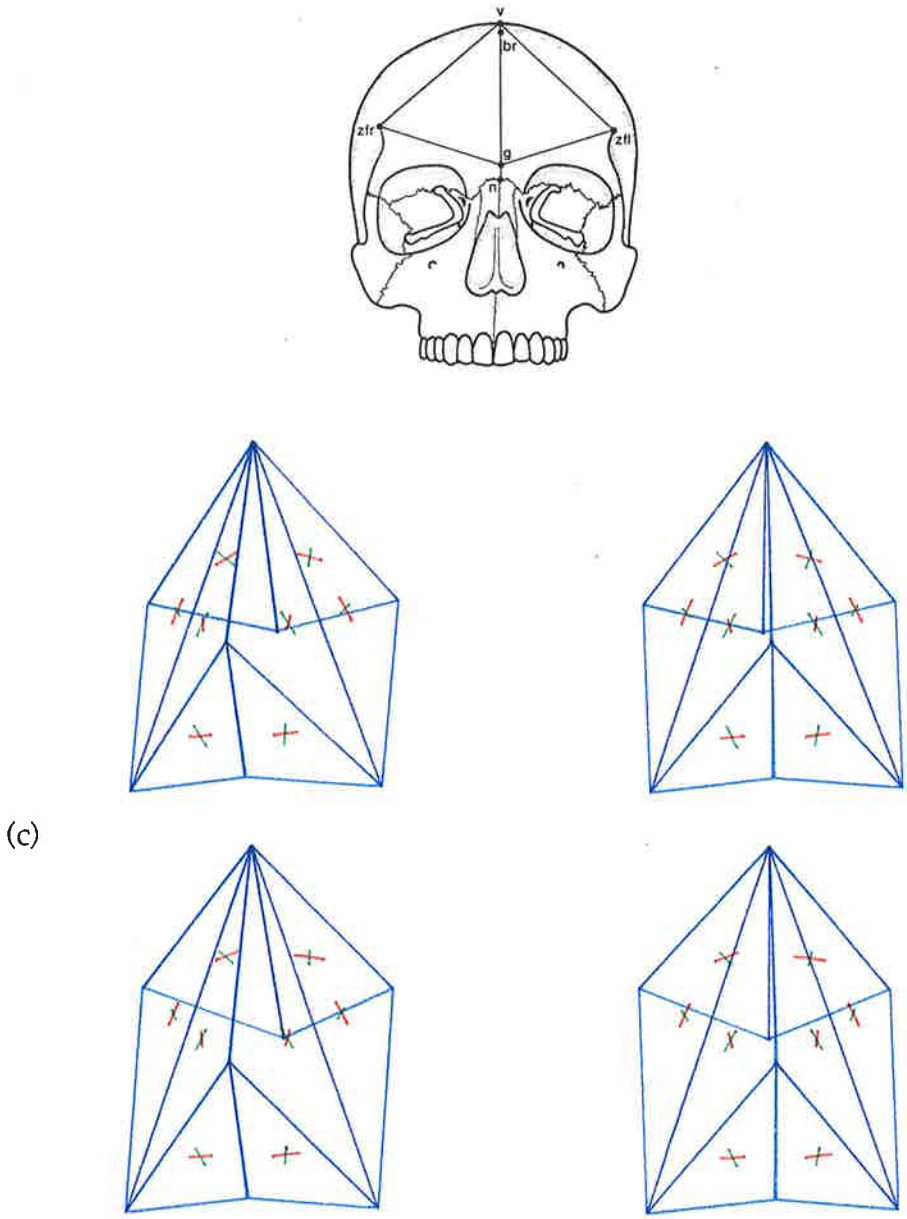

Figure 6.18 (c) Frontal view showing shape comparison between the male's cranium and the experimental reference cranium standard using strain analysis. The upper stereo pairs show the principal strains and directions (red - minor, green - major) required to deform the cranium standard to produce the shape of the male's cranium. The lower stereo pairs show the principal strains and directions (green - minor, red - major) required to deform the male's cranium to produce the shape of the cranium standard.

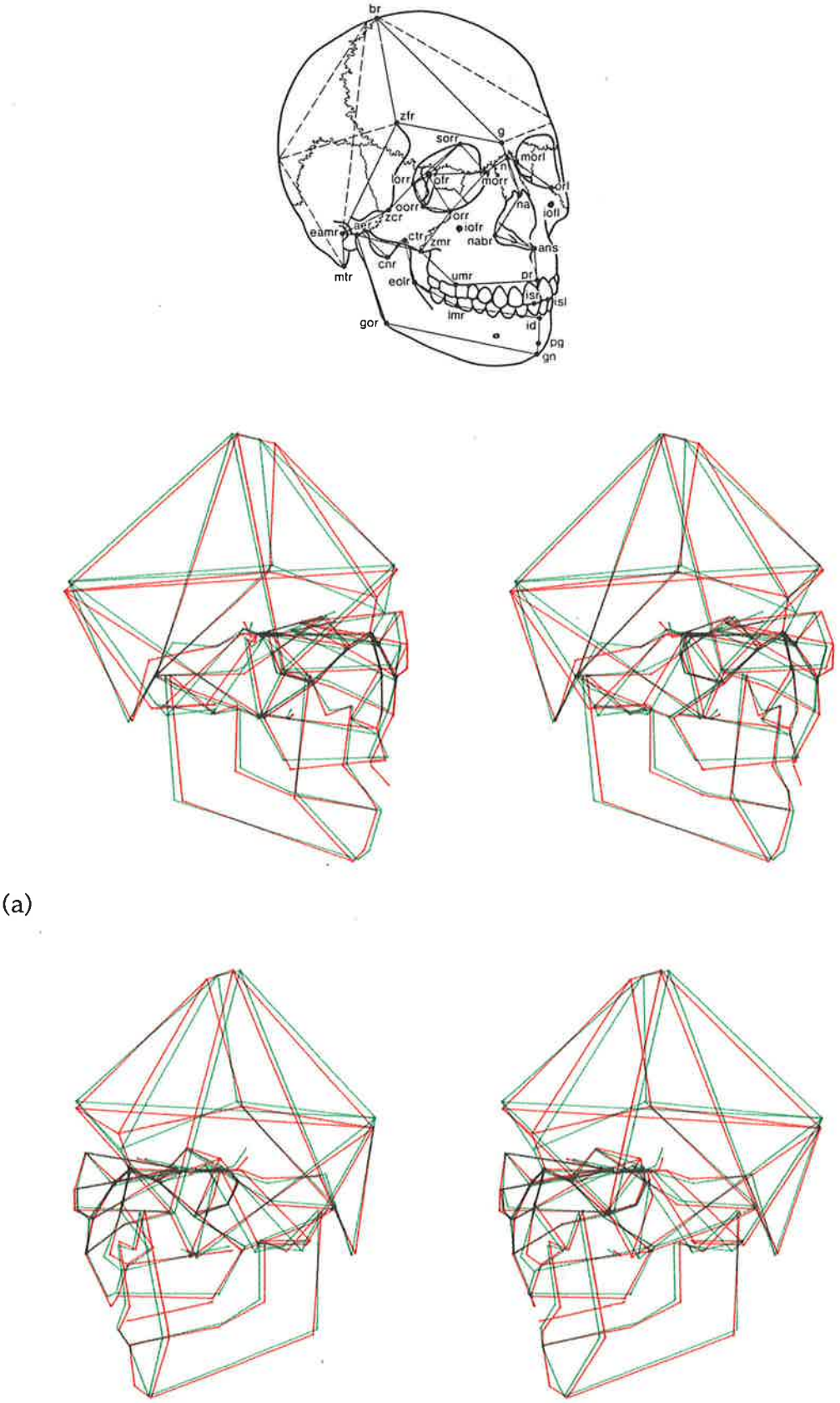

(a)

Figure 6.19 (a) Scaled least squares comparison of the male skull with the least squares skull standard.

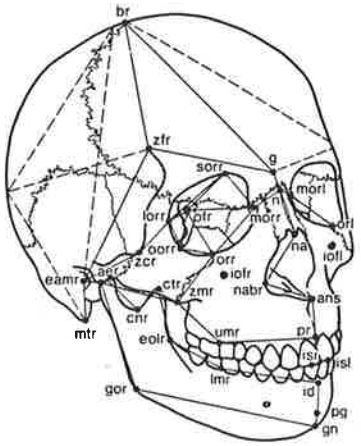

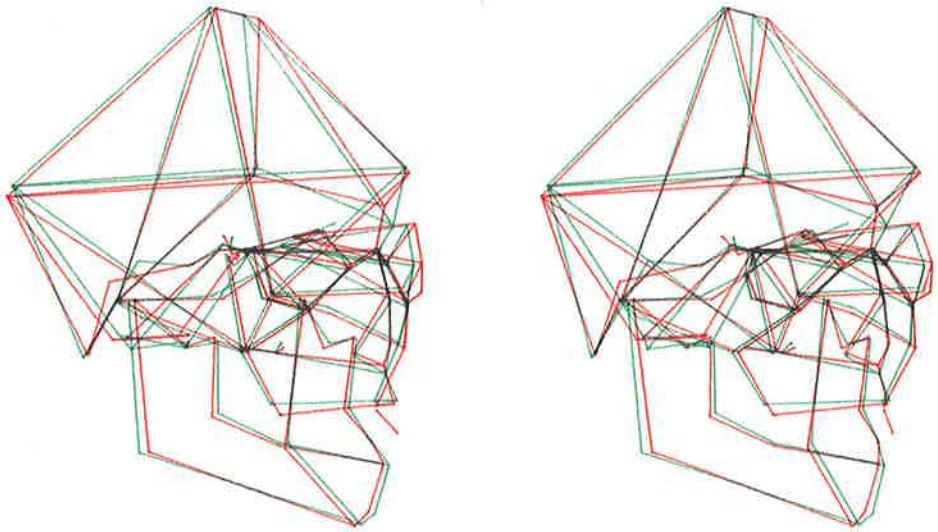

(b)

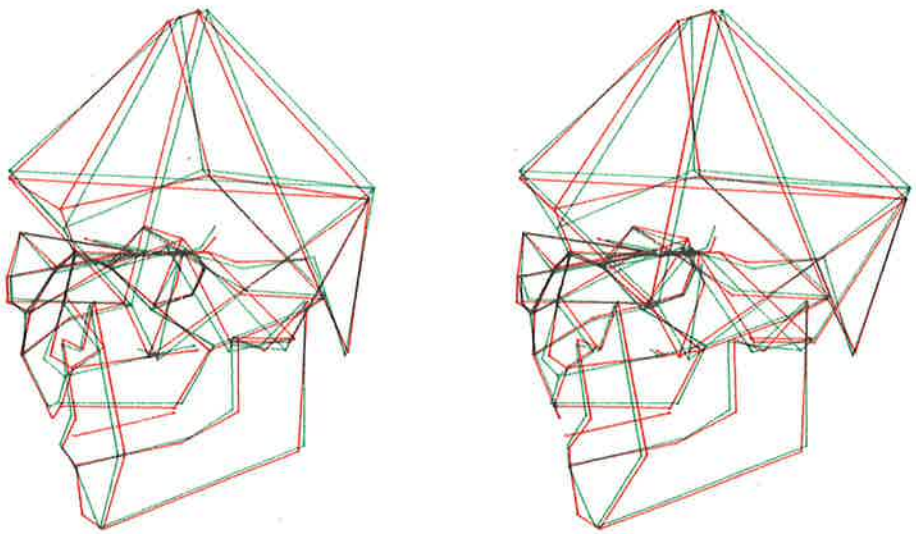

Figure 6.19 (b) Scaled repeated median comparison of the male skull with the repeated median skull standard.

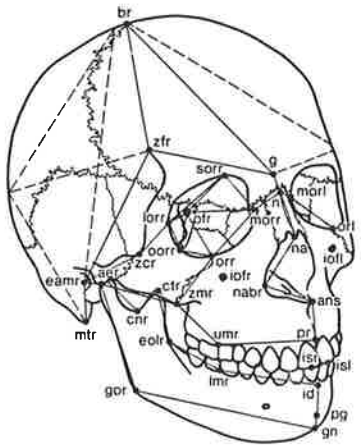

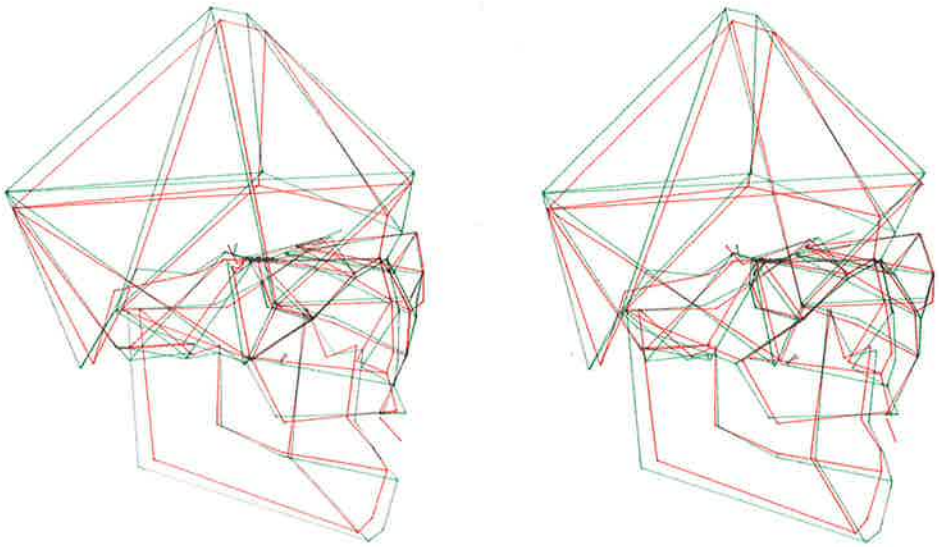

(c)

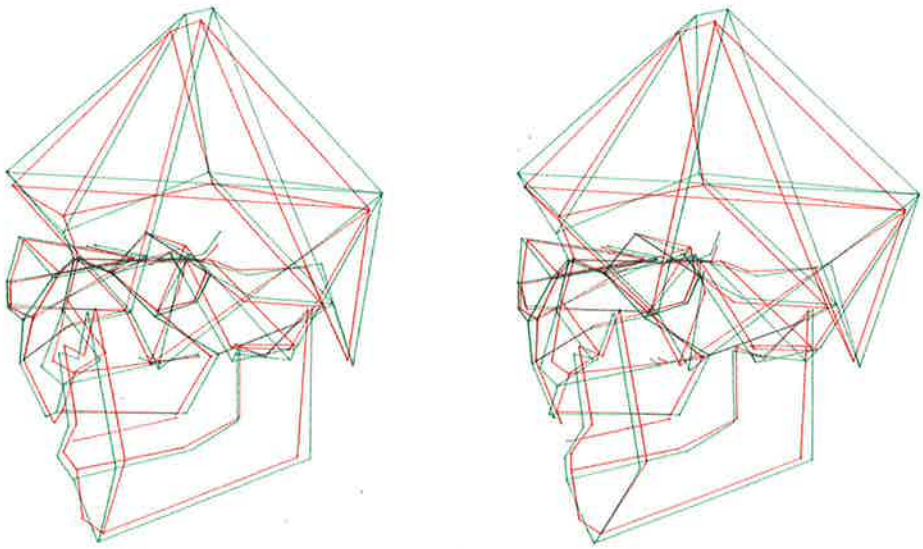

Figure 6.19 (c) Non-scaled least squares comparison of the male skull with the least squares skull standard.

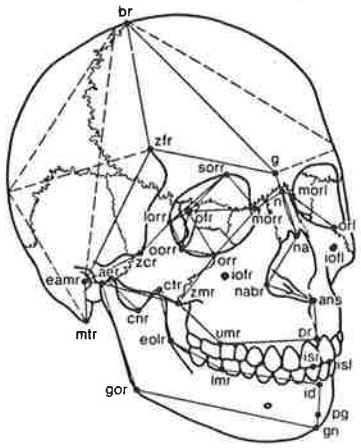

(d)

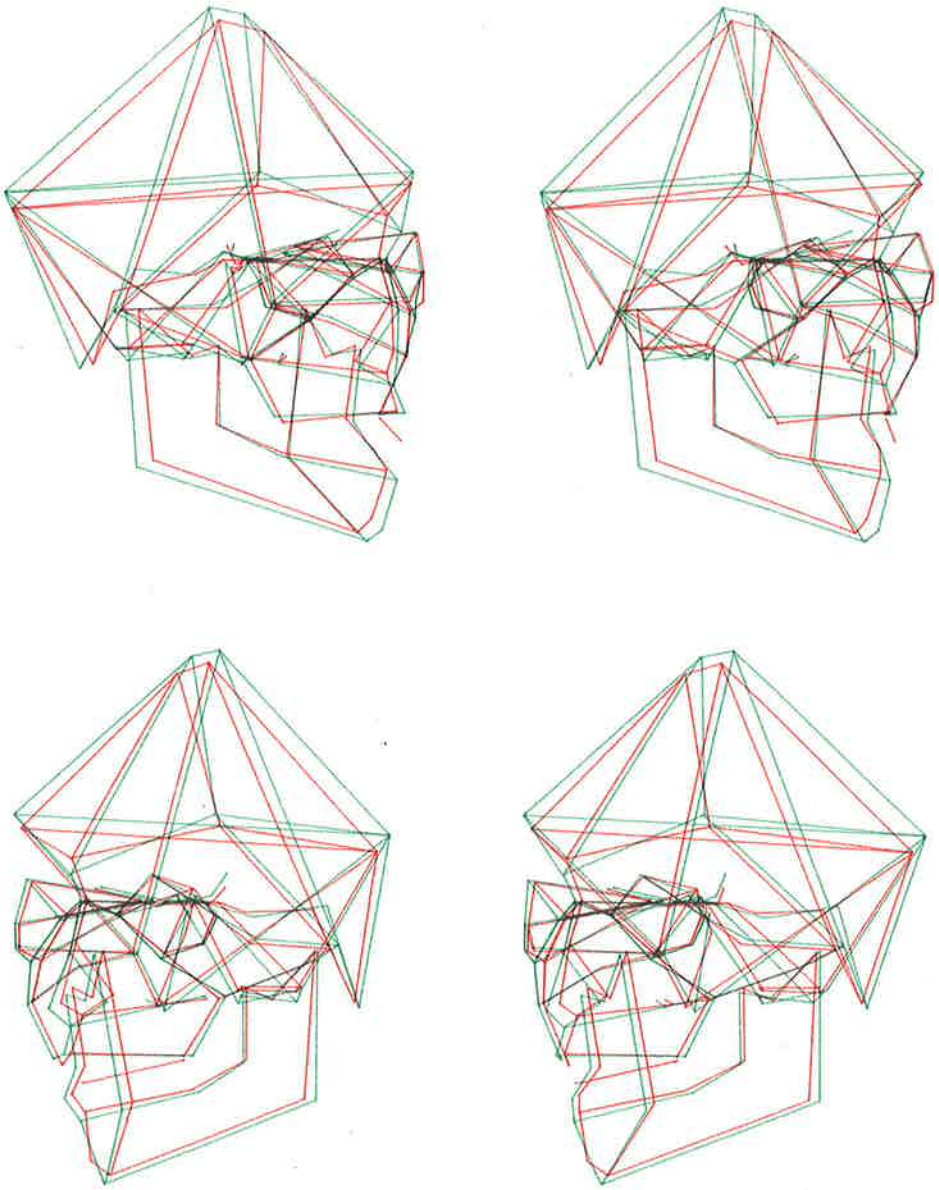

Figure 6.19 (d) Non-scaled repeated median comparison of the male skull with the repeated median skull standard.

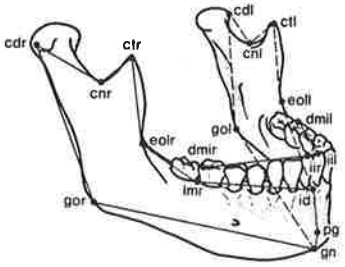

(a)

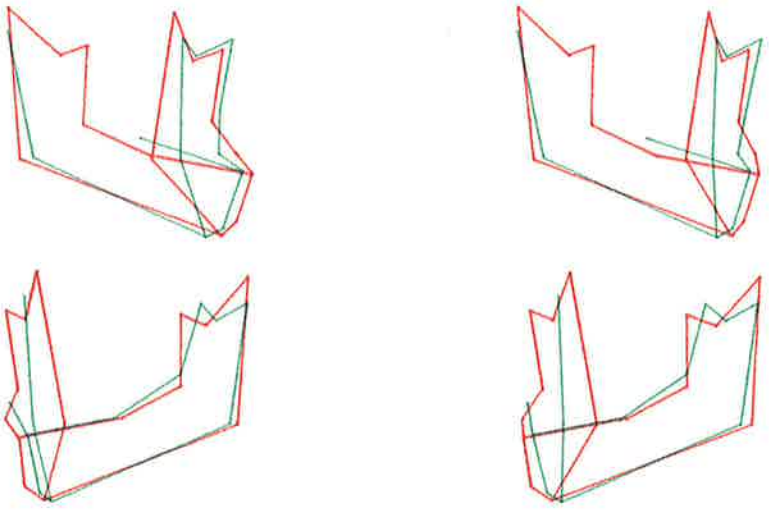

(b)

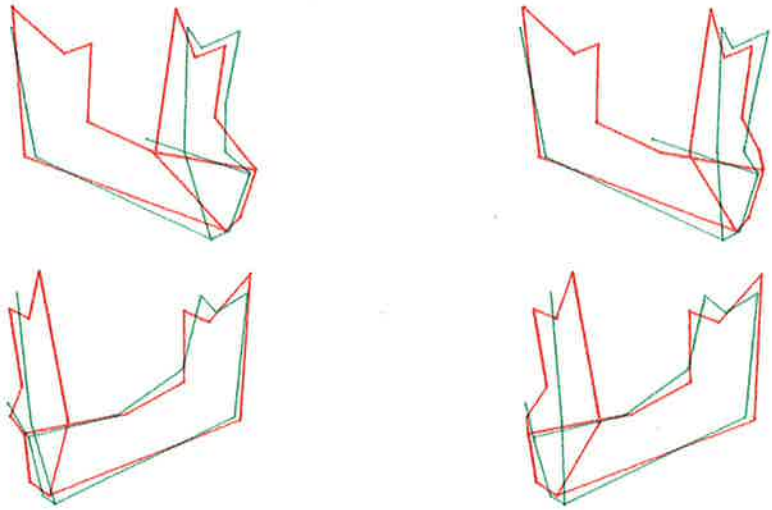

Figure 7.1 (a) Scaled least squares comparison of the Treacher Collins Syndrome patient with the least squares mandible standard.

(b) Scaled repeated median comparison of the Treacher Collins Syndrome patient with the repeated median mandible standard.

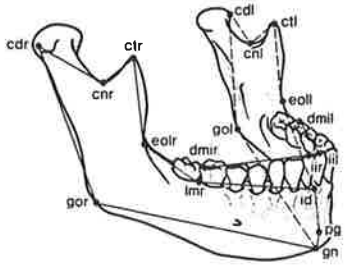

(c)

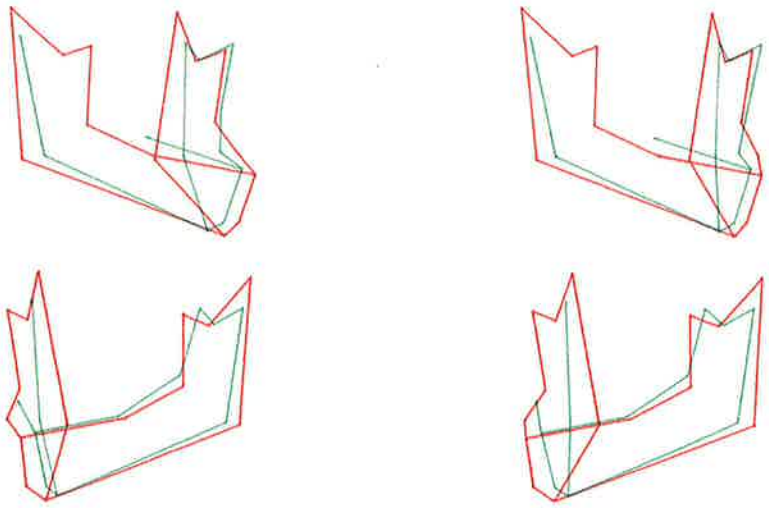

(d)

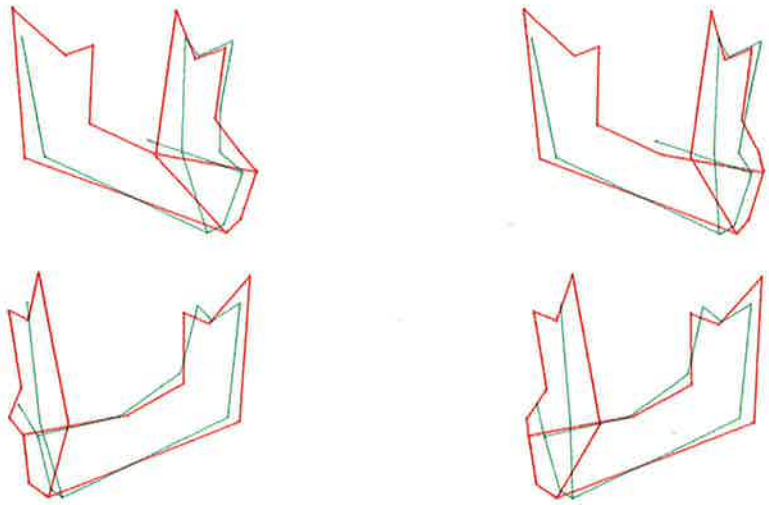

Figure 7.1 (c) Non-scaled least squares comparison of the Treacher Collins Syndrome patient with the least squares mandible standard.

(d) Non-scaled repeated median comparison of the Treacher Collins Syndrome patient with the repeated median mandible standard.

Figure 7.2 (a) Left 45° and (b) right 45° views showing shape comparison between the patient's mandible and the experimental reference mandible standard using strain analysis. The upper stereo pairs show the principal strains and directions (red - minor, green - major) required to deform the mandible standard to produce the shape of the patient's mandible. The lower stereo pairs show the principal strains and directions (green - minor, red - major) required to deform the patient's mandible to produce the shape of the mandible standard.

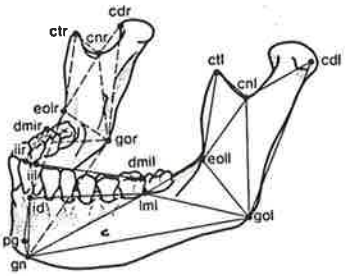
cdr
ctr
cnr
ctl
cnl
cdl
eolr
dmir
gor
eoll
dmil
ili
iil
lmi
gol
c
pg
gn

(a)

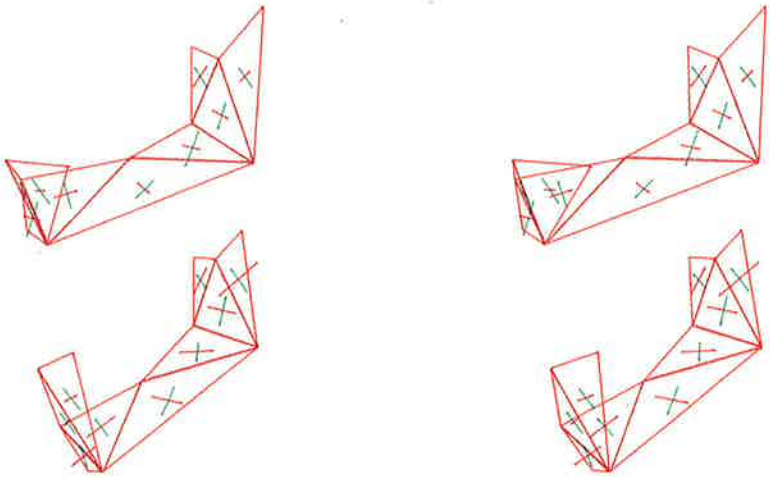

(b)

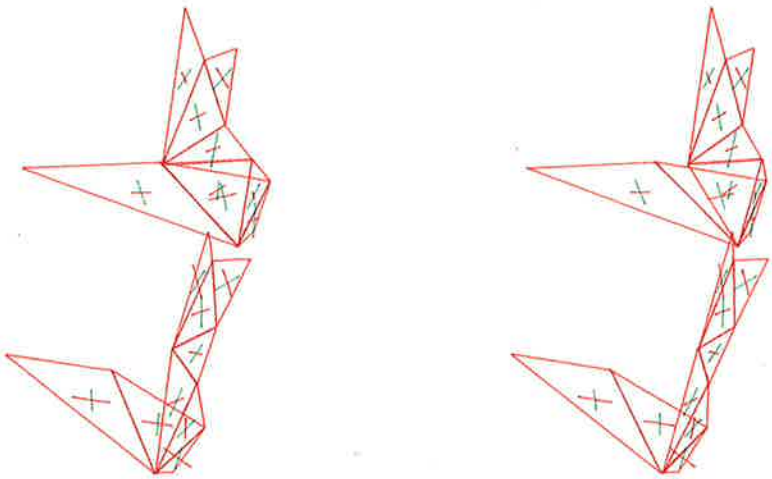

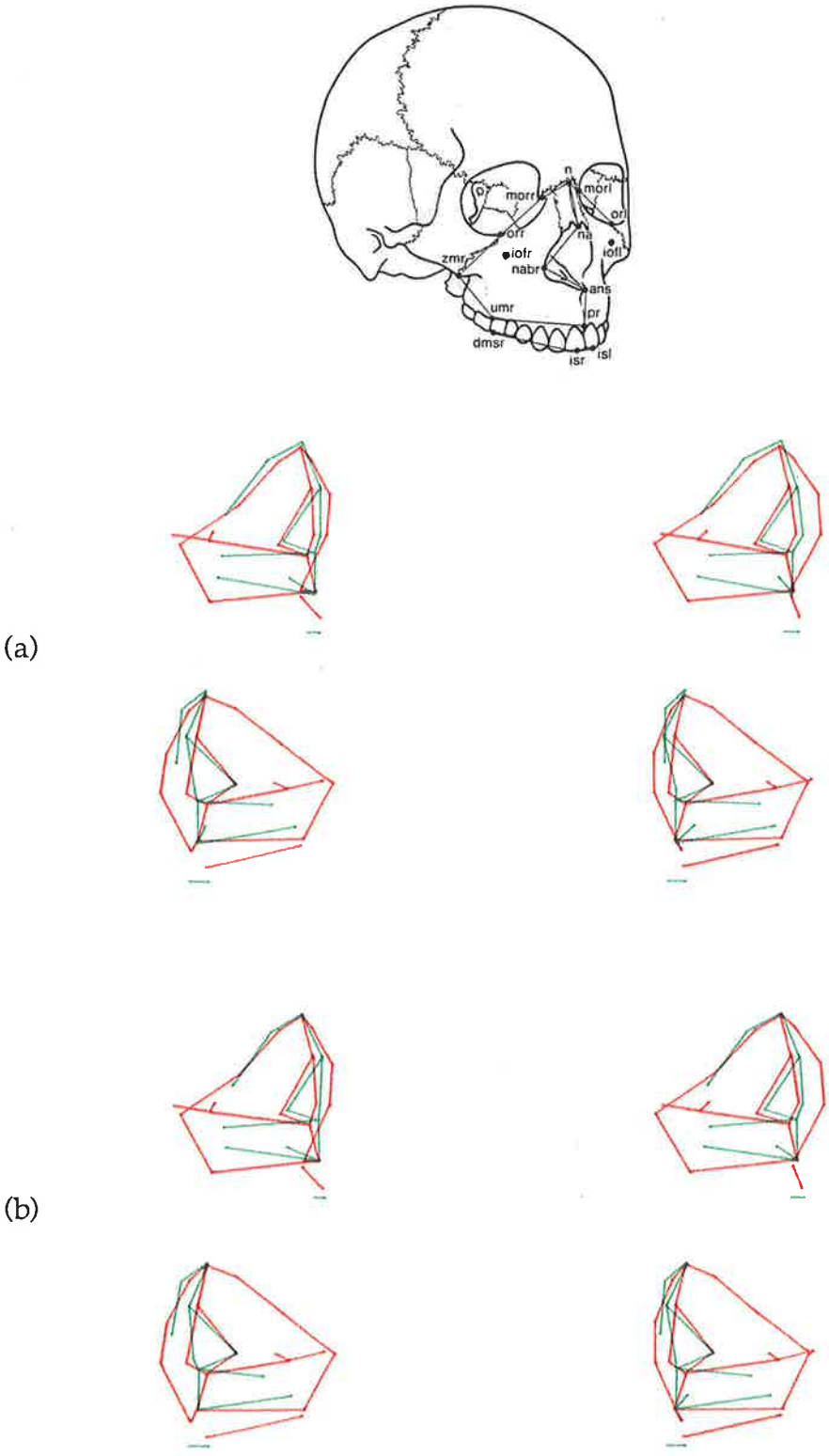

Figure 7.3 (a) Scaled least squares comparison of the Treacher Collins Syndrome patient with the least squares maxilla standard.

(b) Scaled repeated median comparison of the Treacher Collins Syndrome patient with the repeated median maxilla standard.

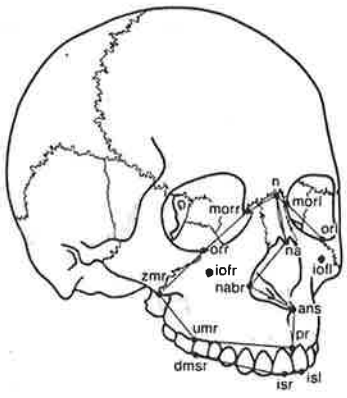

(c)

(d)

Figure 7.3 (c) Non-scaled least squares comparison of the Treacher Collins Syndrome patient with the least squares maxilla standard.

(d) Non-scaled repeated median comparison of the Treacher Collins Syndrome patient with repeated median maxilla standard.

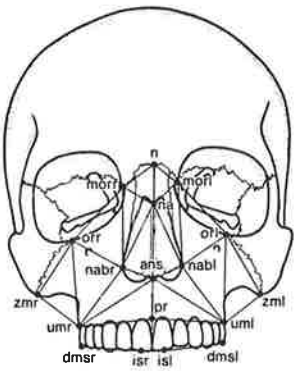

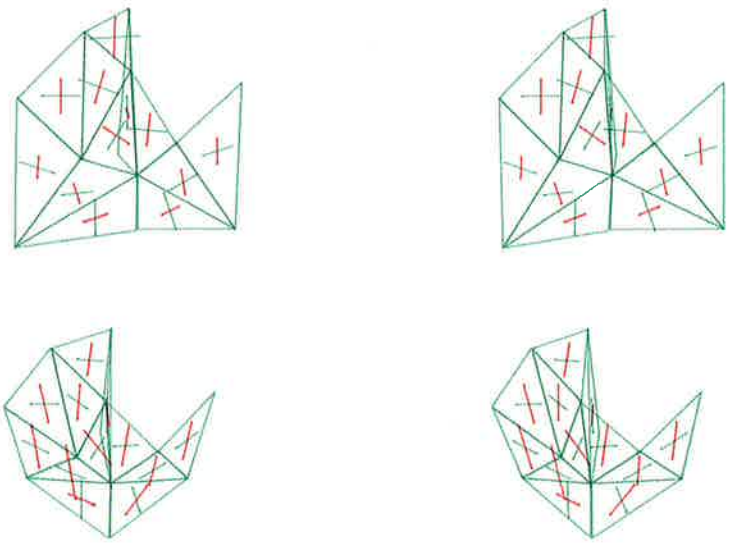

Figure 7.4 Shape comparison between the patient's maxilla and the experimental reference maxilla standard using strain analysis. The upper stereo pair shows the principal strains and directions (red - minor, green - major) required to deform the maxilla standard to produce the shape of the patient's maxilla. The lower stereo pair shows the principal strains and directions (green - minor, red - major) required to deform the patient's maxilla to produce the shape of the maxilla standard.

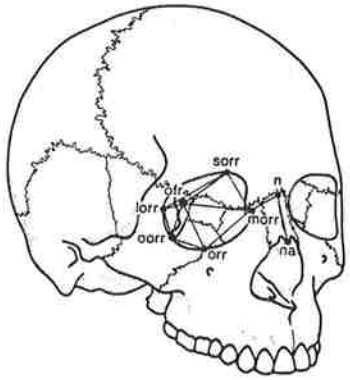

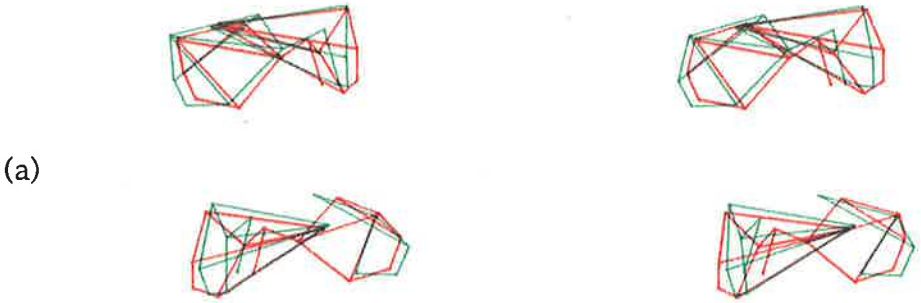

(a)

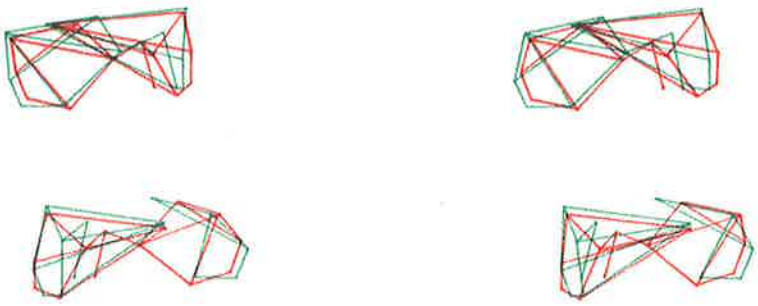

(b)

Figure 7.5 (a) Scaled least squares comparison of the Treacher Collins Syndrome patient with the least squares orbit standard.

(b) Scaled repeated median comparison of the Treacher Collins Syndrome patient with the repeated median orbit standard.

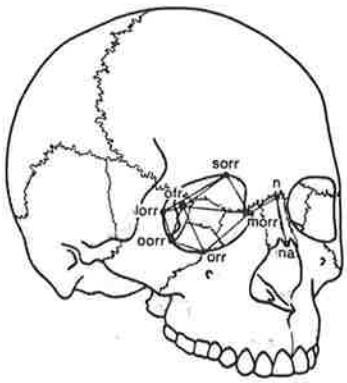

(c)

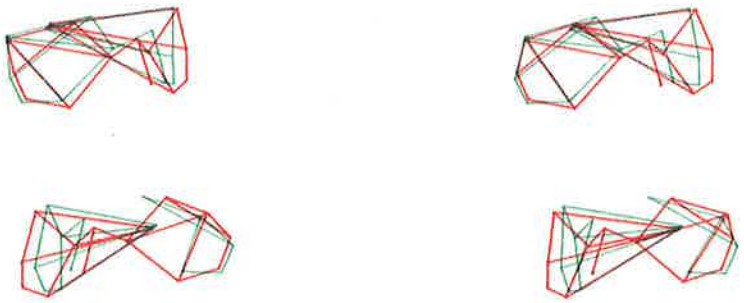

(d)

Figure 7.5 (c) Non-scaled least squares comparison of the Treacher Collins Syndrome patient with the least squares orbit standard.

(d) Non-scaled repeated median comparison of the Treacher Collins Syndrome patient with the repeated median orbit standard.

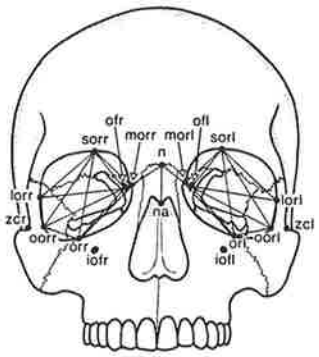

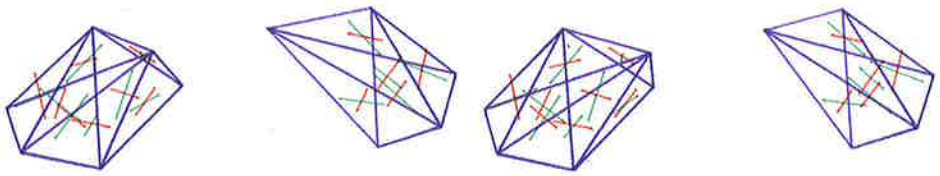

(a)

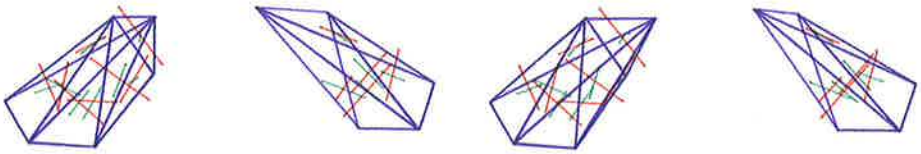

Figure 7.6 (a) Shape comparison between the patient's orbit and the experimental reference orbit standard using strain analysis of both the anterior border of the orbit and the surface of the orbital cone. The upper stereo pairs show the principal strains and directions (red - minor, green - major) required to deform the orbit standard to produce the shape of the patient's orbit. The lower stereo pairs show the principal strains and directions (green - minor, red - major) required to deform the patient's orbit to produce the shape of the orbit standard.

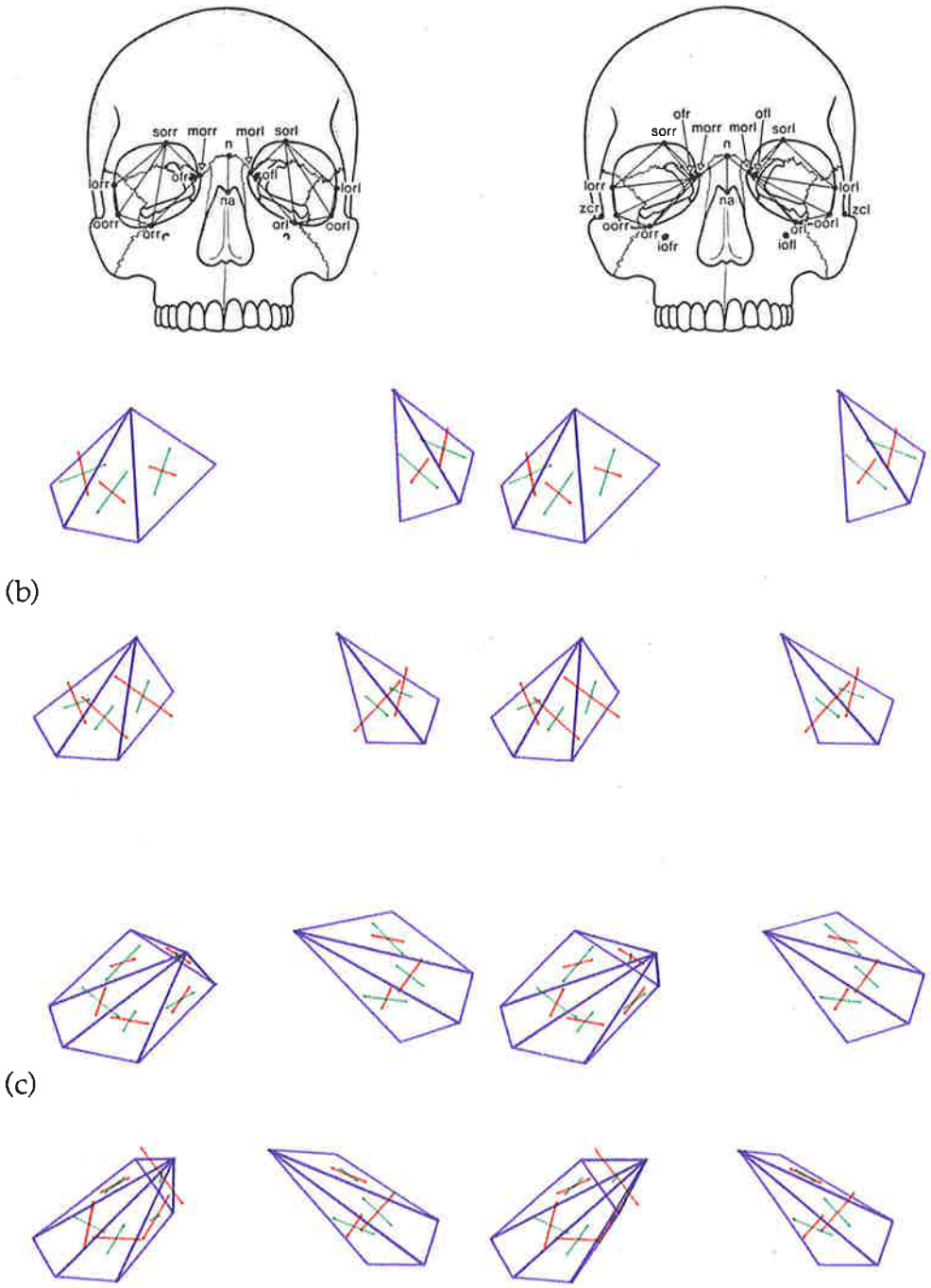

Figure 7.6 Shape comparison between the patient's orbit and the experimental reference orbit standard using strain analysis of (b) the anterior border of the orbit and (c) the surface of the orbital cone. The upper stereo pairs show the principal strains and directions (red - minor, green - major) required to deform the orbit standard to produce the shape of the patient's orbit. The lower stereo pairs show the principal strains and directions (green - minor, red - major) required to deform the patient's orbit to produce the shape of the orbit standard.

Figure 7.7 (a) Both lateral and medial tetrahedra, (b) lateral tetrahedron and (c) medial tetrahedron showing shape comparison between the patient's right orbit and the experimental reference orbit standard using three dimensional strain analysis. The upper stereo pairs show the principal strains and directions (red - minor, green - semi-major, purple - major) required to deform the orbit standard to produce the shape of the patient's orbit. The lower stereo pairs show the principal strains and directions (purple - minor, green - semi-major, red - major) required to deform the patient's orbit to produce the shape of the orbit standard.

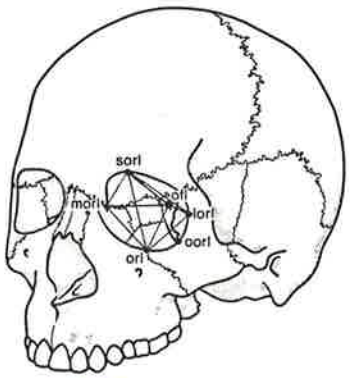

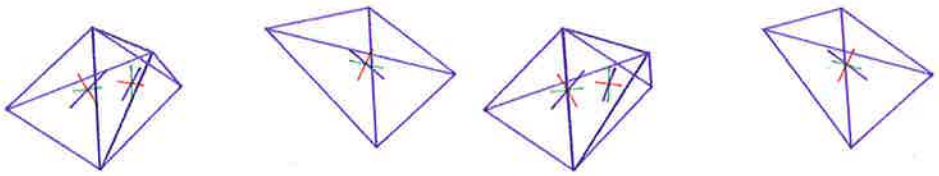

(a)

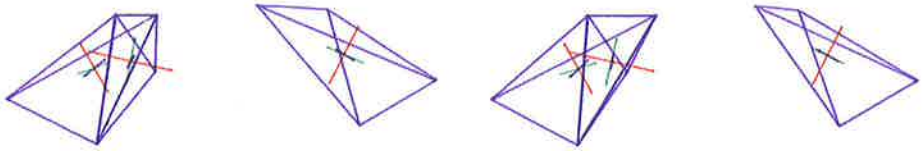

(b)

(c)

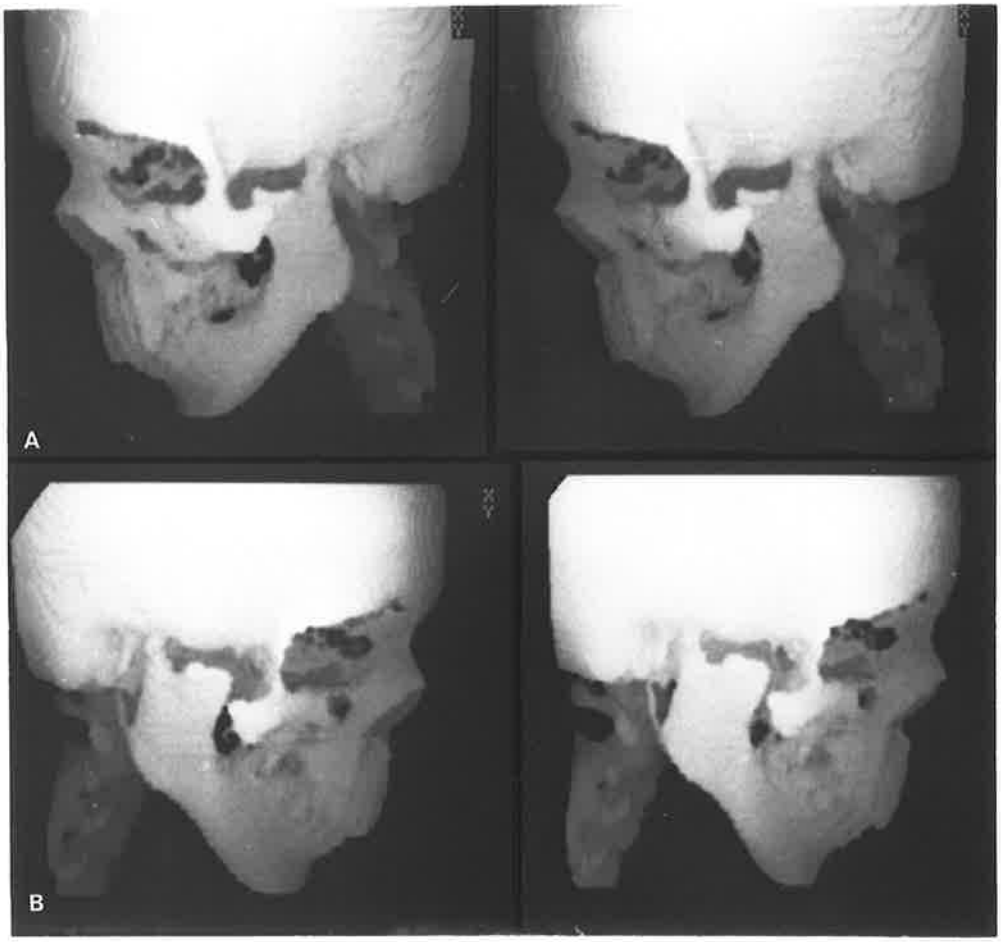

Figure 7.8 Near lateral (a) left and (b) right three dimensional CT reconstructions showing the severe hypoplastic nature of the patient's zygomas and absence of both zygomatic arches.

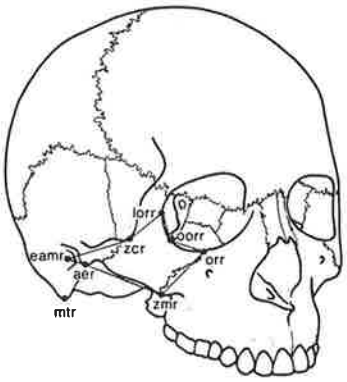

(a)

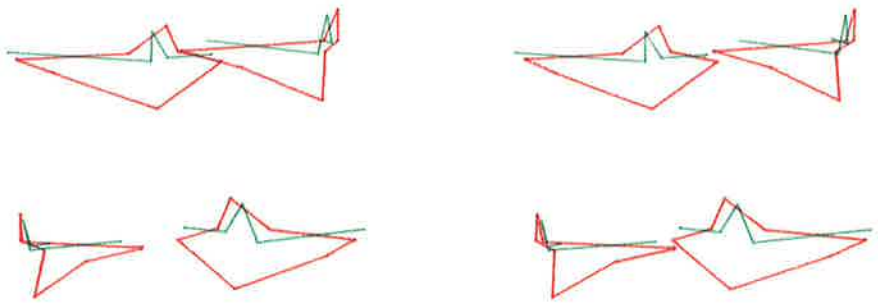

(b)

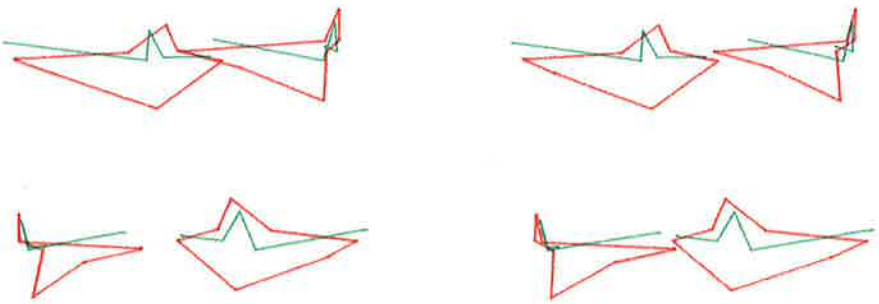

Figure 7.9 (a) Scaled least squares comparison of the Treacher Collins Syndrome patient with the least squares zygoma standard.

(b) Scaled repeated median comparison of the Treacher Collins Syndrome patient with the repeated median zygoma standard.

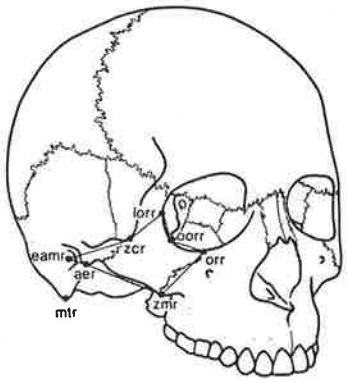

(c)

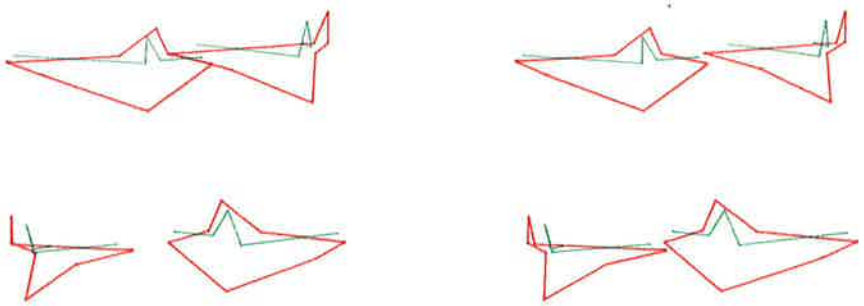

(d)

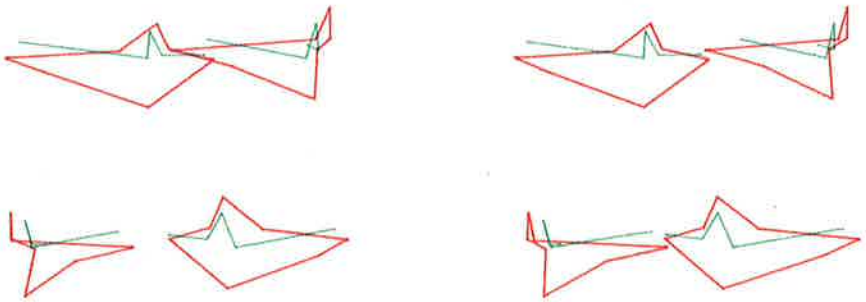

Figure 7.9 (c) Non-scaled least squares comparison of the Treacher Collins Syndrome patient with the least squares zygoma standard.

(d) Non-scaled repeated median comparison of the Treacher Collins Syndrome patient with the repeated median zygoma standard.

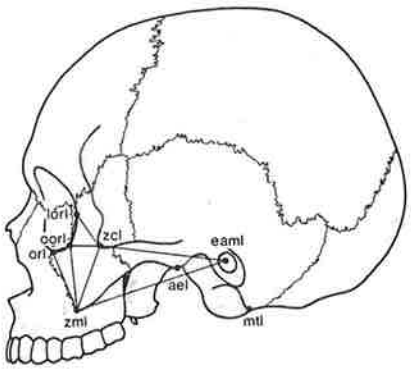

(a)

(b)

Figure 7.10 Shape comparison between (a) the left and (b) the right zygomas of the patient and the experimental reference zygoma standard using strain analysis. The upper stereo pairs show the principal strains and directions (red - minor, green - major) required to deform the zygoma standard to produce the shape of the patient's zygoma. The lower stereo pairs show the principal strains and directions (green - minor, red - major) required to deform the patient's zygoma to produce the shape of the zygoma standard.

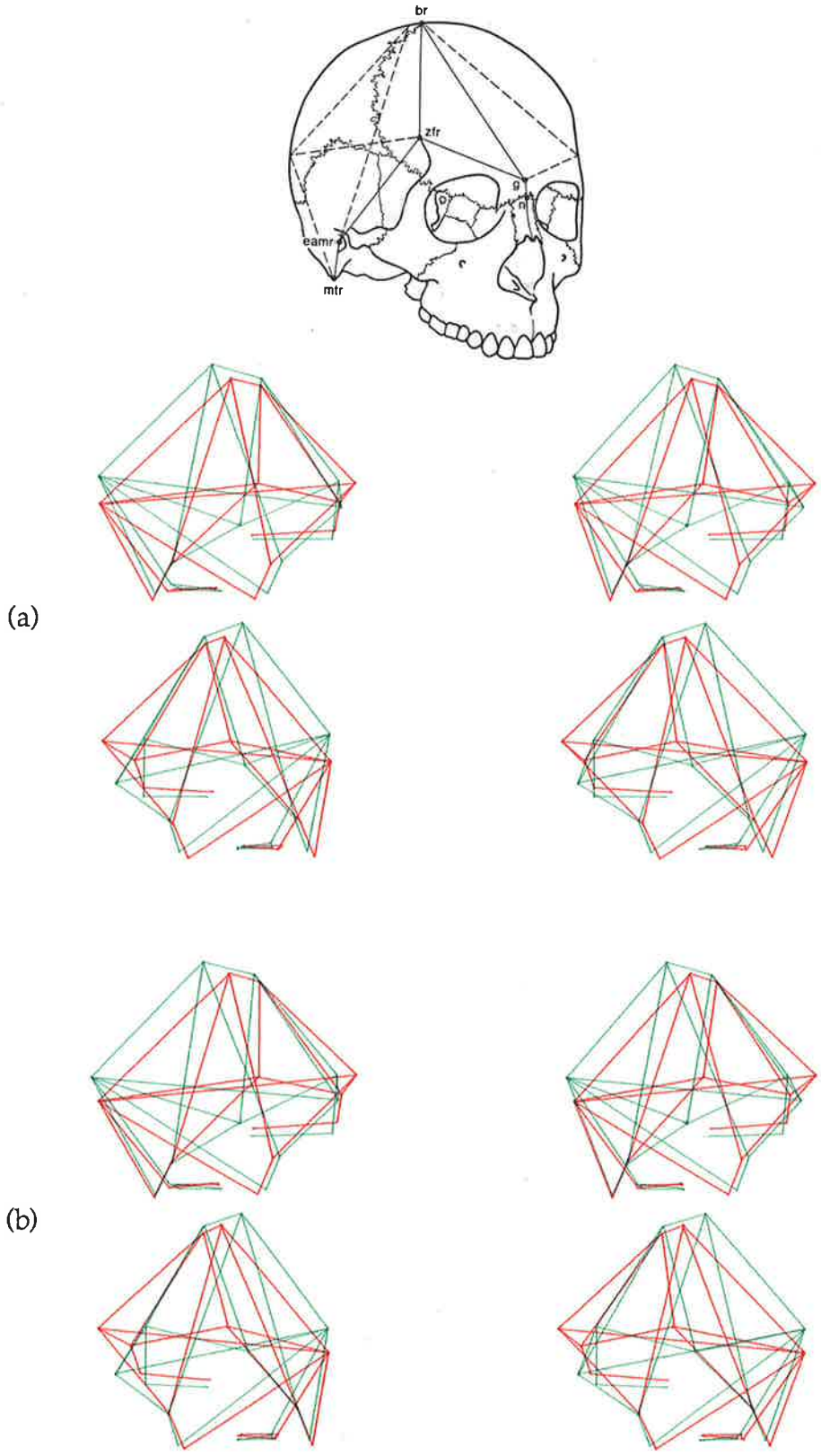

Figure 7.11 (a) Scaled least squares comparison of the Treacher Collins Syndrome patient with the least squares cranium standard.

(b) Scaled repeated median comparison of the Treacher Collins Syndrome patient with the repeated median cranium standard.

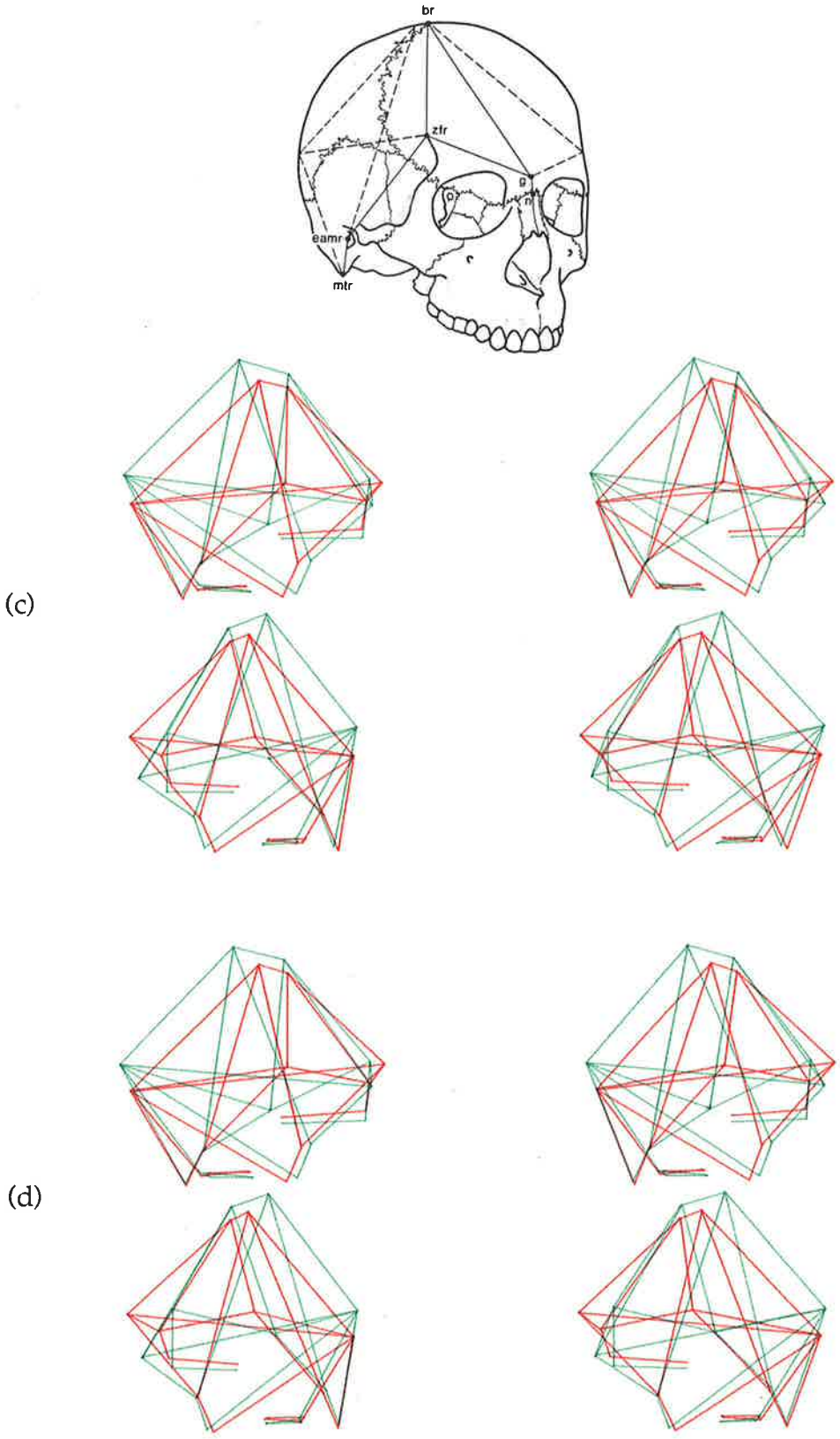

Figure 7.11 (c) Non-scaled least squares comparison of the Treacher Collins Syndrome patient with the least squares cranium standard.

(d) Non-scaled repeated median comparison of the Treacher Collins Syndrome patient with the repeated median cranium standard.

Figure 7.12 (a) Left 90° and (b) right 90° views showing shape comparison between the patient's cranium and the experimental reference cranium standard using strain analysis. The upper stereo pairs show the principal strains and directions (red - minor, green - major) required to deform the cranium standard to produce the shape of the patient's cranium. The lower stereo pairs show the principal strains and directions (green - minor, red - major) required to deform the patient's cranium to produce the shape of the cranium standard.

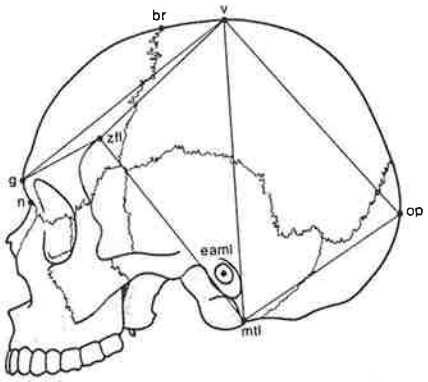

(a)

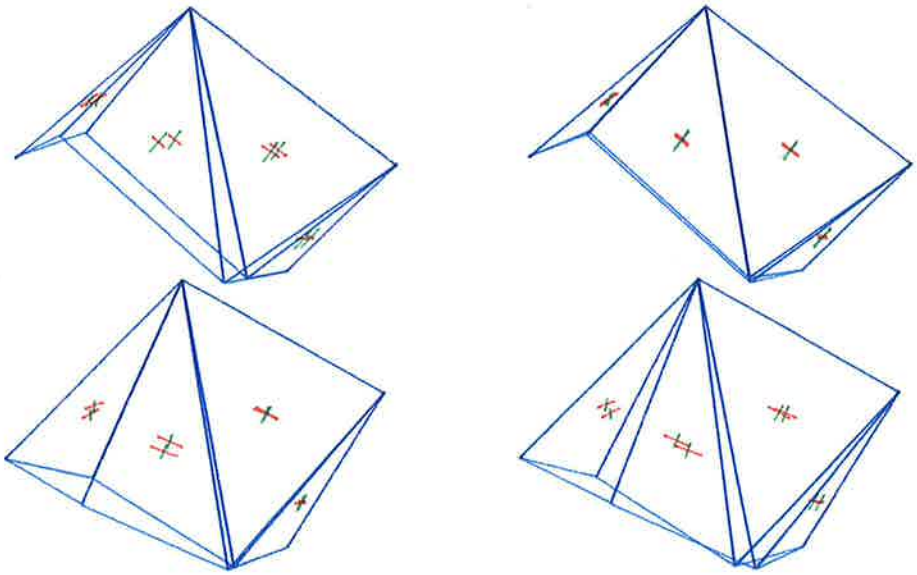

(b)

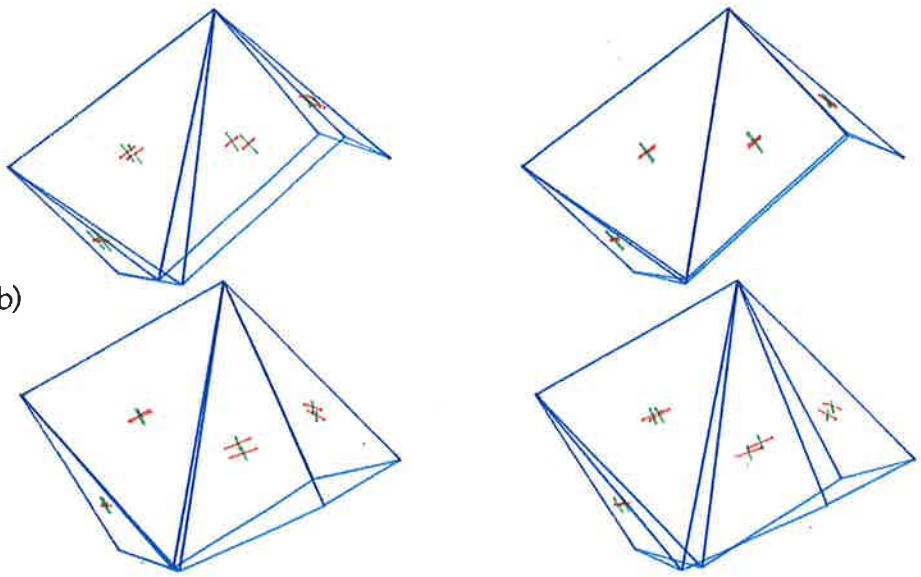

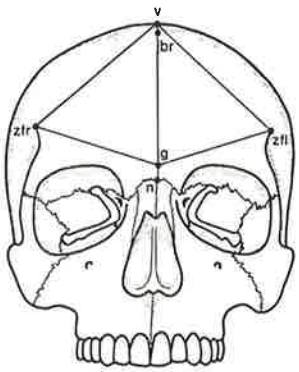

(c)

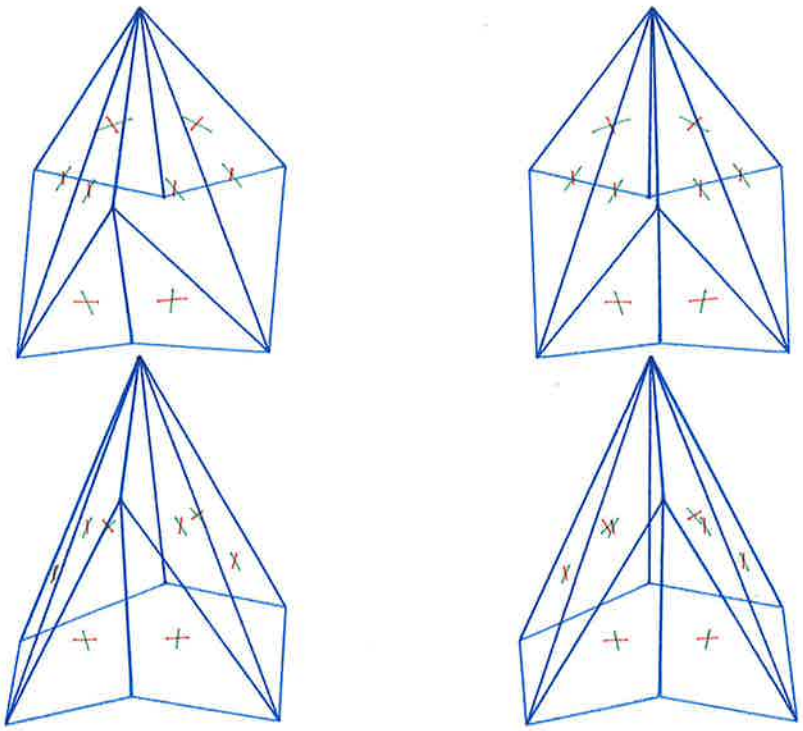

Figure 7.12 (c) Frontal view showing shape comparison between the patient's cranium and the experimental reference cranium standard using strain analysis. Note the bilateral symmetry. The upper stereo pairs show the principal strains and directions (red - minor, green - major) required to deform the cranium standard to produce the shape of the patient's cranium. The lower stereo pairs show the principal strains and directions (green - minor, red - major) required to deform the patient's cranium to produce the shape of the cranium standard.

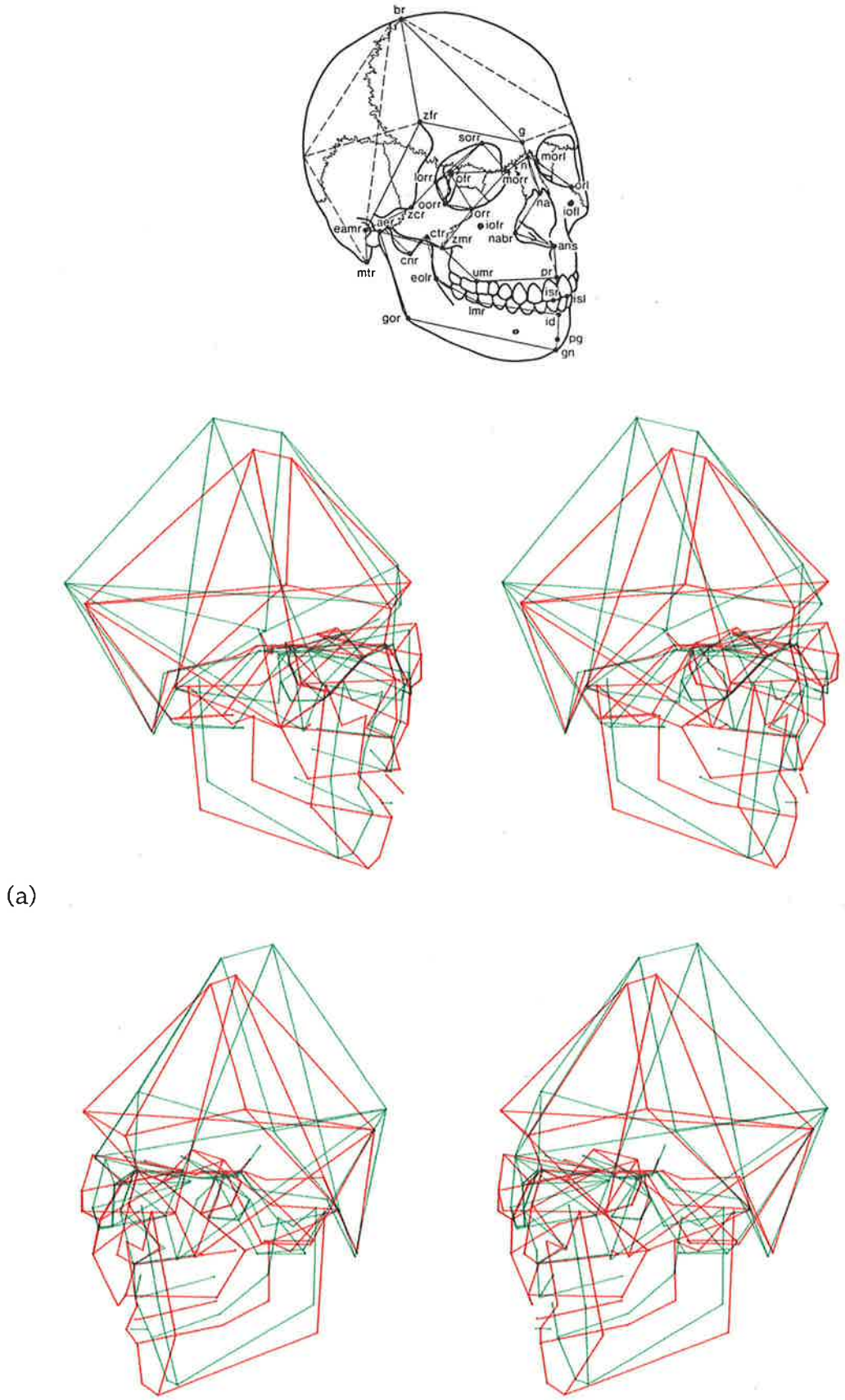

(a)

Figure 7.13 (a) Scaled least squares comparison of the Treacher Collins Syndrome patient with the least squares skull standard.

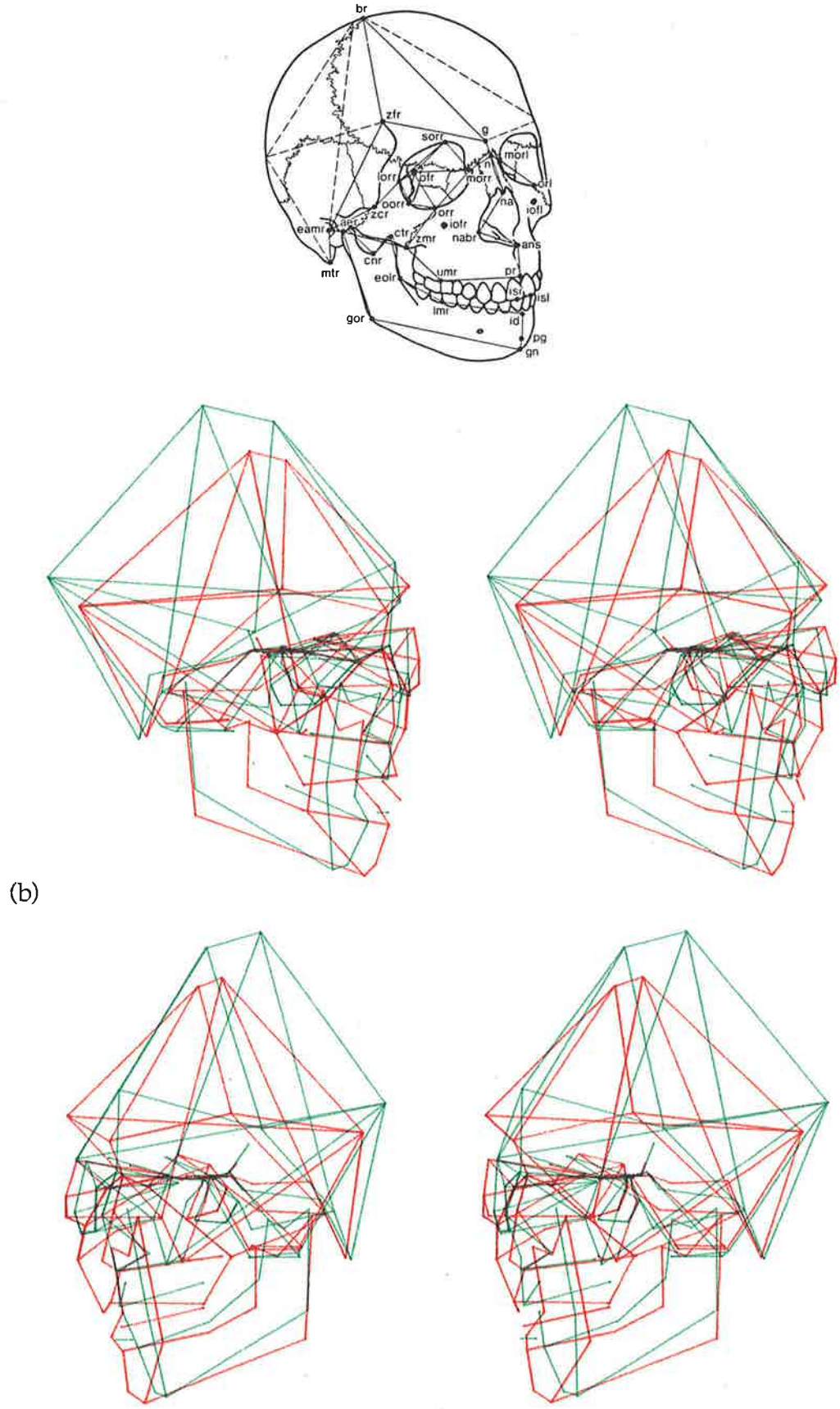

Figure 7.13 (b) Scaled repeated median comparison of the Treacher Collins Syndrome patient with the repeated median skull standard.

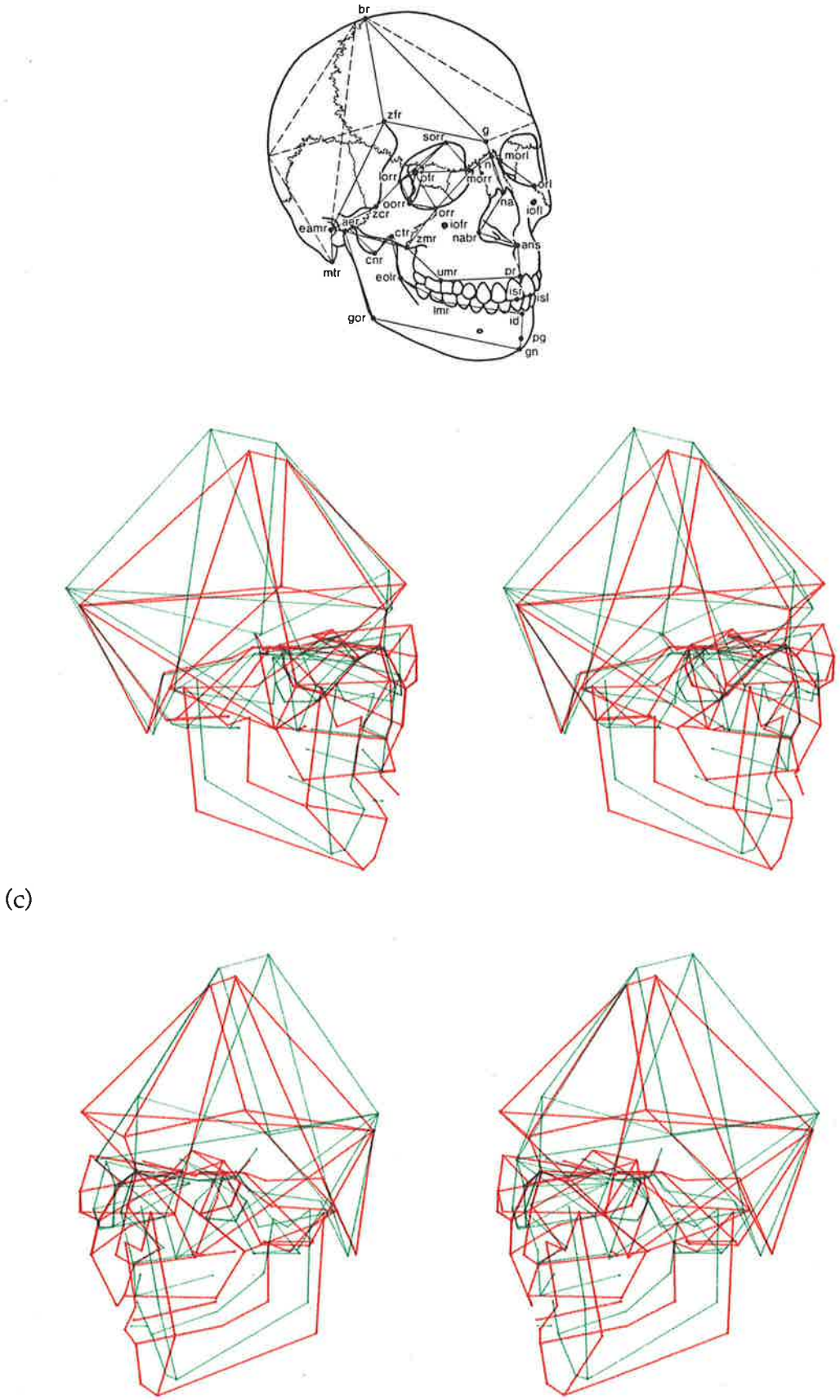

(c)

Figure 7.13 (c) Non-scaled least squares comparison of the Treacher Collins Syndrome patient with the least squares skull standard.

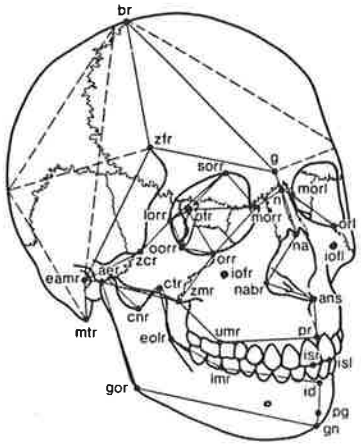

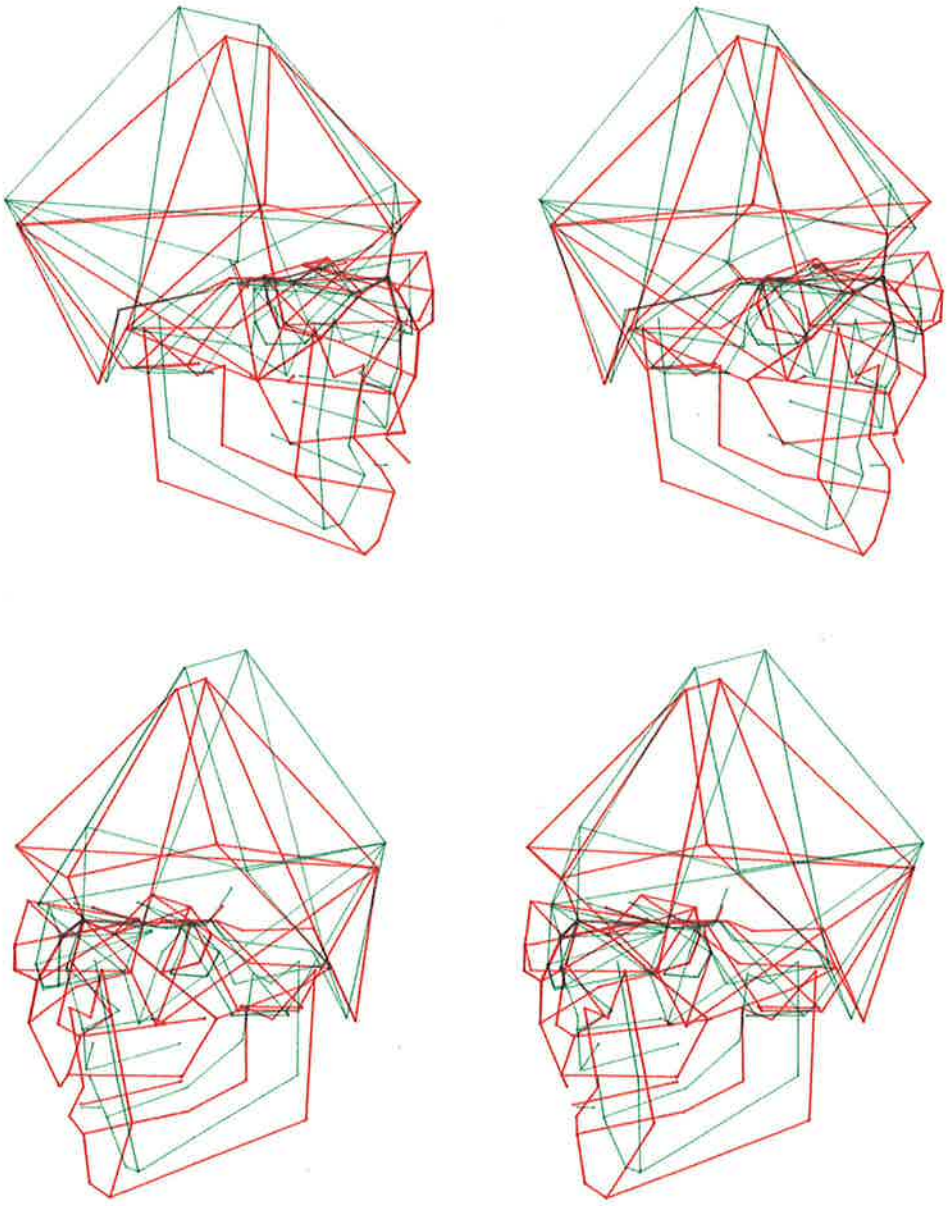

(d)

Figure 7.13 (d) Non-scaled repeated median comparison of the Treacher Collins Syndrome patient with the repeated median skull standard.